A study of the FM-AFM phase transition in FeRh : compositionally graded films and strain control

Doan Nguyen Ba

Communauté
UNIVERSITÉ Grenoble Alpes

THÈSE

Pour obtenir le grade de

DOCTEUR DE LA COMMUNAUTÉ UNIVERSITÉ GRENOBLE ALPES

Spécialité : **Physique des matériaux**

Arrêté ministériel : 7 août 2006

Présentée par

Doan NGUYEN BA

Thèse dirigée par **Nora DEMPSEY** et
codirigée par **Laurent RANNO**

préparée au sein de **l'Institut NÉEL, CNRS**
dans **l'École Doctorale de Physique de Grenoble**

A study of the FM-AFM phase transition in FeRh: compositionally graded films and strain control

Thèse soutenue publiquement le **07 septembre 2016**,
devant le jury composé de :

M. Marc VERDIER
Dr, SIMaP, CNRS DR2, Grenoble — Président

M. E. H. BRÜCK
Professeur, Delft University of Technology, Pays-bas — Rapporteur

M. Massimo GHIDINI
Dr, U. Cambridge & U. Parma, Royaume-Uni & Italie — Rapporteur

M. Vojtěch UHLÍŘ
Dr, Brno University of Technology, Tchèquie — Examinateur

M. Laurent RANNO
Enseignant-chercheur, U. Grenoble Alpes, Grenoble — Co-encadrant

Mme. Nora DEMPSEY
Directeur de Recherche CNRS, Institut Néel, Grenoble — Directeur de thèse

Abstract

This thesis deals with the study and control of phase transition characteristics in magnetic films. In the case of FeRh-based magnetron sputtered films, the influence of both composition and strain were studied. Magnetic, structural and electrical characterization was made as a function of position on compositionally graded films. Addition of a third element (Pt or Ni) was used to shift the transition temperature. We established that a change in optical properties occurs in FeRh-based films on passing from the FM to AFM state. By studying the temperature dependent position of the optical transition, we were able to construct a phase diagram of the Fe-Rh-Pt system. Such a detailed phase diagram based on a continuous variation of composition, evidences an enhanced stability (higher transition temperature) of the AFM phase for a specific composition close to the equiatomic one. Strain control of the phase change in PMN-PT/FeRh heterostructures was investigated through transport measurements using set-ups developed in this thesis. The transition temperature could be shifted by up to 22 K upon application of a low electric field ($10\,\mathrm{V} \sim 0.32\,\mathrm{kV/cm}$). The strain-induced resistance change is large, which is attractive for applications. The AFM state is stabilized in these anisotropically strained films. The anisotropic character of the piezo-electric strain plays a significant role compared to the isotropic volume change. We succeeded in preparing films of $La(Fe,Si)_{13}$ for the first time. While the optimal films show values of Curie temperature, lattice constant, field-induced isothermal entropy change and spontaneous magnetization comparable with values reported for bulk material of similar composition, they also display unusual features, i.e. irreversible M-T curves and an inverse thermal hysteresis. Elucidation of the origin of these effects requires further investigation.

Contents

List of Abbreviations

AFM	Antiferromagnetic
FM	Ferromagnetic
T_C	Curie temperature
H_C	Magnetic coercive field
E_C	Electric coercive field
T_t	First order transition temperature
ME	Magnetoelectric
PMN-PT	(1-x)Pb($Mg_{1/3}Nb_{2/3}$)O_3-x($PbTiO_3$)
SQUID	Superconducting quantum interference device

CHAPTER 1

Introduction

1.1 Context of this thesis

This thesis was carried out in the framework of an EU project dealing with the study of magnetocaloric materials (the "DRREAM" project - http://www.drream.eu). Most studies to date on these magnetic phase change materials have essentially concerned bulk samples and it has been shown that the phase change characteristics (transition temperature, transition width, hysteresis...), and thus the magnetocaloric response of a given sample, depend on the sample composition, crystallographic structure, microstructure, strain... [1, 2]. We proposed to use thin films as model systems to study the influence of composition and strain on phase change characteristics. In the former case, the idea was to prepare compositionally graded films on large substrates, and to study the structural and magnetic properties as a function of position on the wafer. Such an approach can in principle allow high-throughput sample preparation and characterization, and ensures that samples with different composition experience identical post-deposition annealing treatment. In the latter case, the idea was to deposit the film under study onto a piezoelectric substrate and to exploit deformation of the substrate under the influence of an electric field to strain the film. Compared to bulk studies in which hydrostatic pressure was used to apply an isotropic strain, the use of piezoelectric substrates allows us to apply anisotropic strain on the material under study.

FeRh was selected as the main material for this study, as belonging to a binary system, it was expected that it would be relatively easy to prepare compositionally graded films having samples of the appropriate composition. Besides, it shows a very high adiabatic temperature change due to its 1^{st} order antiferromagnetic $\rightarrow$ ferromagnetic transition (see below), making it one of the best magnetocaloric materials known [2]. Though FeRh is unsuitable for large-scale magnetic-refrigeration due to the prohibitive cost of Rh, it may eventually be considered for micro and nanoscale cooling applications where only very small volumes of materials are required. Besides, this phase has seen a renewed interest in recent years due to its potential use in spintronic applications.

Effort was also put into preparing La(Fe, Si)$_{13}$ films. Though this phase is already being produced at an industrial scale for magnetocaloric applications, there have been no reports of the preparation of this material in thin film form. This proved very challenging, and while we did succeed in producing the phase in films, problems with reproducibility prevented

us from extending the study to investigate the influence of strain in films deposited on piezoelectric substrates.

In this first chapter we will very briefly introduce the magnetocaloric effect and then present an overview of the FeRh and La-Fe-Si systems. We will then introduce some concepts related to the use of piezoelectric substrates to modify the magnetic properties of overlaying magnetic layers.

1.2 Phase change materials

The materials which are studied in this thesis belong to the magneto-caloric family. The magnetocaloric effect allows to transfer entropy from the lattice degrees of freedom to the magnetic ones. It is a way to reduce temperature (to make a refrigerator) by cycling the magnetic field applied to such material. In this thesis we study these materials as model systems, i.e. films deposited on thick substrates (piezoelectric or not), which makes that their temperature change is reduced because of the very large volume of the substrate compared to the active film volume. The magnetocaloric effect will not be the way to study these films and we will only give a short description of this effect.

1.2.1 Magnetocaloric effect

The magnetocaloric effect (MCE) refers to the change in temperature of a magnetic material, due to the application of an external magnetic field. Discovered in Fe in 1881, the effect in paramagnetic salts was exploited to reach sub-K temperatures in the 1930s. More recently, near room temperature, refrigeration has been demonstrated with Gd, and there has been a surge in interest following the discovery in 1997 of "giant" magnetocaloric materials ($Gd_5Si_2Ge_2$) [1]. Magnetic cooling offers up to 60 % of Carnot efficiency, much larger than in conventional refrigeration technologies, and is the only alternative technology which would simultaneously eliminate the need for harmful refrigerant gases and reduce the energy requirements, and hence carbon dioxide emissions.

The magnetocaloric effect arises due to the presence of two energy reservoirs in magnetic materials: one with phonon and the other with magnon excitations, the two being coupled through magnetoelastic (spin-lattice) interactions. An external magnetic field affects the spin degrees of freedom resulting in heating or cooling of magnetic materials. The magnetocaloric effect increases with increasing magnetic field and with increasing change in magnetization upon the application of the magnetic field and is thus maximum in the vicinity of magnetic phase transitions.

Giant MCE materials have a strong coupling between crystallographic structure and magnetism whereby a magnetic field can induce a simultaneous change of magnetic and lattice entropies. For example, in $Gd_5Si_2Ge_2$, a magnetic field-induced transformation from the paramagnetic, monoclinic phase to the ferromagnetic, orthorhombic phase brings about a giant MCE where lattice entropy change due to the structural transition contributes to more than half of the total entropy change. The recently reported “inverse MCE” in Ni-Mn-

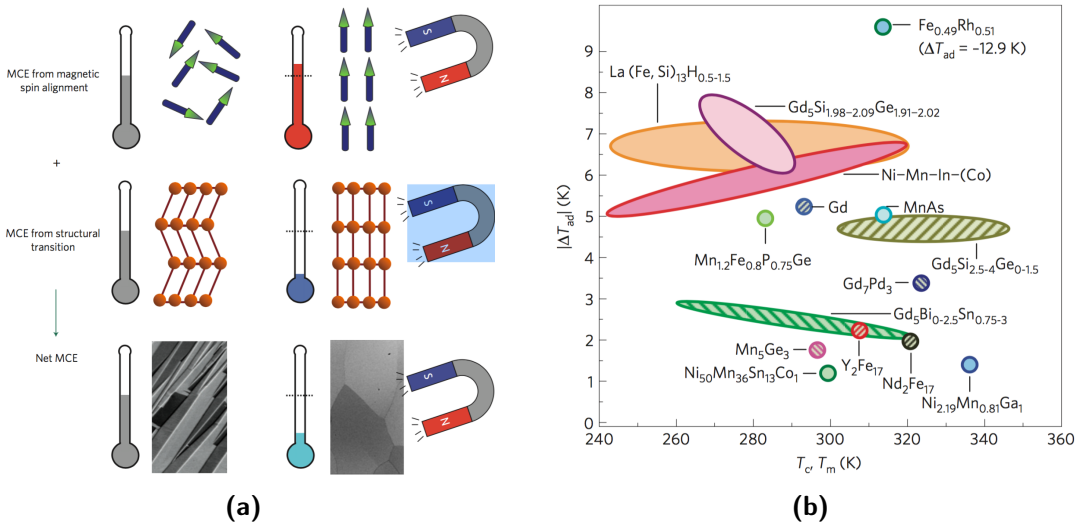

Figure 1.1. *(a) Contributions from the magnetic and structural part for a first order magnetic transition to the magnetocaloric effect (MCE). Alignment of magnetic moments by adiabatic magnetization makes the sample heat (top row); simultaneously the structural transition from low-magnetization and twinned martensitic phase to high-magnetization and high-symmetry austenitic phase leads to a very large cooling effect (middle row). The addition of these opposite contributions results in a net cooling of the sample (bottom row). (b) Adiabatic temperature change ($\triangle\mu_0 H = 2\,T$) for several of the most researched ambient magnetic refrigerants at either a purely magnetic transition temperature T_C (second-order transition, marked by hatched pattern) or magnetostructural coupling transition temperature T_m (first-order transition, solid fill-pattern). (Images taken from [3]).*

based Heusler alloys (the materials cool when magnetized and heat when demagnetized) is due to a structural transition from the paramagnetic/antiferromagnetic martensite phase to the ferromagnetic austenite phase upon the application of a magnetic field (figure 1.1a) [3]. As the absolute amount of heat absorption due to the structural transition exceeds that of heat release arising from the change of magnetic subsystem, the net temperature decreases upon magnetization. A comparison of the magneto-caloric performance of a wide range of materials is shown in figure 1.1b [3].

1.2.2 Thermodynamics of the magnetocaloric effect

Thermodynamics of phase transformation allows to study and understand the origin of transitions between physical states. In a thermodynamic model, a phase (a state of the thermodynamic system) is characterized by its internal parameters and its stability can be modified using external parameters such as pressure, magnetic field or temperature. A phase transition is defined as a transformation from one state to another. The stability of a state is determined by the Gibbs free energy. The Gibbs free energy G is expressed as a function of temperature and pressure as follows [4]:

$$G(T,\ P) = U + P.V - T.S \tag{1.1}$$

where: T - the temperature (K); P - the pressure (N/m^2); U - the internal energy (J); V - the volume (m^3); S - the entropy (J/K).

In a magnetic system, a contribution of the Zeeman energy due to the applied magnetic field should be added to the Gibbs free energy. Hence, the free energy can be expressed [5]:

$$G(T,\ P) = U + P.V - T.S - \mu_0 HMV \tag{1.2}$$

where: μ_0H - the applied magnetic field; M - the magnetization.

It should be mentioned that the entropy in equation 1.2 is a total entropy, which contains contributions from lattice vibrations, electronic and magnetic degrees of freedom. The system will be in a stable equilibrium when it minimizes Gibbs free energy: dG = 0.

When the pressure and temperature are constant (an isobaric - isothermal progress), the differential of the entropy with respect to the applied magnetic field B = μ_0H is given by:

$$dS = \left(\frac{\partial S}{\partial B}\right)_{T,P} dB \tag{1.3}$$

Combining with the Maxwell relation, this equation can be written as:

$$dS = \left(\frac{\partial M}{\partial T}\right)_{B,P} dB \tag{1.4}$$

The isothermal magnetic entropy change $\triangle S_M$ due to a magnetic field change from B_i to B_f can be calculated using an integration as follows:

$$\triangle S_M\left(T,B\right)\left[JK^{-1}m^{-3}\right] = \int_{B_i}^{B_f}\left(\frac{\partial M}{\partial T}\right)_{B,P} dB \tag{1.5}$$

For first order transitions, the Clausius-Clapeyron method is used to determine $\triangle S_M$ [6]:

$$\triangle S_M = -\frac{\triangle M}{\left(\frac{\triangle T}{\triangle B}\right)} \tag{1.6}$$

where: $\frac{\triangle T}{\triangle B}$ - the magnetic field change induced transition temperature change; $\triangle$M - the difference of magnetization between two phases (i.e. the martensite and austenite phases, the ferromagnetic and paramagnetic phases).

The second law of thermodynamics gives a relationship between the latent heat Q of the first order transition and the entropy of system:

$$Q = T(S_f - S_i) \tag{1.7}$$

where: S_i and S_f - the entropy of the initial phase and the final phase, respectively.

Hence, a measurement of the latent heat allows us to track the progress of the transformation.

Besides the magnetic entropy change $\triangle S_M$, the adiabatic temperature change $\triangle T_{ad}$ and the refrigerant capacity RC are also typical quantities to characterise the phase transition. The adiabatic temperature change can be either measured directly by monitoring the temperature change when the sample is exposed to a changing magnetic field or determined from a heat capacity C_H measurement as follows:

$$\triangle T_{ad} = \int_{B_i}^{B_f} \frac{T}{C_H} \left(\frac{\partial M}{\partial T}\right)_{B,P} dB \tag{1.8}$$

The refrigerant capacity RC describes the heat transfer between the cold and hot reservoirs:

$$RC = \int_{T_{cold}}^{T_{hot}} [\triangle S_M(T)]_{\triangle B}\, dT \tag{1.9}$$

where: $\triangle B$ is the difference between the minimum and maximum applied magnetic fields.

So in order to achieve large adiabatic temperature changes or large refrigerant capacity, it is required to choose a material with a large change of entropy around the working temperature range, associated to experimentally achievable magnetic field amplitudes. A phase transition associated to a large magnetic entropy change is required. For example the large change of magnetisation around the Curie temperature of gadolinium, makes it one of the most interesting magnetocaloric materials. A phase transition between an antiferromagnetic state and a ferromagnetic state can also be relevant. It is the case for FeRh. The magnetic entropy change can be enhanced by a simultaneous change of lattice or electronic entropy due to a crystallographic transition. This is the reason why the study of these materials needs to address all these aspects (crystallography, magnetism, ...).

The number of scientific publications about the magnetocaloric effect has recently increased quickly due to the improved energy efficiency which has been obtained. A comparison between several magnetocaloric materials which work near room temperature can be seen in figure 1.1b [3]. In this figure, it can be seen that the near-equiatomic Fe-Rh material has the highest adiabatic temperature change, while La_1(Fe-Si)$_{13}$-(H) and Ni-Mn-In-(Co) have a long working-cooling range and high $\triangle T_{ad}$ which are suitable for applications. Hence, in this research, we chose the Fe-Rh-based system to investigate the magnetostructural phase change in magnetocaloric materials using a thin film approach and piezoelectric strain. Besides that, we also developped the fabrication of La-Fe-Si-(H) as films. The following part is an overview about the FeRh system.

1.2.3 Overview of the Fe-Rh system

The Fe-Rh alloy, discovered in 1938 by M. Fallot [7], is of special interest in the scientific community in the last few years [8, 9, 10]. The ordered near-equiatomic Fe-Rh material

undergoes a first order transition close to room temperature $\sim 350\,\mathrm{K}$ together with a $\sim 1\,\%$ volume change and a large entropy change. The transiton can also be influenced by an applied magnetic field [3]. Besides a giant magnetocaloric effect and high magnetostriction, the magnetoresistance ratio of this material is also very high ($\sim 50\,\%$) [11, 12]. Hence, although the discovery of FeRh alloys was span over 80 years, an interest in FeRh alloys has recently been renewed, due to potential applications and it is still a model system for fundamental studies of the phase transition, where lattice, electronic, magnetic contributions are intertwinned. Its unique transition from antiferromagnetism to ferromagnetism makes it a very special material. New interest around spintronics including the recently created field of spintronics of antiferromagnetic metals has made FeRh still very relevant [8]. In the following part, the phase diagram, influences of temperature, magnetic field as well as elemental substitution on the transition of the FeRh material are presented.

1.2.3.1 Phase diagram and crystal structure

The equilibrium phases of the $Fe_{1\text{-}x}Rh_x$ system proposed by Swartzendruber in 1984 [13] are shown in figure 1.2a and summarized in table 1.1. The α" phase, from this point forward, will be referred to as the AFM state and the α' phase will be referred to as the FM state or the PM state which forms by an FM $\leftrightarrow$ PM transition. In this phase diagram, we can see that the AFM phase exists in a narrow range of composition which is from 48 to 55 at. % Rh. It is well known that the magnetostructural transition in Fe-Rh based systems is extremely sensitive to stoichiometry. The near equiatomic Fe-Rh alloy requires a high quality to show a complete first order transition, which is a quite difficult task.

Table 1.1. *Summary of magnetic and crystal structure data for $Fe_{1-x}Rh_x$ system (Data taken from [13])*

	Atomic % Rh	*Crystal structure*	*Magnetic state*	*Further information*
δ (δFe)	0-3	Bcc-*Im3m*	-	
α (αFe)	0-19	Bcc-*Im3m*	FM at RT	
γ	0-100	Fcc-*Fm3m*	PM	
α'	11-55	Cubic-CsCl structure	FM at RT	PM at high temperature
α"	48-55	Cubic-CsCl structure	AFM at RT	1^{st} order transition

What can be seen on this phase diagram is that there are only a few experimental data points, especially in the AFM zone. Each data point corresponds to a specific sample. Besides, the magnetic phase diagrams in literature do not fully coincide, as shown in figures 1.2b and 1.2c [14, 15]). The big difference between the phase diagram proposed by Swartzendruber and Takahashi et al. is the AFM window of FeRh. Swartzendruber reported the composition range of the AFM window is from 48 to 55 at. % Rh, meanwhile

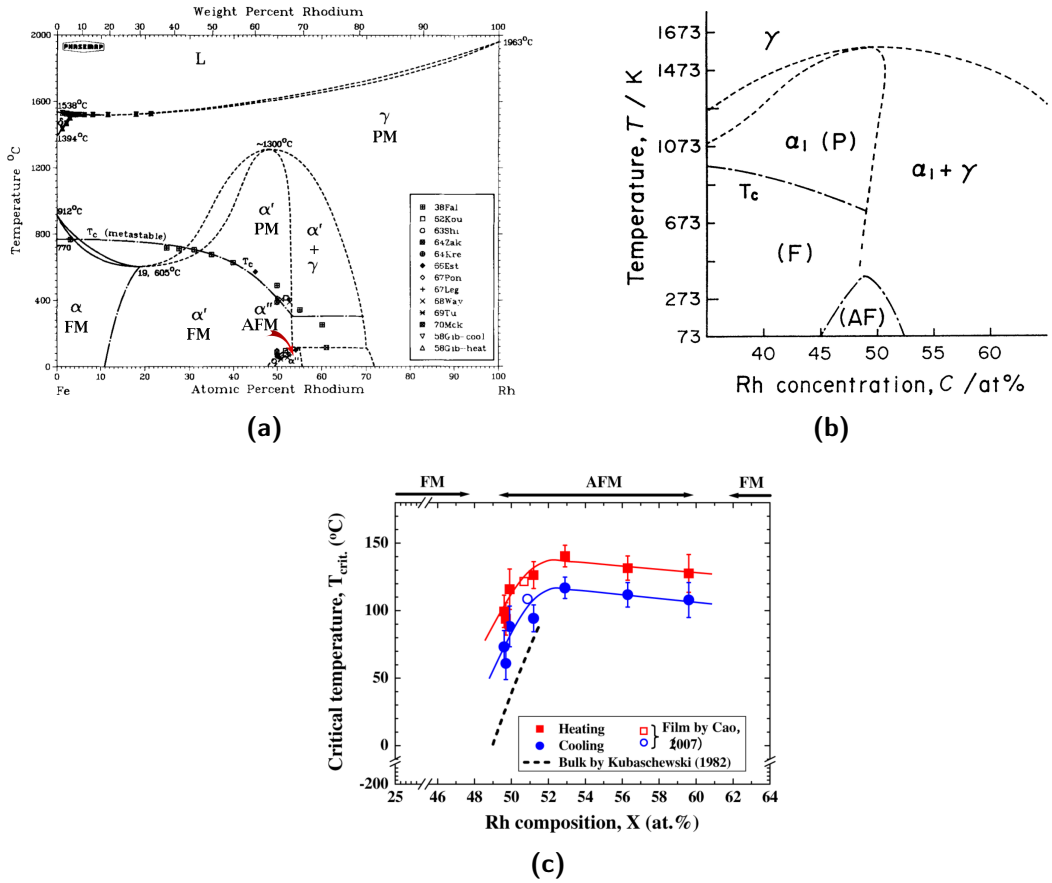

Figure 1.2. *Phase diagrams of FeRh alloy (a) proposed by Swartzendruber in 1984. In this phase diagram, α is the low temperature bcc phase, α' is a chemically ordered phase with CsCl structure, α" is a chemically ordered CsCl structure which forms from α' by the first order transition, γ is the fcc phase (a paramagnetic phase), δ is the high temperature bcc phase, L is the liquid. (Image taken from [13] and the texts of FM, AFM, PM were inserted to describe the equilibrium phases clearly). (b) proposed by Takahashi et al. in 1995 . Here, α - the disordered bcc phase, α_1 - the ordered bcc phase, γ - the fcc phase. (Image taken from [14]) (c) reported by Inoue et al. in 2008 for films and bulk. (Image taken from [15])*

the AFM window suggested by Takahashi et al. is from 45 - 52 at. % Rh, i.e. a similar width for the AFM stability region but composition-shifted.

During the heating process, the Fe-Rh alloy shows a transformation from AFM to FM around $T_t \sim 350\,K$ and then this material undergoes a second order transition from FM to PM with a Curie temperatue $T_C \sim 650\,K$. The crystal structure of the ordered Fe-Rh alloy is still cubic with CsCl-type structure. The AFM configuration of the Fe-Rh system is of type II-AFM with no overall magnetic moment [16, 17, 18], as shown in figure 1.3. Each Rh atom is at the center of a cube occupied by eight nearest neighbour Fe atoms at the corners.

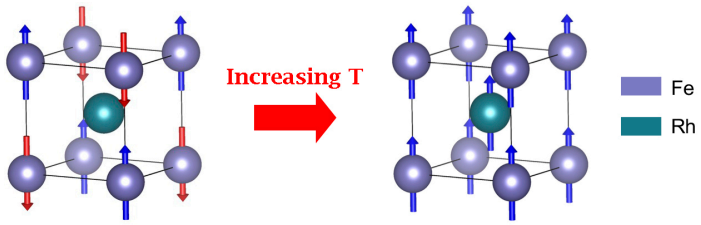

Figure 1.3. *The crystal structure and magnetic ordering of the α" phase in near-equiatomic Fe-Rh alloys. The AFM configuration of the Fe-Rh system is type II-AFM where both intra-plane and inter-plane couplings are AFM (the left-hand image) and* $\mu_{Fe} = 3.3\,\mu_B$, $\mu_{Rh} = 0\,\mu_B$. *Above the transition temperature* $\sim 350\,K$, *the magnetic ordering of Fe-Rh alloys will transform to FM (the right-hand side image).*

1.2.3.2 Influence of temperature and magnetic field on the transition

The transformation of the Fe-Rh-based system can be induced by temperature but also when applying a magnetic field. At low temperature, the Fe-Rh materials is AFM. The magnetization will change abruptly when its temperature is higher than the transition temperature as shown in figure 1.4a [19]. A thermal hysteresis is observed between heating and cooling curves. This transition temperature will be influenced by the applied magnetic field, which stabilizes the ferromagnetic phase. Increasing the magnetic field will lead to a reduction of the transition temperature at the rate of -8 K/T in both bulk and film samples, while the hysteresis width is unchanged (see figure 1.4b).

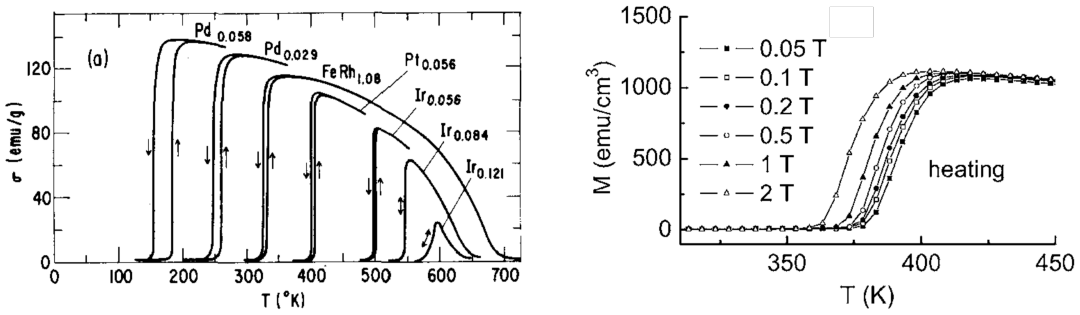

Figure 1.4. *(a) The Fe-Rh-based systems show the first order transition with the applied magnetic field of 7 T (b) The temperature dependence of magnetization at various magnetic field. The transition temperature decreases at the rate of -8 K/T when increasing applied magnetic field. Sample is MgO/FeRh 110 nm (Images taken from [19, 20]).*

The entropy change at this transition can be calculated using the Clausius–Clapeyron equation with the magnetization difference △M between the AFM and FM phases. The value of 14 J.kg^{-1}K^{-1} was found experimentally by Kouvel in 1966 [19]. Besides that, the isothermal magnetization curves are measured in the vicinity of the transition temperature and usually estimated the entropy change of system $\triangle S_M$ using the Maxwell equation above. In general, the large entropy change in Fe-Rh samples is of the order $\sim$ 12.5 - 19.7 J.kg^{-1}K^{-1} [21, 5, 20] depending on the method (calculation or measurement) and the

exact composition.

1.2.3.3 Influence of elemental substitution on the transition

The first order transition temperature in FeRh alloys can be tuned over a wide temperature range from 100 K to 600 K, through an elemental substitution for an atomic small amount (less than 6 %) as shown in the figure 1.4a. Figure 1.5 represents the influence of elemental substitution on the first order transition temperature [22]. This periodic table shows that a substitution of 3d transition metal leads to decrease the transition temperature, while a substitution of 5d transition metal increases the transition temperature. No clear trend is observed for a 4d transition metal substitution.

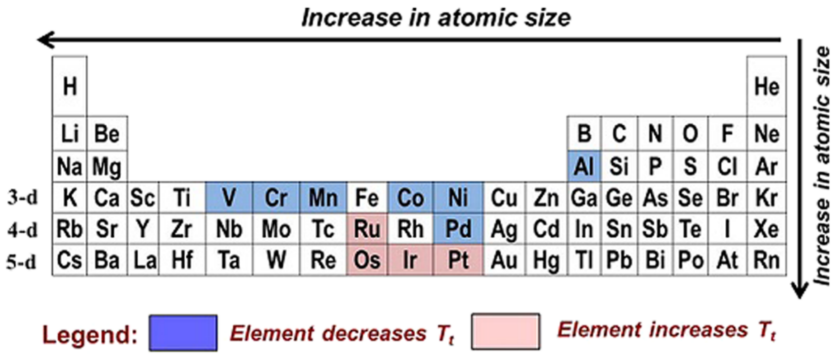

Figure 1.5. *The Periodic table of elements is used to describe the change trend of the transition temperature in FeRh-based systems because of the elemental substitution [22]*

The transition temperature strongly changes with elemenal substitution, meanwhile only a small change was observed in the Curie temperature (about 55 K [19]) as well as a slight change in lattice constants (from 2.979 Å to 2.997 Å [22]). The average density is around 10g/cm^3 [19].

1.2.3.4 Influence of hydrostatic pressure and substrate on the transition

Pressure and substrate stress can influence the transition of FeRh materials. Increasing hydrostatic pressure leads to an increase of the first order transition temperature dT_t/dP = 4.33 K/kbar as shown in figure 1.6 [23, 24, 25], meanwhile a tensile pressure decreases the transition temperature dT_t/dP = -2 K/kbar [26]. Besides that, it was reported that dT_t/dP was decreased with increasing T_t [23]. In FeRh films, the transition temperature T_t can be also tuned using different substrates (i.e. different substrate lattice parameters) [20, 27]. However it is not easy to identify different strain states keeping the composition exactly identical. In this thesis, using a piezoelectric substrate will allow to modify the strain keeping the same FeRh composition.

1.2.3.5 Temperature dependence of resistivity

Dependence of resistivity on temperature in the FeRh materials is shown in figure 1.7 [28]. It was found that below the transition temperature, the resistivity change is the

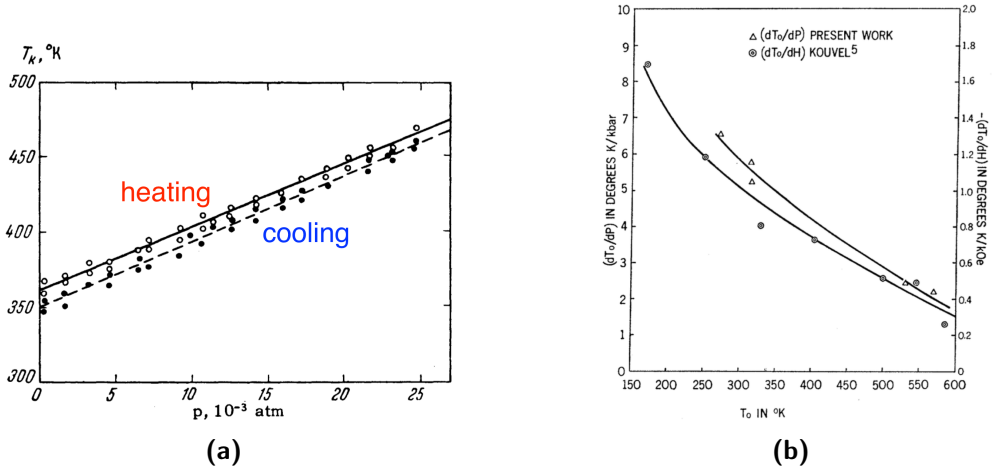

Figure 1.6. *Hydrostatic pressure dependence of the first order transition temperature dT_t/dP in FeRh. (a) dT_t/dP in FeRh during heating and cooling. (b) dT_t/dP as a function of T_t. Here, T_0, T_k in the figure are T_t in our thesis. (Images taken from [24, 23])*

usual metallic behaviour with a linear dependence on temperature. However, a large drop in resistivity $\sim$ 40 - 50 % was observed at the transition temperature. At the transition temperature, a $\sim$ 1 % volume expansion happens. In the elastic regime, this change will modify the geometry of the film by 1 %, the density of carriers can also decrease by 1 %. This cannot explain the experimental drop, which has to be related to a more drastic change across the first order AFM-FM transition.

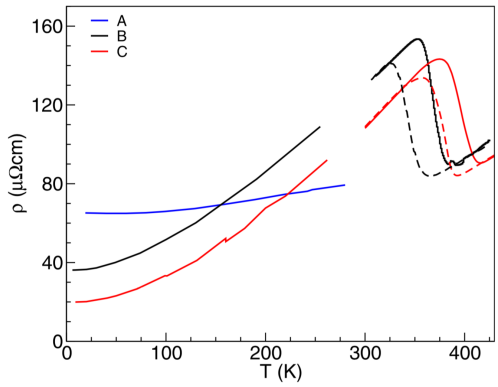

Figure 1.7. *A large change in resistivity of the $Fe_{50}Rh_{50}$ material for the samples B and C which show the first order transition. Sample A is FM with no AFM-FM transition. The solid and the dashed lines are the heating and cooling process, respectively (Image taken from [28])*

1.2.4 Overview of the La-Fe-Si system

La(Fe, Si)$_{13}$–based compounds displaying a giant magnetocaloric effect are of particular interest because of their great potential for magnetic refrigeration applications [29, 2, 30, 31, 32]. The giant MCE in La(Fe, Si)$_{13}$–based alloys stems from the so-called magneto-volume effect, i.e. the magnetic phase transition from the paramagnetic to the ferromagnetic state

is associated with an increase in volume without breaking the cubic lattice symmetry. A strong magneto-volume effect can lead to a sharp change in magnetization and in volume at the Curie temperature (T_C) in a first-order phase transition. However, the magneto-volume effect is also present in a phase transition of second order. In this case, the magnetic phase transition and the volume change take place gradually rather than sharply [33]. By changing composition, substituting elements or introducing interstitials, the magneto-volume effect and the MCE can be modified [34, 35].

$LaFe_{13-x}Si_x$ alloys are stabilized in the $NaZn_{13}$-type cubic structure (space group) in the range $1.2 < x < 2.5$. With increasing the Si content, a changeover from first-order ($x < 1.6$) to second-order ($x > 1.6$) transition, along with an increase in T_C from 175 to 255 K, was observed [34, 36]. Interestingly, the first-order transition in $LaFe_{13-x}Si_x$ alloys shows only a small thermal hysteresis, making them very promising for refrigeration applications [37, 38]. However, a low T_C of ~ 200 K is an obstacle to applications near room temperature. Many efforts have been made to raise T_C, such as introducing interstitial hydrogen atoms [39] or replacing some Fe with Co [40]. While the giant MCE still remains after inserting hydrogen atoms, the substitution of Co for Fe considerably weakens the MCE since the first-order transition is gradually transformed into a transition of second-order. Studies to date have focused on La(Fe, $Si)_{13}$-based bulk alloys, with no reports on La(Fe, $Si)_{13}$ in film form. Thin films may serve as model systems for materials studies and also have potential for use in micro-systems.

1.3 Multiferroic materials and magnetoelectric effect

Multiferroic materials, which exhibit two or more ferroic orders, have recently received much attention, for fundamental reasons and also because of potential applications. The coupling between ferroelectric and ferromagnetic orders has important potential applications in spintronics, in the field of magnetic sensing, for the development of information storage, as well as for energy harvesting. Intrinsic magnetic properties such as T_c, magnetization, anisotropy or extrinsic properties such as magnetization reversal processes (nucleation, propagation) can be controlled by an electric field. Recent research showed a possibility to tune the magnetic order close to room temperature [9], which is important for applications. In this study, we will use an electric field to control the AFM to FM transition in FeRh films near room temperature through the elastic effect. Rapid overviews of magnetism, ferro-electricity and the magnetoelectric coupling are introducted in this section.

1.3.1 Magnetism

Magnetic materials belong to different classes of magnetism such as ferromagnetism, antiferromagnetism, paramagnetism, diamagnetism, ferrimagnetism. The most important classes for this study are ferromagnetism and antiferromagnetism. Hence we will introduce them in the following part and the other magnetic states or long-range orders are described

in many textbooks or publications [41, 42].

Ferromagnetism. Ferromagnetic materials possess a spontaneous magnetization without applying an external magnetic field. Such order is due to the exchange interaction between electrons in neighbouring atoms. In a ferromagnetic material, the magnetic moments of atoms align in the same direction, resulting in a long range order and a spontaneous magnetization. The spontaneous magnetization vanishes at a temperature called the Curie temperature T_C. Above T_C, the long range order disapears and ferromagnetic materials become paramagnetic.

In a finite system, magnetic poles form at the surface of magnetised ferromagnetic material. This leads to a stray magnetic field outside the material. This occurrence of magnetic poles also creates an internal demagnetizing field, that is opposite to the magnetization vector. In order to reduce the energy stored in the stray field, ferromagnetic materials will try to demagnetise in small regions called domains, in which the magnetisation is uniform. Directions of the spontaneous magnetization in domains are different from each other but follow easy axes of anisotropy. Therefore, the total magnetization of the ferromagnetic material will be reduced or even completely demagnetised.

When we apply a magnetic field to the ferromagnetic material, magnetic moments orientate parallel to the field. Sweeping the field, a M(H) hysteresis loop is obtained. On such hysteresis loop, we can define the saturation magnetization M_S, the remanent magnetization M_r, the magnetic coercive field H_C (see Figure 1.8a).

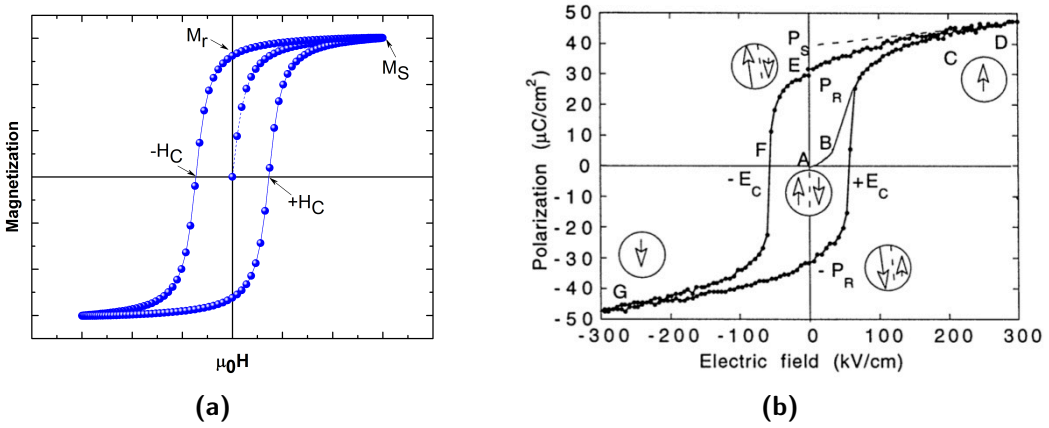

Figure 1.8. *(a) The magnetic hysteresis loop and some typical quantities M_S, M_r, and H_C. (b) The ferroelectric hysteresis loop and typical quantities P_S, P_r and E_C (Image taken from [43])*

Antiferromagnetism. Antiferromagnetism is a microscopic magnetic configuration where magnetic moments of nearest neighbors are aligned antiparallel. It leads to zero net spontaneous magnetization. An external magnetic field must compete with this antiparallel exchange interaction in order to align magnetic moments and typical experimental fields are not strong enough to achieve parallel order. The antiferromagnetic order vanishes at a critical temperature called the Néel temperature T_N. Above this critical temperature, the material becomes paramagnetic. Antiferromagnetic materials can be used as pinning

layers in some spintronics devices, i.e spin valve or to exchange-bias a ferromagnetic layer. Recently, the feasibility of a memory using an antiferromagnetic material has been reported by Marti el al. in 2014 [8] using the AFM state and the AFM-FM transition from FeRh. It opens the field of antiferromagnetic spintronics. The absence of magnetisation associated to a well defined magnetic order and anisotropy make antiferromagnetic materials interesting for many model systems.

Micromagnetism model. The magnetic order in ferromagnetism is due to the exchange energy. The presence of other significant energy terms such as magnetocrystalline anisotropy, magnetoelastic, demagnetising and Zeeman energies leads to non trivial equilibrium magentic configurations whiich can be modeled using the micromagnetic formalism. The total free energy F of a magnetic material is given as follows:

$$U = U_{an} + U_{el} + U_{me} + U_{st} + U_Z + U_{ex} \tag{1.10}$$

where: U_{an} - the energy of magnetocrystalline anisotropy; U_{el} is the elastic energy; U_{me} is the magnetoelastic energy; U_{st} - the magnetostatic energy; U_Z - the Zeeman energy; U_{ex}- the exchange energy.

The magnetization state of the magnetic material is obtained from the minimization of the total free energy: $dF = 0$. This equation is important and used for the simulation of the magnetization behaviour in micromagnetism down to the nanometer scale. In our study, we will use such microscopic model to describe the coupling between the magnetic and piezoelectric materials.

1.3.2 Ferroelectricity

Ferroelectric materials are an electric analog to ferromagnetic materials. Ferroelectricity is a property of some materials that have a spontaneous electric polarization $\overrightarrow{P}$ even without an external electric field. There is an interaction among ferroelectric dipole moments and they are coupled to the lattice. Therefore, if we deform the material lattice, the magnitude of dipole moments will be changed. This makes the ferroelectric material different from other dielectric materials. Ferroelectric materials are a sub-class in the family of piezoelectric materials, in which a generated voltage is proportional to an external strain (or stress). In such a material, applying an external stress generates an electric field (a voltage) (called the direct piezoelectric effect) and applying an electric field induces strain (called the converse piezoelectric effect). Table 1.2 shows piezoelectric coefficients and classes of common piezoelectric materials.

In a ferroelectric material, the typical quantity for the electric polarization is the polarization vector $\overrightarrow{P}$. It is the sum of all dipole moments per unit volume of the dielectric material:

$$\overrightarrow{P} = \frac{\sum \overrightarrow{p_i}}{V} \tag{1.11}$$

where: $\overrightarrow{P}$ is the polarization (C/m^2), $\vec{p_i}$ are the electric dipole moments in a volume V.

The quantitative relation between the electric polarization $\overrightarrow{P}$ and an external electric

field $\overrightarrow{E}$ is:

$$\overrightarrow{D} = \varepsilon_0 \overrightarrow{E} + \overrightarrow{P} \tag{1.12}$$

where: D - the electric displacement.

In the linear regime, the polarization of a ferroelectric material is proportional to the external electric field and follows this equation:

$$\overrightarrow{P} = \chi_e \varepsilon_0 \overrightarrow{E} \tag{1.13}$$

where: χ_e is the dielectric susceptibility, $\varepsilon_0 = 8.86\times10^{-12}$ $C^2N^{-1}m^{-2}$ is the vacuum permittivity.

Similar to the magnetic hysteresis loop, the ferroelectric hysteresis loop is the typical curve of the ferroelectric material under an external electric field (see Fig. 1.8b). The typical quantities defined on such a loop are the spontaneous polarization P_S, the remanent polarization P_r and the electrical coercive field E_C. Like the Curie temperature in ferromagnetism, the ferroelectric order only exists up to the Curie temperature. Above the Curie temperature, the order of ferroelectric materials is paraelectric.

Polarization switching by an electric field in ferroelectric materials leads to strain hysteresis. This strain loop has a butterfly shape (as shown in figure 1.9a). There are three reasons leading to the effect. The first reason is the normal converse piezoelectric effect of the lattice. The second reason is due to switching of domain walls and the third is the movement of domain walls.

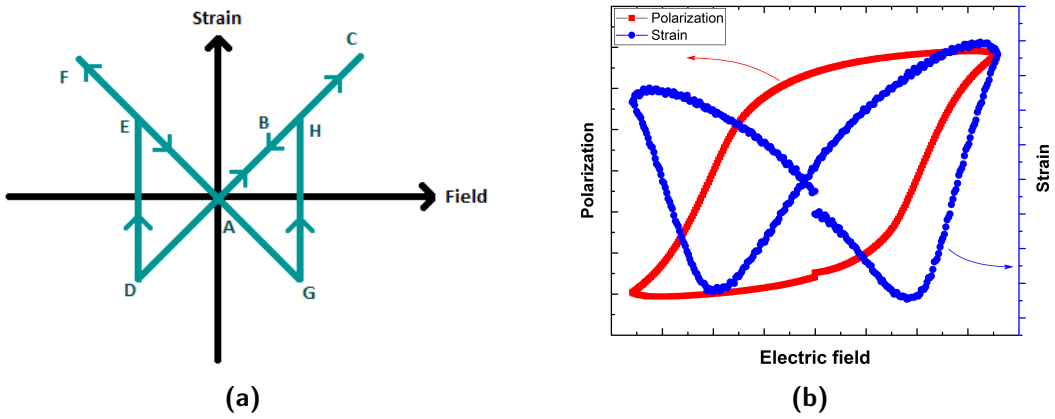

Figure 1.9. *Strain behavior under electric field: (a) an ideal loop in a ferroelectric material that undergoes 180^o switching only (b) actual strain and polarization of a piezoelectric material PZT.*

Assume that polarization can be instantaneously switched by 180^o reversal. Under zero field, strain is zero (point A). When we apply a positive electric field to the piezoelectric material (the positive direction), the lattice will change and the crystal expands because of the piezoelectric effect. The strain traces lines A $\rightarrow$ B $\rightarrow$ C. The expanded lattice continues until the maximum electric field E_S is reached (point C).

- At point C, we will decrease the electric field E, but $\overrightarrow{E}$ is still parallel to $\overrightarrow{P}$. So, the strain of the sample traces the same line in the opposite direction C $\rightarrow$ B $\rightarrow$ A. At point

A, the electric field is zero, the strain is zero.

- When we increase the electric field in the negative direction, the electric field direction is antiparallel to P, the strain becomes compressive.

- At point D, the electric field is large enough to switch the polarization direction. After switching, the polarization is parallel to the electric field, the strain traces line D $\rightarrow$ E. At point E, the strain becomes positive, and the strain reaches the maximum expansion at point F.

- With further cycles of the electric field, the strain curve will trace line F $\rightarrow$ E $\rightarrow$ A $\rightarrow$ G $\rightarrow$ H in the same way as above.

In reality, the strain behavior is complicated because the material usually contains a number of non 180^o domains (Figure 1.9b). Because the coercive field varies in each domain, the contribution of the non 180^o domains leads to the less sudden change when the polarization orientation is altered. If domains do not return to their original position at zero field, there is a remanent strain at zero field.

The switching and movement of non 180^o walls can also create a significant deformation. The strain originated by this non 180^o domain switching can be larger than that of the piezoelectric effect by one or two orders of magnitude. For example, the a- and c-type domains switching can generate a strain $\sim$ 1% in $BaTiO_3$ at 20^oC, or $\sim$ 6% in $PbTiO_3$ at room temperature ([43] and references therein). The electric-field-induced strain in $BaTiO_3$ is mainly due to the domains switching, meanwhile mechanism of strain in other ferroelectric materials is different.

Table 1.2. *Piezoelectric coefficients of common piezoelectric materials [44]*

Material	*ZnO*	*α - quartz*	*$BaTiO_3$*	*Hard PZT*	*Soft PZT*	*PMN-0.3PT*	*PVDF*
Piezoelectric	Yes	Yes	Yes	Yes	Yes	Yes	Yes
Pyroelectric	Yes		Yes	Yes	Yes	Yes	Yes
Ferroelectric			Yes	Yes	Yes	Yes	Yes
d_{33} (pm/V)	12.4	d_{11} = -2.3	149	289	593	2000	-33
d_{31} (pm/V	-5		-58	-123	-274	-1000	21
d_{15} (pm/V)	-8.3	d_{14} = 0.67	242	495	741	2500-4000	-27

Pb(Zr-Ti)O_3 (PZT) ceramics, since its discovery, is a common and important piezoelectric material in both research and applications, because of its high dielectric constant, low dielectric loss over a wide range of temperature and frequency as well as a reasonable price. The electric-field-induced strains of PZT ceramics are composed of strains due to the piezoelectric effect and the reorientation of 90° domains [45].

Park et al. in 1997 [46] reported the strain behaviour versus E-field S(E) for typical piezoelectric materials (see Fig. 1.10a), in which the S(E) characteristic of soft ceramics ($E_C < 10\,kV/cm$ [47]) is large hysteresis due to domain motion, i.e. soft PZT (PZT-5H). On the other hand, hard piezoelectric ceramics ($E_C > 10\,kV/cm$) exhibit low hysteresis but the piezoelectric coefficient is smaller. PMN-PT material offers high piezoelectric coefficients without hysteresis, implying no domain motion.

In general, studying piezoelectric materials leads to classify them into two groups based on the actuation mechanism: materials with high piezoelectric coefficients such as PMN-PT crystals and the other materials characterized by 90° domain switching like $BaTiO_3$ ([48] and references therein).

1.3.3 PMN-PT crystal

In this section, we briefly discuss PMN-PT, focusing on its phase diagram. (1-x)PMN-xPT crystal is a complex solid solution of relaxor ferroelectric PMN ($T_C \sim 263\,K$) and normal ferroelectric PT ($T_C \sim 763\,K$). The crystal structure depends on the composition x. Increasing x leads to a transformation from rhombohedral (R3m) (typical relaxor) to tetragonal (P4mm) (normal ferroelectric) phase. These two phases are separated by a morphotropic phase boundary (MPB). Although the exact MPB position is not consistent in literature, a modified phase diagram proposed by Noheda et al. in 2002 [49] is widely accepted (see Fig. 1.10b).

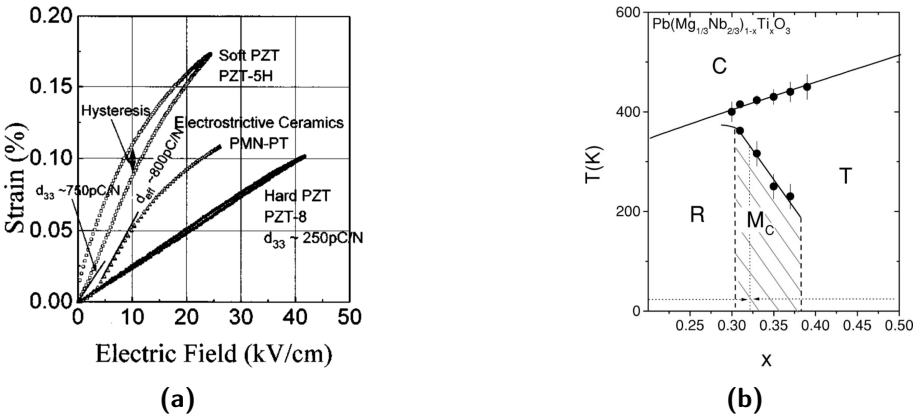

Figure 1.10. *(a) Strain behavior of a piezoelectric material. (b) A modified phase diagram of (1-x)PMN-xPT proposed by Noheda et al. in 2002. (Image taken from* [49]*)*

Figure 1.10b shows 3 regions based on physical properties: (I) $x < 0.3$ - rhombohedral structure region (relaxor), (II) $0.31 < x < 0.37$ - the area of the MPB region, (III) $x > 0.38$ - tetragonal structure region (ferroelectric). The crystal structure of PMN-PT is cubic above T_C. Chemical compositions in the range $0.28 < x < 0.37$ is the most investigated area due to extraordinary electromechanical properties (the relative permittivity and piezoelectric coefficients exhibit maximum values close to MPB), while only a few publications concern the materials in region III.

In this study, we use PMN-0.3PT single crystal as an active substrate to generate the E-field-induced strain. Its main specifications are $E_C \sim 3.2\,kV/cm$, $T_C \sim 425\,K$, $d_{33} \sim 1700$-$2200\,pm/V$, $d_{31} \sim$ -1000 pm/V . Because of high piezoelectric coefficients and an acceptable Curie temperature, this single crystal is a good choice as a piezoelectric substrate in this study.

1.3.4 Multiferroic materials

Multiferroic materials exhibit two or more orders such as ferroelectricity, ferromagnetism, ferroelasticity or antiferroelectricity and antiferromagnetism, simultanenously. Such materials can be divided into two categories based on their structure: single phase materials and composite materials. A ferroic order can be controlled by another order through the coupling between the ferroic orders, which may produce new interesting effects.

Single phase materials. In single phase multiferoics, multiple ferroic properties coexist in the same material. Spontaneous magnetization and polarization can coexist in the same material because the magnetic order is conducted by the exchange interaction of the electron spins, meanwhile the ferroelectric order is in control of the distribution of the charge density in the lattice. Some typical single phase multiferroics are perovskite compounds, i.e., $BiFeO_3$, $BiMnO_3$, $TbMnO_3$,... Table 1.3 shows some single phase materials with their typical properties (Electric and magnetic orders, T_C and T_N). A list of single phase materials can be found in early review [50].

In general, the magnetic order originates from the 3d and 4f electrons in the transition and rare earth metals whereas the ferroelectric order originates from the asymmetry of the crystal structure. In fact, the coupling of different ferroic orders in these materials is often too weak to be used in applications and their main interest is the deep understanding of the very rich phase diagram obtained. The coupling coefficient is also restricted in the single phase multiferroic materials [42]. Finally, the single phase multiferroic materials, which can be used at room temperature, are rare.

Table 1.3. *Some of the single phase materials [50]*

Material	*Electric order*	*Magnetic order*	T_C *(K)*	T_N *(K)*
$BiFeO_3$	FE	AFM	1123	650
$BiMnO_3$	AFE *	FM	773	103
$YMnO_3$	FE	AFM	913	80
$Co_{1.75}Mn_{1.25}O_4$	FE	FIM *	170	170
$Eu_{1/2}Ba_{1/2}TiO_3$	FE	FM	165	4.2

* AFE - antiferroelectric, FIM - ferrimagnetic

Composite materials. A strategy to achieve the higher coupling is the use of composite material where each phase can be independently optimized for the particular purpose. Moreover, the number of ferromagnetic and ferroelectric materials which work at room temperature are large enough. The combination of two optimal phases can generate a higher coupling which is of high interest.

In general, composite multiferroic materials can be classified by the dimensionality of the two constituents of the composite (0D (grains), 1D (rods), 2D (layers), 3D (bulk)), so one can obtain composites from the (0-3 type), laminates (2-2 type) and fiber/rod composites (1-3 type). (Figure 1.11) [51]. The 0-3 type multiferroic structure is a ferroelectric material

with some magnetic grains inside or vice versa. The second structure consists of layers of ferroelectric and magnetic materials, while the last one is a fiber or the columnar material inside a matrix of the other component. Common ferroelectric materials used in the composite multiferroic material are piezoelectric materials such as BTO, PZT, PMN-PT or PZN-PT. Meanwhile, typical magnetic materials are Fe, Ni, Co, $CoFe_2O_4$, $NiFe_2O_4$, Fe_3O_4, Fe-B-Si-C, Fe-Co-B, $La_{0.8}Sr_{0.2}MnO_3$, rare earth compounds,...

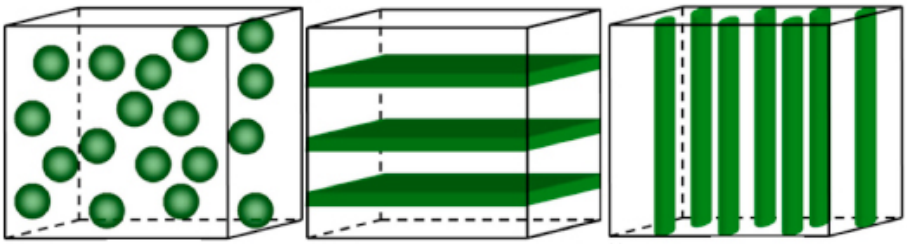

Figure 1.11. *Three common structures of the composite multiferroic material, a 0-3 type (left), a 2-2 type (middle), and a 1-3 type structure (right) (Image taken from [51])*

In multiferroic materials, the coupling interaction between ferroic orders produces new effects. The magnetoelectric effect is produced by the coupling between the ferromagnetic and ferroelectric order. This effect describes the influence of a magnetic field on the polarization (called the direct ME effect), or the influence of an electric field on the magnetization of a material (called the converse ME effect). Depending on the magnetoelectric mechanism, this effect can be divided into three categories: an exchange bias-mediated coupling, an interface charge-mediated coupling and a strain-mediated coupling [52]. These magnetoelectric mechanisms are described in the following part.

1.3.5 The mechanism of magnetoelectric coupling in composites

The exchange bias ME effect. The exchange interaction between the FM order in a FM layer and the AFM order in the multiferroic layer produces an exchange bias effect. Because of the coupling between the AFM order and the FE order in the multiferroic layer, magnetism can then be controlled using an electric field. Demonstration of exchange bias control of the magnetic property was first reported (2010) in the magnetoelectric heterostructure $Cr_2O_3(111)/(Co,Pt)_3$ ([53] and references therein).

The interface charge ME effect. Because a ferrolectric layer with two metallic electrodes is a capacitor and since the magnetic properties of a magnetic metal depend on how the band structure is filled, applying an electric field across a ferroelectric and polarising it, induces surface charges on the electrode. If the electrode is an ultrathin magnetic film, this induced charge may allow to modify magnetic properties. Because only a few atomic layers of the FM layer are affected by this charging effect, only 1 nm-thick magnetic layers are suitable. Weisheit et al. in 2007 showed a modification of coercivity in FePt and FePd films using this interfacial charge effect [54].

The strain ME effect. A deformation of composite system by the applied electric or magnetic field leads to the change in the properties of magnetic layer or ferroelectric

layer, respectively. Under the applied magnetic field, the shape or dimensions of the ferromagnetic materials will change, the strain will be transferred to the ferroelectric layer and an electric response to this magnetic field will be achieved (the direct ME effect - see Eqn. 1.14). A magnetic response to an applied electric field will be achieved in the case of converse effect where the strain is generated by applying an electric field across the ferroelectric material (see Eqn. 1.15).

$$ME_H = \frac{Magnetic\,field}{Strain} \times \frac{Strain}{Polarization} \quad (direct) \tag{1.14}$$

$$ME_E = \frac{Electric\,field}{Strain} \times \frac{Strain}{Magnetization} \quad (converse) \tag{1.15}$$

The Landau theory traditionally used to describe the magnetoelectric effect by writing the free energy of the system in terms of a magnetic field and an electric field can be found in the reference [42] and appendix A. Besides that, the piezoelectric and magnetostrictive effects can be described by using the constitutive equation which presents the strain-electric-magnetic coupling response [51].

In experiment, Eerenstein et al. (2007) defined the magnetoelectric coupling coefficient α_{ME} to be the change of an electrical polarization P (or an electric field) due to an applied magnetic field H (the direct effect) or a change of magnetization M due to an applied electric field E (or a voltage difference $\triangle$V) (the converse effect) [55]:

$$\alpha_{ME}[s/m] = \left(\frac{\partial P}{\partial H}\right)_E = \mu_0 \left(\frac{\partial M}{\partial E}\right)_H = \mu_0 \frac{\triangle M}{\triangle E} \tag{1.16}$$

In this research, we investigate the phase change in a transition material through the strain effect. The sample structure is an heterostructure made out of a piezoelectric substrate and a magnetic film. The coupling will be enforced using glue or direct deposition of the film onto the piezoelectric substrate. Due to this reason, neither exchange bias nor the interface charge effect are expected in our samples. The strain coupling is expected to be the driving force for the magnetoelectric effect. Hence, we focus on the strain-mediated coupling between the ferroelectric and ferromagnetic order in literature.

1.3.6 Literature review of the strain mediated coupling

The direct magnetoelectric effect has been studied for a long time (since at least the 1950s, 1960s). Meanwhile the converse magnetoelectric effect just begun being studied extensively in recent years. Magnetic properties such as the Curie temperature, anisotropy, magnetization or domain propagation can be controlled by the electric field (E-field) through the converse effect. In this part, we only present works done for the electrical control of magnetic properties through the strain-mediated coupling. Selected recent publications to present this field are now summarised.

The E-field control of the Curie temperature and resistance. Thiele et al. in 2005 [56] introduced a hybrid structure of PMN-28PT(001)/$La_{0.7}Sr_{0.3}MnO_3$ with a

variation of the film thickness. These magnetic films were deposited by the pulsed laser deposition method on (001) oriented commercial $10\times10\times0.4\,\mathrm{mm}^3$ PMN-28PT single crystals. Because the difference of lattice contants between PMN-PT substrate and LSMO film (4.02 Å and 3.876 Å [57, 58]), the T_C of the LSMO is reduced by this compressive strain misfit [59]. The strain mediated ME effect was monitored using a SQUID magnetometer to record the strain induced change of T_C and transport measurements to record the resistance change. When they apply a voltage to the piezoelectric substrate, the T_C was increased due to the relaxation of tensile strain. Table 1.4 summarizes changes of T_C with a variation of film thicknesses.

Table 1.4. *Change of T_C in the LSMO film with various thicknesses when they applied a voltage to the PMN-PT substrate. (Data were taken in [56])*

Thickness (nm)	Voltage (V)	T_C(K)	$\triangle T_C$ (K)	$\triangle T_C$/E (K/(kV.cm^{-1}))
50nm	±400	339	+6	+0.6
160nm	0	351		
290nm	250	359	+1	+0.16
Bulk	0	∼ 370		

In their work, the resistance dependence on voltage applied to the piezoelectric substrate of PMN-PT (Fig. 1.12a) exhibits a similar butterfly behavior to the strain behavior shown in figure 1.9.

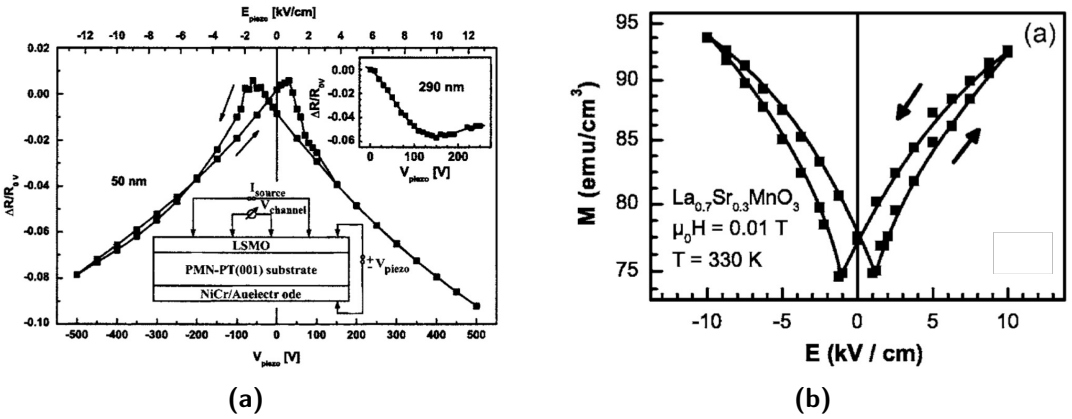

Figure 1.12. *(a) Resistance dependence on applied voltage of the hybrid structrue of PMN-PT/LSMO 50nm. Lower inset is the schematic device structure, the upper inset is the $\triangle R/R_{V=0V}$ as a function of the applied voltage - V_{piezo} of the 50 nm LSMO (Image taken from* [56]). (b) *The responce of magnetization of LSMO film as a function of the applied electric field exhibits a similar butterfly behavior to the strain behavior of the piezoelectric substrate (Image taken from [60])*

The E-field of magnetization. The electrical control of magnetization via the strain mediated coupling was reported by Eerenstein et al. [55] and Thiele et al. [60] in 2007.

Eerenstein et al. introduced a sharp switching and two distinct magnetic states in the structure BTO $4\times4\times0.5\,\mathrm{mm}^3$ (001)/LSMO 40 nm as shown in figure 1.13a [55]. A magnetometer was used to monitor the change in the in-plane magnetization. The mechanism of

the magnetization change in this case is due to the mediated strain coupling between the piezoelectric substrate and the magnetic film.

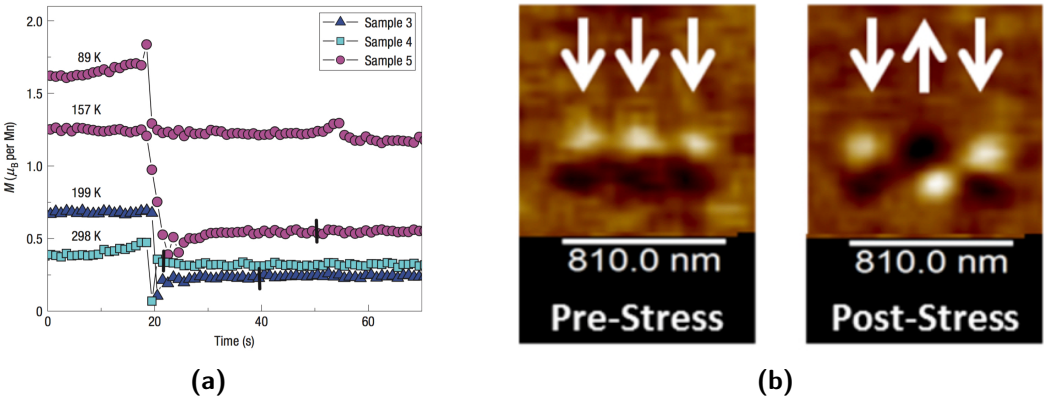

Figure 1.13. *(a) A sharp magnetic switching was observed due to an applied electric field in a heterostructure of ferroelectric and ferromagnetic materials. (Image taken from [55]). (b) Strain induced switching of an array of three nanomagnets in the heterostructure of PMN-PT (001)/Co. The image at the left and right hand side describes the initial state and the state after appling strain, respectively. The white arrow indicates the magnetization direction of Co. The orientation of the 400 kV.m^{-1} electric field was transversal. (Image taken from [61]).*

Thiele et al. in 2007 investigated the strain-dependent magnetization of ferromagnetic manganite films of LSMO and LCMO. At E = 10 kV.cm^{-1}, the change in magnetization of a 30 nm LSMO film is about 25 % at 330 K as shown in figure 1.12. The response of a M(E) ($\overrightarrow{M}$||[100] and $\overrightarrow{E}$||[001]) loop in the structure PMN-PT (001)/LSMO 30 nm has a typical butterfly behavior, which describes a strain-mediated coupling between the piezoelectric substrate and the magnetic film. The ME coupling coefficent is quite large $\sim 6\times10^{-8}$ s.m^{-1} compared to the coupling strength in single phase materials ($10^{-9} \rightarrow 10^{-12}$ s.m^{-1}) ([55] and references therein).

In the works reported by Thiele et al., the magnetization dependence on an applied voltage is reversible. Meanwhile the magnetization is nonvolatile in the work of Eerenstein et al. because of the irreversible switching of domains in the $BaTiO_3$ substrates.

Theoretical works. On the modelisation side, the total free energy can be used to analyse or predict the magnetization change induced by strain (see Eqn. 1.10). Advantages of this equation 1.10 are that a lot of physical quantities can be calculated quantitatively and strain effects can be predicted. However, a large number of parameters is needed for the calculation, and such a set is only available for very classical materials.

Using this approach, Pertsev et al. [62, 63, 64, 65], Hu et al. [66, 67, 68, 69, 70, 71] and other scientists published a series of papers to predict this magnetoelectric effect from 2008 up to now. These predictions showed a good agreement with experiments before and after. They also proposed a resistive switching device using the converse ME effect via the heterostructure made out of a ferroelectric/spin valve structure in which data can be written and read by strain and GMR/TMR effect, respectively [63]. Recently in 2015 an

electric field induced magnetization reversal from in-plane (0^o) to out-of-plane (90^o) or to 180^o through the strain coupling was reported by Hu et al and Peng et al [71, 72].

The perpendicularly magnetic easy-axis reorientation requires a very high electric field in the hybrid structure of FE/FM to generate high strain which is not accessible experimentally. Hence, the idea to achieve this magnetization reversal is the use of electric field associated to an in-built anisotropy via a patterned structure of a square nanomagnet on a good piezoelectric substrate such as PZT, PMN-PT or PZN-PT. Very recently, D'Souza et al. in 2016 reported the experimental implementation of Boolean logic via the heterostructure of Co nanomagnets ($\sim 200\,nm$) on a PMN-PT (001) substrate experimentally (Fig. 1.13b [61]). The ability of strain-induced switching of magnetization is an important key for nanomagnet-based logic.

According to these papers, the advantages of the composite structure compared to the single phase were demonstrated (i.e a higher effect, an easier fabrication). The ability to electrically modify some magnetic properties such as the Curie temperature, magnetization through strain in a reversible or irreversible fashion was proved. In addition, a variation of measurement methods was used to monitor the magnetoelectric effect such as the ferromagnetic resonance [73], [74], or Lorentz force microscopy, MFM.

1.4 Thesis outline

Chapter 2 deals with a description of the experimental techniques used to fabricate and characterize the materials studied in this work. While most equipment used is standard commercial equipment that was available for use, some set-ups were specifically developed in the framework of this thesis. Studies on simple test samples (thin films of Ni and Co) developed to validate the set-ups are included in the annex.

Chapter 3 concerns the preparation and study of compositionally graded FeRh films. The films were sputtered onto Si substrates and their structural, magnetic and optical properties were studied as a function of composition, temperature, magnetic field or E-induced strain.

Chapter 4 deals with a study of the influence of substrate-mediated strain on the transition characteristics of FeRh films. $Pb(Mg_{1/3}Nb_{2/3})O_3$ - $0.3PbTiO_3$ (PMN-PT) was chosen as the piezoelectric substrate because of the high strain achievable in single crystals. Commercial crystals were used and a polishing protocol was developed to produce surfaces suitable for thin film deposition. Transport measurements made using set-ups developed during the thesis, and described in Chapter 2, were used to follow the influence of strain on transition characteristics.

Chapter 5 describes the preparation and characterization of La-Fe-Si films.

Finally, conclusions and prospects for future work are presented in Chapter 6.

CHAPTER 2

Experimental methods

This chapter will describe the preparation of the graded films and the experimental methods which are used to characterize the properties of films and composite structures. The Fe-Rh graded films were prepared by the magnetron sputtering method and then samples were annealed ex-situ under secondary vacuum, either in a rapid thermal processing (RTP) furnace equipped with halogen lamps or in a tube furnace. Section 2.2 describes the preparation technique. The compositionally graded films will be characterized by a number of techniques: (1) structural characterization which includes EDX for the composition estimation of films, XRD for the crystal structure and SEM for the microstructure (the morphology of surface, thickness,...); (2) magnetic characterization using a Vibrating Sample Magnetometer (VSM) - Superconducting QUantum Interference Device (SQUID); (3) electrical properties were characterized by transport measurements which study the dependence of resistivity on temperature and magnetic field; (4) the ellipsometry measurement will be used to characterize the optical properties of graded films after annealing. These techniques will be introduced in section 2.2 except for the transport measurement technique described in a following section. To characterize the ferroelectric properties, I developed an equipment based on the Sawyer - Tower circuit and used the strain measurement technique to evaluate the piezoelectric effect. In this thesis, I also developed a transport measurement rig allowing the application of high voltage to the piezoelectric substrate for an investigation of electrical control of the phase change in the magnetocaloric materials through strain. Section 2.3 will discuss the development of the set-up.

2.1 Sample preparation

2.1.1 Sputtering method

The sputtering phenomenon was discovered in a DC gas discharge tube by Grove in 1852 when he observed the cathode material inside the discharge tube [75]. Nowadays, this phenomenon is one of the most common methods for thin film deposition or etching. In this method, ions are accelerated by an electrical field to bombard the target so as to eject atoms from the target, which then move to the substrate, and condense to form a film. The ionized gas is typically produced with an inert gas such as Xe, Ar, Kr or a mixture of Ar-N_2 or Ar-O_2.

DC diode sputtering. DC diode sputtering in diode configuration, which is composed

of two planar electrodes, is the simplest one. In this configuration, the target plays the role of cathode with a cooling unit at the bottom side and the substrate is the anode. The sputtering process will be started when a DC voltage is applied to electrodes in the presence Ar or another inert gas. This voltage will ionize Ar atoms, create the sputtering plasma and accelerate the ions towards the target, resulting in the deposition of a film on the substrate. During the Ar ionization process, the released electrons moving from the cathode to the anode will collide with Ar atoms, ionize them and continue the cycle.

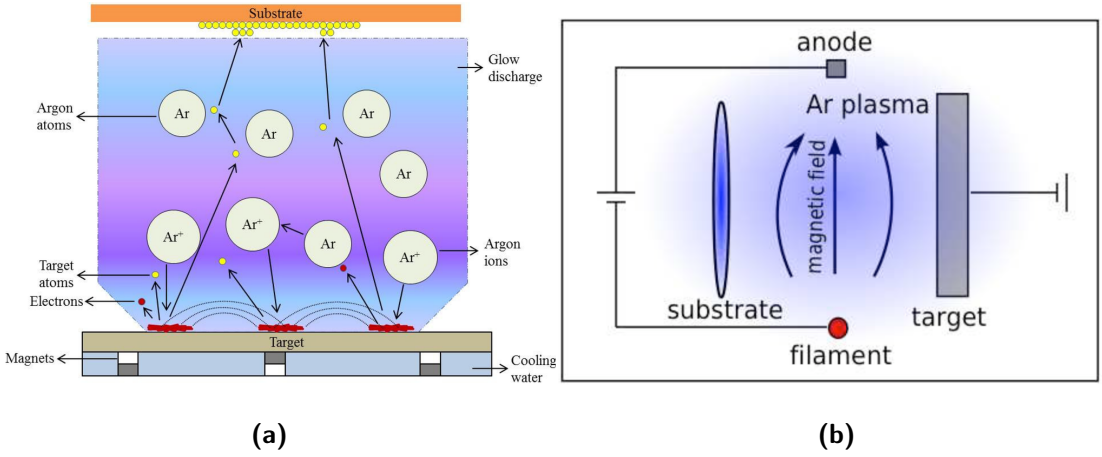

Figure 2.1. *Schematic of two sputtering systems (a) A magnetron sputtering: the plasma is confined to a region of the target by magnets behind the cathode. This brings a higher efficiency than the simple DC method. (Image taken from [76]). (b) A triode sputtering system: the Ar atoms are ionized by electrons emitted from the filament. (Image taken from [77])*

Magnetron sputtering. The advantage of the DC sputtering method is its simplicity but there are some disadvantages such as: the requirement for high voltage, a low ion current density at the cathode and non-applicability to dielectric materials. In the magnetron sputtering method, by positioning magnets behind the cathode, we confine electrons to move along magnetic flux lines close to the target instead of travelling to the substrate (anode) (see Fig. 2.1a). It leads to enhancement of gas ionization due to an increase of the electron path length which means an increase of the probability of collision. The erosion rate of the target material will increase and then it increases the efficiency of the sputtering process. In general, the magnetron sputtering method has the following main advantages: a high uniformity and flatness, applicability to insulating targets if an RF voltage supply is used. In this thesis, the Fe-Rh-based magnetic films have been prepared by the DC magnetron sputtering method.

Triode sputtering. We also use the triode sputtering method to deposit La-Fe-Si films (see Fig. 2.1b). In this method, electrons are introduced through thermionic emission from a tungsten filament. These electrons will ionize the Ar atoms, and thus create a plasma. Ar ions are accelerated to the target under an electric field and eject the particles in a similar way as above. There is also a magnetic field between the filament and its anode which confines electrons to enhance the Ar ionization and thus increase the deposition rate.

Table 2.1 summarizes the specifications of the two sputtering machines which have been used to prepare films in this thesis.

Table 2.1. *Specifications of the magnetron and triode sputtering machines which have been used to prepare films in this thesis.*

	Triode sputtering	*Magnetron sputtering*
Base pressure	$\sim 10^{-6}$ mbar	10^{-6} - 10^{-8} mbar
Substrate-target distance	Typically 7.5 cm	5 - 10 cm
Filament current	$\leq$180 A	–
Target	- 4 DC targets - Size of 10×10 cm^2 or smaller - Voltage $\leq$ 900V	- 4 RF and 4 DC targets - Diameter of 3 inch
Load-lock	No	Yes
Substrate	- With and without rotation - Diameter $\leq$ 10cm - Heater ($\leq$ 800°C)	- No rotation - Diameter $<$ 10cm - 2 sample holders: cold and hot ($\leq$ 800°C)
Deposition rate	Up to 56 Å/s (*)	$\sim$ 1 Å/s (*)

* Depending on the target material, the distance between target-substrate, the electric field,...

2.1.2 The annealing equipment

After deposition, films were annealed ex-situ, either in a commercial RTP furnace equipped with halogen lamps or in a home-made tube furnace where films are introduced at the annealing temperature through the use of a load-lock. The RTP furnace (Jipelec Jetfirst 100) was made by the SEMCO group. The temperature sensor of the RTP furnace is on the bottom side of the sample holder. For the tube furnace, designed and built by Richard Haettel from Institut Néel, the temperature sensor is outside the vacuum tube. Table 2.2 summarizes specifications of RTP and homemade furnaces.

Table 2.2. *Specifications of the RTP and tube furnaces which have been used for heat treatment in this thesis.*

	The RTP furnace	*Tube furnace*
Vacuum	$< 10^{-5}$ mbar	$> 10^{-8}$ mbar
Sample size	Diameter $\leq$ 10 cm	$\leq 6\times10$ cm^2
PID	Yes	Yes
Temperature sensor	- Pyrometer - Thermo-couple (<1000°C)	Thermo-couple (S-type)
Loadlock	No	Yes
Temperature range	RT to 1300°C	RT to 1050°C
Ramp rate	1°C/s to 400°C/s	Not specified (*)
Cooling process	Controlled	Natural cooling ($\sim$ 33°C/h)
Advantage	- Rapid ramp rate - Cooling control	- High vacuun - Temperature is uniform over a large area
Disadvantage	- Low vacumn	- No fast cooling

* In experiment, the ramp rate can be up to $\sim$50°C/min

2.2 Characterization techniques

2.2.1 Crystal structure and microstructure

2.2.1.1 X-ray diffraction technique

In this thesis, films have been structurally characterized using X - Ray Diffraction (XRD) technique. From the diffraction pattern, we can obtain the crystal structure, lattice parameters, texture, orientation or grain size of materials. X - rays are electromagnetic radiation whose wavelengths are from 10 nm to 0.1 nm. The XRD phenomenon originates from the diffraction of the X - ray beam on the crystal surface of material, which occurs over a certain penetrating depth.

Considering an X - ray beam with a wavelength of λ is incident to a crystal material at an angle of θ, when an X - ray beam interacts with a crystal, it will be scattered in all directions. In some directions, the scattered waves will interfer destructively, resulting in intensity minima, and in other directions, constructive interference will occur, resulting in intensity maxima. X-ray reflection by a family of parallel crystal planes is shown in figure 2.2. The diffraction condition for intensity maxima is described by Bragg's law:

$$2dsin\theta = n\lambda, \qquad \text{for } n = 1, 2, 3, ... \tag{2.1}$$

where: d - the interplanar spacing and 2dsinθ - the path length difference.

In order to analyse the crystal structure of a material, peak characteristics such as the

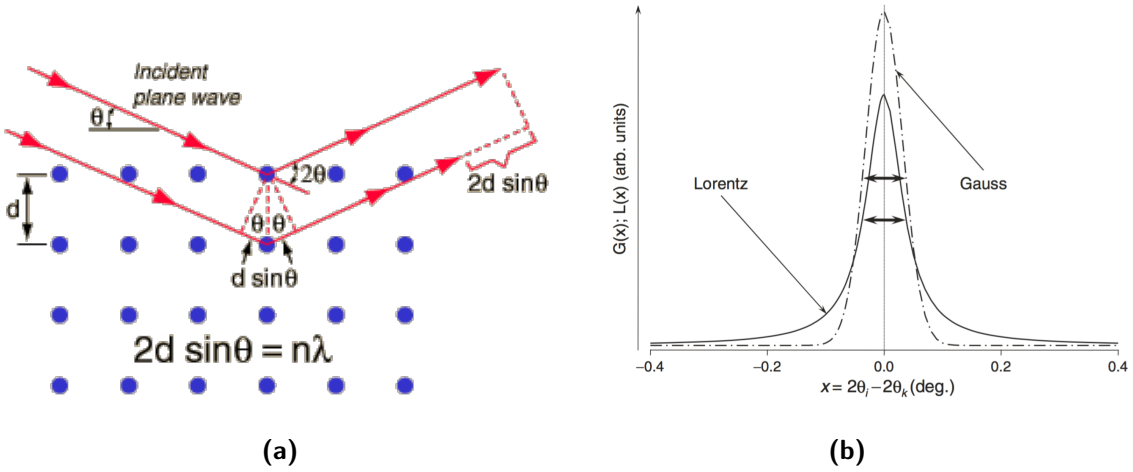

Figure 2.2. *(a) The reflection of X - ray beams on the crystal planes. The diffraction condition required for an intensity maximum is the Bragg's law: 2dsinθ = nλ, (Image adapted from [78]) (b) The Gaussian and Lorentzian peaks profile: the features of Gaussian profile is a rounded maximum and no tails while the Lorentzian profile has a sharp peak and long tails. (Image taken from [79])*

position, intensity, full width at half maximum (FWHM) and shape are important. In 1918, Scherrer observed the contribution of small crystallite size to Bragg peak broadening β. In 1944, Stokes and Wilson observed that the strain or imperfect crystals could also contribute to peak broadening. Broadening effects can be described in a simply combined relationship as follows:

$$\beta = \underbrace{\frac{k_1 \cdot \lambda}{D \cdot cos\theta}}_{\text{Size}} + \underbrace{k_2 \cdot \varepsilon \cdot tan\theta}_{Strain} \tag{2.2}$$

where: D - the average crystallite size; ε - the average strain; k_1- the Scherrer constant which is in the range of 0.87 - 1; k_2 - depending on the definition of the strain.

By plotting $\beta cos\theta$ as a function of $k_2 sin\theta$, the size and strain broadening effects can be deconvoluted, as proposed by Williamson and Hall in 1953 [80]. Although it is basic, this method is also useful to estimate the average crystallite size and strain in the material. The linear Williamson - Hall plot (Eqn. 2.2.) assumes the peak shape has a Lorentzian profile, while the quadratic plot assumes the peak has a Gaussian profile shape. The average Williamson - Hall plot, also known as the Langford method, attributes the strain and crystallite size contributions to the Gaussian and Lorentzian profile shape, respectively. In general, to obtain good values for peak characteristics, the Voigt function or its modified versions is used to fit and deconvolute the broadening effect of materials into Gaussian and Lorentzian contributions. The two most used peak-shape functions are [79]:

Pseudo-Voigt:

$$PV = \underbrace{\eta \frac{C_G^{1/2}}{\sqrt{\pi} \cdot H_k} exp\left(-C_G \cdot X_{jk}^2\right)}_{\text{Gauss part}} + \underbrace{(1-\eta)\frac{C_L^{1/2}}{\pi \cdot H_k}\left(1 + C_L \cdot X_{jk}^2\right)}_{\text{Lorentz part}} \tag{2.3}$$

Pearson-VII:

$$PVII = \frac{\Gamma(\beta)}{\Gamma(\beta - 1/2)} \times \frac{C_P^{1/2}}{\sqrt{\pi} \cdot H_k} \times (1 + C_P \cdot X_{jk}^2)^{-\beta} \tag{2.4}$$

where: C_G = 4ln2; C_L = 4; H_k - the full width at half maximum (FWHM) of the k^{th} Bragg reflection; X_{jk} = ($2\theta_j$ - $2\theta_k$)/H_k with $2\theta_j$ - the Bragg angle of the j^{th} point in the diffraction pattern and $2\theta_k$ - the calculated Bragg angle of the k^{th} Bragg reflection; Γ - the gamma function [79]; $C_P = 4(2^{1/\beta}-1)$; η - the mixing value which is in the range of 0 - 1, 0: pure Lorentz and 1: pure Gauss.

The peak FWHM at a 2θ angle was given by Caglioti et al (1958) (also called Cagliotti equation) as follows [79]:

$$H_k = \sqrt{U \cdot tan^2\theta + V \cdot tan\theta + W} \tag{2.5}$$

where: U, V, W are the refined parameters; U is strongly associated with strain; the crystallite size is associated with U and W.

In reality, the instrument also contributes to the peak characteristics. A standard sample without size and strain contributions such as cerium oxide can be used to calibrate the instrument.

In this thesis, films have been structurally characterized at room temperature, either by a diffractometer equipped with a copper X-ray source (Bruker AXS D8 Discover) or by one equipped with a cobalt source (Siemens K760). The XRD patterns were fitted using the Pseudo - Voigt function. Material identification is achieved by matching the obtained patterns to reported XRD patterns in the ICDD PDF-4 database.

2.2.1.2 Scanning electron microscopy

Scanning electron microscopy (SEM) was used to study the morphology and thickness of films. The principle of SEM is similar to that of optical microscopy, except an electron beam is used instead of light and electric and magnetic fields as used as lens. The sample is scanned with an electron beam and detectors collect signals which are emitted from the interaction of electrons with the material. These signals can be secondary electrons (SE), back scattered electrons (BSE), X-rays or cathoduluminescence photons that carry different characteristic information of the material. The SE detector provides a topographical image while the EsB detector (Energy selective Backscattered detector) is sensitive to the atomic number, and thus the composition. Emitted X-rays can be used for energy dispersive X-ray spectroscopy (EDX) which allows to estimate the composition of material (see blow).

In the determination of morphology and thickness of our films, the Zeiss Ultra Plus Field Emission Scanning Electron Microscope (FESEM) was used with typical specifications such as: resolution of 1 nm at 15 kV or 1.7 nm at 1 kV, an accelerating voltage from 0.1 - 30 kV, a low current (2.10^{-8} A) and various detectors.

2.2.2 Measurement of film composition

EDX analysis was used to characterize the composition of as-deposited films in this thesis. The principle of EDX is as follows. The electron beam emitted from a gun bombards the material and interacts with its atoms which causes shell transitions, resulting in X - ray emission. Because this emission occurs at an energy characteristic of the element being probed, a measurement of this energy can be used to estimate the film composition quantitatively. In contrast to qualitative analysis, quantitative analysis is complex, requiring the establishment of a standard library at various voltages, a calibration of the system, sufficient spectrum statistics, which needs a long time measurement depending on the voltage, current and the post-treatment of data. We describe an analysis using the standard library as follows.

Preparation of the standard library. Spectra of pure elements are acquired at various acceleration voltages to make the standard library. Spectra of pure elements (the standard library) are important, because they contain the peak intensities of elements, which determine the element concentrations. Hence, preparation of pure elements (polishing) is needed, and spectrum counts are at least $\sim$ 1 million counts to achieve high standards (sufficient spectrum statistics).

Acquisition of film spectra. Spectra of films also need to be acquired at various accelerating voltages with a calibration of the system before (calibrate the peak positions and intensities). We note that characterization of sample and standard is measured under identical conditions of beam energy, detector efficiency,...

The ratio of the peak intensities of sample and the standard is defined as follows:

$$K = \frac{I_{sample}}{I_{standard}} \qquad 0 \leq K \leq 1 \tag{2.6}$$

The interaction volume changes with voltage (a simulation of the interaction volume with voltage is not presented here), since the center of the interaction volume moves from the film at low voltage to the substrate at high voltage, the K ratios decreases with increasing voltage. We note that acceleration voltages must be higher than the emitting X-ray energy, i.e. for Pt element, because of $L_\alpha = 9.44\,\text{keV}$ X-ray energy (periodic table of the elements), the acceleration voltage is not smaller than L_α energy.

K ratios are then calculated and plotted against accelerating voltages K(V). A variation of accelerating voltages is needed to achieve the trend of K(V).

In this thesis, the film composition was measured by an EDX system which is coupled with the FESEM instrument. The standard library was prepared by measuring pure elements at various voltages with $\sim$ 1 million counts for each element at each voltage. Spectra of films were acquired with 800 k counts to get sufficient spectrum statistics. Then data was analysed with the support of the STRATAGEM program. This program can simulate K(V) from a film composition and thickness using the physical model (phi-rho-Z). This program also can give film composition and thickness by fitting an analytical X-ray emission model (phi-rho-Z) to the experiment data K(V). The absolute mean deviation

between the experimental and the calculated K values in this study is about 0.2 %.

2.2.3 Principles of vibrating sample magnetometry and superconducting quantum interference device (VSM SQUID)

The magnetic characterization of films presented in this thesis has been carried out with a VSM SQUID. The principle of VSM is based on Faraday's law of induction. The sample connected to a vibrating device is placed inside pick-up coils within an external magnetic field, the latter used to magnetize the sample. Due to the relative motion of the sample with respect to the pick-up coils, a voltage is induced in the pick-up coils, which is proportional to the magnetic moment of the sample.

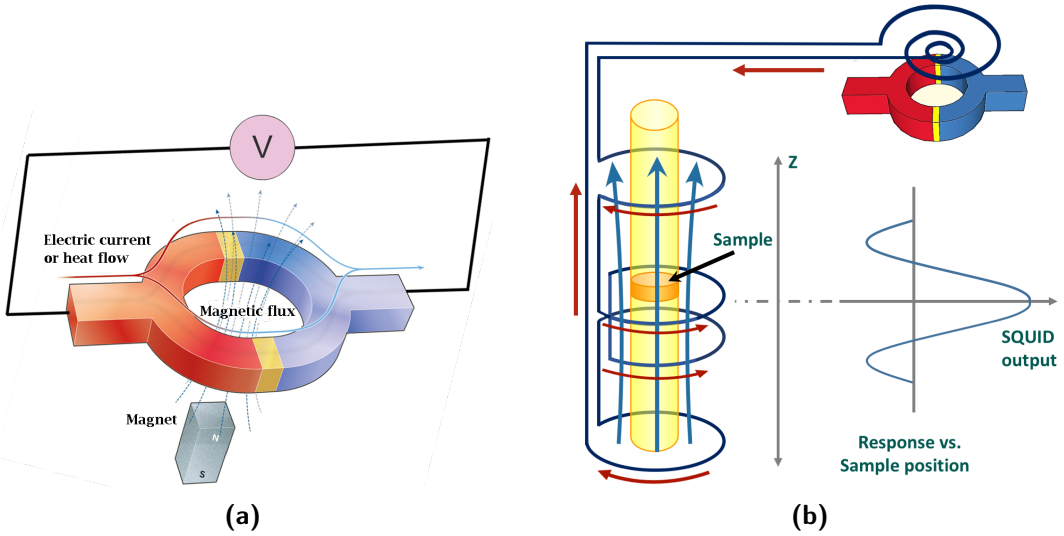

Figure 2.3. *(a) A DC SQUID contains two Josephson junctions, the red and blue colors indicate two superconductors while the yellow one indicates the insulator (Image adapted from [81]). (b) A VSM SQUID circuit combines the detection coils. Here, the DC SQUID unit plays the role of current - voltage converter.*

A SQUID is a device that can measure magnetic flux quanta passing through its loop. It is a superconducting ring with one or two Josephson junctions (SQUID RF or DC) (see Fig. 2.3a). The minimum value of flux causing quantum interference phase change in this junction is $\Phi_0 = h/(2e) \simeq 2.068\times10^{-15}$ Wb with $h = 2\pi\hbar$ and e is the electron charge [82]. Therefore, a SQUID can be used to measure weak magnetic signals. The principle of SQUID is based on the phenomenon of flux quantization and Josephson tunneling. When a magnetic material moves in the vicinity of the superconducting ring which is connected to a conducting circuit, the change in the magnetic flux will cause a change in the current, and then the measured voltage at the junctions responsed with the change in magnetic flux with the voltage oscillation period Φ_0. By measuring this change in the voltage which is proportional to the magnetic signal, the change in flux or the magnetic moment can be determined.

In general, a SQUID has high sensitivity while a VSM can detect magnetic moments more rapidly than SQUID. The combination of VSM and SQUID leads to a magnetometer

which is fast and highly sensitive. In this case, the detection coils are integrated to a SQUID unit as shown in figure 2.3b and the SQUID plays the role of current to voltage converter.

The magnetometer used to characterize the magnetic properties of films in this thesis is a Quantum Design VSM SQUID with specifications as follows: maximum field of 7 T, sensitivity of 10^{-11} Am^2, temperature range of 1.8 - 1000 K, maximum magnetic moment of 10^{-2} Am^2.

The measured magnetic properties of Fe-Rh-based films are interpreted to obtain the first order transition temperature T_t and the thermal hysteresis width $\triangle$T. The definition of the first order transition temperature is the maximum of the derivative of magnetization M with respect to temperature T: $\partial M/\partial T$. Then a Gaussian function is used to fit the $\partial M/\partial T$ against T curve to obtain a more precise value. For the hysteresis width, it is defined as the difference between the heating and cooling transition temperatures $\triangle T = |T_{t\text{-heating}} - T_{t\text{-cooling}}|$. We can calculate the numerical derivative using two consecutive points and locate the temperature at the middle point as follows:

$$\frac{\partial M}{\partial T}\left(\frac{T_{i+1}+T_i}{2}\right) = \frac{M(T_{i+1})-M(T_i)}{T_{i+1}-T_i} \tag{2.7}$$

Formula 2.7 is based on the Taylor series expansion with the order of accuracy of $\mathcal{O}(\triangle T)$. It is well-known that the central difference method is better due to its higher precision. Thus, we use the central difference method to estimate the derivative of M against T for Fe-Rh-based films. It is noted that the first and last points were estimated by using the forward and backward difference methods with the error of $\mathcal{O}(\triangle T^2)$, respectively. The central difference formula is as follows:

$$\frac{\partial M}{\partial T}(T_i) = \frac{-M(T_{i+2})+8M(T_{i+1})-8M(T_{i-1})+M(T_{i-2})}{12\,(T_{i+1}-T_i)} + \mathcal{O}(\triangle T^4) \tag{2.8}$$

The forward difference:

$$\frac{\partial M}{\partial T}(T_i) = \frac{-M(T_{i+2})+4M(T_{i+1})-3M(T_i)}{2\,(T_{i+1}-T_i)} + \mathcal{O}(\triangle T^2) \tag{2.9}$$

The backward difference:

$$\frac{\partial M}{\partial T}(T_i) = \frac{3M(T_i)-4M(T_{i-1})+M(T_{i-2})}{2\,(T_{i+1}-T_i)} + \mathcal{O}(\triangle T^2) \tag{2.10}$$

2.2.4 Ellipsometry measurements

Optical properties of Fe-Rh based films have been characterized using ellipsometry. Ellipsometry is a technique which measures the change in polarization state of light (the phase change $\triangle$ and the light amplitude change ψ upon reflection) when the light reflects from, or is transmitted through, the sample. A complex reflection coefficient ρ is defined as follows: $\rho = \tan\psi \cdot e^{i\triangle}$.

A schematic of an ellipsometry measurement is shown in figure 2.4. The basic principle

of this technique is as follows. A sample is exposed to a linearly polarized light, then the light reflected from the sample becomes elliptically polarized and travels to a rotating analyzer. A detector is used to convert the polarized light to a voltage signal which will be compared to the incident light, resulting in ψ and $\triangle$. This data is analysed to get the optical properties or other information i.e. roughness, thickness. The pseudo dielectric function ε for a bulk material can be written in terms of ρ as follows [83]:

$$\langle\varepsilon\rangle = sin^2\phi_0 \left[1 + tan^2\phi_0 \left(\frac{1-\rho}{1+\rho}\right)^2\right] \tag{2.11}$$

where: $\varepsilon = \varepsilon_1 + i\varepsilon_2$ with ε_1 and ε_2 being the real part and the imaginary part of the dielectric function, respectively; ϕ_0 - the incident angle of light. It is noted that a single ($\triangle$, ψ) is measured at (ϕ_0, λ) with λ the wavelength of incident light.

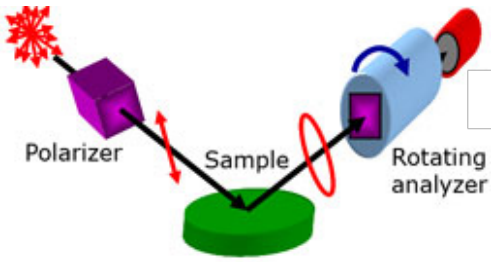

Figure 2.4. *Schematic diagram of spectroscopic ellipsometry. The unpolarized light is polarized by the polarizer before its reflection from the sample surface. Then, the reflected beam is analysed by the rotating analyzer and travels to the detector. (Image adapted from [84]).*

The complex refractive index N can be calculated as the square root of the dielectric function: $N^2 = \varepsilon$. In summary, the relationship between the refractive index N, the dielectric function ε and conductivity σ is present in table 2.3 [85].

The spectroscopic ellipsometer used in this thesis is M-2000 Ellipsometer from J. A. Wool Co. The data were analysed with the help of the program CompleteEASE from J. A. Wool Co. The wavelength is from 211 nm to 1687 nm.

Table 2.3. *Relationships between optical parameters* [85]. *Here, n - the ratio of the speed of light in vacuum compared to in the material; k - the absorption index; σ_1 and σ_2 are the real and imaginary parts of the conductivity; ω - the circular frequency of the light beam; ε_0 - vacuum permittivity.*

	Real part	*Imaginary part*
Refractive index $\langle N \rangle = \mathrm{n} + \mathrm{ik}$	$\mathrm{n} = \varepsilon_2/(2\mathrm{k})$ $\mathrm{n} = \sqrt{\left(\varepsilon_1 + \sqrt{\varepsilon_1^2 + \varepsilon_2^2}\right)/2}$	$\mathrm{k} = \varepsilon_2/(2\mathrm{n})$ $\mathrm{k} = \sqrt{\left(-\varepsilon_1 + \sqrt{\varepsilon_1^2 + \varepsilon_2^2}\right)/2}$
Dielectric function $\langle \varepsilon \rangle = \varepsilon_1 + \mathrm{i}\varepsilon_2$	$\varepsilon_1 = \mathrm{n}^2 - \mathrm{k}^2$ $\varepsilon_1 = 1 - \sigma_2/(\omega\varepsilon_0)$	$\varepsilon_2 = 2\mathrm{nk}$ $\varepsilon_2 = \sigma_1/(\omega\varepsilon_0)$
Conductivity $\langle \sigma \rangle = \sigma_1 + \mathrm{i}\sigma_2$	$\sigma_1 = \omega\varepsilon_0\varepsilon_2$	$\sigma_2 = -\omega\varepsilon_0(\varepsilon_1 - 1)$

2.3 Development of ferroelectric and transport measurements

Piezoelectric materials were used as substrates in the heterostructure multiferroic composites studied here. Characterizing the electric properties of the piezoelectric materials under conditions relevant to their application is important and necessary. The characterization of the ferroelectric properties allow us to determine the important parameters such as polarization, coercive electric field, P(E) loop, breakdown field, strain behavior as a function of voltage (electric field). Transport measurements are used to investigate the phase change in the magnetocaloric materials induced through substrate mediated strain (chapter 4). This section describes the principles and development of these techniques in order to characterize the strain effect.

2.3.1 Ferroelectric measurement

The P(E) loop is a graph of the change in charge or polarization as a function of external electric field at a given frequency, as shown in Chapter 1. A Sawyer - Tower circuit [86] is commonly used to characterize the P(E) loop. The Sawyer - Tower measurement circuit uses a linear reference capacitor called the sense capacitor in series with the ferroelectric sample and measures the voltage drop across the sense capacitor. Figure 2.5a shows a schematic of the Sawyer - Tower circuit. Based on the P(E) loop, parameters such as the dielectric constant, the hysteresis loss or the capacitance of the sample can also be obtained.

Assume that there is a charge Q on the sample surface of area S. Because the sense capacitor is in series with the sample, we have:

$$V_{AC} = \frac{Q}{C_{Ferro}} + \frac{Q}{C_S} \approx \frac{Q}{C_{Ferro}}, \qquad because\ C_{Ferro} \ll C_S, \tag{2.12}$$

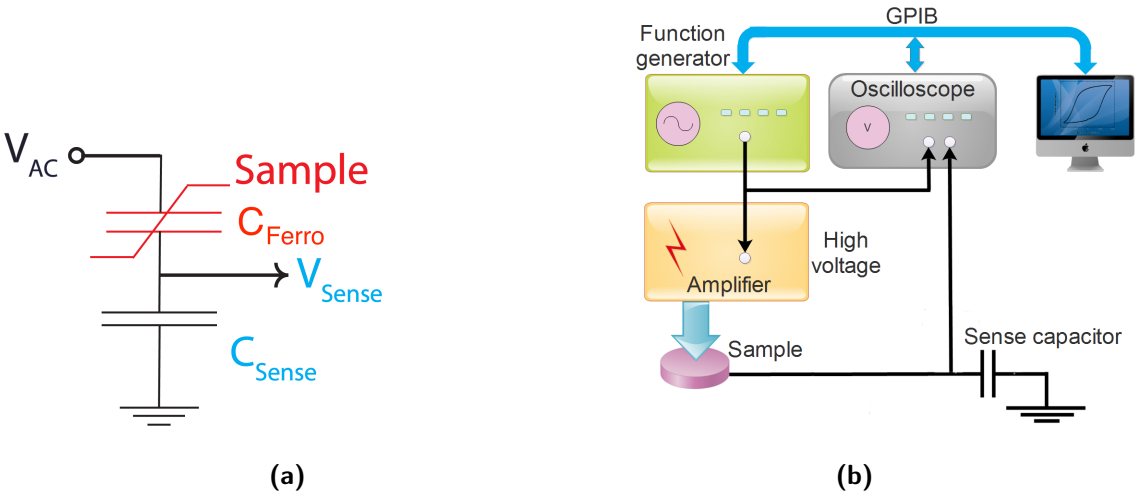

Figure 2.5. *(a) The Sawyer - Tower circuit, (b) Schematic of building blocks for the ferroelectric measurement technique*

The voltage across the sense capacitor V_S is given by:

$$V_S = \frac{Q}{C_S} = \frac{DS}{C_S} \tag{2.13}$$

The polarization of the ferroelectric sample P is calculated with this formula:

$$\vec{D} = \vec{P} + \varepsilon_0 \vec{E} \tag{2.14}$$

$$\rightarrow P = \frac{V_S C_S}{S} - \varepsilon_0 E \tag{2.15}$$

where: C_{Ferro} - the capacitance of the ferroelectric sample; C_S - the value of the sense capacitance; Q - the electric charge; V_{AC} - the applied voltage; V_S - the voltage across the sense capacitor; S - the area of the sample surface; D - the displacement; $E = V_{AC}/d$ - the electric field applied to the sample of thickness d.

The Sawyer - Tower circuit is simple, but the choice of the reference capacitor is not easy. If we chose a large capacitance, most of the applied voltage will fall across the ferroelectric sample, but the voltage of the sense capacitors may be too small. Under an AC voltage, the charge is collected in the sense capacitor and then it generates a voltage which goes back to the sample in the opposite direction with the applied voltage (also called the back voltage). If the capacitance of the sense capacitor is small, the sense voltage is small, resulting in a small back voltage. However, if the sense capacitance is small, the sense voltage is large, which leads to a significantly reduced voltage across the ferroelectric sample. For this reason, we must choose suitable sense capacitors to balance between the sensitivity of the measurement and the amount of voltage across the sample. As a general rule, the sense capacitor should be 10 to 1000 times the sample capacitance. Another matter in the Sawyer - Tower circuit is the parasitic capacitance which is caused by wires, the amplifier or the oscilloscope.

Besides the Sawyer - Tower circuit, other methods are also used to measure ferroelectric hysteresis loops. A comparison between ferroelectric measurement techniques is shown in table 2.4. The Shunt method substitutes the sense capacitor of the Sawyer Tower circuit by a reference resistor called the Shunt resistor. This method is based on current measurement in which the current is measured as a function of voltage drop across the shunt resistor and later integrated to get the charge Q. The Sawyer - Tower and Shunt methods are limited by the precision of the reference capacitor/resistor and the influence of the capacitance of cables and measuring devices on the result. The virtual ground method, which uses a current to voltage circuit to observe the P(E) loop, does not have these limitations. It is based on a current measurement using a feedback resistor across an operational amplifier. The advantage of this method is its highest precision. However, the stability, bandwidth and phase shift of the operational amplifier may cause problems. While the Sawyer - Tower and the Shunt circuits use the reference capacitor/resistor, the current step method has no references. This method uses an applied current as an excitation signal. This current induces a directly measurable voltage drop over the ferroelectric material.

Table 2.4. *Comparison between ferroelectric characterization techniques [87]*

Method	*Measured quantity*	*Reference*	*Integration necessary*	*Bandwidth requirement*	*Parasitics*
Sawyer - Tower	Q	Capacitor	No	Moderate	High
Virtual ground	I	No	Yes	High	Low
Shunt	I	Resistor	Yes	High	High
Current step	V	No	No	Moderate	Moderate

In this thesis, we mainly used bulk $Pb(Mg_{1/3}Nb_{2/3})O_3$-0.3$PbTiO_3$ (PMN-PT) as the piezoelectric substrate. Because of the high quality of PMN-PT single crystals with high polarization and low leakage current, we chose the Sawyer - Tower circuit for this technique. The Sawyer - Tower printed circuit board was made and packed in a closed box to perform the ferroelectric measurement. The typical capacitance of the piezoelectric material we used is $\sim 40\,\mathrm{nF}$, so a sense capacitor with the equivalent capacitance of $\sim 42.1\,\mu\mathrm{F}$ was chosen. A high voltage amplified from an initial waveform is applied to the sample, and a divider circuit is used in order to scale the input high voltage to a smaller one with the ratio 1000:1, which can connect to the measured device. We also can connect the initial waveform from the function generator to the oscilloscope and then it is multiplied with an amplification factor of 100. The sense capacitor is connected to the oscilloscope. A computer is used to control, obtain and process raw data to get the desired quantities. Because of the use of high voltage, Zener diodes are added to protect the measured device. A schematic of the building blocks is shown in figure 2.5b and specifications of devices are summarized in table 2.5. The raw data acquired is the voltage of the sense capacitor as a function of the applied electric field E. Data treatment is required to get the P(E) loop and the feature parameters such as P_S, E_C. This process is performed with a Matlab program

using equation 2.15 .

Table 2.5. *Specifications of equipments which are used to construct the ferroelectric measurement system*

Device	*Model*	*Function*
Sawyer - Tower box (in-house)	Home made	Measure P(E)
Function generator	Agilent 33120A	Generate waveforms
Voltage amplifier	Kepco BOP 1000M	Amplify the initial waveform
Data acquisition	Tektronic DSO TDS 220	Acquire data
Computer	PC	Control, obtain and process data using GPIB cards

2.3.2 Characterization of strain behavior

The strain effect, also called the butterfly behavior, is a result of polarization switching under an applied electric field (see Chapter 1). The strain behavior depends on the applied voltage, temperature, the sample quality, and is typically less than 0.5 % for PMN-PT, the material used here (see figure 2.6a). The behavior of the PMN-PT substrate has been characterized using a strain gauge and the lock-in amplifier together with a Wheatstone bridge. A schematic of the strain measurement technique for the piezoelectric behavior is shown in figure 2.6b. Here, we present the principle of the strain measurement using the strain gauge as follows.

Due to the applied electric field, the ferroelectric material will be deformed. When the strain gauge is bonded to the material under study, the strain of the material is transferred to the strain gauge assuming that the two deform together. Changes in the dimensions of the gauge lead to a change in the resistance of the strain gauge. By measuring the change of the resistance in the strain gauge, the strain behavior of the piezoelectric material can be calculated as:

$$\varepsilon = \frac{\triangle R/R}{GF} \tag{2.16}$$

where: $\triangle$R/R - the change in resistance of the strain gauge; GF - the gauge factor of the strain gauge, which expresses the sensitivity of the gauge material to strain (also called the sensitivity factor). The factor of the strain gauge used in this thesis is GF = 2.1.

The strain behaviour of a ferroelectric material also depends on temperature. Above its Curie temperature, a ferroelectric material becomes paraelectric. For PMN-PT, this critical temperature is $\sim$ 120 - 155°C. Integrating the strain gauge measurement with a temperature control system, we can explore the effect of an external electric field and temperature on the strain behavior, which can be useful for the investigation of the electrical control of magnetic properties through strain.

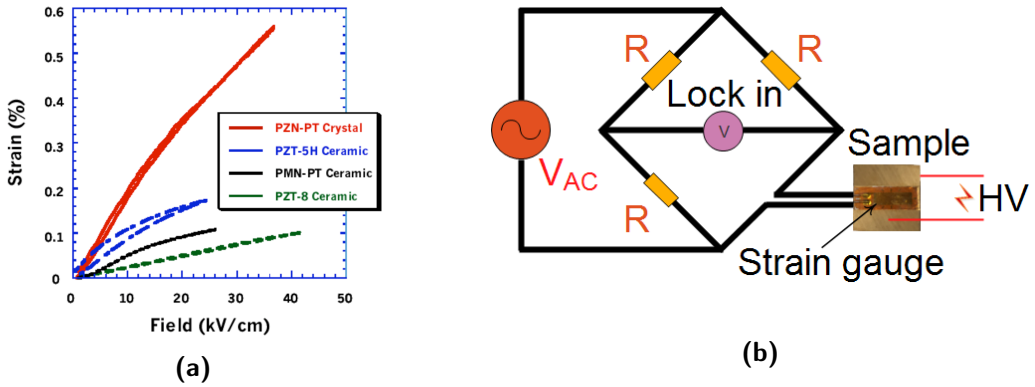

Figure 2.6. *(a) The strain behavior of different ferroelectric materials (from the supplier's datasheet). The strain depends on the applied voltage, its chemical composition, quality and the measured temperature. (b) An electric circuit of the strain gauge technique using the Wheatstone bridge.*

2.3.3 Transport measurements

Transport measurements are in general made using one of two methods: the "two - probe" or "four - probe" (also called "four - contact" method). The advantage of the two - probe approach is simplicity, but when the resistance of the sample is small, because the resistance of contacts and the connected wires contribute to the result, a precise measurement of resistance is difficult. In the four - probe circuit (Fig. 2.7a), the current I is forced through the sample using its contacts and an ammeter will measure the current, while the voltage across the sample V is measured using two other contacts and a voltmeter. In a series loop, the current will be the same at all points and the wires of the voltmeter carry a negligible current, while the voltage drop due to the current - carrying wires will not be measured, therefore only the voltage across the sample is measured. Then the resistance value can be calculated using: R = V/I.

In this thesis, we have used the four contact method to investigate the phase change induced in magnetic materials, deposited on a piezoelectric substrate, upon application of an applied voltage. Because a system characterizing resistance as a function of an electric field and temperature was not available at the start, we developed a transport measurement system to perform such measurements. A schematic of the building blocks is shown in figure 2.7b. Here, the four contacts used as electrodes are made using an epoxy adhesive or four spring contacts. An AC home - made current source I, which is generated by an AC-voltage waveform from a lock - in amplifier, flows the current into the sample through two contacts. The current source is synchronized with the lock-in amplifier which is used to measure the voltage of the sample (V) through the two remaining contacts.

A high voltage is applied to the piezoelectric substrate in order to investigate the phase change of the magnetic material due to strain. The sample is heated using heaters with a thermo-couple and a "Pt 1000" thermoresistance as temperature sensors. The thermo-couple is packed together with heaters while the Pt 1000 is close to the sample in order to get a precise measurement of temperature. The ensemble (sample, contacts, temperature

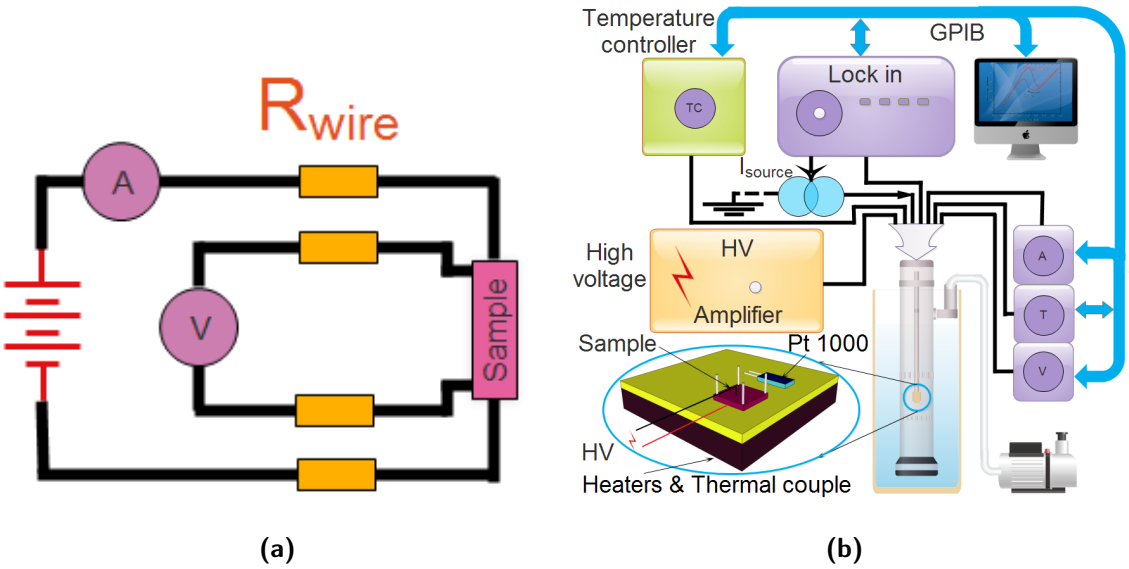

Figure 2.7. *(a) The four - probe circuit, (b) Schematic of building blocks for the transport measurement technique. This technique is used to investigate the phase change in Fe-Rh based films through strain.*

sensors, heaters) is inserted in a tube which is pumped (primary vacuum) and embedded in a liquid nitrogen tank in order to vary temperature below room temperature. The vacuum also protects the sample from oxidation when it is measured at high temperature. In principle, this system can measure resistance as a function of external electric field, external magnetic field and temperature. However, the measurement of resistance as a function of magnetic field and temperature is only carried out at or above room temperature, because of space limitations.

Various devices have been used to explore electrical control of the phase change and related works as follows. (1) bipolar high voltage, which is generated by the Kepco BOP 1000M, can apply up to ±1000 V to the sample. (2) An electromagnet is used to produce the magnetic field. The maximum magnetic field that can be achieved is 15 kOe and 100 Oe at room temperature and high temperature, respectively. (3) A bipolar Kepco power supply as a current source for the electromagnet. (4) A home - made AC current source for the four - probe method. (5) The lock - in amplifier which has been used in this thesis is a Stanford Research Systems SR830. (6) Agilent 33120 devices are used as voltmeter, ammeter and ohmmeter (for a temperature measurement of Pt 1000). (7) The temperature controlling system is a Eurotherm 3208. The temperature range is from 150 K to 1250 K with the use of liquid nitrogen and heaters for cooling and heating. (8) A rotary pump is used to produce a primary vacuum ($\sim 10^{-2}$ mbar). (9) A program based on Labview was written to control and measure automatically. The electric contacts are made from epoxy Epotek H21D which can be used up to 623 K. For low temperature, a four - spring contact was also used as electrodes. Zener diodes are used to protect the highly sensitive input of the lock in amplifier.

CHAPTER 3

Compositionally graded Fe-Rh films

3.1 Introduction

Fe-Rh-based system shows a first order AFM to FM transition close to room temperature and large effects such as a magnetoresistance effect of 50 % at transition [11], a giant magnetocaloric effect of $\triangle$T $\sim$ -12.9 K with $\mu_0 H_{max}$ = 2 T [88], a giant magnetostrictive effect of $\sim 8.2\times10^{-3}$ [89] and a magnetic entropy change $\triangle$S = 12.6 - 18.3 J.kg^{-1}.K^{-1} [5, 19]. Recently, this material has been revisited because of potential applications in spintronics, sensing or energy havesting. In 2014, Marti et al [8] demonstrated the feasibility of a spintronic AFM memory resistor at room temperature using Fe-Rh with some advantages such as an insensitivity to a strong magnetic field, a negligible stray field, which could be important for the high density memory. At the same time, Cherifi el al [9] showed the possibility to control the magnetic order by electric fields in the composite structure of BTO/FeRh with a higher ME coupling coefficient $\alpha_{ME} \sim 1.6\times10^{-5}$ s.m^{-1} than previous studies. This coefficient is five orders of magnitude larger than in single phase materials and at least one order of magnitude higher than in other composite materials such as BTO/LSMO. This opens a perspective for the use of Fe-Rh not only in storage technology but also for high sensitivity sensors. In 2015, Lee et al [10] reported a 8 % change of the resistivity when applying a voltage through the strain mediated coupling in the hybrid structure of a piezoelectric material of PMN-PT and an AFM material of FeRh. This large effect is attractive for potential applications in FeRAM since two different logic states can be written using a voltage. In fundamental physics, the Fe-Rh system is interesting as a model system to explore the magnetostructural phase change in magnetocaloric materials with or without an external field due to its relatively simple cubic crystal structure and the giant effects mentioned above.

The composition range having the first order transition is narrow, from 48 to 55 at. % Rh, so it is not easy to produce the desired AFM phase. In this work, we will use a combinatorial approach to obtain AFM samples. In this approach, the Fe-Rh film is compositionally graded in order to realize the idea: only one wafer and one deposition, one annealing protocol but this wafer provides many samples with a continuous spread of composition. Samples were prepared using the magnetron sputtering method and annealed ex-situ. EDX analysis was used to characterize the spread in composition of as-deposited films. The magnetic properties of the films were characterized by a VSM-SQUID and MOKE.

Microstructure was determined using XRD and FESEM. Transport measurements were made on samples to monitor the change of resistance as a function of temperature and follow the first order AFM-FM transition. Optical and ellipsometry measurements were used to assess the optical properties of samples after annealing. The thickness and roughness of samples were also checked by FESEM and AFM. These characterisation tools are described in Chapter 2.

3.2 Sample preparation

Compositionally graded Fe-Rh films were prepared by magnetron sputtering of composite targets consisting of a base of pure Fe (the diameter is 75 mm) and superposed pieces of Rh foil of surface area $25\times25\,\mathrm{mm}^2$. The distance between the target and sample was 50 mm. In the beginning, we used just one piece of Rh on top of the iron target, but to increase the Rh content in the film, 2 pieces of Rh foil were used as shown in figure 3.1a. The axes of target and wafer are the same and defined on the same figure. Because of this deposition configuration, we can expect the composition of the film to vary linearly along the x-axis and not to depend on y.

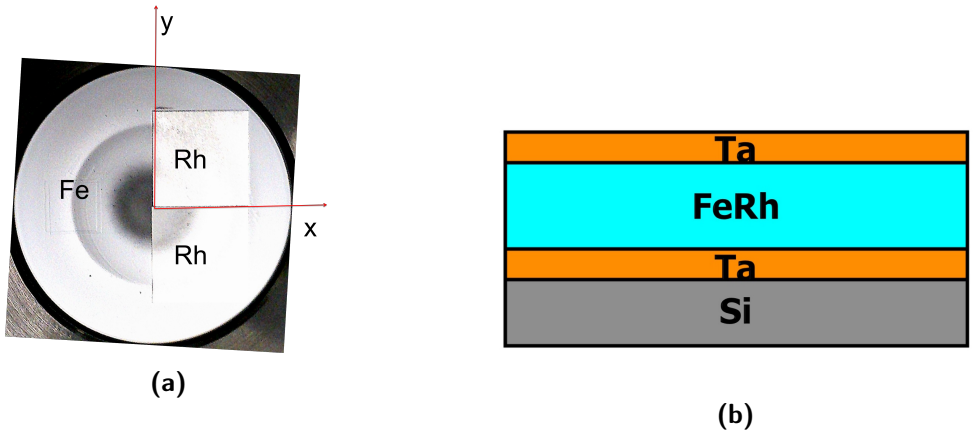

Figure 3.1. *(a) Composite targets consisting of a base of pure Fe and 2 pieces of Rh foil, and (b) the film structure on the Silicon wafer: $Si/SiO_2\|\,Ta\ 10\,nm/FeRh/Ta\ 1\,nm$.*

All samples were deposited at room temperature in a main sputtering chamber with a base vacuum of $P_{base} \sim 10^{-6} \rightarrow 10^{-7}$ mbar. Tantalum is used as buffer and capping layers. The structure of the film is Ta/FeRh/Ta as shown on the figure of 3.1b. After deposition, samples were annealed ex-situ under secondary vacuum, either in a RTA furnace equipped with halogen lamps ($P_{base} = 10^{-5}$ mbar) or in a tube furnace ($P_{high\ temperature} \sim 10^{-8}$ mbar) in which the sample is introduced at the annealing temperature through the use of a load-lock. The best results, including those reported hereafter, were achieved using the latter furnace, which we attribute to the better vacuum. Samples were annealed at different temperatures (500°C and 650°C) for 90 minutes. For the home-made tube furnace, the heating rate is 150°C/h to reach the annealing temperature. Finally, the

sample is cooled under natural conditions to room temperature, which took $\sim$ 1.5 days. After these processes, samples are ready to be characterized.

3.3 Sample characterization

3.3.1 Structural characterization

The Fe-Rh films were deposited on 2 inch Silicon wafers with a thermally oxided layer of 100 nm SiO_2. After annealing, using a FESEM, the fractured cross-sections along the x-axis and y-axis of the wafer were measured to estimate the thickness of the films (Fig. 3.2). Samples have a structure of Si/SiO_2 100 nm$\|$ Ta 10 nm/FeRh/Ta 1 nm. The in-lens image has a good resolution and shows a continuous film without cracks or intermixing between sample and substrate. The backscattered electron image clearly shows the constrast difference between layers due to the atomic composition. The thickness of the Fe-Rh film as a function of the position on the Silicon wafer is shown in figure 3.3 and has an average value of 250 nm$\pm$10 %. These thicknesses are quite similar along the x-axis and homogenous in a circle with the diameter of 15 mm. Along the y-axis, the thickness of the film is slightly different (20 %), maybe due to the relative position of the Rh piece on the iron target, the way to fracture the sample. Because the thickness of the film is quite uniform, difference in properties between samples should not be due to different thicknesses.

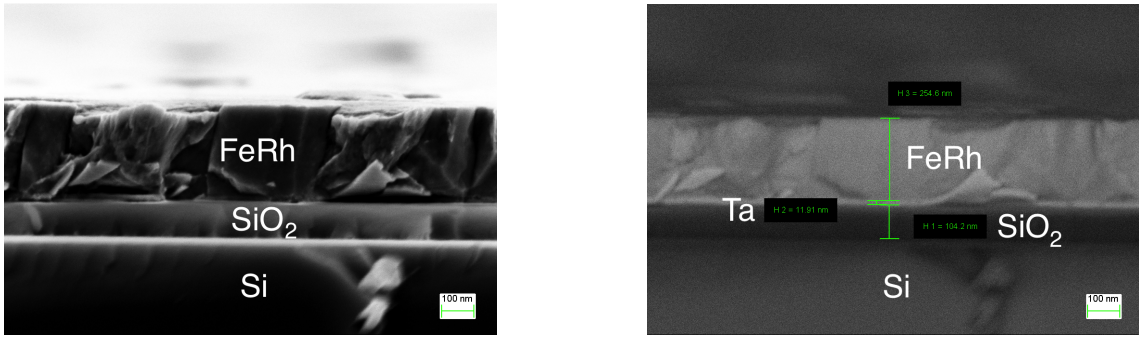

(a) In-lens image provides a topographical information

(b) ESB image shows a difference in compositional contrast among layers

Figure 3.2. *The cross-sectional SEM images, the film structure is Si/SiO_2 100 nm$\|$ Ta 10 nm/FeRh/Ta 1 nm*

Images of the surface made on the Fe-rich, near equiatomic and Rh-rich regions are shown in figure 3.4. Morphology between the Fe-rich region and the equiatomic region did not show a noticeable change, but there is a clear difference in the surface morphology of the Rh-rich region compared to two first ones. A decrease of the average grain size with the increase of Rh content is observed on these images. In literature, Ohtani et al [90] observed a decrease in grain size from 400 nm at 45.4 at. % Rh to 30 nm at 54 at. % Rh in the 200 nm thick sputtering deposited Fe-Rh films annealed at 600°C for 4h. While the

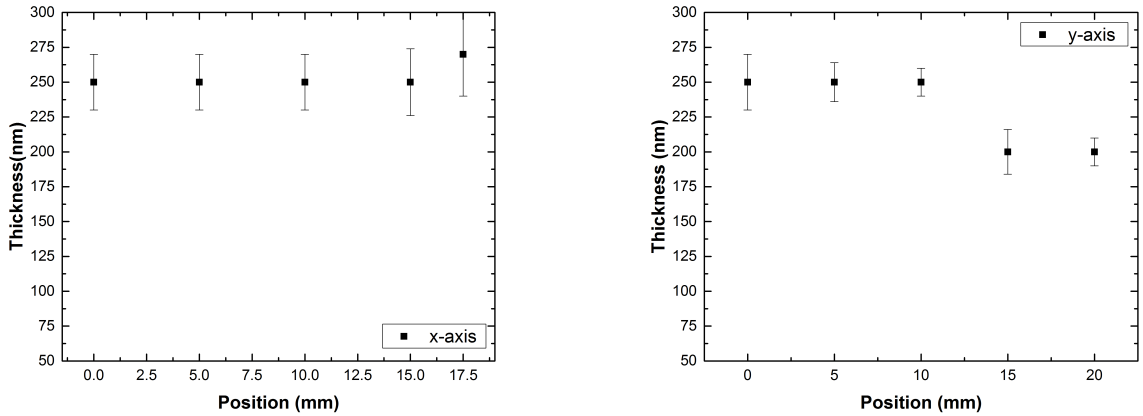

(a) Measured along x-axis **(b)** Measured along y-axis

Figure 3.3. *Thickness of the film on the Silicon wafer after annealing*

average grain sizes of 100 nm thick Fe-Rh films ranges from 130 nm at 41.2 at. % Rh to 80 nm at 49.1 at. % Rh after annealing at 697°C for 4h obtained van Driel et al [12].

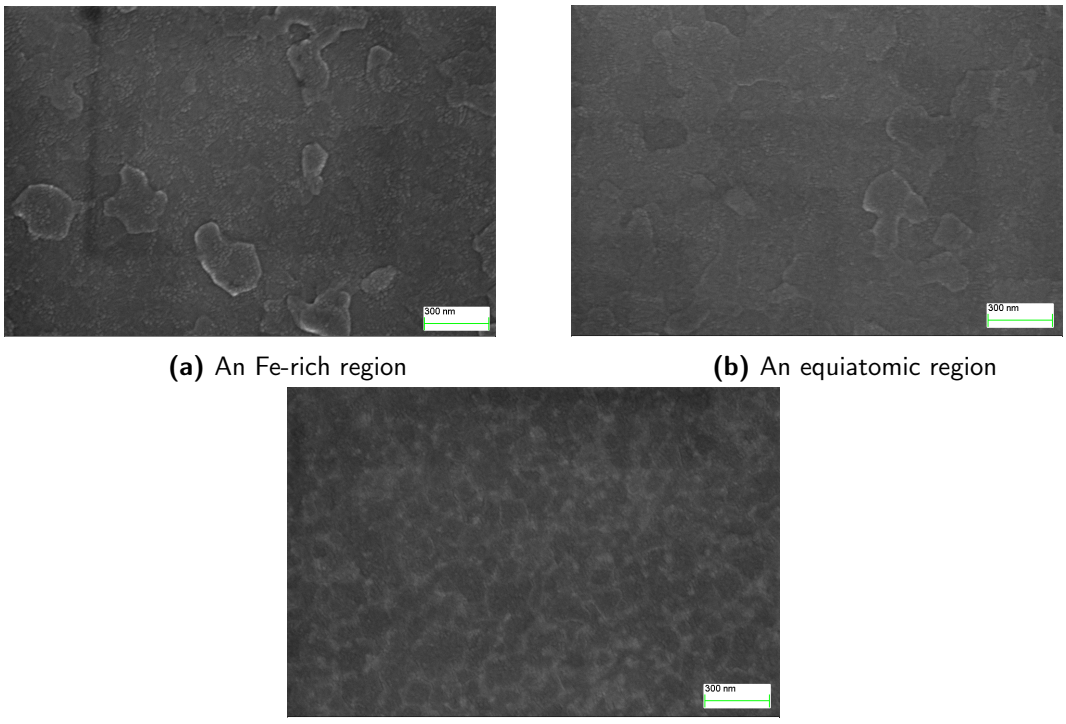

(a) An Fe-rich region **(b)** An equiatomic region

(c) A Rh-rich region

Figure 3.4. *The surface of the Si/SiO_2 100 nm‖ Ta 10 nm/FeRh 250 nm/Ta 1 nm sample. Measurements were made on Fe-rich, equiatomic and Rh-rich (∼ 56 at. % Rh) regions.*

3.3.2 Compositional characterization

3.3.2.1 Composition of the film across the substrate

EDX measurements were used to estimate film composition. A first set of measurements was done along the x-axis, for a sample prepared with one piece of Rh (figure 3.5). The film composition was shown to vary linearly across the substrate. With only one Rh foil on the Fe target, the maximum Rh content in the film on a 2 inch substrate was $\sim 32\,\%$ when the Si substrate was concentric with respect to the iron target and 42.5 % when it was horizontally displaced on top of the position of the Rh foil. The Rh content in the films varied from 16 % to 42.5 % atomic and a linear gradient of 3.4 at. % Rh/cm was found. However, the desired composition range having the first order AFM-FM transition is from $48 \rightarrow 55\,\%$. One Rh foil was insufficient to produce the expected Fe-Rh phase, so 2 Rh foils were used. The Rh content in the film increased when using 2 Rh foils and spans the range of $35 \rightarrow 62\,\%$ across a concentrically positioned substrate with a linear gradient of 5.4 ± 0.1 at. % Rh/cm. In both cases, the distance between the substrate and the target is 50 mm. To get more homogeous films and decrease the linear gradient of the composition, this distance could be larger, up to 100 mm, but we prepared all samples at 50 mm.

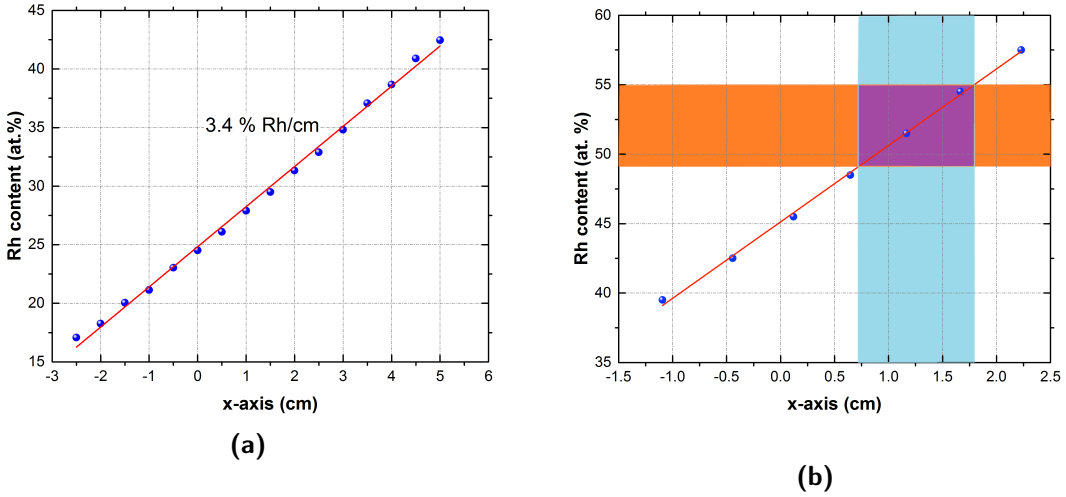

Figure 3.5. *Composition of the graded Fe-Rh films was shown to vary linearly across the x-axis of the wafer using (a) one Rh foil, (b) two Rh foils. When two Rh foils were used, the wafer contained the desired composition range.*

3.3.2.2 2D map of composition

A 2D Fe-Rh composition map of a Si/SiO_2 100 nm||Ta 10 nm/FeRh 250 nm/Ta 1 nm deposit made using 2 Rh foils is shown in figure 3.6. In this image, the film composition varies linearly along the x-axis and is quite uniform along the y-axis within the range of $|y| \leq 15$ mm. When $|y| > 15$ mm, the composition is not symmetric probably due to the relative position of both Rh foils (not symmetric, or a small gap between both pieces). Due to this reason, we observe an "S" shape asymmetry on the EDX result. The asymmetry could

also be due to a non uniform magnetron magnetic field but repositioning the Rh pieces suppressed this "S" shape, so the first hypothesis is the correct one. The composition range across the substrate contains the AFM zone from the phase diagram. Thus we could expect to produce the AFM Fe-Rh phase.

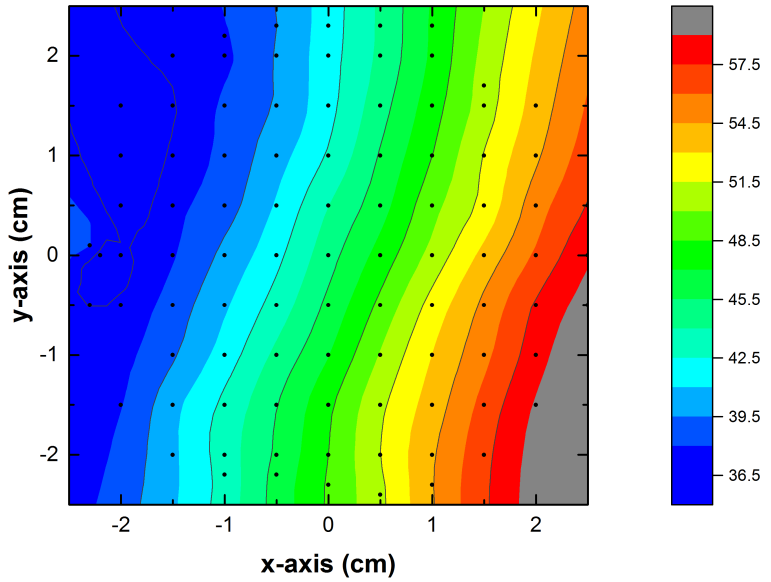

Figure 3.6. *2D Fe-Rh composition map for a composite target made with 2 Rh foils on a base Fe target. The Fe-Rh film was deposited on substrate concentric with the iron target .*

3.3.3 Magnetic characterization

3.3.3.1 Magnetization dependence on the composition, annealing conditions

Magnetization measurements as a function of temperature M(T) and magnetic field M(H) were performed using a VSM-SQUID. The measurement is made on samples of size $\sim 2.5\times2.5\,\mathrm{mm}^2$ diced from a graded Fe-Rh films (along the x-axis of the substrate), and exposed to a given temperature and time of annealing. A comparison of samples annealed under different conditions is shown in Fig. 3.7. As expected from literature, both the film composition and annealing conditions influence the magnetic properties of films. A minimum Rh content is required to produce the desired AFM Fe-Rh phase and no AFM-FM transition was observed below 47.6 at.% Rh. This is in good agreement with the bulk Fe-Rh phase diagram in which the AFM phase is reported from 48 at. % Rh. In figure 3.7b, the red curve is a mixture of AFM and FM phases.

The transition characteristics depend on the chemical ordering quality, and thus will be influenced by annealing conditions. Overall, annealing Fe-Rh films at high temperatures plays an important role to achieve the AFM-FM transition and the quality of the magnetic order. To obtain a sharp transition, the annealing tempeature should be higher than 600°C. Decreasing the annealing temperature, the transition becomes broader and shifts to lower temperatures (Fig. 3.7).

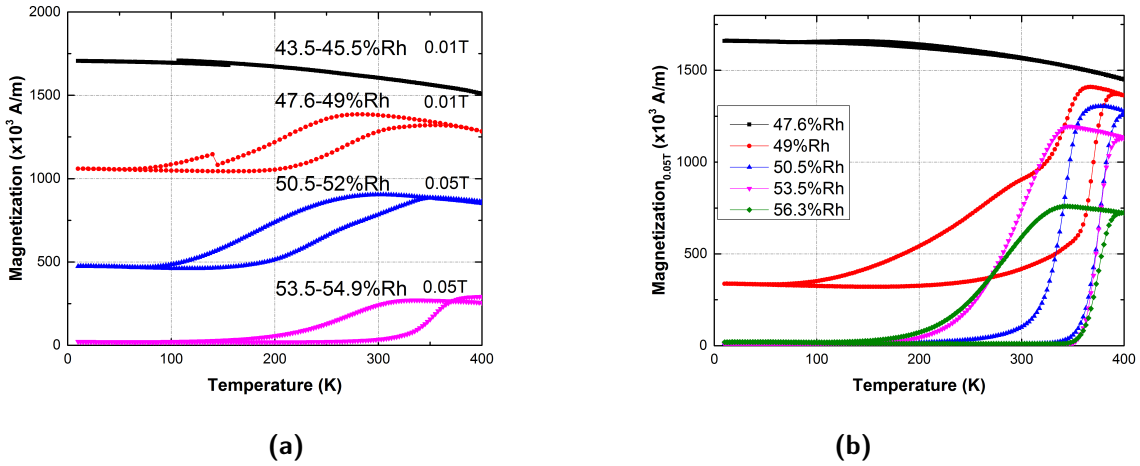

Figure 3.7. *Magnetization as a function of temperature and composition measured across compositionally graded Fe-Rh films. Figures show Fe-Rh films annealed at (a) 500°C for 30 minutes and (b) 650°C for 90 minutes.*

It was reported that no transition happens for annealing temperatures below 400°C (see fig. 3.8a [91]). We did not deconvoluate the effect of the annealing temperature and the annealing time. However, in the reference, the annealing time is less effective than the annealing temperature. Lu et al in 2012 [92] made an in situ annealing at 600°C from 2h to 20h-long on 100 nm thick FeRh and see no difference in the crystal structure. They define the transition temperature as the temperature at half change of the magnetization and see a small change in the transition temperature as shown in the figure 3.10. But we can see no rule for this small change among in their samples with different annealing times, and especially the curve annealed for 10h was quite broad. The reason for this small change is not clear, maybe a longer annealing time reduces the compositional fluctuation or it comes from the difference in composition between samples or a difference of the grain size. Van Driel et al [12] studied the influence of annealing time at high temperatures (from 300°C to 700°C), in the range 1 min to 16h, on Fe-Rh films using magnetic and transport measurements. They reported no influence of the annealing time on the magnetic properties and no distinct change in XRD was observed (the cooling and heating rate were approximately 10 K/min). Thus, the better results in our study are attributed to the higher annealing temperature.

Although many papers have been published focusing on Fe-Rh alloy, most papers describe bulk samples and the Rh content is equiatomic. We only found two papers from Ohtani and van Driel (as mentioned above) reporting about the Fe-Rh thin film with the larger Rh content range (28 % $< x_{Rh} <$ 57 % in the Ohtani's paper and 41 % $< x_{Rh} <$ 59 %in the van Driel's paper). Our compositionally graded Fe-Rh films are similar to Ohtani's samples in the sputtering deposition technique, thickness of sample, and annealing conditions. Using Mössbauer spectroscopy, besides the ordered CsCl type structure, they also found pure iron (around 20 %) and between 15 % and 28 % fcc phase in samples with 45.4 % and 54 % Rh. The magnetization data also agreed with this result

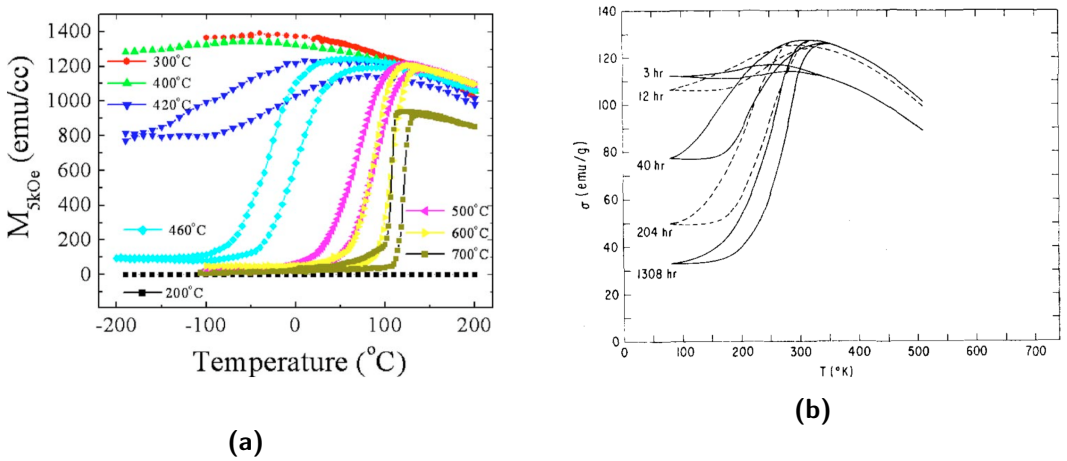

Figure 3.8. *(a) The influence of the annealing temperature on the magnetic properties of Fe-Rh films: MgO (001) $\parallel$ $Fe_{49}Rh_{51}$ 150 nm. Samples were annealed for 2h in vacuum at difference temperatures. Increasing annealing temperature led to the first order transition and a sharpening of the curve. (Image taken from [91]). (b) Filings made from a* 51 *at. % Rh alloy ingot had been annealed at* 975^oC *for 48h and quenced, then samples were annealed at* 237^oC *to study the thermal treatment on the structure and magnetization as a function of the annealing time. After 10 minutes, a transformation from the fcc disordered phase to bcc ordered phase. After 3h, they started to see the first order transition but the transition is broad, very thermally hysteresic. No change in the crystal structure. After 40h, no change in the magnetization magnitude could be detected. After that, several temperature stages can be used to improve a sharpness in transition and a reduction in the hysteresis width [93].*

(see figure 3.9a). Compared to this paper, our samples show a sharp transition with a narrow thermal hysteresis width together with a low magnetic signal at low temperature. The Curie temperature is around 640 K, which is the expected value of ordered Fe-Rh samples. Thus less than one percent of other phases appears in our samples beside the ordered phase. The figure 3.7b shows no transition below $\sim$ 48 at. % Rh, while an AFM-FM transition was observed within a wider composition range in Ohtani's paper [90].

Hofer et al [94] studied the magnetic properties of bulk Fe-Rh alloys between 50 and 64 % Rh (shown in figure 3.9b). They clearly see both fcc γ and an ordered phase in the alloys containing 55, 57, 59% Rh (and the percentage of the ordered phase: 66.7, 53.3, 40 % respectively). We take the average density for Fe-Rh samples of 10 g/cm^3 [19], and our results are comparable to their results in the magnitude of the magnetization and the percentage of an ordered phase assuming 100 % ordered phase in the 50 % Rh sample. Besides that, the thermal hysteresis width in our films is comparable to their value.

3.3.3.2 Magnetization dependence on the external magnetic field

From M(T) curves, the best results were achieved for a film containing $\sim$ 50.5 at. % Rh annealed at 650°C for 90 minutes with the thermal hysteresis width $\sim$ 33 K (the heating and cooling transition temperature of 377.7 K and 345 K respectively). Sample also has a small magnetic signal at low temperature (less than 1 % of the maximum moment). The

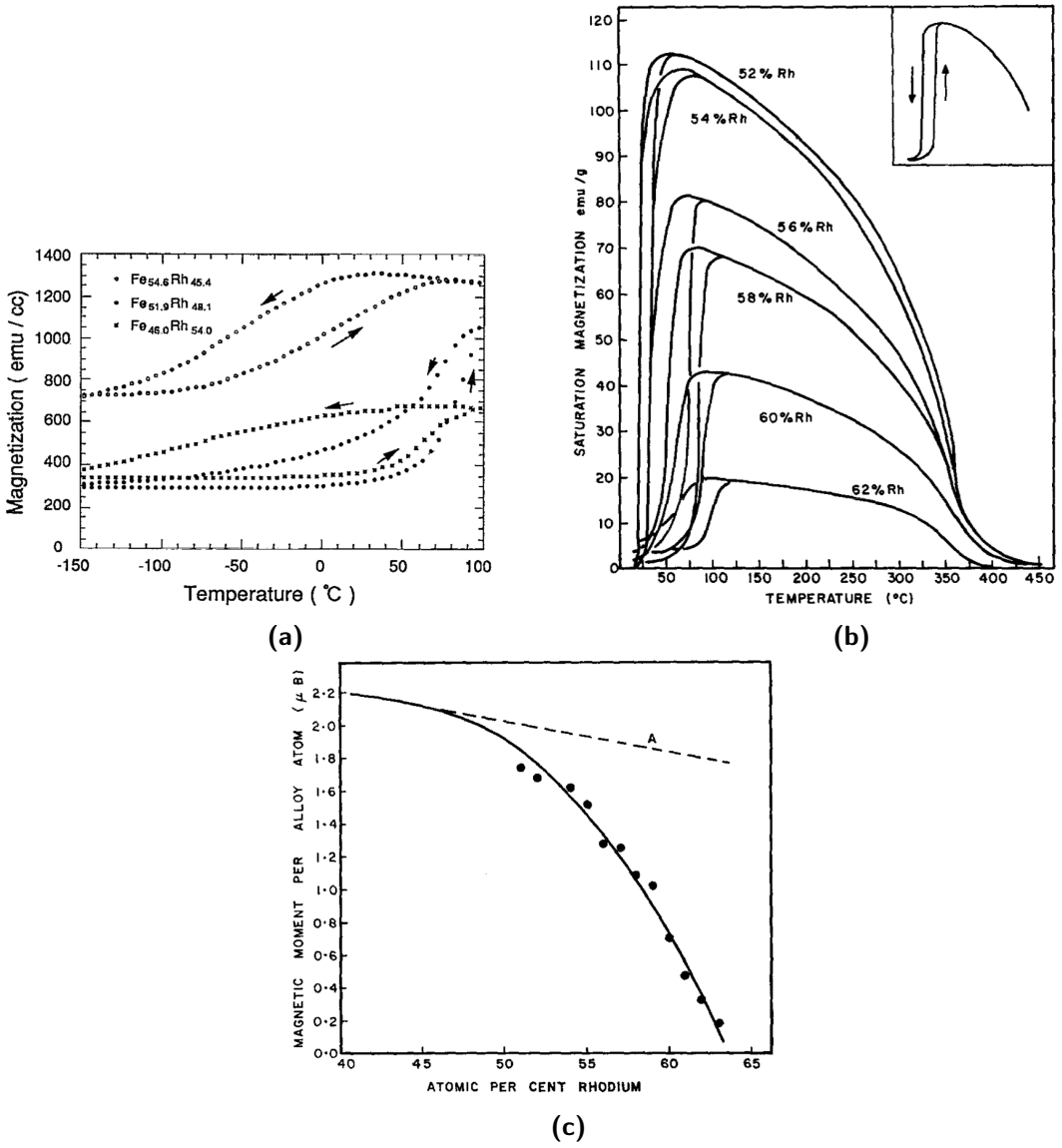

Figure 3.9. *Temperature and composition dependence of magnetization in (a)* 200 *nm Fe-Rh films with 45.4, 48.1, 54 % Rh [90], (b) bulk Fe-Rh alloys [94]. Figure (c) shows the dependence of magnetic moment per atom on the Rh content (the full line) [94].*

in-plane M(H) measurements on this sample at temperatures above, across and below the M(T) transition are shown in figure 3.11. Above the AFM-FM transition temperature, the sample is ferromagnetic and during the transition, the sample clearly shows a metamagnetic behaviour. Because disordered fcc Fe-Rh structure is transformed to the ordered bcc structure in a first order transition through a thermal treatment [93, 12, 90] as mentioned above and the fcc phase is paramagnetic, the small magnetization measured at low temperature is unlikely to be from paramagnetic phase grains. Another possible reason for this small magnetization is a residual FM phase representing less than 1 % of the film volume. The shape of the M(H) loop at low magnetic fields (see the M(H) curve 3.11) can be an evidence for this ferromagnetic contribution. Finally, the small magnetization could be caused by the sample holder or plastics which are used in the VSM-SQUID measurements, but careful

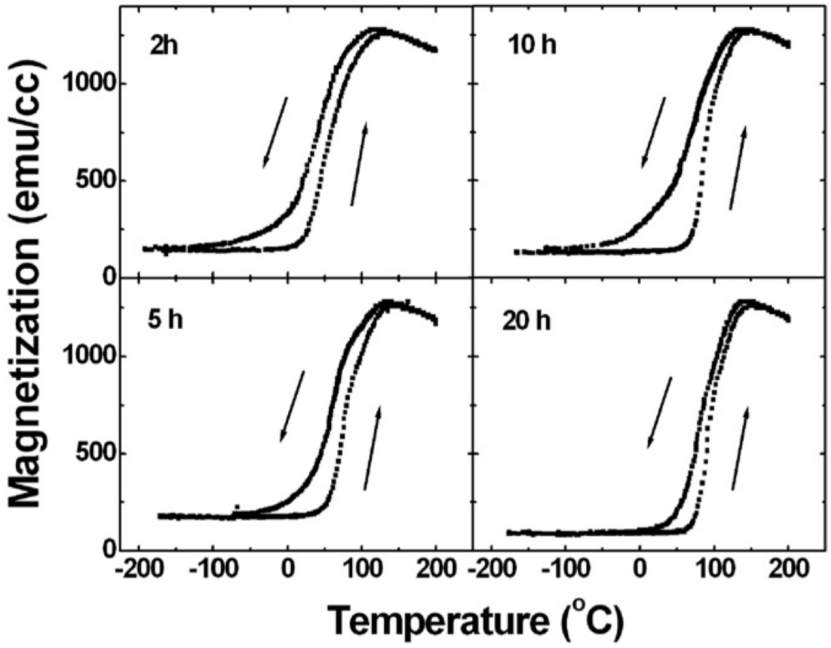

Figure 3.10. *A small increase in the transition temperature of polycrystal Fe-Rh samples of Glass‖Fe-Rh 100 nm deposited using sputtering. Samples were in situ annealed at* 600^oC *[92])*

sample mounting minimizes such an origin.

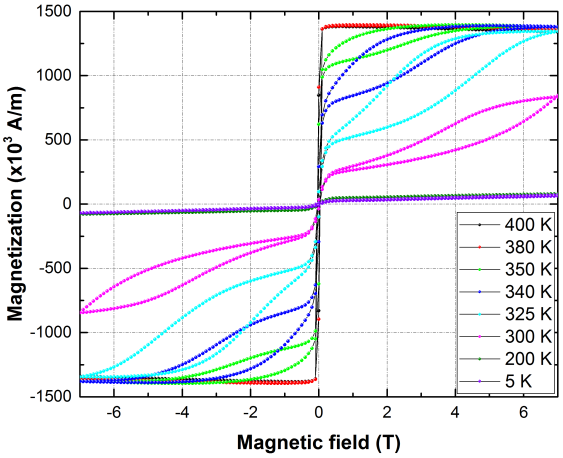

Figure 3.11. *M(H) curves of the optimal Fe-Rh sample containing* ~ 50.5 *at. % Rh annealed at* 650^oC *for 90 minutes measured between* $400\,K$ *and* $100\,K$ *shows a metamagnetic transition.*

3.3.3.3 Transformation dependence on temperature

In our study, the transition temperature T_t is defined as the maximum of the derivative of magnetization with respect to temperature $\frac{dM}{dT}\big|_H$ (figure 3.12 and 3.13) which is fitted using a Gaussian profile as mentioned in chapter 2. The Gaussian function in Matlab performs this task and error bars are estimated from the lower and upper bounds of the

transition temperature. Then, thermal hysteresis width is calculated from the difference between the heating and cooling curves: $\triangle$T = $T_{t\text{-heating}}$ - $T_{t\text{-cooling}}$.

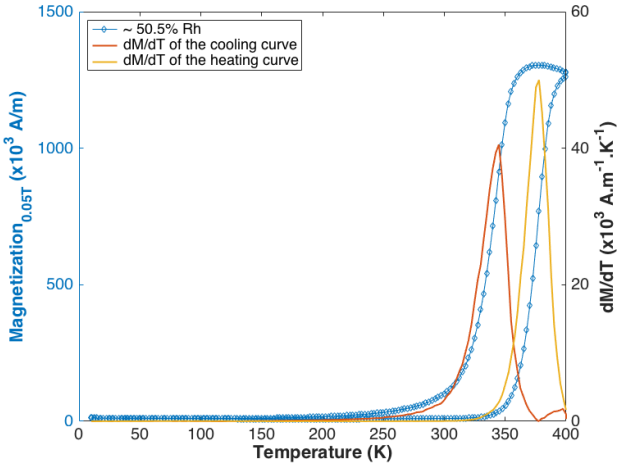

Figure 3.12. *The defination of the transition temperature T_t as the maximum of the derivative of M with respect to T plotted against T ($\frac{dM}{dT}\big|_H$ vs. T). Sample in this figure is the 250 nm thick $Fe_{49.5}Rh_{50.5}$ film (the blue curve as shown in figure 3.7b).*

A comparison of transition temperature and hysteresis width is shown in table 3.1. We can see that the heating transition temperature does not show a considerable change, while the cooling transition temperature clearly show decreases when the Rh content is increased. The M(T) curve is broader when increasing the Rh content, resulting in an increase of the thermal hysteresis from 25 K at 49 % Rh to 93 K at 56.3 % Rh. Since all samples come from the same wafer, so have the same thickness and same annealing conditions, this change can be attributed to the composition.

Table 3.1. *Transition temperature T_t and hysteresis width $\triangle T$ is as a function of composition. The 49 % Rh sample, corresponding to the red curve in figure 3.7b, is a mixed phase, thus there are two transition temperatures.*

% *Rh*	$T_{t-heating}$ (K)	$T_{t-cooling}$ (K)	$\triangle T$
47.6 - 49	-	-	-
49	369.7 ± 0.1	344.7 & 262.4	25 & 107.3
50.5	378.7 ± 0.3	345.1 ± 0.25	33.6
53.5	376.7 ± 0.3	309.1 ± 6.65	67.6
56.3	376.4 ± 1	283.6 ± 1.6	92.8

An asymmetry between the heating and cooling curves is observed in Fe-Rh films. Figure 3.13 shows dM/dT curves for Fe-Rh films with the Rh content from 50.5 to 56.3 %. dM/dT curve of the 50.5 % Rh sample shows distint peaks and rapid change in both heating and cooling curves. In contrast to the 50.5 % Rh sample, the 53.5 and 56.3 % Rh samples show sharp peaks when samples transform from an AFM state to a FM state during heating,

while rounded peaks are observed when samples transform from a FM state to an AFM state during cooling. Increasing the Rh content leads to an reduction of the sharpness of the curve in either heating or cooling. As a result, the shape changes from a sharp peak to a rounded peak as the increase of Rh content. In addition, the higher temperature transitions have steeper slopes than the lower temperature ones.

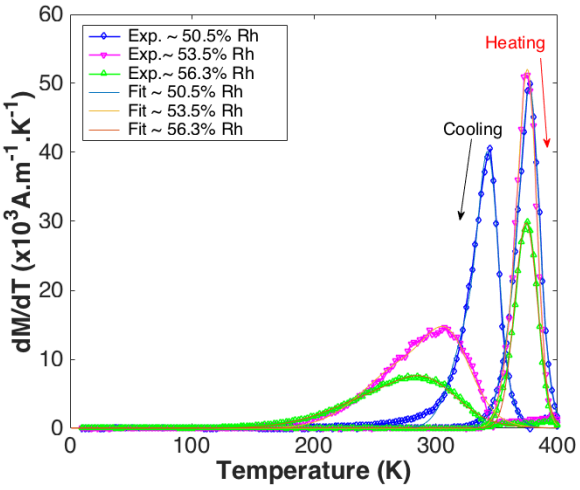

Figure 3.13. *dM/dT vs T plots for Fe-Rh films. Curves with and without marks are experimal data and fits, respectively.*

The asymetric behavior observed in graded Fe-Rh films has been studied in liquid-solid transitions such as a water-ice transition and also observed on the first order transition in $Ce(Fe_{0.96}Ru_{0.04})_2$ alloy [95]. From water to ice, nucleations of ice crystals is initialized then the nuclei develop and finally, all liquid becomes solid ice. While in the melting process, melting starts at the surfaces in which no nucleation energy barrier exists. If water is pure, an abrupt water-ice transition can happen. We try to explain our results using an analogy with this phenomenon.

On the heating process, the FM phase is formed through nucleations of domains in the AFM matrix throughout grains. In contrast to the heating process, the FM $\rightarrow$ AFM transtion starts at grain boundaries during cooling. Using the liquid - solid transition analogy, we can anticipate an asymmetry between the heating and cooling curve in Fe-Rh films, especially for the Rh-rich samples such as 53.5 or 56.3 % Rh samples. The nucleation of the AFM to FM first order transition observed in FeRh above is also supported by XMCD results [97, 98]. Because XMCD cannot image the AFM phase, it is difficult to clarify the FM to AFM process. However, both the heating and cooling cycle of the 50.5 % Rh sample are sharp which indicates a homogeneous nucleation throughout grains, and hence an abrupt phase change is observed either in heating or cooling. In addition, the dM/dT curve is broader when increasing the Rh content either heating or cooling, which infers nucleation to be more heterogeneous. Using the water - ice transition is not enough to explain all details in the observed phenomenological asymmetry in graded Fe-Rh films but can bring useful ideas.

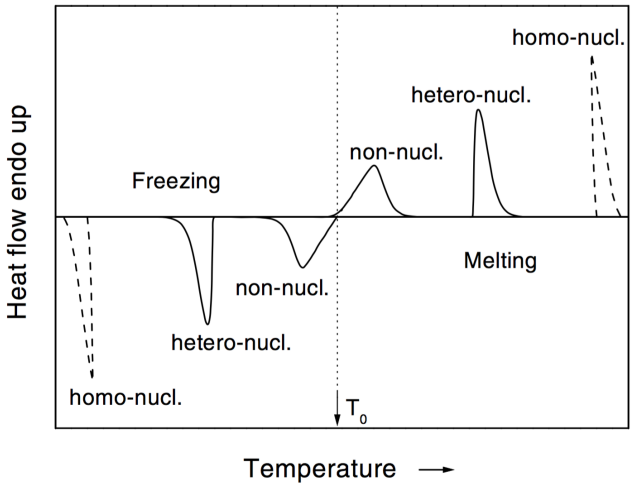

Figure 3.14. *Schematic of the nucleation-and-growth model for melting and freezing behaviour illustrates shapes of non-nucleation, heterogeneous and homogeneous nucleation. The y-axis is the derivative of the fraction of new phase. (Image taken from [96])*

A schematic overview of phenomenological kinetics nucleation-and-growth model for melting and freezing, which illustrates the shapes of homogeneous nucleation rate, heterogeneous nucleation rate and non-nucleation rate during heating and cooling, is shown in figure 3.14 [96]. One can see that the 50.5 % Rh sample corresponds to the case of homogeneous nucleation, which shows a sharp transition from a AFM state to a FM state and vice versa. Meanwhile, the 53.5 % Rh sample has a homogeneous nucleation from AFM to FM and a heterogeneous nucleation from FM to AFM. Furthermore, a qualitative agreement between experiment and theory is also observed, in which the higher temperature edge of the cooling curve in the heterogeneous nucleation is steeper than in lower temperature side during cooling (see figure 3.13 and 3.14). We note that dM/dT values are actually negative in the FM to AFM transition during cooling, but here we plot the magnitudes $\left|\mathrm{dM/dT}\right|$ (Fig. 3.13). For the 56.3 % Rh sample, the heterogeneous nucleation is observed when sample transforms from a AFM state to a FM state, meanwhile the transformation from FM to AFM follows a non-nucleation based mechanism. In general, the heterogeneous nucleation and non-nucleation are common mechanisms in experiment of the liquid - solid transition, resulting in an asymmetry between heating (or melting) and cooling (or freezing). Interestingly, we can see three different kinds of mechanisms: homogeneous, heterogeneous and non-nucleation with only one wafer of graded Fe-Rh films through the combinatorial approach. In literature, Maat et al [20] reported the nucleation process in FeRh on the MgO and Al_2O_3 substrates. Based on results mentioned above, we would like to interpret the nucleation in the MgO/FeRh as a non-nucleation mechanism rather than heterogeneous nucleation and the latter Al_2O_3/FeRh as heterogeneous and non-nucleation for cooling and heating, respectively rather than homogeneous nucleation. In the following part, we discuss heterogeneity which could cause the nucleation mechanism change in graded Fe-Rh films.

Nevertheless some heterogeneities such as defects, stress affect the transition. The

heterogeneity can also be from a mixture of the ordered and disordered phase (the γ phase) in Fe-Rh films with lattice constant of 2.989 Å (in the AFM phase) and 3.724 Å, respectively. An increasing Rh content leads to an increase in γ phase content and a reduction of grain size which can also lead to a change in stress. In bulk Fe-Rh samples, the dependence of thermal hysteresis width on the composition and the coupling between grains was reported [99]. In this paper, the 53.9 % Rh sample containing both ordered and disordered phases showed a larger thermal hysteresis width than the 49.6 % Rh sample. The dM/dT curves (Fig. 3.13) above show that the heterogeneity affects the FM to AFM transition rather than the AFM to FM transition. This result is also supported by Ohtani et al [27] based on a study of broad transition in FeRh film.

3.3.3.4 Magnetic entropy change of the optimal Fe-Rh sample

Figure 3.15 shows the isothermal magnetization loops of the $Fe_{49.5}Rh_{50.5}$ sample measured around the transition temperature at an maximum applied magnetic field of 7 T and at discrete intervals of 5 K. Initially, at 400 K, the Fe-Rh sample is ferromagnetic. From 400 K to 370 K, the sample is predominantly ferromagnetic and hysteresis in magnetization loop is observed at 365 K. From 365 K to 270 K, the opening of the loops increases, then reaches a maximum and gradually decreases. A small magnetic signal is observed below 200 K as mentioned before.

The temperature and magnetic field dependence of magnetization is constructed by extracting values from isothermal magnetization curves and shown in 3.15b. It was reported that the transition temperature T_t decreases at a rate of -8 K/T with increasing the external magnetic field in Fe-Rh bulk or film samples [20]. In our optimal Fe-Rh film, the dependence of the transition temperature on the applied field is shown in figure 3.15c. A linear function with slope of $dT/d\mu_0H$ = -7.8 K/T$\pm$0.2 describing the rate of the transition temperature change with the magnetic field is obtained and consistent with the Fe-Rh bulk value.

From these isothermal loops, we can calculate the magnetic entropy change $\triangle S_M$ using the Maxwell relation or using the Clausius–Clapeyron equation as mentioned in chapter 2. Here we use the latter relation which currently used for the first order transtion with $dT/d\mu_0H$ = -7.8 K/T and the observed value of $\triangle M = 1.3{\cdot}10^5$ A/m when the AFM to FM transition is complete. Calculation leads to a $\triangle S_M \sim 16.6\,mJ.g^{-1}.K^{-1}$ which is in good agreement with the value of $\triangle S_M = 14\,mJ.g^{-1}.K^{-1}$ in literature (Kouvel 1966 [19]). Actually, magnetic properties of Fe-Rh samples are strongly dependent on the composition and annealing conditions, the entropy change in literature ranges from 12.6 to 18.3 $J.kg^{-1}.K^{-1}$.

3.3.4 Transport measurements

The temperature dependence of the resistivity or resistance R(T) for our samples was measured using the transport measurement set-up developed during this thesis. Figure 3.16 shows the resistivity change with temperature of a compositionally graded sample with 53.5 to 55.1 % Rh content. Below the transition temperature, the resistivity change has a metallic behaviour with a linear temperature dependence while heating. At the transition

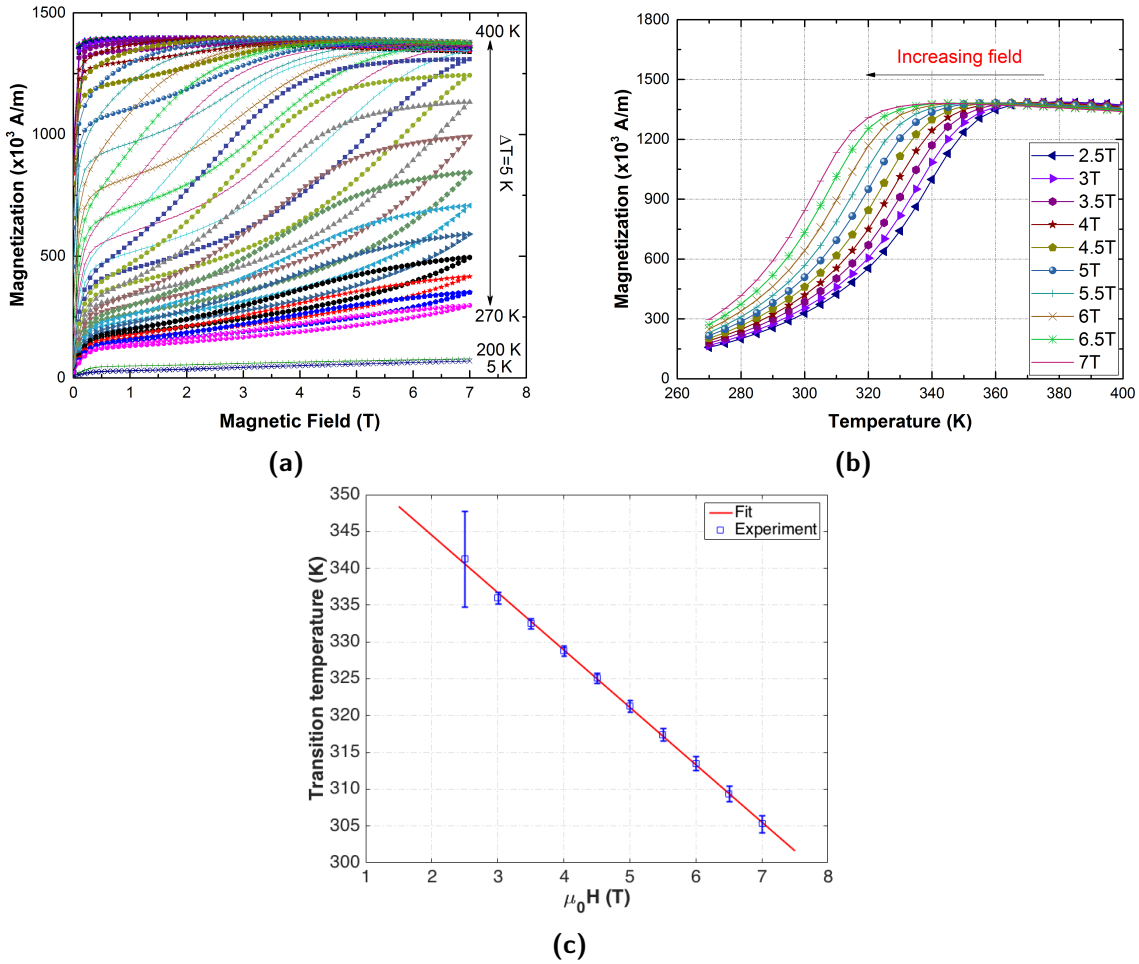

Figure 3.15. *(a) Isothermal magnetization curves of the Fe-Rh sample with* $\sim$ 50.5 *at. % Rh annealed at* 650^oC *for 90 minutes measured in the vicinity of the first order AFM-FM transtion temperature, (b)*

temperature, a large drop in resistance happens, as expected from literature, corresponding to the AFM-FM transition. The lattice constant in the FM phase at high temperature is 0.3 % higher than in the AFM phase. Thus, the large change in resistivity at the transition temperature cannot be attributed to the pure geometry variation (strain gauge effect) but is intrinsic to the first order AFM-FM transition. A change of the resistance in Fe-Rh films because of changes in length l, width w, thickness t and resistivity ρ can be expressed as follows:

$$\frac{\partial R}{R} = \frac{\partial l}{l} - \frac{\partial t}{t} - \frac{\partial w}{w} + \frac{\partial \rho}{\rho} \tag{3.1}$$

As the geometry variation (0.3 %) is much smaller than the observed change, the change in the resistance at the transition temperature is due to the change in resistivity $\partial\rho/\rho$.

In order to compare the change in resistance with literature, we defined the relative change of magnitude in resistance as the difference between the resistance at the local maximum and minimum over the resistance at the local maximum as follows (see Fig. 3.16 for an illustration):

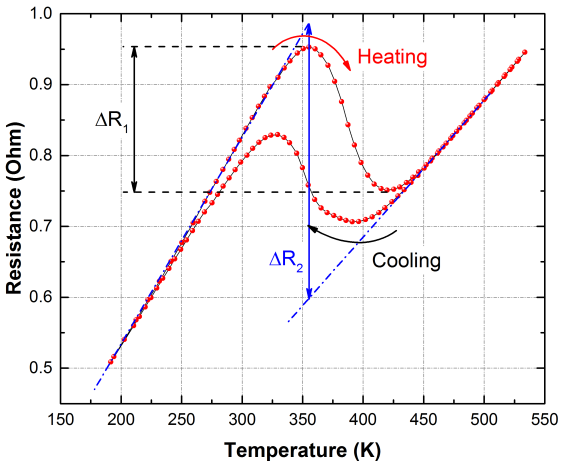

Figure 3.16. *Resistance is as a function of temperature for a graded Fe-Rh film containing 53.5 to 55.1 at. % Rh. A large drop can be also used to measure the transition temperature and monitor the phase change due to the magnetoelectric effect.*

$$\frac{\triangle R_1}{R} = \frac{|R_{max} - R_{min}|}{R_{max}} \times 100\% \tag{3.2}$$

A large drop in resistance of $\sim 23\,\%$ was observed in our Fe-Rh sample on the heating side as shown in this figure. In literature, Kouvel in 1963 [100] obtained a change in resistivity of $\sim 40\,\%$ in a bulk $Fe_{50}Rh_{50}$ alloy. In Fe-Rh films, De Vries el al in 2013 [28] obtained from $\sim$ 37 - 41 % for $Fe_{50}Rh_{50}$ samples. The smaller change in our 53.5 - 55.1 % Rh containing sample may originate from a difference in composition. Indeed, Fe-Rh films with a ~50 % Rh content on the PMN-PT substrate show a large change in resistance similar to bulk (see Fig. 4.10a). The heterogeneity in 53.5 - 55.1 % Rh samples causes a smaller change in resistance at the transition temperature. As the γ phase does not contribute to the change in resistance at the transition temperature, the higher the γ phase content is, the smaller the change in resistance. As a result, when the Rh content is increased, the change in resistance decreases. In addition, resistance also depends on the microstructure and grain boundaries, which are a source of spin-independent scattering. A decrease of the average grain size will lead to an increase of the relative contribution of grain boundary scattering to the total resistance and so the change in resistance at the transition temperature could decrease.

Furthermore, the definition of $\triangle R_1/R$ above (Eqn. 3.2) makes this ratio depends on the sharpness of the transition. Because the transition in FeRh films is broader than bulk samples, our equation 3.2 leads to a contribution of temperature to the calculated result which is quite complicated, since resistances in equation 3.2 are measured at different temperatures, or different changes of resistance with temperature between the AFM state and the FM state. Hence, the equation 3.2 underestimates the magnetoresistance of our films compared to bulk. A definition based on extrapolated FM and AFM resistivities at the transition temperature would give larger magnetoresistance ratio. Such a definition would also be slightly temperature dependent since the slope of the AFM and FM R(T)

are not the same. We define the change in resistance $\triangle R_2$ as shown in the figure 3.16. The change in resistance $\triangle R_2$ is about 40.2 % which is consistent with literature.

The large change in resistivity of the R(T) curve can be used to monitor the first order transtion. One remark is that the signal is very stable considering that this measurement was made over a time span of roughly 6 hours, and the curve is reproducible. The transport measurement result also validates our developped setup for the transport measurement. As shown in the next chapter, we can now use this measurement set-up not only to measure the resistance but also to monitor the phase change in Fe-Rh films using piezoelectric substrates.

3.4 Influence of elemental substitution on the magnetic properties of Fe-Rh

Occurance of the transition at room temperature can be problematic for certain measurement set-ups. Previous reports in literature ([19, 22] and references therein) show that the transition temperature in bulk Fe-Rh alloys can be tuned by substituting Rh by a small addition of Os, Ru, Ir, Pt or Al, V, Cr, Mn, Co, Ni, Pd, Au to increase or decrease the transition temperature, respectively. Most works only concern the equiatomic phase of Fe-Rh alloys ($Fe_{50}(Rh_{1-x}M_x)_{50}$ or $(Fe_{1-x}M_x)_{50}Rh_{50}$ with M = Os, Ru, Ir, Pt, Pd, ...) though it is well known that the transition temperature is very sensitive to composition. In this work, we chose to substitute Pt and Ni elements to increase and decrease the transition temperature, respectively. The Rh content was varied from 37 to 56 % for a fixed the Pt and Ni content. Because of the similarity between Rh and Pt (or Pd, Ir), it was reported a substitution of Pt for Rh [19]. Meanwhile, a substitution of Ni for Fe is expected for the ternary Fe-Rh-Ni case because of the similarity between Fe and Ni [101].

3.4.1 Substitution of Pt for Rh

3.4.1.1 Sample preparation

The Ta buffer and capping layers were replaced by Pt layers. The structure of as-deposited samples is Si/SiO_2 100 nm‖Pt 10 nm/FeRh/Pt 1 nm. Then, samples were annealed at 700°C for 2h. Thanks to the diffusion of Pt into the Fe-Rh film during the annealing process, we obtained homogenized $Fe_{1-x}(Rh\text{-}Pt)_x$ samples. The thickness of Fe-Rh-Pt films is about $\sim$ 250 nm as measured using FESEM machine.

3.4.1.2 Composition of the Fe-Rh-Pt films

The compositional quantitative analyses of Fe-Rh-Pt films were estimated by energy dispersive spectrometry in a scanning electron microscope as mentioned in chapter 2. Here, we remind some key factors. Spectra of pure Fe, Rh, Pt elements were performed to record a standard database. Spectra of Fe-Rh-Pt films and of pure elements were acquired with acceleration voltages of 7, 10, 12, 15, 20, 25, 30 kV with 1 million and 800k counts for

the standard library and samples, respectively to get sufficient spectrum statistics. The K ratios are defined by the peak intensities of each element in samples over the value in the standard library: $K = I_{measured}/I_{library}$. The results were processed using the STRATAgem software.

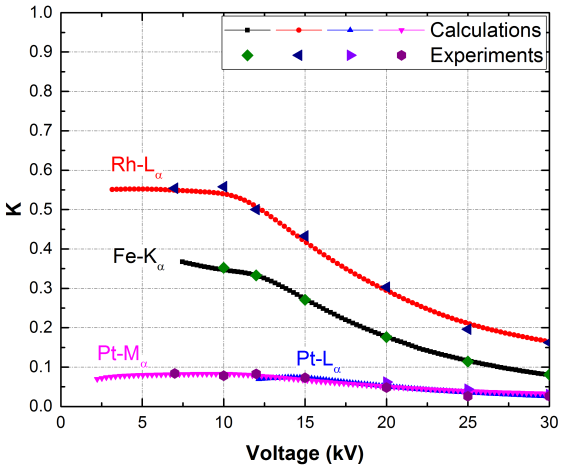

Figure 3.17. *The experimental data are in good agreement with the theoretical K ratios.*

The K ratios of experiment data and theoretical calculations as a function of voltage show good agreement (Fig. 3.17). As the center of the interaction volume changes with the acceleration voltage and moves from the film at low voltage to the substrate at higher voltage, the K ratios will decrease with increasing voltage. Because K_α energy of Fe is 6.4 keV (taken from periodic table of the elements), acceleration voltage must be higher than this, hence the K(V) curve for Fe element in figure 3.17 started from 10 kV. For Pt element, both M_α = 2.05 keV and L_α = 9.44 keV energy X-rays are used to estimate composition.

EDX results show that the amount of Pt is constant at $\sim$ 4.3 - 4.85 % in the Fe-Rh-Pt films. The Rh content was shown to vary linearly across the x-axis of the substrate with a linear gradient of 5.35 % Rh/cm which is similar to that in the graded Fe-Rh films described previously. The fitting densities of 10 - 11 g.cm^{-3} are in good agreement with the literature values (10 g.cm^{-3} for the average density of binary or ternary Fe-Rh alloys [19]). The film thickness is estimated about 249 nm which is in good agreement with the value from FESEM mentioned above.

3.4.1.3 The grain structure of graded Fe-Rh-Pt films

The microstructure of the Fe_{1-x}(Rh - Pt)$_x$ films with x = 45.2 $\rightarrow$ 55.8 % is also studied using FESEM, and shows that the grains have grown after annealing. The change of grain size with composition is shown in figure 3.18 for annealed samples with x = 45.2, 49.9, 55.8 % (images of films with other compositions are not shown at here).

A decrease of the average grain size with increasing of Rh content was observed clearly in annealed Fe_{1-x}(Rh - Pt)$_x$ films. These results are consistent with Fe-Rh films in our samples above and in literature. A remark is the appearance of terraces on our films in the

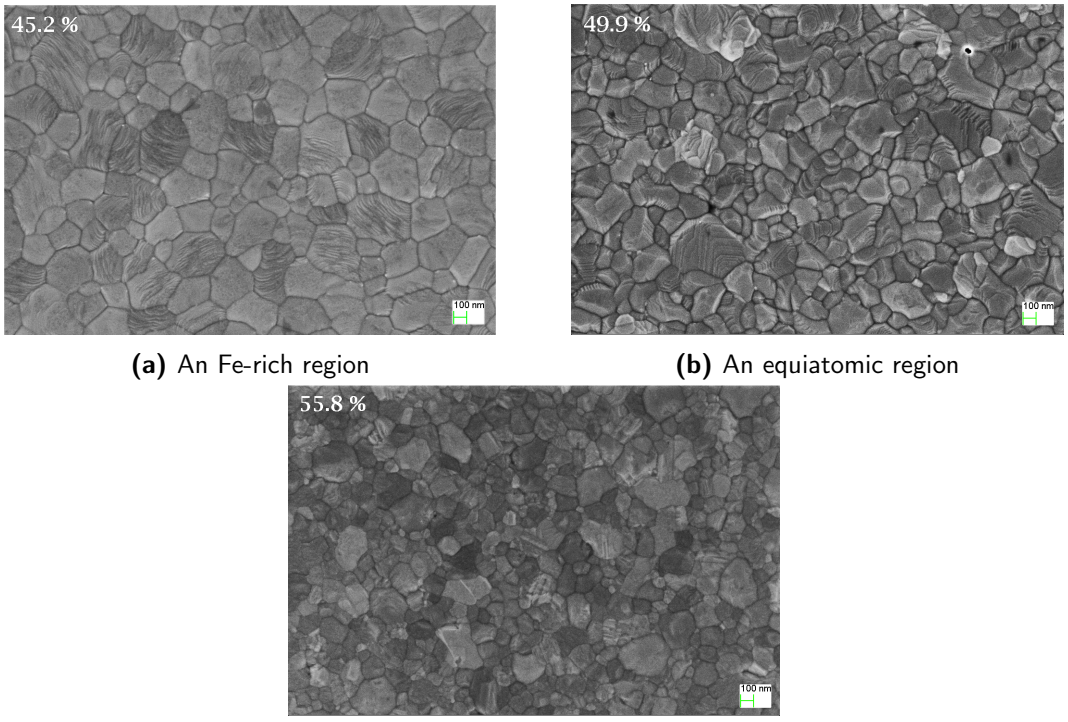

(a) An Fe-rich region

(b) An equiatomic region

(c) A Rh-rich region

Figure 3.18. *FESEM surface images for annealed* $Fe_{1-x}(Rh-Pt)_x$ *films in (a)* $x = 45.2\,\%$*, (b)* $x = 49.9\,\%$ *and (c)* $x = 55.8\,\%$ *show a difference in the average size. It is found that terraces appear on the annealed samples and almost disappeared at the fcc phase.*

Fe-rich and equiatomic regions, and their decrease with increasing the Rh content. They almost completely disappear in the Rh-rich region where mainly the fcc phase exists (Fig. 3.18c). Such terrace steps which may be due to the bcc ordered crystal structure in the equiatomic region (Fig. 3.18b). In literature, van Driel et al (1999) also observed terraces at the Fe-rich region but they did not report about the terrace like steps appearing close to the equiatiomic region. It seems that our films contain two kinds of grains: (1) grains of the ordered phase with the composition of x = 50 % and (2) grains of the disordered phase (the γ phase). When the Rh content increases, the first kind will decrease while the later will increase.

Ohtani el al (1993) observed the fcc (111) phase in their Fe-Rh films, and the higher Rh content, the higher the amount of retained fcc phase. They reported that this fcc phase caused a significant decrease of the α" ordered phase in Fe-Rh films. The influence of the substrate on the martensitic transformation and the 2-D diffusion in films during the annealing process may be the reason for the retained fcc phase in Fe-Rh-based systems [90]. The ESB images qualitatively show the difference in contrast between these films (Fig. 3.19). When x = 45.5 % corresponding to 80.7 % bcc, the contrast is quite uniform on the image (Fig. 3.19a). The grains with steeper terraces are little bit darker. It is found that the brighter regions appear and increase while increasing the Rh content in film (Fig. 3.19b-d). The ESB cross-section images (not shown here) show an overlay of the regions having a contrasted difference. However, it is too soon and other measurements such as

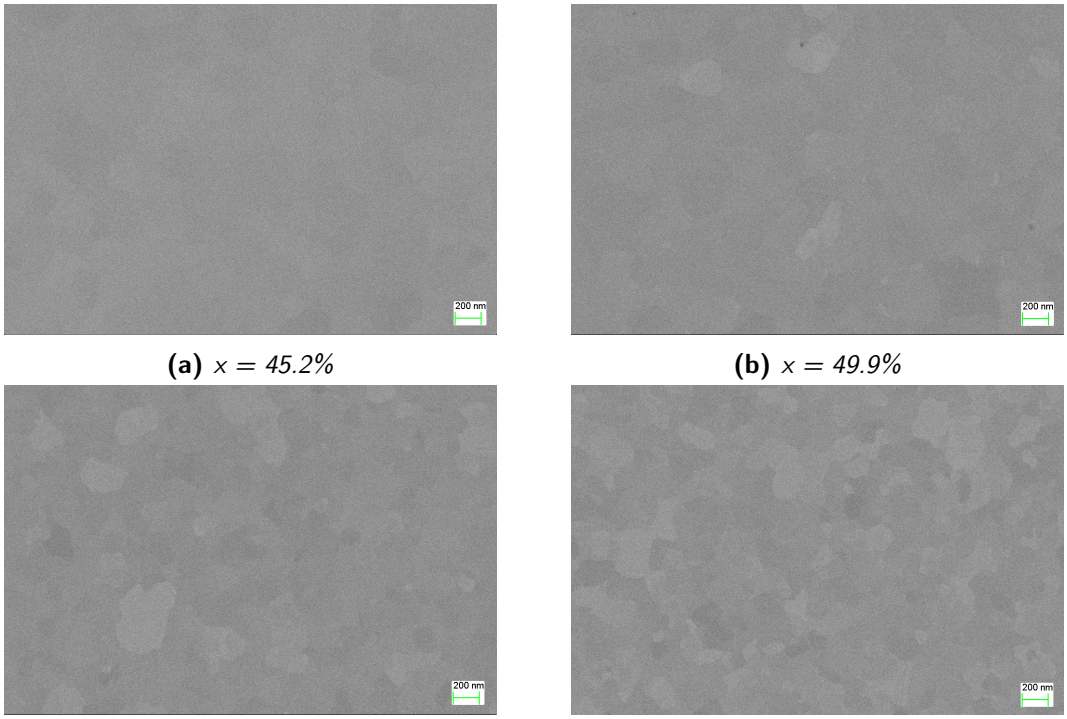

(a) *x = 45.2%* **(b)** *x = 49.9%*

(c) *x = 52.4%* **(d)** *x = 55.8%*

Figure 3.19. *ESB images for annealed $Fe_{1-x}(Rh-Pt)_x$ films highlight the contrast between grains for (a) $x = 45.2\,\%$, (b) $x = 49.9\,\%$, (c) $x = 52.4\,\%$ and (d) $x = 55.8\,\%$. The grain with twists is darker than the ones without twists. It is found that when the Rh content increases, grains with a brighter contrast increase.*

EBSD are needed to understand about these twists. In brief, increasing the Rh content led to: (1) an increase of the fcc phase content, (2) a decrease of the average grain size, (3) a decrease of the twisted grains, (4) an increase of the brighter regions and a larger contrast between grains.

3.4.1.4 Crystal structure

Figure 3.20 shows the crystal structure of $Fe_{1\text{-}x}(Rh\text{-}Pt)_x$ ($44.3\,\% < x < 57.5\,\%$) films measured across the x-axis of the substrate using a diffractometer equipped with a copper X-ray source. The measurement is performed at room temperature. The sample is a strip of $\sim 24\,mm$ in length and $\sim 2.5\,mm$ in width. Each XRD pattern was measured on a surface of $\sim 5{\times}2.5\,mm^2$, the sample stage being moved between measurements. In this figure, the black dashed lines and markers identify the peaks of the substrate, the blue dashed lines and diamond markers identify the bcc phase and the red dashed lines and triangle markers identify the fcc phase (the γ phase). In measured films, both a fcc disordered and a fully bcc ordered phase were found to be present, and the superstructure is clearly observed in all the Fe-Rh-Pt films. In the disordered bcc phase, the atomic scattering factor is the same for (001) and (002) planes (i.e., in the disordered phase), then the periodicity along c becomes c/2 and (00 2n+1) diffraction peaks disappear. In the ordered bcc structure of Fe-Rh alloys, the Rh atoms will be in the center of the cube

occupied by Fe atoms at the corners. Because of the different scattering factor between Fe and Rh, the periodicity along the c-axis becomes c and leads to the apperance of the (00 2n+1) lines called the superstructure peaks. The appearance of this superstructure in all films confirms the formation of the bcc ordered phase in Fe-Rh-Pt samples.

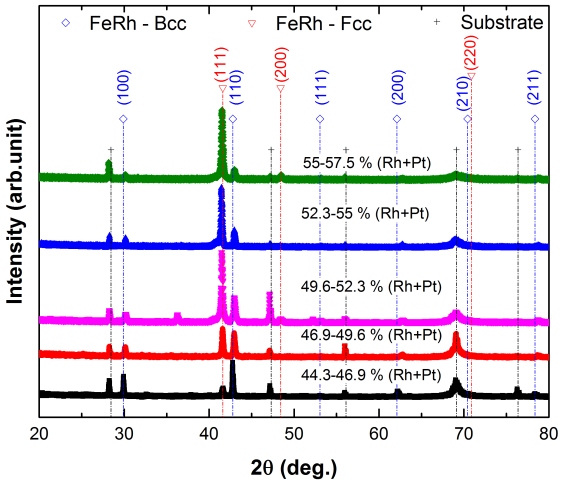

Figure 3.20. *X-Ray diffraction patterns of annealed* $Fe_{1-x}(Rh-Pt)_x$ *films, with* $44.3\,\% < x_{Rh+Pt} < 57.5\,\%$ *at room temperature*

The lattice parameters of the annealed Fe-Rh-Pt films is 2.978 Å for the bcc phase and 3.764Å for the fcc phase, which are in good agreement with the values of the bcc phase (2.983 Å ± 0.007) and the fcc phase (3.7594 Å) in the bulk Fe-Rh alloy from literature [13]. Because the atomic percentage of Platinum in Fe-Rh-Pt films is small, it does not lead to a strong change in the lattice parameters. These results also coincide with other Fe-Rh-based ternary alloys in literature as cited.

Increasing the Rh content led to an increase of the fcc phase in the films. This result also agrees with the previous analysis in Fe-Rh films and in literature. To estimate the change of the bcc ordered phase in Fe-Rh-Pt films with the Rh content, we define the amount of bcc phase using XRD data as follows:

$$\%\,bcc = \frac{I_{bcc(110)}}{I_{bcc(110)} + I_{fcc(111)}} \tag{3.3}$$

Adding the structure factor, the multiplicity factor and the Lorenz polarization factor, the amount of bcc phase can be given as:

$$\begin{aligned} \%\,bcc &= \frac{I_{bcc(110)} / \left(|F_{bcc}|^2 . p_{bcc} . LP_{bcc} \right)}{I_{bcc(110)} / \left(|F_{bcc}|^2 . p_{bcc} . LP_{bcc} \right) + I_{fcc(111)} / \left(|F_{fcc}|^2 . p_{fcc} . LP_{fcc} \right)} \\ &\simeq \frac{I_{bcc(110)}}{I_{bcc(110)} + 1.38 I_{fcc(111)}} \end{aligned} \tag{3.4}$$

where: I_{bcc} and I_{fcc} - the experimental intensity of the bcc and fcc phase, respectively; F_{bcc} and F_{fcc} - the structure factor of the bcc and fcc phase, respectively. The structure

factors are calculated from atomic scattering factors [102]. LP_{bcc} and LP_{fcc} - the Lorenz polarization factor, $LP = (1 + \cos^2(2\theta))/(\sin^2\theta\cos\theta)$; p - the multiplicity factor, $p_{bcc} = 12$ for the bcc phase, $p_{fcc} = 8$ for the fcc phase.

Figure 3.21a shows the amount of the bcc phase as a function of composition. Each data point in this figure corresponds to a complete XRD measurement and the composition is estimated from EDX. One can see that when the Rh content increases, the bcc ordered phase decreases and the fcc disordered phase increases continuously from 0 to 100 %. Based on the fitting curve, we estimate that the increase of the fcc phase in Fe-Rh-Pt films from zero to fully fcc phase takes place within $\sim$ 18 % (Rh+Pt) (Fig. 3.21a).

In bulk, Hofer et al (1966) reported an increase $\sim$ 15 % from 0 % fcc phase at 50 at. % Rh to 100 % fcc phase at 65 at. % Rh [94] (Fig. 3.21b). They did not report on films containing less than 50 % Rh. However, in the magnetic phase diagram of the bulk Fe-Rh alloy (see chapter 1), the sample is single phase (α' phase - FM at RT) when the Rh content is less than $\sim$ 48 %. In general, papers about bulk Fe-Rh alloys agree that the α'' phase stability window (AFM at RT) startes from 48 - 49 at. % Rh. Based on the XRD measurements, the fcc phase was observed even for the Rh content below 48 % in our films. Nevertheless, an observation of the fcc phase below 48 % Rh content was already reported in FeRh films [90].

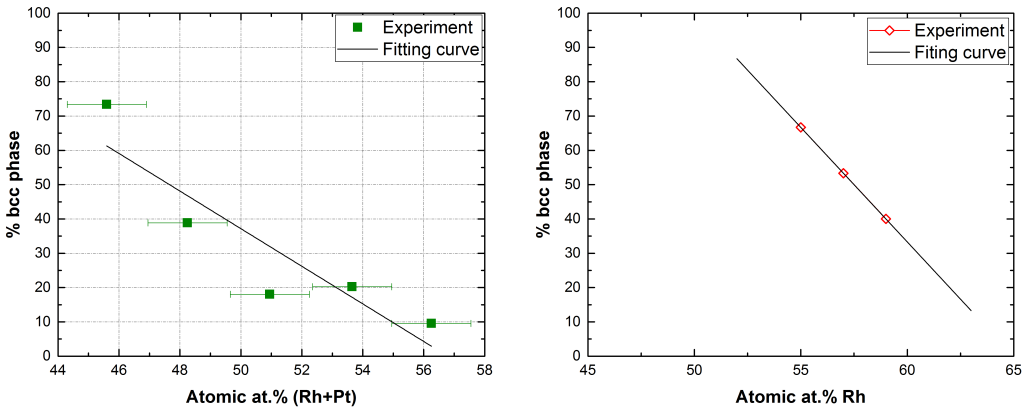

(a) In this study **(b)** In literature

Figure 3.21. *Composition dependence of the amount of bcc phase in (a) annealed $Fe_{1-x}(Rh-Pt)_x$ films, with 44.3 % $< x <$ 57.5 %. X-ray diffraction measurements were performed on a strip of $\sim 24 \times 2.5\,mm^2$. The solid line is the linear fit with the slope of -5.5 % bcc/% atomic. Error bars in the x-axis indicate the composition range of the measured sample. (b) bulk $Fe_{1-x}Rh_x$ alloys with the slope of -6.7 % bcc/% atomic in literature. (Data taken from [94])*

The mixture of the disordered and ordered phases in a wider composition range (below 48 % Rh) in films was also reported by Ohtani et al [90]. They observed an incomplete AFM-FM transition at 45.4 % Rh which is wider than in the bulk. Using Mössbauer spectroscopy, Ohtani reported that there is 64 % of an ordered phase (the α' and α'' phase) and 15 % of a fcc disordered phase (γ phase) in their Fe-Rh sample containing 45.4 % Rh, but 21 % of pure Fe phase (the α_{Fe} phase) is also found in all their samples. When the Rh

content increased, the bcc phase decreased and the fcc phase increased (the amount of α_{Fe} is constant). Later, van Driel et al (1999) [12] also studied $Fe_{1-x}Rh_x$ ($41\,\% < x < 59\,\%$) and reported that below 48.8 % Rh, samples were FM, above 49 % Rh, the films consist of a phase mixture of the disordered (the γ phase) and ordered phases. In this study of Fe-Rh-Pt films, the first order AFM-FM transition does not appear below 48 % (Rh + Pt), and the pure Fe phase α_{Fe} above 48 % (Rh + Pt) is very small (less than 0.5 %) if there is any, as shown in magnetization measurements in the following section.

In summary, Fe-Rh-Pt films show the superstructure diffraction peaks describing the ordered phase. The calculated amount of the bcc phase from X-ray diffraction patterns indicates that the film change from a fully bcc phase to a fully fcc phase in ~18 % (Rh + Pt) wide. The following section will discuss the magnetic properties based on magnetization measurements and explore the correlation between the crystal structure and the phase transition.

3.4.1.5 Magnetization dependence of the Fe-Rh-Pt films on composition and measurement temperature

Magnetization measurements as a function of temperature were made on samples of typical size $2.5\times2.5\,mm^2$ under 0.05 T using VSM-SQUID. M(T) curves measured across compositionally graded $Fe_{1-x}(Rh - Pt)_x$ films ($44.3\,\% < x < 57.5\,\%$) are shown in figure 3.22a. The composition of each sample was measured at its center using EDX. Compared to binary Fe-Rh films (Fig. 3.7b), there is an increase in the transition temperature ($T_t \sim 440\,K$), a sharpening of the transition and a reduction in the hysteresis width. Besides that, the calculated magnetization using the Brillouin function for $S = 1$ is in good agreement with the experimental data of the 48.6 % (Rh + Pt) film (see Fig. 3.22b).

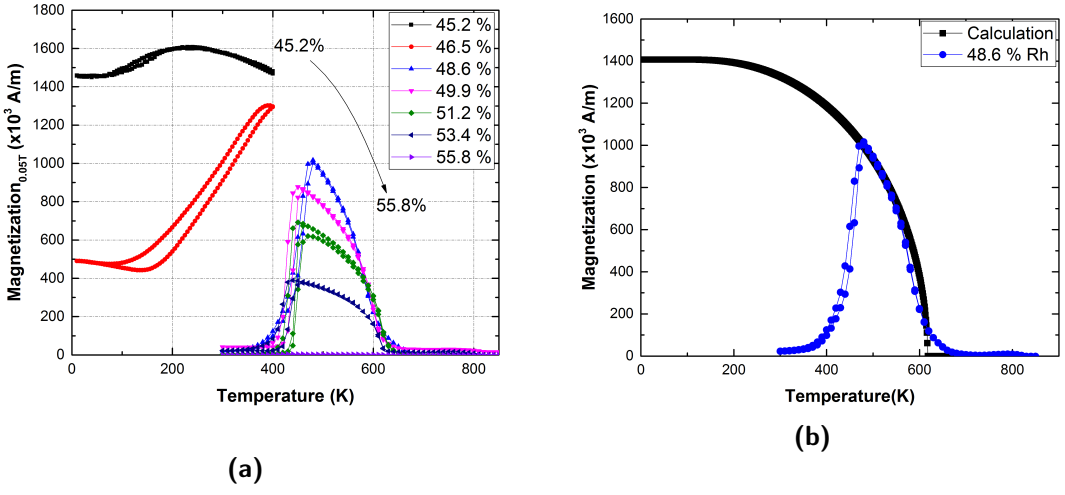

Figure 3.22. *(a) Temperature and composition dependence of magnetizations in annealed $Fe_{1-x}(Rh-Pt_{4.3})_x$ films, with $44.3\,\% < x < 57.5\,\%$. Measurements were made on samples of typical size $2.5\times2.5\,mm^2$ with 0.05T in the range of 5 K - 850 K. (b) The magnetization is calculated by the Brillouin function for $S = 1$.*

Table 3.2. *Temperature and composition dependence of transition temperatures and hysteresis widths in Fe-Rh-Pt films.*

$\%\,Rh$	$T_{t-heating}$ (K)	$T_{t-cooling}$ (K)	$\triangle T$
45.2	-	-	-
46.5	304 ± 5.6	275 ± 5.8	29
48.6	459.7 ± 1.6	450.6 ± 1.1	9.1
49.9	440.4 ± 0.3	427.3 ± 0.3	13.1
51.2	445 ± 0.1	431.6 ± 0.8	13.4
53.4	434.2 ± 1.1	417.9 ± 0.4	14.3
55.8	432 ± 3.5	411 ± 2.1	21

The definitions of the transition temperature and the hysteresis width in Fe-Rh-Pt films are the same as for Fe-Rh films as mentioned in chapter 2, which are the maximum of $\left|\partial \mathrm{M}/\partial \mathrm{T}\right|$ and $\triangle \mathrm{T} = \left|\mathrm{T_{t\text{-}heating}} - \mathrm{T_{t\text{-}cooling}}\right|$, respectively. Table 3.2 summarizes the transition temperature and the hysteresis width as a function of composition. When the Rh content is above 48 %, compared to the Fe-Rh films discussed above, the first order AFM-FM transition is sharper with a smaller hysteresis width. These values are the same order as the values for the bulk Fe-Rh.

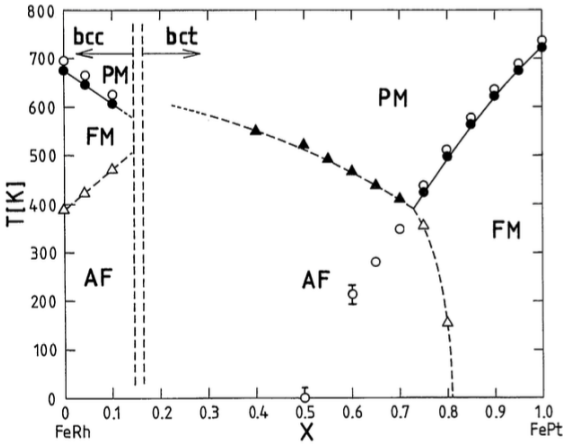

Figure 3.23. *The magnetic phase diagram of the $Fe_{50}(Rh_{1-x}Pt_x)_{50}$ alloy [103]. The broken and solid lines present the first and second order transition, respectively. Below 14 % Pt, the crystal structure is bcc and around ∼5 % Pt, the transition temperature is ∼ 440 K.*

Figure 3.23 describes the phase diagram of the ternary $\mathrm{Fe_{50}(Rh_{1\text{-}x}Pt_x)_{50}}$ alloy with the substitution of Pt for Rh keeping 50 at. % Fe [103]. When Rh was substituted by Pt ($\mathrm{x_{Pt}}$ $< 14\,\%$), it led to an increase in the transition temperature, and the crystal structure remained a bcc structure (the FM phase is destablized, resulting in an increase of $\mathrm{T_t}$ and decrease of $\mathrm{T_C}$). Interestingly, when the Pt content is larger than 14 %, the crystal structure becomes bct but samples are still antiferromagnetic. According to this magnetic phase diagram, the transition temperature for the substitution ∼ 4 - 5 at. % Pt for Rh is

around $\sim$ 440 K. The transition temperature and the crystal structure in our Fe-Rh-Pt films are consistent with these values implying the success in obtaining Fe-Rh-Pt films by the combinatorial approach and using the buffer and capping layers to produce the ternary system while controlling the amount of Pt in the few percents atomic range.

The Curie temperature. One can see that the first order transition temperature in Fe-Rh-Pt films is sensitive to the composition while the Curie temperature T_C does not have change significantly. In literature, the unsensitivity of T_C in the ternary bulk alloys of FeRh was reported [19, 22]. This can be explained when looking at the microscopic origin of T_C [22], by the fact that the Curie temperature is dependent on the atomic magnetic moments in the system as follows [41]:

$$T_C = \frac{2ZJS(S+1)}{3k_B} \tag{3.5}$$

where, Z -the nearest neighbor coordination number; J is the strength of exchange interactions; S is the total spin angular momentum; k_B is the Boltzmann constant.

This formula shows that the Curie temperature scales with the exchange interaction. Because the lattice parameters in Fe-Rh-Pt films do not change compared to FeRh bulk alloys ($\sim$ 2.978 Å in our Fe-Rh-Pt films vs 2.983 Å$\pm$0.007 in FeRh alloys as mentioned above), the exchange interaction, which is related to wave function overlap, does not change. On the other hand, because Pt is similar to Rh and becomes magnetic $\sim$1 μ_B, the number of magnetic neighbors does not change. In literature, Barua et al. in 2013 [22] used this formula to explain the weak dependence of T_C with substitution of composition in their ternary alloys of FeRh. Because T_C is proportional to S, it leads to a small change in the Curie temperature with a small elemental substitution.

Thermal hysteresis width. The reduction of the hysteresis width when increasing the transition temperature is also consistent with literature. Kouvel in 1966 [19] showed experimentally that the hysteresis width increased or decreased when the transition temperature was decreased or increased when substituting Rh. Although many studies reported experimentally the change of transition temperature and thermal hysteresis width in the ternary systems of FeRh, to date the theoretical approach is limited.

For the theoretical side, Gibbs free energy G is expressed as a function of temperature and pressure and is represented (see chapter 1)

$$G(T,\ P) = U + P.V - T.S \tag{3.6}$$

where: T - the temperature (K); P - the pressure (N/m^2); U - the internal energy (J); V - the volume (m^3); S - the entropy (J/K).

The system will be in a stable equilibrium at the minimum energy of the Gibbs free energy: dG = 0. Figure 3.24 illustrates a variation schematic of the Gibbs free energy for a transformation from initial to final state [4]. For a phase transition, the system must overcome an energy barrier E_a (the activation energy) separating two equilibrium states. In 1899, the Swedish chemist Svante Arrhenius reported the influence of temperature on the

activation probability based on a combination of the activation energy and the Boltzmann distribution law:

$$k = A.e^{-\frac{E_a}{RT}} \tag{3.7}$$

where: k - the rate constant (unitless); A - the pre-exponential factor (unitless); E_a - the activation energy (J/mol); R = 8.314 J/(K.mol) - the ideal gas constant.

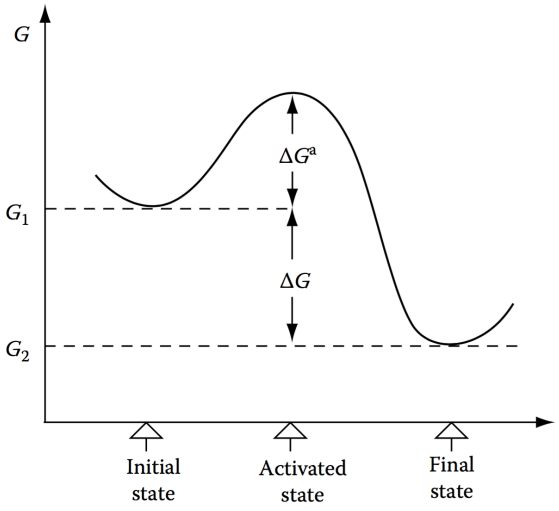

Figure 3.24. *A variation schematic of the Gibbs free energy describes transformation from initial to final state. Here, $\triangle G$ is the difference in energy between two states, $\triangle G^a$ is the activation energy barrier which is notated E_a in our study. (Image taken from [4]).*

It is known that in a closed system, where pressure and magnetic field are constant, the difference between the energy of the FM and AFM states ΔG decreases with increasing temperature [5]. Element substitutions (intrinsic parameter), pressure or magnetic fields (extrinsic parameters) can decrease or increase the transition temperature, where both phases have the same energy. The thermal hysteresis width $\triangle$T can increase or decrease because of the activation mechanism (the mechanism to go AFM to FM or FM to AFM) and the temperature where this mechanism takes place.

As higher the temperature, the atomic mobility should be higher, it leads to a higher probability of atoms to overcome barriers. However, it is unclear what the influence of an element substitution, or strain on the activation energy barrier E_a will be. Because the hysteresis width is directly related to E_a, a reduction of the hysteresis width will happen if E_a decreases and the hysteresis width will increase as E_a increases. Thus, estimating E_a is useful to understand a cause of the change in thermal hysteresis width. In general, studying the activation energy barrier will help us to understand the transformation.

Based on the Arrhenius equation, Kissinger [104] described the activation energy related to the transition as follows:

$$ln\left(\frac{\phi}{T_t^2}\right) = -\frac{E_a}{RT_t} + A \tag{3.8}$$

where: ϕ - the heating rate (K/s).

By plotting $\ln\left(\frac{\phi}{T_i^2}\right)$ and $\frac{1}{T}$, the activation energy can be determined. Lu et al in 2012 [92] estimated $E_a \sim 228.6\,kJ.mol^{-1}$ for the first order transition in a 100 nm thick polycrystalline FeRh film. However, the value E_a for ternary systems of FeRh is not reported yet. In other word, the influence of substitution on E_a is not yet determined and this study seems an interesting prospects for future studies using our films.

Sample-to-sample variations coupled with the sensitivity of the properties to composition in FeRh-based systems are difficulties to a study the substitution influence on the phase transition mechanisms. Thanks to the combinatorial approach and buffer/capping layer, this matter can be solved to produce the binary and ternary samples of FeRh. Samples are available as well as our magnetometer can perform this task, so measurements to determine the activation energy are planned for future work.

Estimation of the amount of bcc phase using magnetization data. Figure 3.22a again shows that when the Rh content is increased, the magnetization will smoothly decreased. As mentioned above, the fcc phase in the Fe-Rh sample is paramagnetic and the bcc phase is the magnetic phase responsible for FM and/or AFM, thus we can consider that only the bcc phase contributes to the magnetization of films. To estimate this contribution, we define an estimation formula as 3.3, calculated using the sample magnetization over the magnetization of the pure bcc phase when the transition is complete as follows:

$$\%\,bcc = \frac{M_{sample}}{M_{pure\ bcc\ phase}} \tag{3.9}$$

where: M_{sample} - the maximum magnetization of film when the transition is complete, $M_{pure\ bcc\ phase}$ - the maximum magnetization of the pure bcc sample. The M_{sample} is obtained from M(T) curves in the figure 3.22a. While the $M_{pure\ bcc\ phase}$ is obtained from the calculated magnetization curve using the Brillouin function (Fig. 3.22b) at the same temperature with M_{sample} above, which allows us to avoid the temperature effect.

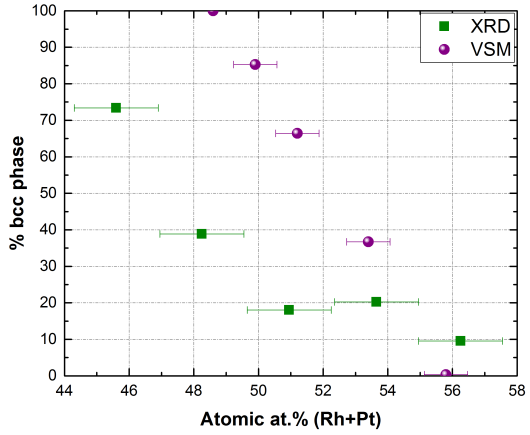

Figure 3.25. *The amount of the bcc phase in annealed $Fe_{1-x}(Rh-Pt)_x$ films ($44.3\,\% < x < 57.5\,\%$) as a function of composition was estimated through the VSM data and XRD (the previous part). The error bar in the x-axis indicates the composition range of the measured sample.*

The calculated results for the amount of bcc phase using our magnetization data are

shown in figure 3.25. This figure shows that the magnetization of Fe-Rh-Pt films changes from fully magnetic to fully non-magnetic (paramagnetic - the γ phase) over 7.2 at. % (Rh + Pt) which corresponds to 13.5 mm along the x-axis of the Fe-Rh-Pt wafer. In this figure, we also add the bcc phase obtained from the X-ray diffraction patterns above. VSM identifies two bcc ordered phases: α' and α" (the FM - PM and AFM - FM - PM transition). However, it does not pick up the AFM and PM signal. While XRD can identify the bcc and fcc phase, but it cannot separate bcc ordered phases. From XRD, the γ phase in the Fe-Rh-Pt films occurs at the lower Rh content than bulk. From VSM, the α" phase stability window (the AFM - FM transition) is similar to the bulk FeRh phase diagram. The difference between XRD and VSM can be attributed to the estimation of the sample volume, possible texture and an underestimation of the $M_{\text{pure bcc phase}}$.

3.4.2 Substitution of Ni for Fe

The successful achievement of the high quality Fe-Rh-Pt films to increase the transition temperature hints that we can use a similar combinatorial approach to decrease the transition temperature. It was reported that the substitution of Ni for Fe in Fe-Rh alloys led to a stronger change in transition temperature under hydrostatic pressure than binary FeRh alloys [101]. In this part, we will discuss $(Fe\text{-}Ni)_{1\text{-}x}Rh_x$ films obtained using the combinatorial approach with a focus on tuning the transition temperature.

3.4.2.1 Sample preparation and crystal structure

Si/ SiO_2‖ Ni 1.1 nm/ FeRh 250 nm/ Ta 1.1 nm samples were prepared using magnetron sputtering. Then, samples were annealed at 700°C for 2h. After the annealing process, we obtained Fe-Rh-Ni samples with the thickness of $\sim$ 250 nm. For the Fe-Rh-Ni films, the Ni content in films is constant, while the Fe content will vary linearly across the x-axis of the substrate.

One can see that the thickness of Ni is much smaller than FeRh. The Ni content in the Fe-Rh-Ni films can be estimated to be 0.5 at. %. A more precise measurement of composition using EDX is not feasible. The fabrication of compositionally graded Fe-Rh films is stable and reproducible. Thereby, the compositions of Fe-Rh-Ni films were estimated based on the film position on the silicon wafer. It means that the Fe-Rh-Ni wafer still has compositionally graded film behaviour with a linear variation of composition, but the absolute value of composition can be slightly shifted. The agreement between the Rh content and an appearance of the first order transition, shown in figure of M(T) curves in the following part, proofs that this assumption is reasonable.

The crystal structure of a $(Fe\text{-}Ni)_{51}Rh_{49}$ film after the annealing process is shown in figure 3.26. The Bragg peaks observed in this sample are consistent with those of the bcc phase in the equiatomic FeRh alloy. The appearance of the superstructure peak also indicates the presence of the bcc ordered phase in this sample. No other crystalline phases (i.e. the fcc phase, the α_{Fe} phase) were found in this sample. Because we only substitute Ni for a small amount of the Fe atomic content, no change in lattice parameters is expected.

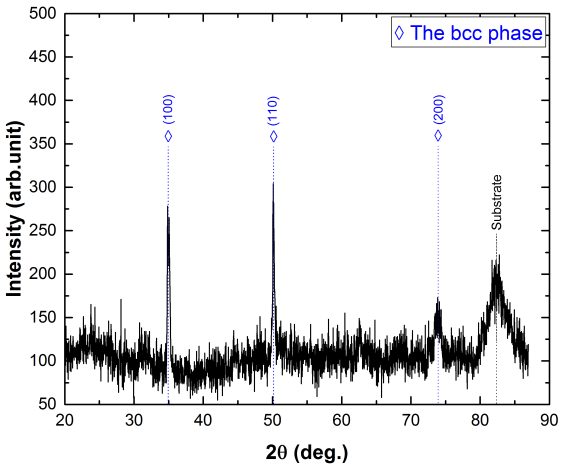

Figure 3.26. *X-ray diffraction pattern of the annealed (Fe-Rh)$_{51}$Ni$_{49}$ film using a diffractometer equipped with a cobalt X-ray source at room temperature. The obtained peaks are of the bcc phase and the substrate. The appearance of the* $(100)_{bcc}$ *superstructure peak demonstrates the ordered bcc phase presence.*

3.4.2.2 Temperature dependence of the Fe-Rh-Ni films magnetization

The temperature and composition dependence of magnetization in annealed $(Fe\text{-}Ni)_{1\text{-}x}Rh_x$ films was investigated using a VSM SQUID in the temperature range of 10 - 400 K under 0.05 T, as shown in figure 3.27. The composition of Fe-Rh-Ni films is taken from the composition of FeRh films at the same position on the silicon wafer measured by EDX above. In the figure 3.27, below 47.7 % Rh, no transition was found in the $(Fe\text{-}Ni)_{1\text{-}x}Rh_x$ films, then when the Rh content is increased, the first order AFM-FM transition was observed and the magnetization decreased with an increase in the hysteresis width.

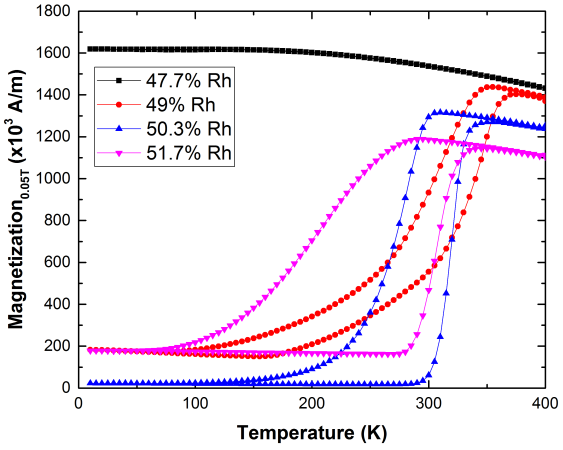

Figure 3.27. *Dependence of magnetization on composition and temperature in annealed (Fe - Ni)$_{1\text{-}x}$Rh$_x$ films. VSM data showed a decrease of the transition temperature compared to Fe-Rh by substituting Ni for Fe.*

As expected from previous studies in literature, the first order transition temperatures were lowered because of the small substitution Ni for Fe. On the cooling curve of the 50.3 % Rh sample (the blue curve), the transition temperature is below room temperature.

Meanwhile, the transition temperature is above room temperature on the heating curve. At x = 51.7 %, the transition temperatures of both the heating and cooling curves were below room temperature. As a result, there are three zones on the Fe-Rh-Ni wafer. The Fe-rich side corresponding to the left side of the wafer is ferromagnetic (x < 47.7 %), the next region is antiferromagnetic at room temperature and ferromagnetic at high temperature, and the last region at the Rh-rich side is ferromagnetic at room temperature and antiferromagnetic at low temperature. This structure is well suitable for the following optical study.

In brief, we fabricated good Fe-Rh-based films showing a well defined transition from AFM to FM through a study of compositionally graded films. Ternary substitution to tune the transition temperature was done through simple pure element deposition using buffer and capping layers. The Fe-Rh-based films using this approach are reproducible which is important not only for fundamental research but also in applications. In addition, with controlling deposition within the nm thickness range, it gives us a high precision for ternary compositions.

3.5 Optical transition of the graded Fe-Rh based films

3.5.1 Introduction

An abrupt change in reflectivity of the annealed wafers occurs on all our Fe-Rh-based systems including $Fe_{1-x}Rh_x$, $Fe_{1-x}(Rh\text{-}Pt)_x$. A photograph of a 2″ wafer of annealed $Fe_{1-x}(Rh\text{-}Pt)_x$ film is shown in figure 3.28a, with the Fe-rich and Rh rich regions at the left and right side, respectively. Clearly, there is an abrupt change in reflectivity between the left and the right side which can be seen by eye or using a standard camera. No report about this phenomenon was found in literature.

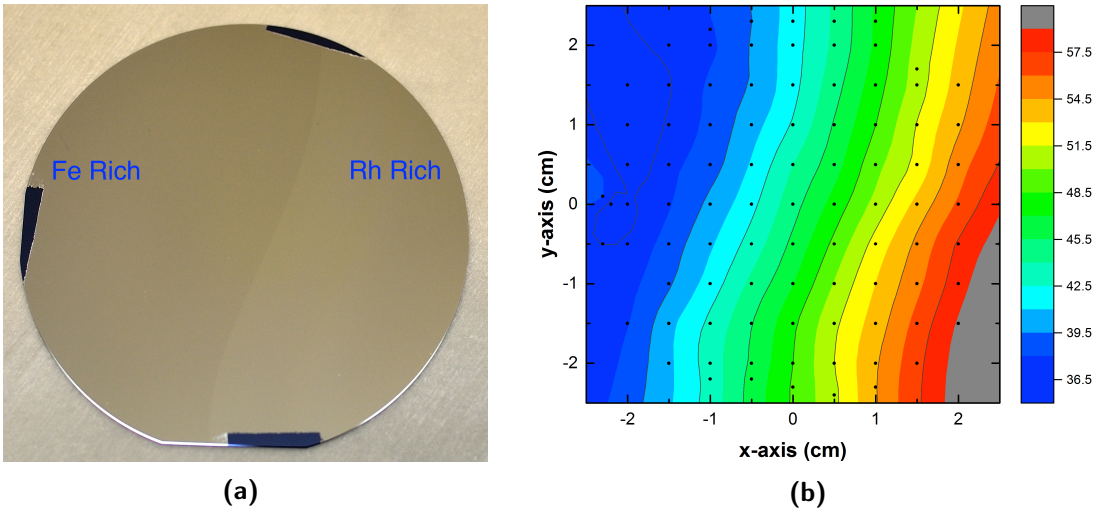

Figure 3.28. *(a) The abrupt change in colour between the Fe-rich side (dark) and the Rh-rich side (bright) around ∼ 48 % Rh content in the annealed $Fe_{1-x}(Rh-Pt)_x$ wafer. (b) The EDX map of Fe-Rh films replotted from figure 3.6.*

The shape of the dark to bright interface (the optical contrast interface) line follows iso-composition lines in the EDX 2D map (see Fig. 3.28b replotted from figure 3.6). The "S" shape can be recognised. Possible reasons for this dark to bright contrast include variations in: (1) thickness, (2) crystal structure, (3) magnetism, (4) roughness and (5) oxidation.

We mention magnetism and crystal structure because of the magnetic and structural changes with composition in the magnetic phase diagram of Fe-Rh alloys (see Fig. 1.2a and table 1.1). We remind these changes as follows. The crystal structure changes from a bcc disordered phase (0 - 19 at. % Rh) $\rightarrow$ a bcc ordered phase (including both of FM and AFM phases at room temperature in the range of $\sim$ 11 - 55 at. % Rh $\rightarrow$ a fully fcc phase ($>$ 72 at. % Rh). For the change in the magnetic order, Fe-Rh samples are ferromagnetic from $\sim$ 11 - 48 at. % Rh and antiferromagnetic from $\sim$ 48 - 55 at. % Rh at room temperature. Due to these reasons, the crystal structure and magnetism may be the origin of the optical contrast interface. In the following, we will consider each possible origin for this optical contrast.

3.5.2 Optical properties of Fe-Rh(-Pt) films

According to magnetization measurements (Figures of 3.7b, 3.22a and 3.27), the first order transition in $Fe_{1-x}Rh_x$ occurs at room temperature, which complicates characterization in setups that operate either from low temperature up to room temperature, or from RT to high temperature. Thus we choose the $Fe_{1-x}(Rh\text{-}Pt)_x$ wafer which has a transformation fully above room temperature to study the optical transition.

Thickness. The thicknesses of films along both the x and y-axis of the wafer were about $\sim$ 250 nm $\pm$ 10 %, as measured by FESEM and no thickness step was observed. Across the wafer, the thickness is always larger than the optical penetration depth and the film should behave as a semi-infinite medium from the optical point of view. Thus, thickness variation is not the cause for this dark to bright interface.

Crystal structure. Concerning the crystal structure, figure 3.25 showed that the percentage of the bcc ordered phase decreases continuously across 33.6 mm wide corresponding to 18 % atomic. As the width of the optical transition is sharp ($<$ 0.5 mm) compared to the width of the bcc to fcc transition, the third reason (crystallographic contrast) is also discarded.

Magnetism. From the VSM measurements, the FM phase is in the dark zone and the AFM phase is in the bright zone with the first order AFM $\rightarrow$ FM transition. To study the origin of this optical transition, we heated films on a hot-plate. The wafer was glued on a Cu base using silver paste. Then, the Cu base was placed on a hot-place. Applied temperatures were measured using a calibrated Pt-1000 temperature sensor stuck to the bottom side of the wafer.

Figure 3.29 showed images of annealed $Fe_{1-x}(Rh\text{-}Pt)_x$ films at various temperature during both heating and cooling. At room temperature, we see an "A_1" interface and this interface moved to the right hand side during the heating process. Above 450 K, we saw the appearance of one more interface called the "A_2" interface and the "A_2" interface

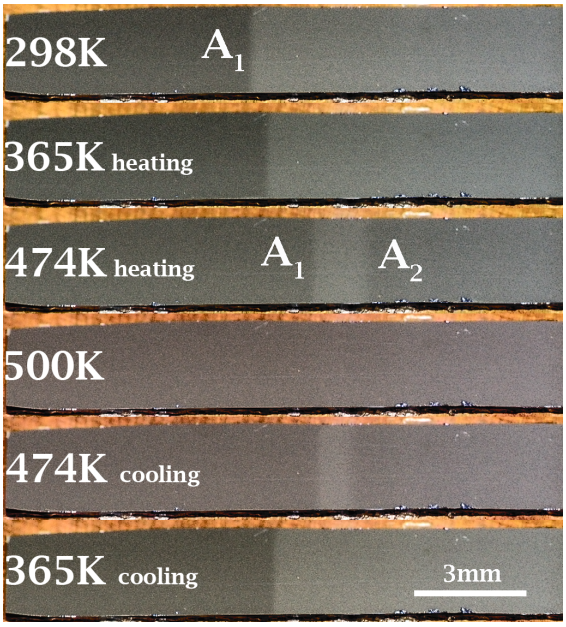

Figure 3.29. *Photographs of annealed Fe-Rh-Pt films at various temperatures during heating and cooling. The Fe-rich and Rh-rich regions are on the left and right hand side, respectively. The A_1 and A_2 interfaces converge on heating and separated on cooling, with a hysteresis of the position of the interfaces between two processes (clearly see the difference in the 474 K images). This series of images suggests that the dark to bright interface corresponds to the FM → AFM transition. (The contrast was enhanced using Matlab)*

moved to the left side on heating. This opposite movement leads to a convergence of "A_1" and "A_2" around 500 K. Then above 500 K, we did not see the "A_i" (i = 1, 2) interfaces anymore. On cooling, we see the "A_i" interfaces again. There is a hysteresis in the position of the interface between heating and cooling. As a result, we can see a different gap width between "A_1" and "A_2" at the same applied temperature, i.e. at 474 K in this figure, when the films are heated and cooled. Because the dark to bright interface can be moved in a quasi-reversible fashion by heating and cooling, we can conclude that this optical transition corresponds to the FM-AFM transition.

The hysteresis of the position of the "A_i" interface between the heating and cooling processes is attributed to the hysteresis of magnetization against temperature presented in the M(T) measurements. These observations rule out the fourth and fifth possible reasons (the roughness and oxidation), which should not evolve in a quasi-reversible way when heating and cooling. The abrupt change in reflectivity between the FM and AFM phase suggests a significant difference in DOS between the FM and AFM phase which supports the hypothesis of an important contribution of the electronic entropy to the transformation in Fe-Rh-based systems. A discussion about the origin of the first order transition in Fe-Rh-based systems is presented in the final part of this chapter.

3.5.3 Construction of a magnetic phase diagram for Fe-Rh based systems with only one wafer

A major advantage of the combinatorial approach is that we can obtain various samples in only one fabrication process, so that the samples have the same deposition and annealing conditions. This is in contrast to the traditional method of constructing a phase diagram in which a series of separately prepared samples are used. In this part, we will present the construction of a magnetic phase diagram for Fe-Rh-Pt based on optical measurements of the above described transition and magnetic characterization in a VSM-SQUID.

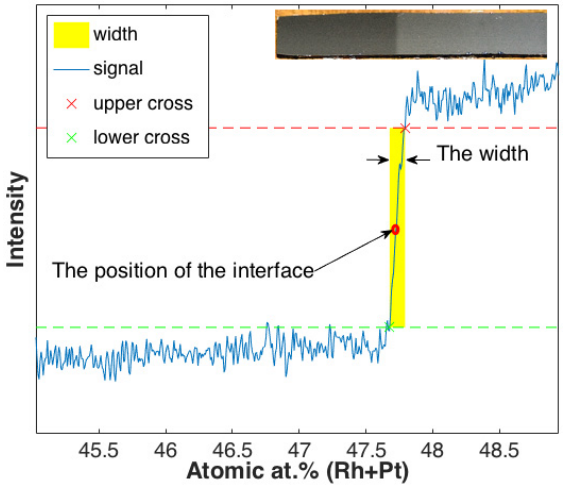

Figure 3.30. *Intensity of the annealed $Fe_{1-x}(Rh-Pt)_x$ photograph is as a function of the Rh content (the Pt content is constant). This photograph also shows definitions of the position of the dark and bright interface (the red dot) and the transition width. The inset picture is the Fe-Rh-Pt strip at 292 K which is used to plot this intensity profile.*

When the sample changes from a FM state to an AFM state, the reflectivity will abruptly changes from dark to bright. In order to study the reversible movement of the interface with temperature, we defined the position of the dark to bright interface as shown in figure 3.30 (the red dot), in which the interface position is defined as the position at half maximum of the intensity. The position of the interface can be correlated with the film composition, known from EDX map. Because the dark to bright interface corresponds to the FM to AFM transition, applied temperatures in optical measurements are considered as transition temperatures.

The transition temperature in annealed $Fe_{1-x}(Rh\text{-}Pt)_x$ films estimated from optical measurements was plotted as a function of composition (Fig. 3.31). Transition temperatures measured using the optical contrast are in good agreement with those measured by VSM SQUID, even though results from VSM SQUID are an average over a certain area of the sample. This is also an evidence to prove that the optical transition corresponds to the FM to AFM transition. When the Rh content is increased, the transition temperature increases with a slope of $\sim 180\,\mathrm{K}/\%$ atomic (Rh + Pt) up to a maximum at around $\sim 49\,\mathrm{at.}\,\%$ (Rh + Pt). Beyond that, the transition temperature decreased. The same behavior was also obtained on the cooling process, and comparison of the heating and cooling curves reveal

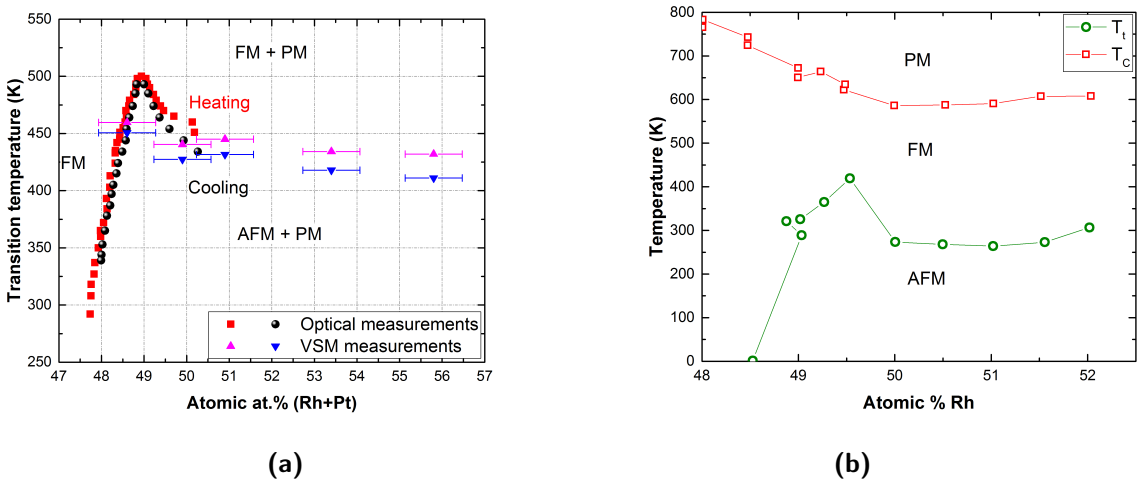

Figure 3.31. *(a) Construction of a magnetic phase diagram of* $Fe_{1-x}(Rh-Pt)_x$ *with one wafer from optical measurements, in a comparison with VSM measurements. The red and magenta curves show measurements on the heating site; the black and blue curves show measurements on the cooling cycle. (b) Phase diagram of binary Fe-Rh measured on bulk and film samples. (Image taken from [105])*

a thermal hysteresis.

In literature, published phase diagrams of Fe-Rh based systems are not detailed close to 50% (see Fig. 1.2) and they do not fully coincide (see Fig. 3.31b, 1.2c). These phase diagrams of the FeRh alloy are replotted in figure 3.32 for an easier observation. In the figure of 3.31b, the transition temperature reaches a the maximum value around 49.5 at. % Rh but only one measured point showed that. Besides that, the fluctuation of transition tremperatures is about 50K in literature, while this value is around 5 - 10 K in our phase diagram. These measurements in figure 3.32b showed that the transition temperature increases with the increase of the Rh content and maybe get the maximum value at round 52 at. % Rh, then it may slightly decrease with increasing the Rh content. Meanwhile, this peak is not so clear in the phase diagram reported by Swartzendruber (see Fig. 3.32a).

Unlike these published phase diagrams before, thank to the combinatorial approach. Our phase diagram shows an obviously maximum value of the transition temperature around $\sim$ 49 at. % (Fig. 3.31a). Our phase diagram is in qualitative agreement with literature results for FeRh. Shift in the transition temperatures is due to substitution of Pt for Rh. The enhanced transition temperature for a very specific composition which could be the exact 50-50 composition hints at an enhanced stability of the AFM phase for the perfect equi-atomic composition (even in a ternary alloy).

When the composition is above 51 %, the contrast change fades away and seems to be less composition dependent. We did not plot above 51 % in our phase diagram.

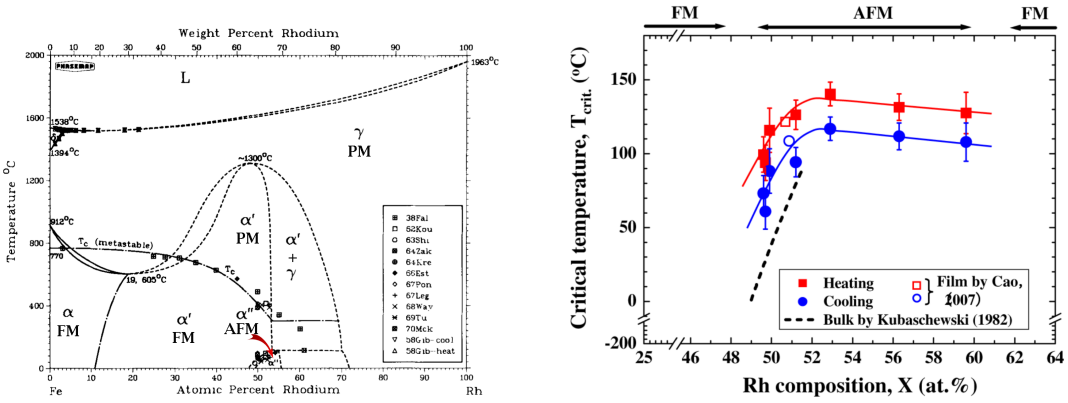

(a) (b)

Figure 3.32. *Magnetic phase diagram of FeRh alloy is replotted from chapter 1, reported by (a) Swartzendruber [13], (b) S. Inoue et al [15].*

3.5.4 Quantitative optics

In order to quantify the optical transition related to a change in DOS and understand this AFM - FM transition, ellipsometry measurements were made across graded $Fe_{1-x}(Rh\text{-}Pt)_x$ films at room temperature. Nine measurements were made on a long strip, consisting of 4 measurements in the FM zone (1 - 4), 4 measurements in AFM zone (6 - 9) and 1 measurement on the intermediate zone (5) (see Fig. 3.33).

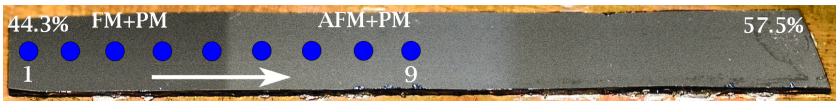

Figure 3.33. *Ellipsometry measurements were made across an annealed $Fe_{1-x}(Rh-Pt)_x$ strip, from the FM side to the AFM side. The measured points are illustrated with blue circles in this image. The composition shown on this figure is the (Rh + Pt) content.*

The imaginary parts of the dielectric functions are shown in figure of 3.34a. It is clear that the data in the 0.74 - 3 eV range consists of two group of curves on this figure, with the group of the AFM state ((6) → (9)) at the higher position than the ones of the FM state ((1) → (4)). Curve of No. 5, measured on the intermediate zone is in-between both two groups. In contradiction to a previous publication, a clear difference is found in the optical properties of FM and AFM phases which reflects a difference in the DOS.

Chen et al in 1988 [106] measured dielectric constants using the ellipsometry technique and did not see a noticeable difference between their samples at room temperature (see Fig. 3.34b). The difference they measured between FM and AFM samples was of the same order as the difference between samples. For all their samples, they observed no change in the dielectric function with temperature. Samples which are antiferromagnetic at room temperature showed identical curves even at higher temperature than the transition temperature (samples were the FM state at this temperature). They infered that the absence of difference across the magnetic transition was related to identical DOS between both magnetic states.

However, the separation we observe into two groups of curves for different states of FM and AFM is supported by calculations from Khan et al. in 1983 [107]. They calculated the dielectric functions in all three phases of AFM, FM, PM in Fe-Rh alloys and found a difference in DOS with the AFM curve at a higher position than the FM curve between 1 eV and 1.75 eV. In addition, they found that there is a peak at 1.686 eV for the FM state only.

In our results, a peak also appears at around $\sim$ 1.7 eV for only the FM state which is in good agreement with their calculations (Khan et al. (1983)). Measurements of Chen el al. (1988) showed this peak to be present in the spectra of both phases, which contradicts our measurements and calculations by Khan et al. (see Fig. 3.34b). To make a quatitative comparison between our measurements and calculations, the contribution of the free electrons needs to be subtracted (the Drude contribution). However, our ellipsometry measurements are made on the Fe-Rh-Pt films, which can lead to different magnitudes when compared to calculations made for the FeRh alloy. It means that measurement results of Fe-Rh-Pt films still show the difference between two phases with the appearance of the peak in the FM state, and the Pt substituion does not qualitatively modify the theoritical prediction.

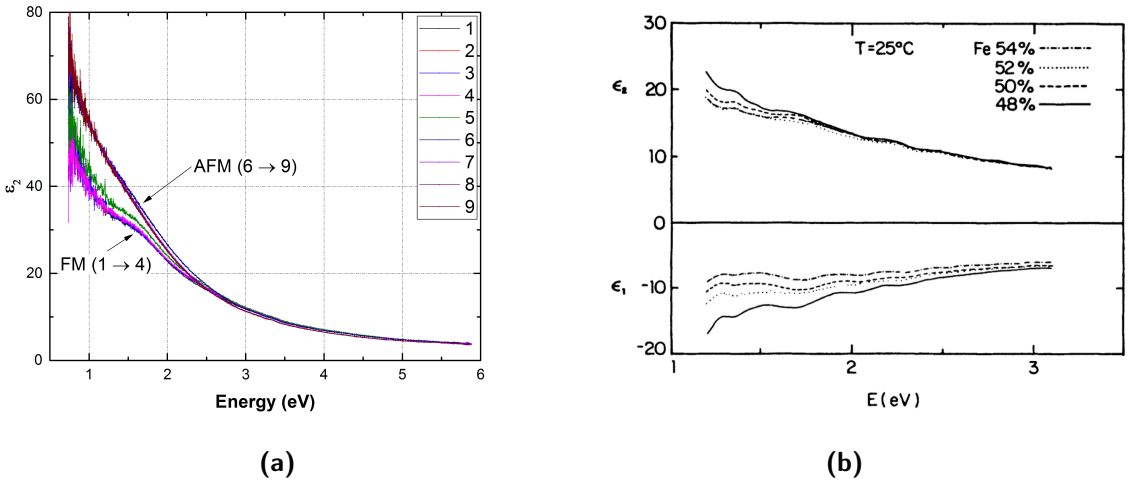

(a) (b)

Figure 3.34. *Imaginary parts of the dielectric function ε_2 of annealed $Fe_{1-x}(Rh-Pt)_x$ films measured in the AFM (6 - 9), FM (1 - 4) regions as well as at the interface between both (5), measured using ellipsometry (a) and the previous publication by Chen et al (1988) (b). (Image taken in [106]).*

In conclusion, the dielectric functions in our ellipsometry measurements compare well with predictions by Khan el al (1983). The dielectric constants is clearly different between both phases, evidencing the large change in the density of states across the transition. The difference between each phase can be seen by eye and can be quantitatively investigated using ellipsometry measurements.

This result shows that we should not ignore the electronic contribution to entropy change when discussing the origin of FeRh phase transition.

3.5.5 The robustness of the optical transition in Fe-Rh based systems

One question concerns the robustness of the optical transition in other Fe-Rh systems. Does this optical transition only appear in the Fe-Rh-Pt samples or on other Fe-Rh(-M) ternary systems and how to control it? To further investigate the optical transition, we deposited $(Fe\text{-}Ni)_{1\text{-}x}Rh_x$ films with the first order transition and transition temperatures spanning from below to above room temperature, depending on the composition and the heating or cooling process as discussed above. We studied the optical transition in the $(Fe\text{-}Ni)_{1\text{-}x}Rh_x$ system using optical measurements and also a scanning Hall probe measurement (SHPM) made in collaboration with Imperial College London (M. Kustov). In this part, we present the optical transition in the annealed $(Fe\text{-}Ni)_{1\text{-}x}Rh_x$ films. Results of the SHPM are described in the following section.

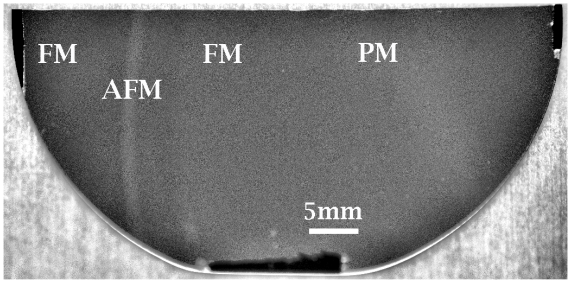

Figure 3.35. *Optical photograph of an annealed $(Fe\text{-}Ni)_{1\text{-}x}Rh_x$ wafer. Two dark and bright interfaces corresponding to the AFM - FM transition. The width of the bright AFM band on this image is about ∼1.1 mm.*

An optical photograph of an annealed $(Fe\text{-}Ni)_{1\text{-}x}Rh_x$ wafer taken at room temperature is shown in figure 3.35. This image contrast was enhanced and converted from the truecolor image RGB to the grayscale image. When studying the optical transition in the Fe-Rh-Pt films (Fig. 3.28a), because of the high transition temperature, only one dark to bright interface, corresponding to the AFM - FM transition exists at room temperature, with one more dark to bright interface appearing in the temperature range 450 to 500 K. By substituting an adequate amount of Ni for Fe, the transition temperature can be tuned to lower temperature and the peak in this phase diagram above occurs closer to room temperature.

In this substitution Ni for Fe, the transition temperature in the phase diagram of $Fe_{1\text{-}x}(Rh\text{-}Pt)_x$ was moved to lower temperatures and two interfaces, each corresponding to the phase transition, are seen at room temperature (see Fig. 3.35). When we heat the Fe-Rh-Ni films, the two interfaces move during heating and cooling. This proves again that the interfaces correspond to the FM-AFM transition and are not due to a change in crystal structure, thickness, roughness or oxidation.

3.5.6 Visualizing magnetically the optical transition

Studies of the optical transition discussed above were performed using optical measurements in a comparison/combination with FESEM, EDX, XRD and VSM results. It is also of interest to study the dark to bright interface using a technique that is sensitive to the stray magnetic field produced at the interface. The interface on $(Fe\text{-}Ni)_{1\text{-}x}Rh_x$ films was probed using a scanning Hall probe in cooperation with Imperial College London. The temperature of the sample can be reduced below room temperature, thus the interest in using Fe-Rh-Ni, which shows a transition below room temperature. Results are shown in figures 3.36 and 3.38. An optical image showing A_1 and A_2 interfaces is shown in figure 3.36a. We remind that A_1 and A_2 interfaces correspond to the dark and bright interface (the FM and AFM transition).

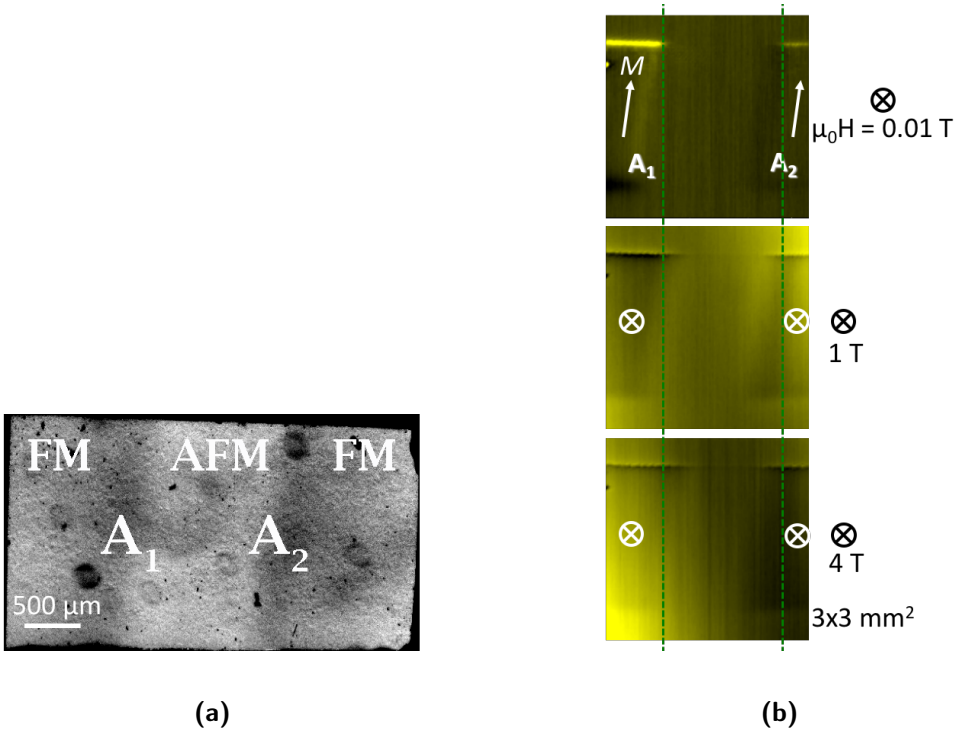

Figure 3.36. *(a) The optically contrast-enhanced image of annealed $(Fe\text{-}Ni)_{1\text{-}x}Rh_x$ films showing two dark and bright interfaces corresponding to the AFM-FM transition. (b) SHPM maps of the stray field at room temperature with various out-of-plane applied magnetic fields. The measured area is $3 \times 3\,mm^2$. The green lines are a guide to eye. These measurements were made at Imperial College London.*

Influence of external magnetic field on the interface. *Experiment.* The movement of the dark to bright interface as a function of external out-of-plane magnetic field at room temperature is shown in figure 3.36b. The optically contrast-enhanced image of the sample showed two dark and bright interfaces, corresponding to the two interfaces in Fig. 3.36a. The two dark bands are FM and the in-between bright band is AFM, as discussed above. Thanks to this structure, a magnetic stray field can be expected due to magnetic poles, either at the edges (cleaved) of the film (the FM zone) or the AFM-FM interface.

When we apply a small magnetic field of 0.01 T in the out of plane direction, the

direction of the magnetization is still in-plane as indicated by the assumed arrows with two clear stripes corresponding to the FM bands in the figure of 3.36b. Two stripes at the left and right hand side grew gradually and converged with increasing magnetic field. When the magnetic field is reduced, the two stripes moved back (not shown here).

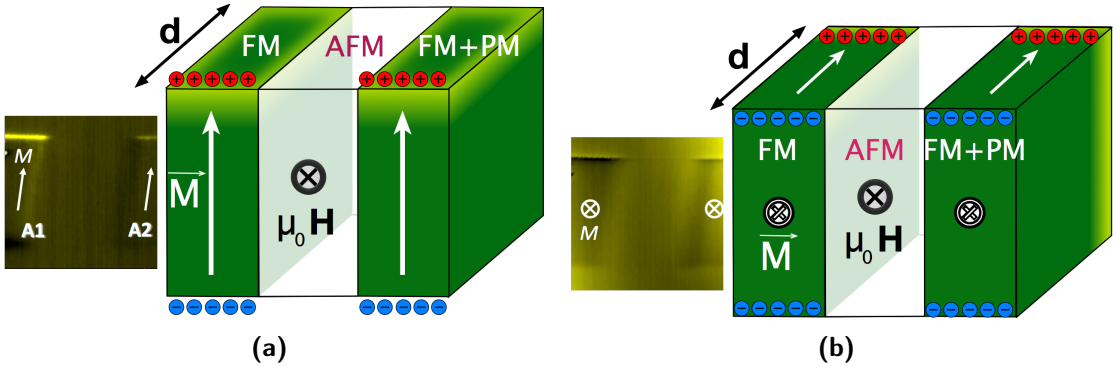

Figure 3.37. *Magnetic moments and poles at room temperature under magnetic fields of (a) 0.01 T, (b) 1 T or 4 T. Images of the SHPM result are replotted from the figure 3.36b. (d is the thickness of the film)*

Discussion and model. The dark to bright interfaces move with external magnetic field, which is characterized using SHPM magnetically through sensing the stray field. The FM zone also has magnetic poles at the edge, resulting in a contrast in SHPM results at the top and bottom of stripes (the edges of the sample). However, these magnetic poles does not move (grow) with magnetic fields. Although the Fe-Rh-Ni sample is not patterned, the special structure of sample consisting in FM/AFM/FM+PM zones creates stray fields. So, we observed two stripes at the left and right hand side of sample.

The growth of two stripes with increasing magnetic field is due to the phase transition from the AFM state to the FM state. We estimate the change of the transition temperature under magnetic fields as follows. In figure 3.36b, an increase of ~1/3 mm is observed under 4 T, which corresponds to a change of ~0.18 at. % Rh. The phase diagram of Fe-Rh-Pt constructed in the previous part (Fig. 3.31a) gives a rate of 200 K/1 at. %. Therefore, a change of 36 K is estimated using SHPM and optical measurements. Now, we calculate the change of the transition temperature under magnetic fields using VSM SQUID measurements. Because we only substitute Ni for a small amount of Rh, we can assume that the change of the transition temperature under the applied magnetic field for $(Fe\text{-}Ni)_{1\text{-}x}Rh_x$ films is similar to Fe-Rh systems, which is at a rate of -8 K/T. Hence, a change of 32 K in the transition temperature is calculated with a magnetic field of 4 T, which is consistent with the estimated value above. This agreement proves that two stripes corresponds to the dark and bright interfaces (the AFM and FM transition).

Models with magnetic moments and poles are drawn to explain these SHPM results as shown in figure 3.37. Figure 3.37 illustrates a model for the magnetic moment in the FM zones as well as poles at room temperature under magnetic fields (Fig 3.36b). When the external magnetic field is small (0.01 T), the magnetic moment in the FM bands is in-plane with poles at the edge of the film indicated by negative and positive notations (blue and

red) as shown in the figure 3.37a. In this figure, one can see that the left band (the left stripe) has a higher magnetic signal than the right band (the right stripe), meanwhile the in-between band has no net magnetic signal. It can be explained by the magnetic order of these bands, in which the left band is the FM state (mainly the bcc phase), the right band is the FM and PM states (the bcc and fcc phase) and the in-between one is the AFM state. This result also indicates that increasing Rh leads to increase in the fcc phase fraction (PM), which is in good agreement with previous results above (VSM, XRD).

In the left stripe in 3.37a, we can see that the top edge has a higher contrast than the bottom edge, which can be explained using negative and positive poles. The positive pole is assumed to be a higher contrast edge (the top edge), meanwhile the negative pole at the bottom edge has a lower contrast. When the OOP magnetic field increases up to 1 or 4 T, the magnetic moments are in the same direction as the external field as shown in figure 3.37b. In this case, poles at the sample surface close to the edges of the FM zone are negative, meanwhile the poles at the opposite position are positive (see Fig. 3.37b). Therefore, a lower contrast is observed around the edges of the FM bands.

Influence of applied temperature on the interface. *Experiment.* The sample was magnetically characterized using SHPM as a function of temperature between 150 K and 290 K. An applied in-plane magnetic field was 0.01 T (see Fig. 3.38). Upon cooling, two interfaces can be seen at a temperature of 290 K and they moved with temperature. Decreasing temperature, the left and right strips moved to the left and right hand side, respectively. While the right stripe disappeared below 270 K, the left stripe continued to move to the left hand side gradually and then it stopped below 150 K. On the heating process, the left stripe moved back towards the right hand side. However, the right stripe corresponding to the "A_2" interface did not move back.

Discussion. These SHPM results can be explained as follows. Because two stripes corresponds to the AFM and FM transition, two stripes changes with temperature. Decreasing temperature from 290 K to 150 K, the sample undergoes the FM to AFM transition. Hence, the left stripe moved to the left hand side gradually. While the right stripe moved to the right hand side and then disappeared below 270 K because of no stray field in the AFM state of Fe-Rh-Ni films. The left hand stripe is the Fe-rich side consisting of two phases of the pure FM phase at the left of the stripe (which has no first order transition) and the phase with the first order AFM-FM transition. Therefore, only the later part will transform between FM and AFM states under temperature or magnetic field. Below 150 K, the left stripe will not move because it is only the pure FM phase (without the AFM-FM transition). On the heating process, the left stripe moved back because of the AFM to FM transition. However the right stripe did not move back because of the transition temperature above 300 K, demonstrating a thermal hysteresis.

An average of the magnetic stray field probed in the measurement at 290 K is shown in figure 3.39b, in which the stray field is averaged along the y-axis (perpendicular to the dark to bright interface). Because no measurement was done at the left edge of the left stripe in the FM zone (the cut edge of the sample) corresponding to the negative pole,

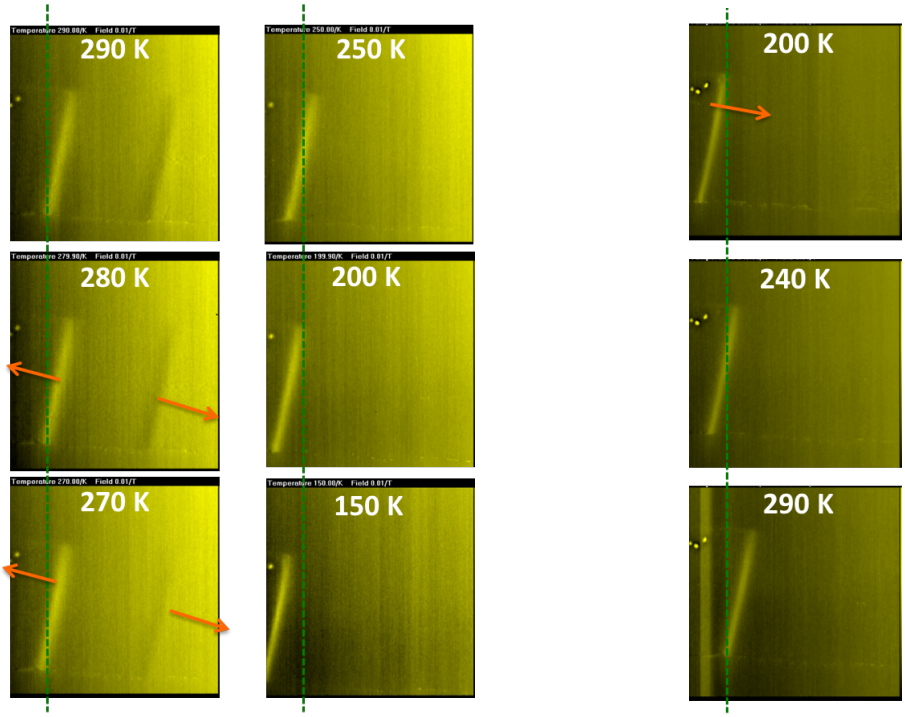

(a) On cooling side **(b)** On heating side

Figure 3.38. *SHPM images recorded stray fields of annealed* $(Fe\text{-}Ni)_{1\text{-}x}Rh_x$ *films as a function of temperature (a) on the cooling process, (b) on the heating process. The magnetic field of 0.01 T is in-plane to the sample surface and the size of the measured area is* $4 \times 4\,mm^2$. *The green lines are a guide to human eyes.*

the negative peak is not observed. Meanwhile, the positive peak is observed on the SHPM result clearly.

Figure 3.39b also shows both the negative and positive peak in the FM and PM zone (the bcc and fcc phase or the α" and γ phase), corresponding to the negative and positive pole with a lower magnitude than the positive peak in the FM zone. An appearance of the negative and positive peak closely as well as the lower magnitude implies a shortening of the FM zone, because of the increase of the gamma phase (the PM state) when the Rh content increases. As the gamma phase does not contribute to the magnitude of the magnetic stray field, the higher the gamma phase, the lower the magnitude of the magnetic signal indicated through a lower contrast. As a result, we observed a lower magnetic signal as well as a shorter distance between poles. We express the stray field $M_{\alpha"\text{-}\gamma}$ in this zone as follows: $M_{\alpha"\text{-}\gamma} = M_S(1 - x/x_0)$, where: x = 0 - the AFM/α"-γ edge (the left edge of the right stripe - the "A_2" interface), x_0 - the end of the α"-γ zone. A volume charge can be given as: $\rho = M_S/x_0$.

Model. Figure 3.39a shows magnetic moments and poles for the Fe-Rh-Ni films at 290 K with the 0.01 T in-plane magnetic field. The magnetic moment is parallel to the in-plane magnetic field and has the same direction from left to right. The stray field can be found at the pole close to the edge of the FM band in the left stripe, with the positive pole at

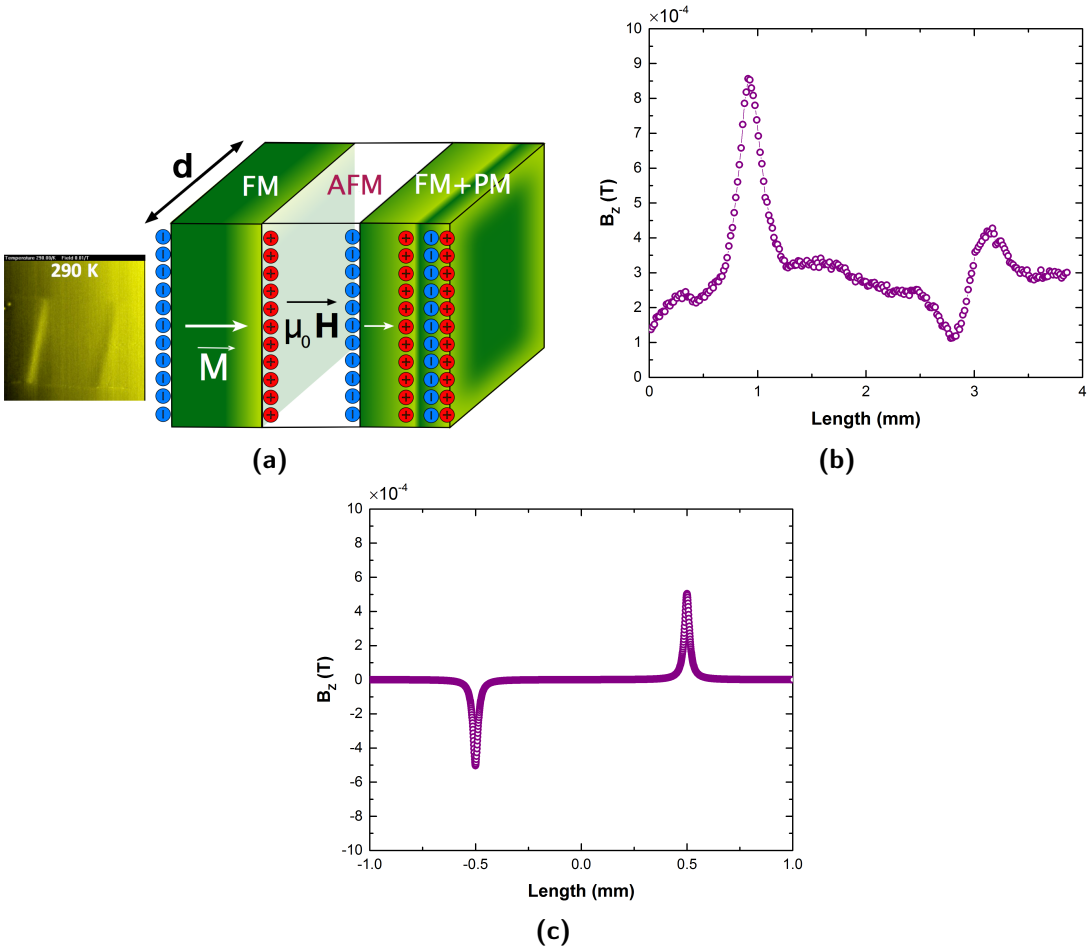

Figure 3.39. *(a) Magnetic moments and poles at 290 K with a 0.01 T in-plane magnetic field. The SHPM image at the left hand side is replotted from the figure 3.38a. (b) Stray field B_Z along the length of sample extracted from the figure 3.39a. (c) The calculation for the magnetic stray field along the length of the first FM zone. (d is the thickness of the film)*

the right edge. Hence, the right edge of the left stripe (the FM zone) has a higher contrast than others. Meanwhile the FM and PM zone (the right stripe) has a lower contrast than the left stripe.

Calculation. The magnetic stray field can be calculated using equations from (5) to (7) reported by Engel-Herbert et al in 2005 [108]. The calculation of the stray field in the 1 mm FM zone in the figure 3.39a is shown in figure 3.39c, assuming that the film thickness and the magnetic flux density are 250 nm and 1.5 T, respectively, and the Cartesian coordinate system is at the center of this FM zone. The calculation result shows an appearance of two peaks at the edges of the FM zone, in which the negative peak appears at the left edge (the cut edge of the sample) and the positive peak appears at the right edge of the FM zone (see Fig. 3.39a). This calculation result can be explained as follows.

The magnetic moment vector is in the same direction as the in-plane magnetic field, with negative and positive poles as shown in the figure 3.39a. From left to right of this left stripe, we encouter in turn the negative pole and the positive pole. When we encounter

the negative pole, a negative peak will be observed as shown in the calculation result (Fig. 3.39c). Meanwhile, a positive peak will be observed when we encounter the positive pole. As a result, two peaks in the calculation result correspond to the negative and positive pole close to the edges of the FM zone.

In brief conclusion, thank to Fe-Rh-Ni films with various transition temperatures, we proved the robustness of the optical transition in Fe-Rh-based systems. This phenomenon occurs on all our films including Fe-Rh, Fe-Rh-Pt and Fe-Rh-Ni. The SHPM on the Fe-Rh-Ni films to probe the AFM - FM transition is quite challenge. It requires Fe-Rh-Ni films with a special structure of FM/AFM/FM(+PM) with suitable transition temperatures to creat stray fields for the given SHPM set-up. Besides, a small signal scanned on a large size can leads to a change of contrast because of a change of the sensor-sample distance. The SHPM results support our conclusion that the "A_i" (i = 1, 2) interfaces correspond to the AFM-FM transition.

3.5.7 Studying the origin and the mechanism of transformation in FeRh alloys

Although many studies have been made to clarify the origin and mechanism of the first order AFM-FM transition in Fe-Rh alloys, this transition is still under debate in the scientific community. In order to explain the origin of this first order phase transition, at first an exchange-inversion model presented by Kittel in 1960 [109] was used. The idea of this model is that the interatomic distance determines the exchange energy. Then due to thermal expansion of the Fe-Rh lattice, there is a change in the sign of the Fe-Fe atoms exchange interaction at a critical value driving the first order AFM-FM transition.

Experiments by Kouvel in 1966 [19], Lommel in 1969 [110], Tu et al. in 1969 [111], McKinnon et al. in 1970 [21] and other studies (references therein - i.e. calculation by Zakharov et al. in 1964) evidenced a large difference between the total measured entropy change and the change in lattice entropy at the first order AFM-FM transition in Fe-Rh alloys. According to these studies, the model suggested by Kittel was at fault in the explanation for the first order transition in Fe-Rh alloys.

The work presented by Tu et al. (1969) also suggested that a change in the electronic band structure and thus in the electronic entropy was the main driving force for the transition. Later theoretical work by Koenig in 1982 [112] showed a large decrease of the total density of states at the AFM-FM transition in agreement with previous experimental results. Then Khan, Koenig and Riedinger in 1983 [107] predicted the dielectric constants in all three phases (AFM, FM and PM) but no experimental data existed to verify their calculation.

However, the model suggested by Tu et al. (1969) was contradicted in Fe-Rh-Ir alloys. Measuring the specific heat at low temperature $C_p = \gamma T$, in which γ is the electronic heat coefficient and is proportional to the density of electron states at the Fermi surface, showed an inverse relationship [113, 114]. Besides, the electronic heat coefficient of the AFM phase was too large to be attributed to the electronic specific heat alone. Fogarassy et al. in

1972 [114] also suspected there was a magnetic contribution to the specific heat.

Since the FM phase in stoichiometric $Fe_{50}Rh_{50}$ cannot be stabilized at low temperature, no measurement of the contributions could be extracted for the FM phase. However, specific heat was measured in iron rich alloys, with composion away from the AFM-FM range. This means that no direct measurements have been made on one sample and/or similar samples. The properties of Fe-Rh based systems are strongly sensitive to composition and there was a large deviation in the values for the AFM phase, so it was impossible to confirm the hypothesis from Tu et al. and other people.

The driving force for the first order transition in Fe-Rh based systems could consist of three competing contributions: lattice vibrations, magnetic and electronic contributions, as studied by Ricodeau et al. in 1972 [5] (figure 3.40).

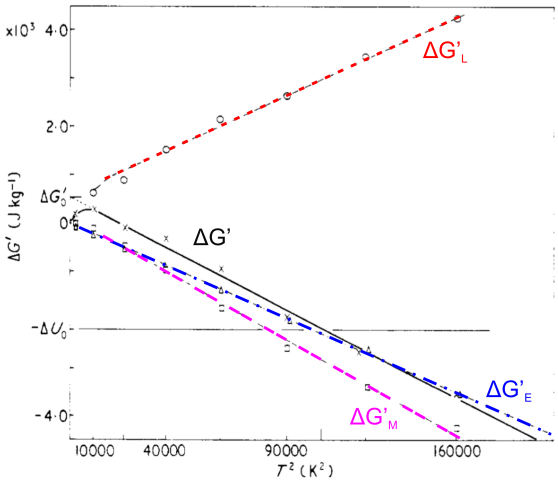

Figure 3.40. *The competing contributions of the lattice vibration $\triangle G'_L$, the electronic contribution $\triangle G'_E$ and the magnetic contribution $\triangle G'_M$ to the total driving force $\triangle G'$ as a function of temperature square in Fe-Rh alloys [5]. The influence of pressure or magnetic field will shift $\triangle G'$ vertically up or down, respectively, without changing the slope.*

Calculations from Ricodeau et al (1972) showed that the lattice vibration contribution to G increases with increasing temperature which means it prevents the AFM to FM phase transition. While the electronic and magnetic contributions to G decrease with increasing temperature which indicates a stabilization of the FM phase. They concluded nothing about the origin of the change in physical properties at the transition temperature, but they tried to point out in a comparison with experiments that this physical change may be due to the change of the electronic band structure which enables to explain the large change in elastic modulus and resistivity in Fe-Rh alloys.

The interpretation of this calculation result was also debated in the scientific community. One interpretation is that because the lattice vibration and electronic contributions are roughly equal and opposite in magnitude, these contributions will cancel each other out. Then the magnetic contribution is the primary driving force for the transition. Another interpretation is that the changes in lattice, electronic and magnetic energy are roughly equally important for the AFM-FM transition in Fe-Rh based systems.

The dielectric constants of Fe-Rh alloys have been measured by Chen and Lynch in 1988 [106] and Rhee and Lynch in 1995 [115] using ellipsometry. They concluded that the large change of the specific heat at the transition temperature was not from electronic contributions and can be attributed to a magnetic contribution. These ellipsometry results were not in agreement with previous experimental and theoretical works [5, 111, 107]. We summarized main points in results of the ellipsometry measurements by Chen, which are discussed in the previous part as follows: (1) No change was observed in the dielectric constants with a variation of temperature in all samples. Identical curves were observed between measurements at room temperature (the AFM state) and high temperature (the FM state). (2) The difference between the AFM, FM and PM states is the same order as the difference between samples. (3) A peak at $\sim 1.7\,\mathrm{eV}$ appeared in the spectra of both phases.

Moruzzi et al in 1992 [116] performed first principles band-structure calculations to study the volume dependence of the total energy for 3 possible magnetic configurations in the Fe-Rh system (FM, type I-AFM and type II-AFM). This theoretical result showed that the ground state of Fe-Rh alloys was the type II-AFM where both intra-plane and inter-plane coupling are antiferromagnetic. In a comparison to other studies of the DOS, the values for AFM and FM states from Moruzzi's work are 2.75 and 2.34 states/eV, respectively, those in Koenig's work [112] are 1.02 and 4.76 states/eV (theory), and in Tu's work [111] are 1.08 and 4.04 states/eV (experiment). Although Moruzzi's calculation for the total DOS at the Fermi energy was in contrast to Koenig's result, this calculation was consistent with Chen's conclusion (1988) in term of the less affected electronic contribution.

Recently, Cooke et al in 2012 [117] measured specific heat on 200 nm $Fe_{52}Rh_{48}$ (Fe rich-FM phase) and $Fe_{50.5}Rh_{49.5}$ (AFM phase) films in the temperature range between 2 and 380 K (previous studies carried out at lower temperatures) and tried to get the lattice, electronic, magnetic contributions separately. The data indicate that lattice vibrations stabilize the AFM phase, the electronic contribution is small, and they proposed that magnetic fluctuations play the largest role in driving the transition. The negative sign on the lattice contribution in their data was consistent with the calculation of Ricodeau et al (1972), but the electronic contribution is much smaller than the lattice and magnetic contributions, in contrast to Ricodeau's calculation. The peak in the heat capacity occurs at lower temperature ($\sim 100\,\mathrm{K}$) than in the prediction of the magnetic fluctuation models proposed for the phase transition in Fe-Rh based systems before [118, 119].

Gruner et al in 2003 [118] extended the study of Moruzzi and Marcus using Monte Carlo simulations of an Ising model and proposed that the nature of the Rh moment in each magnetic state is the origin of the phase transition which has a moment of 0 or $1\,\mu_B$. This moment is 0 in the AFM state or $1\,\mu_B$ in the FM state which induces a larger entropy in the FM state. Their model predicted a peak of the specific heat at $\sim 200\,\mathrm{K}$ in the FM state. However, the magnitude of the free energy change in their model was too small to compensate for the internal energy loss for the phase transition occurrence which was indicated through the small difference between the low temperature specific heat of both

phases.

Gruner et al (2003) treated both Fe and Rh moments as Ising one dimensional spins, meanwhile Gu and Antropov in 2005 treated both Fe and Rh moments as Heisenberg-type 3D vectors in their DFT calculations [119] and suggested that the phase transition in FeRh occurs because of magnon excitations. Their result predicted a peak of the specific heat difference between FM and AFM phases around $\sim 300\,\mathrm{K}$.

Later in 2011, Sandratskii and Mavropoulos performed a DFT calculation and suggested that noncollinear magnetic excitations and Fe-Rh hybridization are important factors to understand the origin of the phase transition in Fe-Rh-based systems.

Origin of the discrepancy. The divergence among experiments and calculations was explained by some authors. Chen et al. (1988) (and reference therein) explained that the measurements were never made on FeRh alloys which had identical compositions while the properties are strongly sensitive to composition. This explanation is similar to the previous one from Fogarassy et al. (1972) and later in 1992 by Moruzzi et al.. They interpreted the divergence between their results and others to be due to the compositional differences.

In summary, despite over 80 years and many studies, the origin and mechanism of the first order transition in Fe-Rh-based systems is still under debate. Based on the published studies in literature, we can summarize the present models about the main driving force in the phase transition: (1) the lattice vibrations are not at the origin of the transformation, (2) the electronic contribution is the main force, (3) both the electronic and magnetic contributions contribute to the transformation (but it is not clear about the weight of each contribution), (4) the magnetic contribution is the main force in driving the phase transition. However, there is a common point that sample-to-sample variations coupled with the strong dependence of properties on composition are considered as the reason for the divergence between studies. Thus, the combinatorial approach to material preparation with only one deposition on one wafer, same annealing conditions and the desired compositional range is a good solution for this matter.

Contribution of thesis. Recent models consider that the magnetic change is the main contribution to transformation, but it is difficult to explain the large change in elastic modulus and resistivity. In the previous part, we discover that a strong optical change at the transition temperature, which reflects the change in DOS when the transformation occurs.

As mentioned above, a large decrease of the total density of states at the AFM-FM transition was reported in agreement with experiment results by Koenig (1982) [112]. In the further step, Khan, Koenig and Riedinger (1983) [107] predicted the dielectric constants in phases of AFM, FM and PM. However, the verification using the ellipsometry measurement by Chen (1988) [106] did not show an agreement. In contradiction to the Chen's publication, we found a difference in the optical properties in the infrared range between FM and AFM phases which implies a difference in the DOS.

Thank to the combinatorial approach, compositionally graded Fe-Rh films show a clearly optical transition. We prove that the optical transition originates from the FM-AFM first

order transition using a variation of measurement methods consisting of VSM, XRD, EDX, the optical measurement, ellipsometry, SHPM. Not only does the optical transition appears in FeRh films, but also in ternary films such as Fe-Rh-Pt, Fe-Rh-Ni. Besides that, our ellipsometry measurements show an quanlitative good agreement with theoretical work by Khan et al. (1983). It implies a difference in DOS between the FM and AFM states. Nevertheless, our observation is still early for an understanding of the transformation origin, more experiment and theoretical work are needed. We have no conclusion about the main driving force for the origin of the transformation in FeRh-based systems, however, the discovery of the strong optical transition support the idea of a large negligible electronic contribution to the transition.

3.6 Chapter summary

In summary, compositionally graded Fe-Rh-based films were prepared using magnetron sputtering. The effects of the annealing conditions, temperature, magnetic field and elemental substitution on the magnetostructural transformation of Fe-Rh-based systems were studied. According to various measurements, high quality films with a quasi-complete first order AFM -FM transition were obtained. The combinatorial approach was used to obtain the desired AFM phase which only exists over a narrow composition range. These results show that this combinatorial method is a good way to get the high quality Fe-Rh films without some disadvantages such as a requirement of the optimal procedure, and the fabrication of series of samples. The annealed films also evidenced an optical transition which corresponds to the AFM-FM transition. The appearance of the optical transition due to the AFM-FM transition was not previously detected in the literature and proves the electronic contribution to the phase transformation and cannot be neglected in the study of the transformation origin for Fe-Rh-based systems. The optical contrast can also be used to detect quickly the phase transition without using other complicated methods (i.e. VSM SQUID, transport measurements) and it allows us to determine carefully the phase diagram close to the equi-atomic composition, with greater details that existing litterature.

Having succeeded in producing Fe-Rh films with a well defined transition, these films can serve as model systems to explore the strain control of phase change in the magnetocaloric material through a combination with a piezoelectric substrate. The experimental study of strain-induced effects in FeRh will be discussed in the next chapter.

CHAPTER 4

Strain control of the phase change in Fe-Rh films

4.1 Introduction

The investigation of the electrical control of magnetic properties is of interest for fundamental physics and applications. A series of studies has been reported either in homogeneous multiferroic materials (single phase materials) or in composite materials (hybrid systems). In recent years, the intrinsic magnetic properties such as the Curie temperature, magnetization, anisotropy, spin polarization value but also more complex processes such as magnetization reversal have been modulated by an electric field either in a reversible fashion or in a nonvolatile way [56, 60, 55, 120, 121, 122]. Since this thesis started, the electrical-induced-magnetic phase transition on the heterostructure of $BaTiO_3$/FeRh was reported , in which a voltage of 21 V shifted the transition temperture by 25 K [9].

The Fe-Rh-based system with first order AFM-FM transition has attracted the attention of the scientific community for the last 80 years. A first order transition temperature close to room temperature, a big change in resistivity at the critical temperature, a highly magnetocaloric effect together with a simple crystal structure are some outstanding properties of Fe-Rh. The complex task of fabrication to achieve an AFM phase of the Fe-Rh material has been addressed in this thesis using the combinatorial approach presented in chapter 3. We chose such Fe-Rh films as a model system to study the phase change as a function of strain. Because of the high quality and large strain of PMN-PT piezoelectric crystals, this ferroelectric relaxor single crystal was chosen as the active substrate to transfer strain to the magnetic layer in order to explore the strain-tuned phase change.

In this chapter, we explore the strain-induced phase change of Fe-Rh films under the electric field. Nickel based hybrid structures were used as test structures to validate the developed set-ups. The advantages of Nickel are that it is a well-known material, a prototype of 3d ferromagnetism. It has a Curie temperature above room temperature which facilitates characteristisation, and has a rather large magnetization and magnetostriction at RT. Besides, its magnetoelastic properties are also well-known at room temperature. Measurement of strain-induced easy-axis reorientation in a PZT/Glass/Ni hybrid structure are presented in appendix A. This work demonstrates strain control of the anisotropy field of Ni in the hybrid structure which is changed by 54 mT with an electric field of 17.8 kV/cm. Finally, strain control of the magnetic coercive field H_c in a ultra thin film Co ($\sim$ 0.8 nm)

was also studied, and is reported in appendix B.

4.2 Sample preparation and characterization

4.2.1 Characterization of the piezoelectric substrate

The PMN-PT substrates we used in this study are commercial (001) oriented PMN-0.3PT single crystals from TRS Technologies, Inc.. The $10\times10\times0.3\,\mathrm{mm}^3$ crystals were bought in the as-cut state, with electrodes of Cr/Au deposited onto both sides (Fig. 4.4b). In order to characterize the PMN-PT substrate, XRD patterns, ferroelectric hysteresis loops and strain behavior were measured. Figure 4.1a shows the XRD pattern of an as-received PMN-PT single crystal. The sample exhibits a high intensity diffraction line with an (001) orientation. Assuming that the crystal structure of PMN-0.3PT is rhombohedral, the latice parameter is estimated about 4.025 Å which is consistent with literature (Noheda et al. in 2002 [49]). The diffracted peaks of the Au electrode are also seen on this diffraction graph.

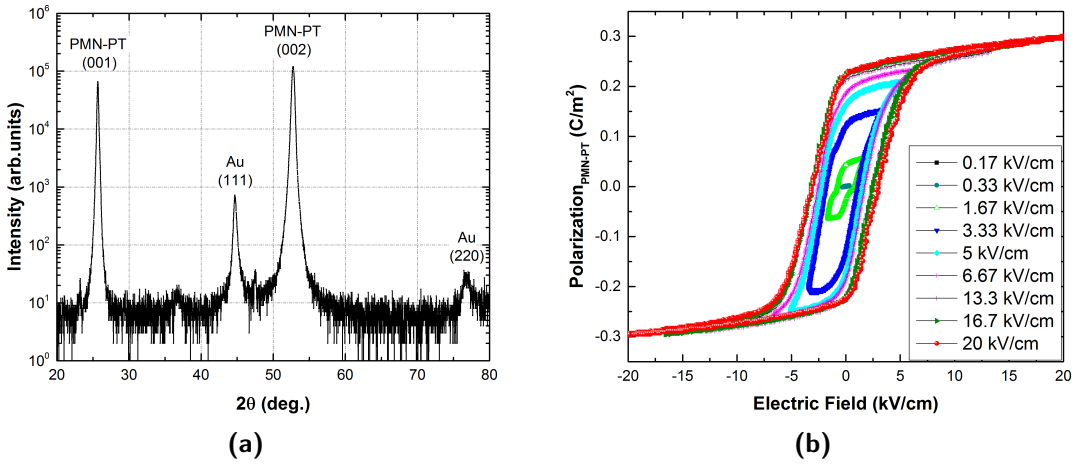

Figure 4.1. *Characterization of the as-received PMN-PT single crystal substrate (a) XRD (X radiation), (b) P(E) loops at various maximum electric fields at the frequency of 5 Hz.*

Properties of the piezoelectric substrate such as the P(E) loop, the coercive electric field E_C and the saturation polarization P_S have been characterized using our Sawyer - Tower ferroelectric set-up described in Chapter 2. Figure 4.1b shows the ferroelectric hysteresis loops of the PMN-PT substrate which have been measured at various maximum electric fields (see legends in this figure). When the the electric field (E-field) is small (below 0.17 kV/cm), the P(E) loop is linear. Increasing the electric field, the loop is expanded, non-linear and becomes hysteresic. This is explained as follows. When the external electric field is applied, domains more favorably aligned with the field grow and the polarization of the ferroelectric material increases. If the field is small, it is not large enough to align or switch all dipole moments. When the electric field is large enough, dipoles align with the field and the polarization reaches the saturated state. The coercive field E_C and the saturation polarization P_S are about 2.86 kV/cm and $\sim 0.29\,\mathrm{C/m}^2$ ($29\,\mu\mathrm{C/cm}^2$), respectively, which are in good agreement with the datasheet from the company ($E_C \sim 1.8$ - 3.2 kV/cm; P_S

$\sim$ 26 - 30 μC/cm^2). One can see the hysteresis loops are only slightly changed when the applied maximum field increases from 16 kV/cm to 20 kV/cm. This means that a 500 V limit across the 0.3 mm thickness ($\sim$ 16.7 kV/cm) can be set for the next experiment to avoid crack formation and reducing leakage current, while maintaining the characteristic properties of the sample.

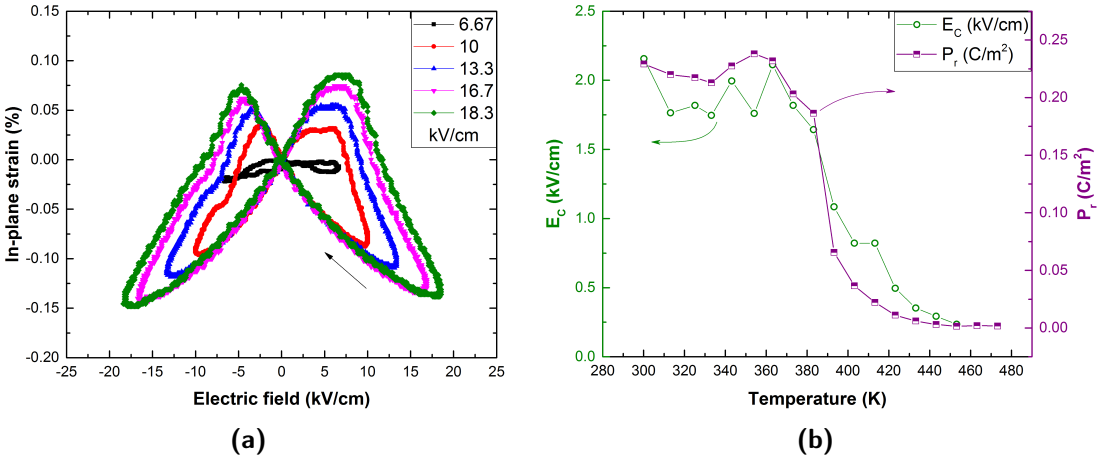

Figure 4.2. *(a) The strain of the PMN-PT substrate exhibits the butterfly behavior under bipolar electric fields at room temperature. (b) The temperature dependence of the coercive field and the remanent polarization of the PMN-PT substrate.*

Because PMN-PT is used as the piezoelectric substrate in the multiferroic composite, in order to investigate the strain-induced modifications of the magnetic film, its strain behavior under electric field S(E) is an important parameter. It was characterized using an aluminum strain gauge glued on the surface of PMN-PT. Figure 4.2a shows the in-plane strain of PMN-PT at various maximum bipolar electric fields. One can see that the strain exhibits a butterfly behavior which is typical of piezoelectric materials due to polarization switching, as presented in Chapter 1. When the electric field is small, the curves are asymmetric. The curves become more symmetric when the electric field increases. The measured in-plane strain of our PMN-PT is quite large, up to $\sim$ -0.15 % at the maximum electric field of 18.3 kV/cm, which is consistent with values in literature [60]. A negative strain means that the in-plane strain is compressive. Suppose that the strain created by the applied electric field is linear before the polarization switching occurs, we can have a relationship between strain and E-field of $\sim$ 0.01 %/(kV/cm) (this slope was calculated using the green curve at the maximum electric field of 18.3 kV/cm in figure 4.2a). Characterization of the properties of PMN-PT indicates that the PMN-PT crystals used here are of high quality. It also validates our P(E) and S(E) set-ups.

In order to investigate the strain-induced phase change in Fe-Rh films, transport measurements, in which the resistance is measured as a function of temperature at various E-fields, is used. Hence, characterization of PMN-PT substrates at different temperatures was carried out. Figure 4.3 shows the temperature dependence of the P(E) curve at a maximum E-field of 13.3 kV/cm. One can see that this dependence is non-linear. The coercive field

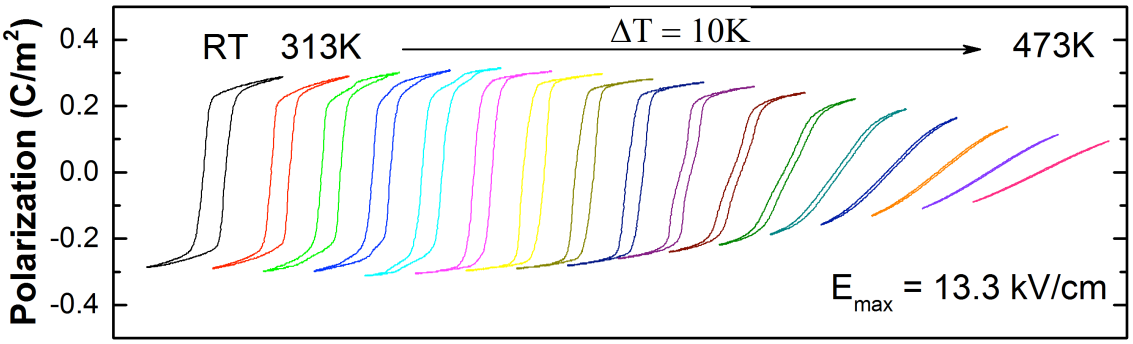

Figure 4.3. *The polarization as a function of electric field at various temperatures in the PMN-PT substrate. The P(E) curves are measured at a maximum E-field of 13.3 kV/cm from room temperature to 473 K with a step of 10 K.*

and the remanent polarization against temperature extracted from the P(E) curves are plotted in figure 4.2b. It is found that E_C and P_r slightly change with temperature below 380 K and then a big drop occurs. The transition from a ferroelectric state to a paraelectric state happens between 393 and 428 K, which is consistent with literature [123, 124].

Having sourced good piezoelectric crystals, a polishing process was required to use them as substrates for thin film deposition (see Fig. 4.4b). The following sections will describe substrate preparation and deposition of the Fe-Rh films on the prepared PMN-PT substrates.

4.2.2 The heterostructure sample preparation

4.2.2.1 Substrate preparation

The PMN-PT substrates used as the piezoelectric substrate to grow films of Fe-Rh, were polished before film deposition. It should be noted that the polishing process may reveal ferroelectric domain structures which is interesting for the study of the strain-induced phase change either in the piezoelectric material or the magnetic material. Reaching an optical quality after polishing allows the use of polarised microscopy to study ferroelectric domains. The birefringence property of ferroelectric domains is used.

Various tools have been used in the polishing process. These tools include a polishing machine (Mecatech 234 from PRESI Metallography), a variety of grit papers and suspensions/colloids together with the corresponding clothes, an optical microscope equipped with a polarizer and an atomic force microscope to measure the surface topography. The polishing process included three steps: a preliminary polishing, a base polishing and a relief polishing, as now described in detail.

The as-cut substrate is firstly stuck onto a sample holder with a crystal bonding glue and undergoes a preliminary polishing. A graded series of grit papers has been used in this step, beginning with papers with 15 μm grit then with 10 μm and 5 μm. Because the material is fragile and the as-received sample is quite rough, the rotation of the head and the plate are initially at a slow speed and then this speed is increased. The graded

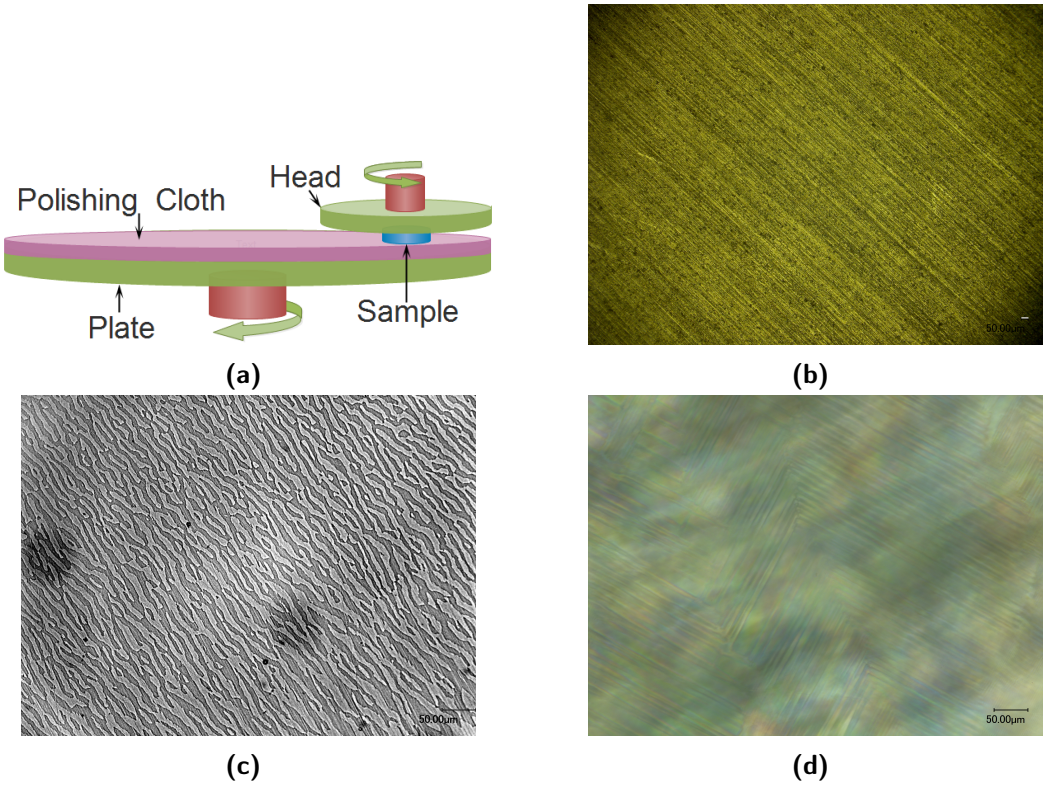

Figure 4.4. *(a) Schematic diagram of the polishing machine. The suspension solution is distributed on top of the polishing cloth. (b) Optical image of the as-received sample. (c) and (d) Polarised optical images of various domain structures of PMN-PT after polishing. Sample on the figure (d) was polished for a longer time than the one in figure (c).*

increase of speed is also used at all steps when changing the grit size where the roughness of material is greater than the size of grit or colloid, in order to avoid cracks.

Afterward, the polishing process continues using a 3 μm polycrystalline diamond solution, finishing with a 1 μm polycrystalline diamond solution. The diamond abrasive solutions of Metadi 3 μm and 1 μm suspension are products of Buehler. After this base polishing, samples are optically transparent and display fairly smooth surfaces, which are optically flat. The ferroelectric domain structure of the sample can be observed after this step.

In the last step, samples are polished using a 250 nm diamond abrasive solution and finally with a 50 nm polycrystalline suspension of either diamond or colloidal silica. The diamond abrasive solutions of 250 nm and 50 nm suspensions are products of Buehler (named Metadi), while the 50 nm colloidal silica solutions are from either Logitech Ltd. (SF1) or ESCIL (REF SS25). In all steps, the head rotation is always in the opposite direction to the plate rotation and the applied force to the sample is 0.01 daN. A combination of the rotation speed of the head and plate is tested from 50 to 600 rpm with steps of 50 in order to get an optimal speed. Below 300 rpm, we did not get a reasonably smooth surface which may be due to insufficient polishing time in the experiments. The optimal speed of head and plate were found to be around 350 - 400 rpm. Using this speed, a smooth surface was reached in a short time. Above 450 rpm, micro-scratches are detected on the

surface, which can be attributed to dust in the air or the loss of the polishing solution on the cloth due to the high speed. For the choice of the 50 nm suspension solution, a smooth surface can be achieved with the diamond oil solution as well as the colloidal silica solution. However, crystallization of the solution containing the colloidal silica suspension during the polishing process may cause micro-scratches on the sample surface which we encountered. To remove these scratches, the base polishing step is repeated. Therefore, the polycrystal diamond suspension solution was selected for the relief polishing process.

After polishing, the sample is optically transparent, smooth and reveals various domains (see Fig. 4.4c, 4.4d). Because the hardness in differently oriented/polarized grains/domains can be different, the abrasion rate will be sightly different which can lead to a match between the surface topography and the domain structure. Although the influence of the polishing process on the observation of ferroelectric domain and the surface topography is interesting, it is not the focus of this work, so the interaction between the polishing process, ferroelectric domain and the topography was not studied in more detail. As an important result of the polishing process, the surface roughness (root mean square) was estimated to be 18 nm, as measured with an atomic force microscope.

4.2.2.2 Film preparation

Having succeeded in producing Fe-Rh films on standard silicon substrates showing the desired first order transition through the combinatorial approach, we deposited such films on polishing PMN-PT substrates to explore magneto-elastic effects. The preparation of Fe-Rh films on PMN-PT substrates is similar to that on silicon substrates, for which we used the magnetron sputtering and a post-annealing treatment. In the previous chapter, in order to study compositionally graded films, Fe-Rh films were deposited on a 2" or 3" Silicon wafer in which the film composition was varied linearly across the substrate in the range 36 - 60 at % Rh. However, only the film showing a well defined transition is interesting for the strain-mediated tuning of the phase change. Hence, a polished PMN-PT substrate with a much smaller size of $3\times3\,\mathrm{mm}^2$ was placed where the first order transition was achieved on Silicon wafers. The structure of the composite is PMN-PT/Ta 10 nm/FeRh/Ta 1 nm. The thickness and magnetic properties of the Fe-Rh film will be described in the following section.

4.2.3 Characterization of the magnetic film

Thickness and composition. The thickness of the Fe-Rh film on the PMN-PT substrate is about 220 nm ± 30 nm, measured by FESEM. EDX analysis was used to estimate the composition of Fe-Rh films on the $\sim 3\times3\,\mathrm{mm}^2$ PMN-PT substrate. The result shows that the Fe-Rh film composition at the middle of the substrate is near-equiatomic, as expected. Hence, we expect to get a well defined transition from the AFM state to a FM state.

Magnetic properties. Magnetization as a function of temperature was measured on an annealed sample, in a magnetic field of 0.05 T using a VSM-SQUID. Figure 4.5a shows the M(T) curve measured in the virgin state of the PMN-PT substrate immediately

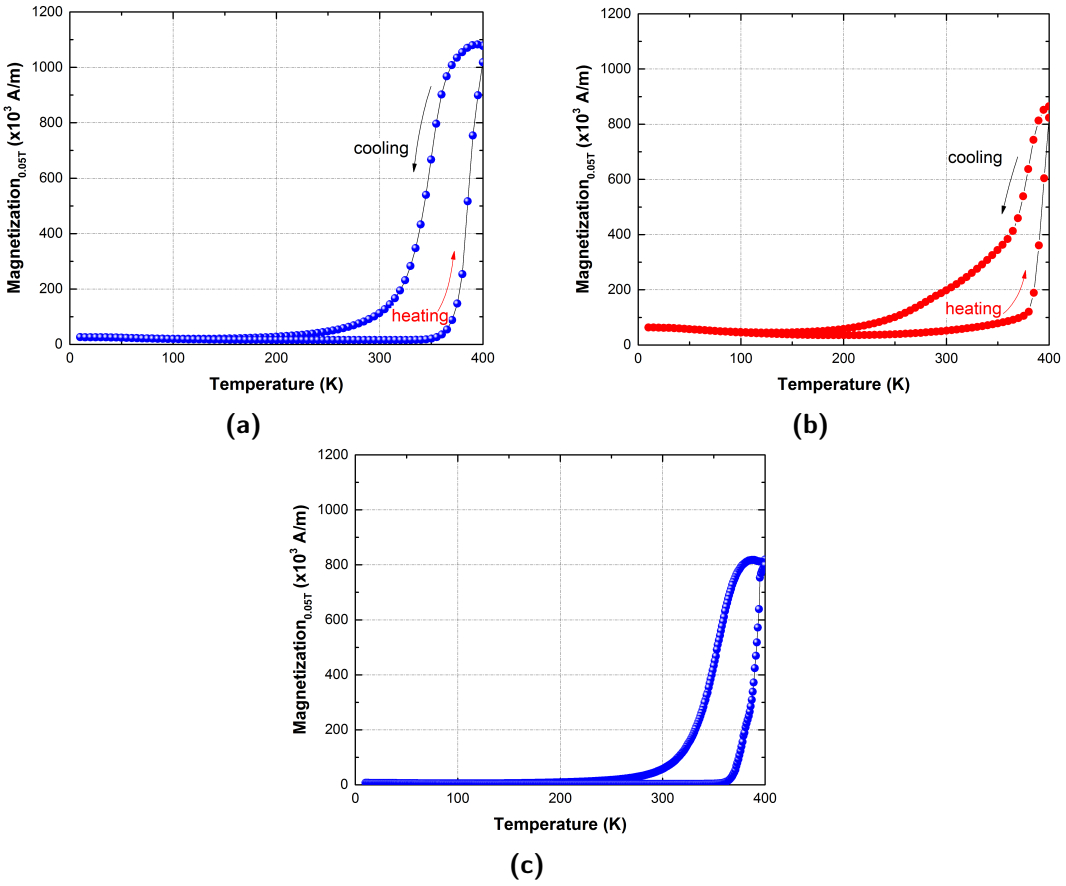

Figure 4.5. *The temperature dependence of magnetization in a PMN-PT/Ta/FeRh/Ta heterostructure in an applied magnetic field of $\mu_0 H_{app}$ = 0.05 T with the Rh content graded from (a) 49.8 - 51.8 % ±1.5 % (sample #1), (b) 48.9 - 49.8 % ±1.5 %. (c) sample #2 - a reproduction of the heterostructure.*

after annealing at 923 K (650°C). The polarization of the substrate is reset using such an annealing temperature (the Curie temperature of PMN-PT ∼ 398 - 428 K). One can see that a relatively sharp transition from the AFM to the FM state occured on heating, with a very low value of magnetization measured at room temperature (see Fig. 4.5a). The transformation is incomplete at room termperature on the cooling cycle. Such thermal hysteresis is expected for Fe-Rh films. It is found that Fe-Rh films on PMN-PT substrates show the first order transition with $T_{t\text{-cooling}} \sim 350$ K, $T_{t\text{-heating}} \sim 385$ K and a hysteresis width ∼ 35 K (see Fig. 4.5a). The low value of magnetization measured at low temperature, corresponding to ∼ 2 % of the maximum magnetization measured at high temperature can be attributed to the spread in composition over the film, resulting in the presence of a small amount of FM phase. This FeRh sample will hereafter be referred to as sample #1.

Another measurement made on a neighbouring piece of sample #1, which is Fe-richer than sample #1, shows a higher amount of FM phase, i.e. a larger magnetisation at low temperature (see Fig. 4.5b). The curve in figure 4.5b is similar to the red curve of graded Fe-Rh films on a Silicon substrate (see Fig. 3.7b). While the top part of this curve shows a sharp transition with a narrow hysteresis width, the lower part exhibits a

broader transition. In this magnetization measurement, the transition was not complete at the applied maximum temperature of 400 K. The first order transition temperature of Fe-Rh films on (001) PMN-PT substrate is higher than in films deposited on silicon. Another PMN-PT/FeRh sample, hereafter referred to as sample #2, was produced with the PMN-PT substrate positioned on the sputtering system sample holder very close to where sample #1 had been placed. A well defined transiton from AFM to FM, with transition characteristics comparable to those of sample #1 was measured (figure 4.5c). The value of the magnetisation measured at low temperature is less than that of sample #1.

In brief, the heterostructure shows a well defined transition which is desired for investigating the electrical control of phase change. In addition, the ability to reproduce the heterostructure is also obtained.

4.3 Influence of substrate on the transition temperature

It is found that the transition temperature of the Fe-Rh films grown on PMN-PT substrates is higher than that on silicon substrates, treated to the same annealing conditions. The increase of the first order transition temperature in the composite PMN-PT/Ta/Fe-Rh/Ta films may be caused either by substrate-induced strain (in-built strain) or composition variation. Additionally, defects and imperfections in the Fe-Rh films will also affect the transition. In this part, we will discuss each possible reason.

Defects. Defects and imperfections in Fe-Rh films destroy the AFM phase, thus stablize the FM phase, which causes a decrease in the transition temperature and an increase of the thermal hysteresis width. Since the transition temperature in the composite structure increases and the thermal hysteresis width is reduced, we deduce that defects and imperfections are not at the origin of the modification in transition characteristic.

Composition difference. Fe-Rh films are strongly sensitive to composition with the optimal (critical) composition, being defined as the composition for which the transition temperature is maximum (see our Fe-Rh-Pt phase diagram in figure 3.31a). The existence of a peak in transition temperature can be used to explain the higher transition temperature of the Fe-richer side sample in figure 4.5b than the sample shown in figure 4.5a, which is poorer in Fe.

A growth-induced strain (the in-built strain). The clamping effect of a thin film deposited on a substrate is similar to the influence of pressure. In literature, Maat et al studied the influence of substrate on the transition temperature of 110 nm Fe-Rh films grown onto MgO (001) and Al_2O_3 (0001) using a sputtering method [20]. They reported that Fe-Rh films on MgO were compressed in-plane and expanded out-of-plane, while out-of-plane compression and in-plane expansion was found with Al_2O_3 substrates. When Fe-Rh undergoes an AFM to FM transition, it also experiences a 1 % volume increase. In the tetragonal distortion of MgO/FeRh, the transition temperature was increased due to in-plane compressive strain. On the other hand, in-plane expansion of Fe-Rh deposited on an Al_2O_3 substrate stablizes the ferromagnetic phase, resulting in a reduction of the

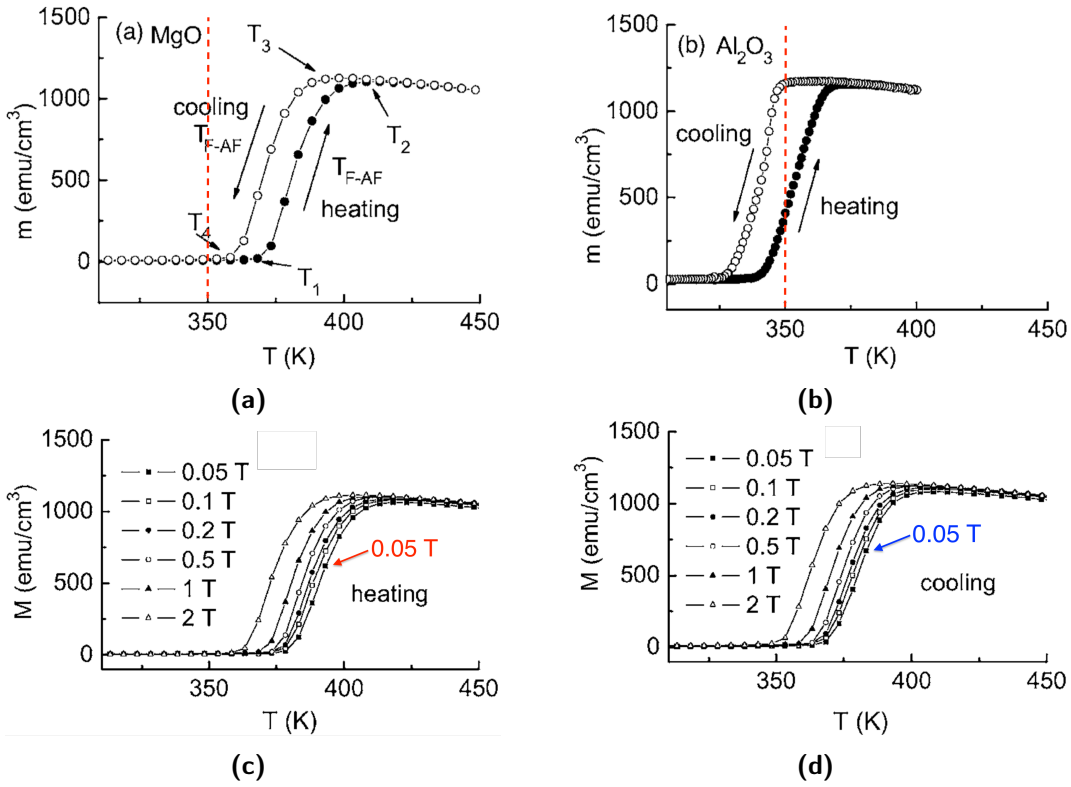

Figure 4.6. *Magnetization characterization of 110 nm FeRh films grown onto (a) the (001) MgO and (b) the Al_2O_3 (0001) subtrate at an applied magnetic field of $\mu_0 H_{app} = 1$ T. The magnetization curves M-T at various magnetic fields for MgO/FeRh in the heating side (c) and in the cooling side (d). (Images adapted from [20]. The red lines and texts were added).*

transition temperature (see Figure 4.6a, 4.6b).

It was also reported in literature that the [100] axis of the bcc cube of FeRh-Ga was rotated by 45° with respect to the [100] axis of the $BaTiO_3$ substrate, in composite $BaTiO_3$/FeRh-Ga samples [125]. The latice parameters of $BaTiO_3$ in the cubic phase is 4.01 Å , which is close to the value of PMN-PT (4.02 Å), which suggests a similar behavior for Fe-Rh films (2.986 Å) deposited on PMN-PT. In this case, grains of Fe-Rh films can be distorted tetragonally where the c-axis of a unit cell will be stretched, while the a and b-axes will be compressed. This can lead to an increase of the transition temperature and a reduction of the hysteresis loop.

The thickness of Fe-Rh films grown on (001) PMN-PT substrates in this thesis is about 220 nm which is twice thicker than the films grown on MgO substrate discussed above. When the thickness is increased, the film are more likely to be relaxed. It becomes energetically favorable for a misfit dislocation to develop at the interface substrate/film in order to reduce the stress, resulting in a mitigation in the strain or relaxing epitaxy strain. This will lead to a smaller influence of the misfit strain on the transition temperature, which means that the transition temperature should have a smaller change than in literature.

On the contrary, the transition temperature in the PMN-PT/Ta/FeRh/Ta heterostructure is of the same order or even higher, as shown in figure of 4.5. To really compare to

literature, the complete growth process has to be taken into account. Fe-Rh films in this thesis were deposited onto (001) PMN-PT substrates at room temperature, then films have undergone a post deposition annealing process. Therefore, an epitaxial relation between the film and the substrate is not expected. Moreover the post-deposition high temperature annealing induces 3D grain growth and relaxation of the deposition stresses.

The existence of strain in Fe-Rh films on PMN-PT can be due to the cooling process after annealing at high temperature. Although the temperature dependence of the thermal expansion coefficient in PMN-PT is non-linear [126], its value is similar to the one of Fe-Rh materials (5 - 10×10^{-6} /K) at high temperature [89, 24]. However, during cooling down, PMN-PT will experience a large crystallographic transformation(cubic to tetragonal distorsion at T_C, and tetragonal to rhombohedral at ∼358 K). Hence, a large strain in Fe-Rh films can be created during the cooling process. The strain will depend on the polarisation state of PMN-PT in the ferroelectric state. For unpoled PMN-PT, two axes contract and the c axis become longer in the low temperature phase. For (001) cut, decreasing the temperature through T_C induces an in-plane compression strain on PMN-PT.

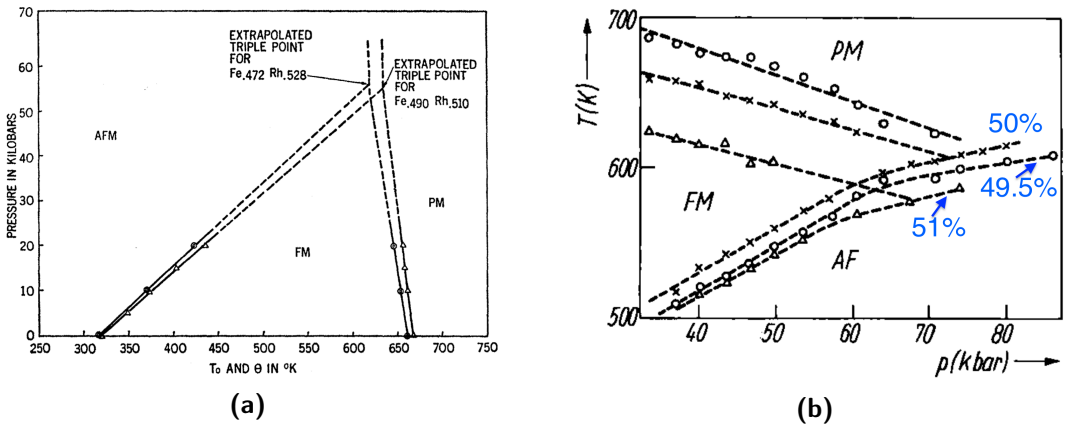

Figure 4.7. *The magnetic phase diagram of Fe-Rh versus pressure. (a) The pressure dependence of the first order transition temperature T_0 and the Curie temperature θ for the 51 and 52.8 % Rh samples in a pressure range from 0 to ∼20 kbar. Notations of T_0 and θ in this figure are called T_t and T_C in this thesis, respectively. (Image taken from* [23]*). (b) The relationship between the Rh content, the critical temperature and the pressure in a temperature range from ∼35 to ∼83 kbar. (Image taken from [25], the blue texts were added for a guide to the eye).*

Moreover, the composition dependence of dT_t/dP (the change of the transition temperature with hydrostatic pressure - an isotropic strain) can also affect the transition temperature. Wayne in 1968 [23] reported the composition dependence of the sensitivity of critical temperatures with pressure (see Fig. 4.7a). Figure 4.7a shows that the 51 % Rh sample has a higher change in the critical temperature against the applied pressure ($\partial T_t/\partial P$ and $\partial T_C/\partial P$) than the 52.8 % Rh sample. Besides, we can see that at ∼ 50 kbar, the AFM state switches to the PM state directly (without an intermediate FM state). Because the volume of the AFM cell is smaller than the FM cell, pressure effect can be

directly related to the volume change, i.e. stablizing the smaller cell (AFM).

It is known that the easy-axis orientation is coupled to strain. Above room temperature, within the AFM phase, a huge volume magnetostrictive constant $\sim 8.2{\cdot}10^{-3}$ was reported in Fe-Rh alloys [89]. This suggests the easy-axis reorientation of Fe-Rh films on PMN-PT substrates. However, more experiments and calculations are needed to clarify this matter.

In brief, the change of transition temperature in the PMN-PT/Ta/FeRh/Ta composite structure compared to films on Silicon is attributed to contributions of the inbuilt substrate strain and sensitivity of strain to composition. Nevertheless, other contributions such as defects may have a small influence, as discussed above. Although using a substrate can change the transition temperature in Fe-Rh films, it is difficult to know the magnitude of the inbuilt strain, because the reference lattice parameters are not known. Normally, an assumption, where the lattice parameters of films are assumed to be the same as in bulk, must be performed. In addition, an in-built strain is not easy to control and modify. Hence, an active strain which can be controlled using an electric field, is more interesting. In the following, we will investigate control of the transition temperature in PMN-PT/Ta/Fe-Rh/Ta films, through the E-field-induced strain.

4.4 Influence of controllable strain on Fe-Rh films

Hydrostatic pressure (isotropic strain) influences the transition temperature of Fe-Rh alloys. The transition temperature was increased (a stablization of the AFM state) because of compressive stress induced by isotropic strain (see chapter 1). While the FM phase was stablized under a tensile strain, which leads to a decrease of T_t [26]. In the composite structure of PMN-PT/Ta/FeRh/Ta, the E-field-induced strain is different. The strain in the Fe-Rh film induced by the substrate (E-field-induced strain) is anisotropic, in which the in-plane direction is stressed and the out-of-plane one is free to relax (no stress). As a result, the response of the Fe-Rh film in the anisotropic case could be different from the isotropic one which was reported in literature. Moreover, E-field-induced strain can be either expansive (tensile) or compressive depending on the magnitude and direction of E-field with E_C and the polarization of the substrate, which can be controlled. Therefore, a study of the anisotropy strain-induced transition temperature is needed to explore this matter.

The influence of strain on the phase change in Fe-Rh films, under the application of an electric field to the piezoelectric substrate was monitored using the transport set-up described in Chapter 2. The gold layer on the bottom side and the film on the top side play the role of electrodes to apply the electric field to the substrate. Four contacts for the transport measurement were made by glueing 50 μm silver wires to the sample surface using epoxy. While the schematic of the transport measurement was shown in figure 2.7b, the sample with four contacts is schematised in figure 4.8a. The influence of strain on electrical transport and the phase change will now be described.

4.4.1 Strain control of resistance

Transport measurement versa an applied electric field. Transport measurements, R(T), in which resistance or resistivity are measured as a function of temperature, have been carried out from 220 K to 405 K with a step of 5 K. An electric field has been applied to the PMN-PT substrate in the out-of-plane direction to study the strain-induced change of the electrical properties of the Fe-Rh films. Despite the high quality of the PMN-PT substrate, it was reported in literature that a small leakage current of about 0.3 - 0.5 μA was observed around the electrical coercive field [56]. When the applied electric field exceeds the coercive field, the leakage current is very small ($<$ 20 nA). In order to avoid a contribution from this leakage current, an AC current source I_{source} was used in all resistance measurements. Besides that, the signal is acquired by a lock-in.

Figure 4.8b shows the result of transport measurements for sample #1 at various electric fields. The zero-field case is firstly discussed. The resistance as a function of temperature has the usual metallic behaviour, rising with a linear temperature dependence from low temperature up to T_t. There are large changes in resistance during the heating and cooling processes. We defined the transition temperature to be at the maximum of the derivative of resistance R with respect to temperature T: $\partial R/\partial T$. Using this definition, the large drop in resistance occurs at $\sim$ 379 K and the sharp increase happens at $\sim$ 341 K which are around the transition temperature from AFM $\rightarrow$ FM and vice versa when no voltage is applied. It can be seen that the thermal hysteresis width defined from the R(T) curve is $\sim$ 38K, which is consistent with that in the M(T) measurements ($\sim$ 35 K). The difference in resistance of the heterostructure between the local maximum and minimum values on the heating side (equation 3.2) is about 25 % , which is the same order as for the film deposited on the silicon substrate (see Fig. 1).

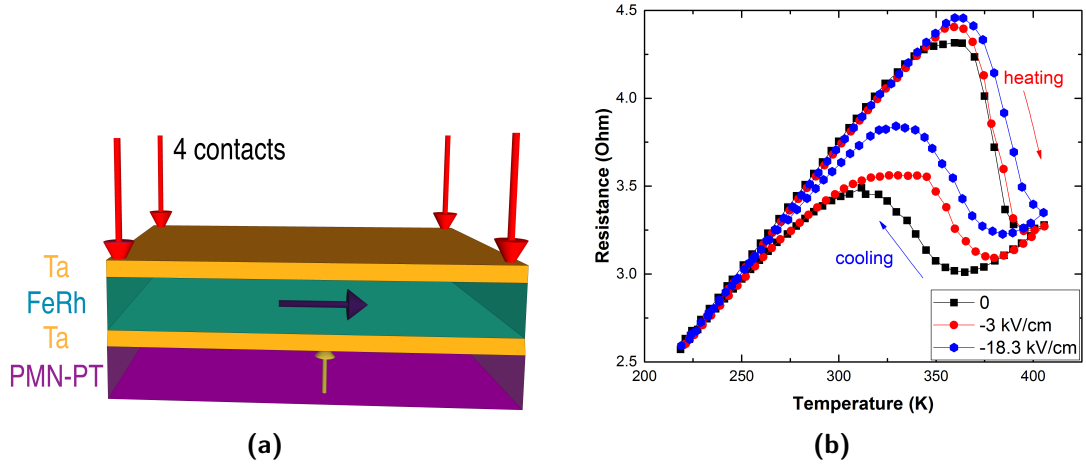

Figure 4.8. *(a) Structure of sample and four contacts in the transport measurement and (b) the temperature and electric field dependence of resistance in the heterostructure of PMN-PT/Ta/FeRh/Ta*

When voltages (E-fields) are applied to the (001) oriented PMN-PT substrate in the out-of-plane direction $\left(\vec{E} \| [001]\right)$, PMN-PT substrate shows a butterfly strain behavior

as shown in chapter 1 and experimental S(E) curves above. Here, we note that E-fields are applied in the OOP direction, so when the PMN-PT substrate expands in the OOP direction, it is compressed in the in-plane direction and vice versa.

Changes of resistance due to applied E-fields are shown in figure 4.8b. We can see that changes of resistance around the transition are remarkable with respect to both the shape of the R(T) curve and the resistance value. However, the change in resistance at other temperatures, i.e at low temperatures, is quite small. Although the R(T) curve under the applied voltage of -80 V $\sim$ -3 kV/cm still keeps the shape of the usual metallic behaviour as the zero-field result, it moves to higher temperature, shows a reduction in the thermal hysteresis width and an increase of resistance. Both transition temperatures on the heating and cooling processes under voltage are higher than those without applied voltage. It is found that the changes of resistance in the cooling side is stronger than that in the heating side either in the resistance value or the transition temperature. As a result, the R(T) curve under the applied electric field is contracted. These changes are also observed when the applied voltage is increased to -500 V $\sim$ -18.3 kV/cm.

The R(T) curves measured in a cycle from 0 $\rightarrow$ 18.3 kV/cm $\rightarrow$ 0 $\rightarrow$ -18.3 kV/cm $\rightarrow$ 0 are shown in figure 4.9b, and the corresponding polarization states of the PMN-PT substrate are shown in figure 4.9a. One can see that the R(T) curves measured in the zero-field case is reproducible. Under the applied E-field, the curves are contracted and move to high temperature direction. Moreover, the R(T) curves show a similar behavior with the E-fields of $\pm$18.3 kV/cm. Other transport measurements at the E-fields of $\pm$3 kV/cm also shows this phenomenon (see Fig. 4.9c). On this figure 4.9c, the R(T) curve under a positive field of 3 kV/cm is identical to the curve under a negative field of -3 kV/cm. The reason for this result will be discussed in the next section.

Application of an electric field leads to an increase in resistance, especially around the transition tempeature. It was reported that the AFM phase of Fe-Rh films has a higher resistivity than the FM phase [12]. This suggests that the fraction of the AFM phase is increased due to the applied electric field. To evaluate the influence of the electric field on the resistance, we define a ratio of the relative change in resistance at a fixed temperature due to the electric field as follows:

$$\left.\frac{\triangle R}{R(E=0)}\right|_T = \left.\frac{R(E)-R(E=0)}{R(E=0)}\right|_T \tag{4.1}$$

where: $\triangle$R is the difference between the resistance in the applied electric field R(E) and the zero-field case R(0).

The relative change in resistance as a function of temperature on the cooling curve is shown in figure 4.9d. From this figure, one can see that the E-field only changes the resistance slightly below 300 K and above 385 K. As the temperature decreases from 385 K to 300 K, a very sharp increase is observed and the rate of change is maximum at $\sim$350 K, which corresponds to the FM $\rightarrow$ AFM transition temperature. The maximum rate of change is reached about 14 % and 21.5% for the applied electric fields of -3 and -18.3 kV/cm, respectively. This ratio indicates the sensitivity of resistance to piezoelectric strain.

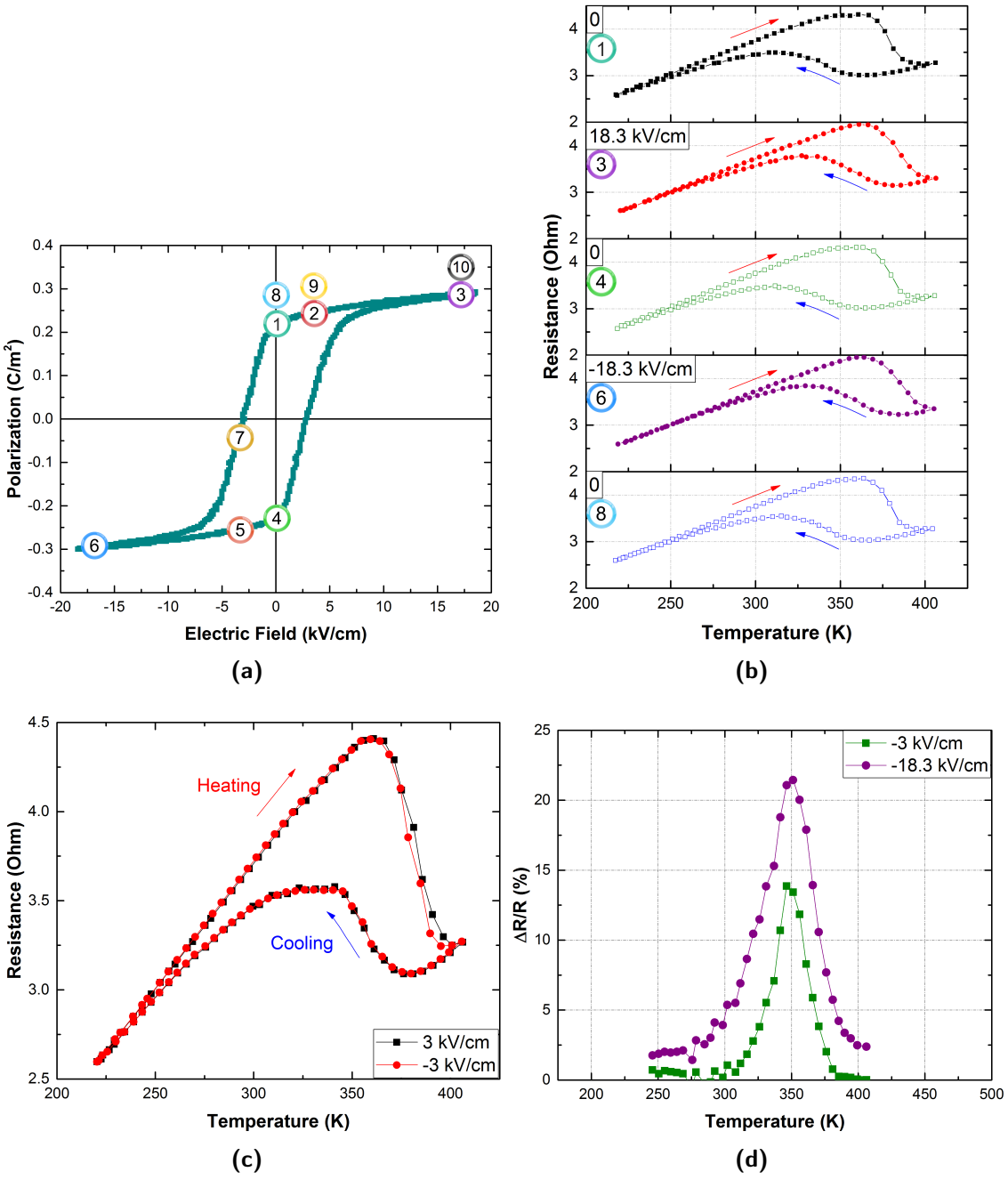

Figure 4.9. *(a) The P(E) curve of the PMN-PT substrate under the maximum electric field of 18.3 kV/cm at room temperature. (b) The electric field dependence of the transport measurement in a cycle from 0 → 18.3 kV/cm → 0 → -18.3 kV/cm → 0. (c) The R(T) curve at the applied field of 3 kV/cm is identical to the curve at the field of -3 kV/cm. (d) The relative change in resistance of the Fe-Rh film in the heterostrucutre due to the applied electric fields of -3 and -18.3 kV/cm on the cooling curves.*

Measurement of R(T) under E-field is also made on sample #2, as shown in figure 4.10a. The transport measurement in the zero-field case shows a normal metallic behaviour before the transition as well as a large change at the transition temperature. The difference in resistance at the drop is the same order as the FeRh bulk in literature (see Eqn. 3.2

and Fig. 1.7). The relative change in resistance $\triangle R/R(E=0)$ (Eqn. 4.1) as a function of temperature on the cooling curve is huge, up to ∼26.8 % around the transition temperature (see Fig. 4.10b).

Sample #1 cracked upon cooling from elevated temperature measurements, and all the following measurements were performed on sample #2. In figure 4.8b, applied E-fields are larger than E_C which implies that E-field-induced strains in the OOP direction is expanded, resulting in the compressive in-plane strain. In order to study the behaviour of resistance at lower E-fields (less than E_C), we applied a small E-field ∼ -0.47 kV/cm to the heterostructure as shown in figure 4.10a. We can see that a large change in the resistance with only a small applied E-field of -0.47 kV/cm corresponding to -15 V.

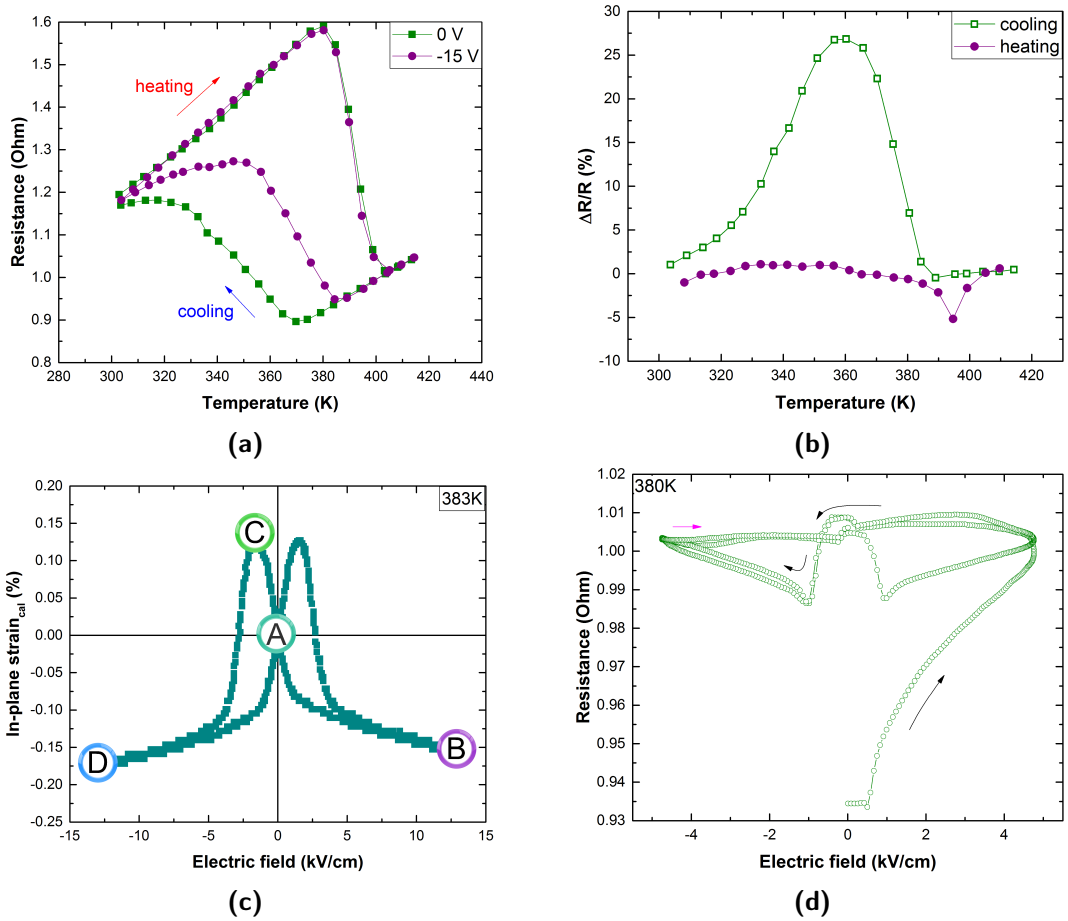

Figure 4.10. *(a) The M(T) curve of the heterostructure sample 2. (b) The R(T) curve at the zero-field and applied E-field cases. (c) The in-plane strain of the PMN-PT substrate at 383 K calculated from the P(E) curve. (d) The E-field dependence of resistance in the heterostructure.*

The E-field control of resistance at fixed temperature. We measured the resistance of the Fe-Rh film versus applied E-fields along the [001] direction in order to explore the magnetoelectric effect through the strain-mediated coupling. Figure 4.10d shows the resistance of the Fe-Rh film R(E) as a function of an applied DC voltage at 380 K. Before this measurement, the PMN-PT substrate was polarized. One can see that local minimum peaks appeared at V ∼ ± 33 V (∼ ±1 kV/cm) which is consistent with the electric coercive

field E_C of the PMN-PT substrate in the P(E) curve (see Fig. 4.2b). In order to describe the R(E) curve, an in-plane strain S(E) curve is used to illustrate the in-plane strain of the substrate as shown in figure 4.10c. This in-plane strain S(E) curve is just calculated from a P(E) curve at 383 K, which is present in the section 4.4.3. When an E-field is applied to the PMN-PT, the strain of the substrate traces a curve A $\rightarrow$ B $\rightarrow$ C $\rightarrow$ D. This results is described as follows.

From A to B, because the PMN-PT substrate is expanded in the out-of-plane direction, the Fe-Rh film is compressed in the in-plane direction, an increase of resistance of the film is observed. When we decrease the E-field from B $\rightarrow$ A, the strain of the PMN-PT substrate traces the same line in the opposite direction. Meanwhile, it seems that the resistance of the Fe-Rh film does not change. From A $\rightarrow$ C, the in-plane strain of the PMN-PT substrate is expansive, and it increases with the increase of the E-field magnitude, then reaches the local maximum value at "C". The behaviour of the strain-induced resistance in the Fe-Rh film is more complex. The resistance of the Fe-Rh film does not change until the applied E-field reaches -0.44 kV/cm. When the applied field magnitude is bigger than 0.44kV/cm, the resistance decreases and reaches a local minimum value at $\sim$ -1kV/cm. The in-plane strain of the substrate is compressive when the $E_{applied} > E_C$ (from C to D), resulting in an increase of the resistance of the film. Strain does not depend on the sign of the polarisation nor on the sign of the electric field. As expected, the strain curve, the resistance curve are symmetric when the opposite electric field is applied. The variation in resistance is larger for the first sweep. The R(E) curve is reproducible from the second sweep onwards.

4.4.2 Strain-modified phase change characteristics

In order to explore the strain-induced modification of the phase change, R(T) curves were measured as a function of electric field at all points circled in (see Fig. 4.9a). Results of transport measurements are treated to extract the transition temperature T_t. T_t is defined as the maximum of the derivative of resistance R with respect to temperature $\partial R/\partial T$. The derivatives of $\partial R/\partial T$ with respect to T are fitted using a Gauss function in order to obtain the transition temperature more precisely.

Transition temperature versus compressive in-plane strain. The transition temperature as a function of the applied electric field is shown in figure 4.11. Each data point in this figure is extracted from a R(T) loop at an applied E-field. First, we discuss the effect of electric field on the phase change on the cooling side, corresponding to a FM to AFM transition (Fig. 4.11a). The transition temperature is around 341 K$\pm$3 without an external electric field (the measured point is circled 1 in P(E) at 300K - (Fig. 4.9a)). It is found that the AFM phase is stablized with a DC voltage of 80 V ($\sim$ 3 kV/cm), resulting in a shift of the transition temperature up by $\sim$16 K ($T_t \sim$ 357 K$\pm$2) (circle 2 in Fig. 4.9a). As the applied voltage increases to 500 V ($\sim$ 18.3 kV/cm) (circle 3 in Fig. 4.9a), the transition temperature is now shifted up 18 K$\pm$5 ($T_t \sim$ 359 K$\pm$2). Without E-field (circled 4), the transition temperature returns to its value at about 340 K$\pm$3. Then the electric field

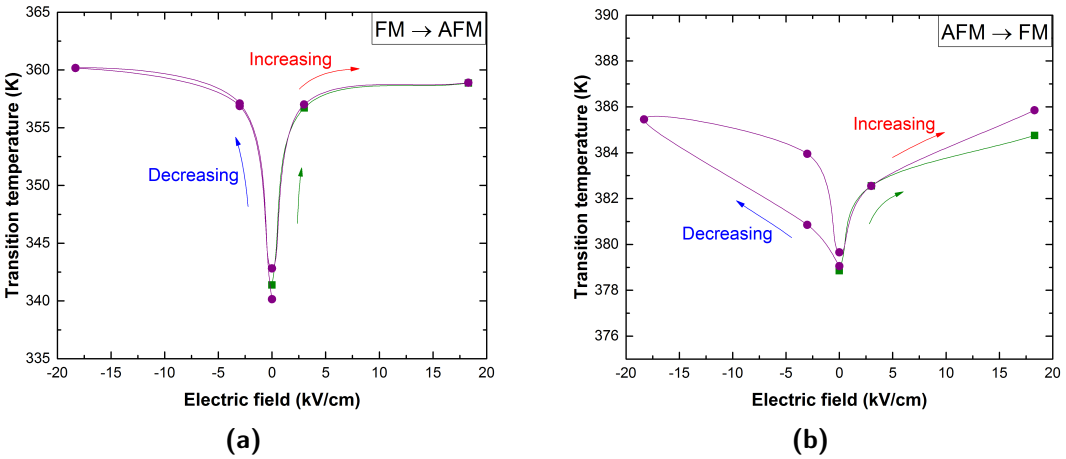

Figure 4.11. *The strain-mediated tuning of the phase transition in the heterostructure of PMN-PT/Ta/FeRh/Ta on (a) the cooling side (a) and (b) the heating side.*

was decreased to -3 kV/cm (circle 5), which resulted in a reduction of the onset of T_t with a shift of 16 K ($T_t \sim 357$ K±2), which is identical to the value at 3 kV/cm. At the 6th circled point, the R(T) curve under -18.3 kV/cm seems similar to that of the 3rd circled curve. As a result, the transition temperature is shifted up by 20 K and observed at 360 K±2. The similarity of R(T) curves at the E-fields of ±18.3 kV/cm imply the symmetry of strain as a function of the external electric field S(E). At -3 kV/cm (circle 7), the transition temperature is the same magnitude as that at the 2nd and 5th circled points. The reason could be the same strain between these points. When no external electric field is applied (the 8th circled point), the R(T) curve is similar to the previous zero-field case and the transition temperature recovers its value from the FM state to the AFM state, as above. Transition temperatures at the points circled 9 and 10 are similar to the values at the points circled 2 and 3, respectively. Besides that, the R(T) curves as well as the transition temperature at the zero field case and the external fields is reproducible. A point worth remarking is that the resistance signal is stable even though the measurements are made over a week.

By constrast with the change on the cooling curve (FM to AFM transition), the transition temperature on the heating side (AFM to FM transition) is only changed slightly by E-fields (see Fig. 4.11b). The maximum shift of the transition temperature due to the field is about $\sim$ 7 K which is significant smaller value than that on the cooling side.

Transition temperature versus tensile in-plane strain. The general behavior of the transition temperature in response to the electric field was investigated with applied E-fields larger than the electric coercive field E_C. The response of the transition temperature for a smaller field than E_C of the PMN-PT substrate is also interesting due to the tensile in-plane strain of the substrate. The in-plane strain of the PMN-PT substrate is tensile when applied E-fields are smaller than E_C and the E-field is in the opposite direction to polarization, shown as the positive part of the in-plane strain S(E) in figure 4.2a. In this section, the dependence of the transition temperature on the tensile in-plane strain is investigated.

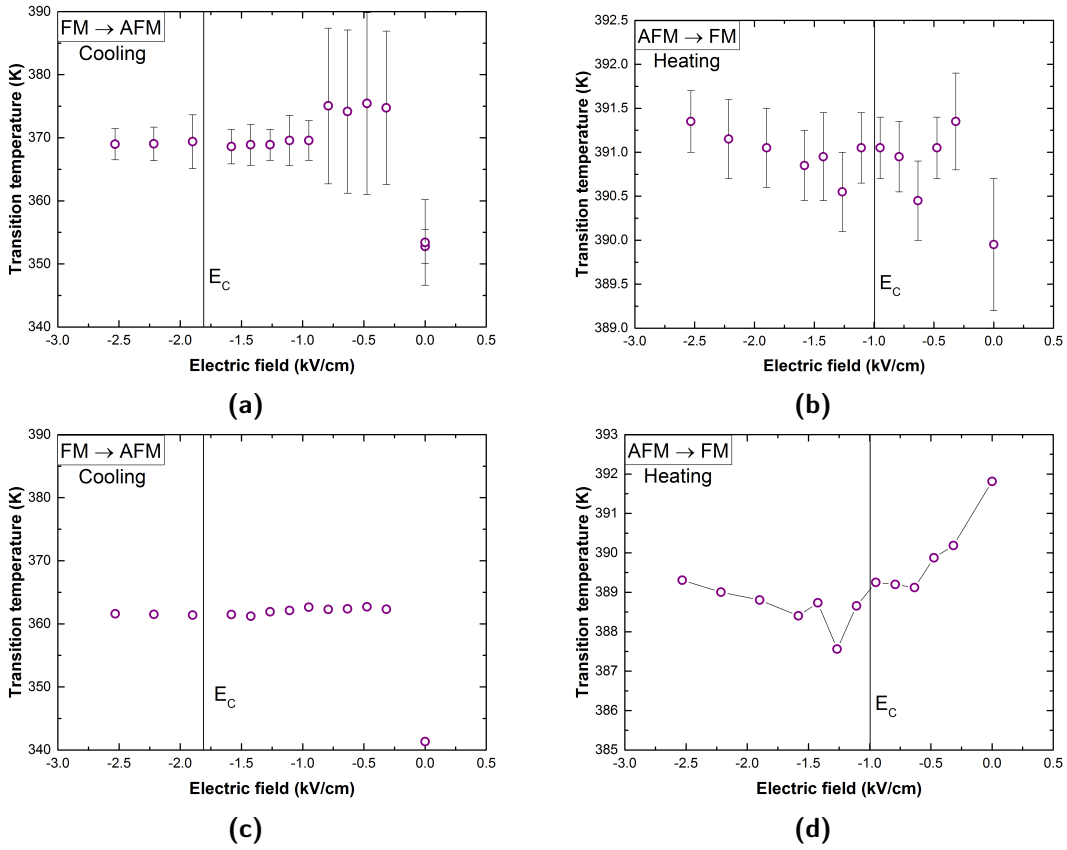

Figure 4.12. *The strain-mediated tuning of the phase transition in the heterostructure of PMN-PT/Ta/FeRh/Ta on (a) the FM → AFM transition and (b) the AFM → FM transition. (c, d) Transition temperatures are determined using another defination. We note that scale bars are different.*

Voltages from a range of -10 V to -80 V, which corresponds to E-fields from -0.32 to -2.53 kV/cm, are applied to the PMN-PT substrate of sample # 2. The coercive fields E_C of the PMN-PT substrate is estimated to be $\sim$ 1.8 kV/cm and 1 kV/cm (see Fig. 4.2b) at $T_{t\text{-cooling}}$ ($\sim$ 353 K) and $T_{t\text{-heating}}$ ($\sim$ 390 K) of Fe-Rh films, respectively, as shown in figure 4.12. Hence, this range of applied voltage (E-field) covers regions either before polarization switching or after polarization switching (the vicinity of E_C) of the PMN-PT substrate.

Figure 4.12 shows the transition temperature as a function of E-field. The change in the transition temperature as a function of E-field is significant on the cooling side, while it is not so on the heating side. On the cooling side, the transition temperature is shifted up to 22 K ($T_t \sim 375$ K) with $E_{applied} < E_C$ fields. In the case of $E_{applied} > E_C$ fields, the transition temperature T_t is about 369 K, corresponding to a shift of 16 K. This leads to a difference of 6 K in the transition temperature between both cases. In this figure (Fig. 4.12a), we can see the error bar is quite large although the change in the FM to AFM transition temperature is clear (see Fig. 4.10a). The transition temperature is defined as the maximum of $|\partial R/\partial T|$ and then it is fitted using a Gaussian function. However, the difference in the slope of the R(T) curve when the film is AFM and FM leads to this large error bar. Another defination, in which the transition temperature is defined as

the temperature at half maximum of the resistance during cooling and heating could be suitable in this case (see Fig. 4.12c, 4.12d). This defination does not change the magnitude of the shift of T_t due to the E-field induced strain as shown in the figure 4.12c ($\sim 21\,K$).

When $E_{applied} < E_C$, a tensile in-plane strain is transfered from the PMN-PT substrate to the Fe-Rh film. A decrease of T_t is predicted in this case, assuming that the influence of the tensile strain on T_t is the same as the isotropic pressure. In contradiction to this prediction, T_t in $E_{applied} < E_C$ cases does not decrease, it even looks to increase in the $E_{applied} > E_C$ case. However, the error bar is quite large in the $E_{applied} < E_C$ case. The direct measurement of the resistance against the applied E-field R(E) may be useful in this case (see Fig. 4.10d).

Figure 4.10d shows that the resistance in the $|E_{applied}| < 0.44\,kV/cm$ case is higher than that in the $|E_{applied}| > 0.44\,kV/cm$ case. This result implies that the transition temperature in the $E_{applied} < E_C$ case can be slighly higher than that in the $E_{applied} > E_C$ case. As a result, the AFM phase is stablized both under compressive strain and under expansive strain. However, in order to create an in-plane tensile strain, the magnitude of the applied E-field must be lower than E_C, which depends on the temperature. The coercive field decreased from $2.2\,kV/cm$ at room temperature to $0.82\,kV/cm$ at $413\,K$, as shown above. Because the measurement is made from RT to $414\,K$, which is close to the Curie temperature, this tensile strain is limited.

In brief, although the strain of the PMN-PT is transmitted either as a compressive strain or as a tensile strain, the strain-induced modification of the phase change in the Fe-Rh film is non-linear with in-plane strain, which implies that the transition temperature is not a linear function of the in-plane strain unlike what is expected from a linear dependence on volume (hydrostatic (isotropic) pressure experiments).

4.4.3 Mechanism discussion

The PMN-PT/TaFe-Rh/Ta heterostructures show a phase change and a large change in resistance under the electric field. Unlike hybrid system where the electric field is applied across the piezoelectric substrate and the strain is transmitted through a bonding glue, here the magnetic film is directly one of the electrodes. The change in the Fe-Rh film on the PMN-PT substrate is a magnetoelectric effect, which may correspond to mechanisms: the interfacial charge mechanism and strain-mediated coupling. In the following part, we will discuss the influence of each regime on the phase change in the Fe-Rh film.

4.4.3.1 The interfacial charge effect

Interfacial charge - mediated coupling can have an effect on the phase change characteristic of Fe-Rh films deposited on a the PMN-PT substrate. The heterostructure consisting of a piezoelectric substrate and a magnetic film is similar to a field effect transistor or a capacitor, where the induced or spontaneous polarization of the substrate is modulated by the application of E-field, leading to accumulation or depletion of charge carriers at the

interface with the metallic magnetic film, changing the charge carrier concentration, so filling or emptying the band structure, which thus allows a control of magnetic properties.

The thickness of the film over which properties are modified, is determined by the screening length of the material. Because of good conductivity in metal (resistivity in FeRh $\sim 10^{-6}$ Ω.m), the effect of the interfacial charge should be small. With a carrier density n of the order of $\sim 10^{21}$ cm^{-3}, the Thomas-Fermi screening length r_{TF} is less than 1 Å in FeRh determined using the following equation [127]:

$$r_{TF}^2 = \frac{\pi^2 \hbar^2 \varepsilon_0}{me^2 (3\pi^2 n)^{1/3}} \tag{4.2}$$

The physical change of the FeRh film induced by the electrostatics of the PMN-PT substate may only exist in first few lattice unit cells. This screening length is much smaller than the thickness of the Fe-Rh film on the PMN-PT substrate. The induced magnetic moment in the Fe-Rh film can be estimated assuming that the Fe-Rh layer has the same surface charge as the PMN-PT substrate and that all electrons contribute to the extra magnetic moment. The surface charge density σ of the PMN-PT substrate under an electric field E is defined as the total amount of charge Q per unit area S as follows:

$$\sigma = \frac{Q}{S} = D = P + \varepsilon_0 E \tag{4.3}$$

where: D - the electric displacement, P - the polarization of the PMN-PT substrate.

Then, the charge variation per unit cell of the Fe-Rh film can be estimated [54]:

$$q = \sigma \frac{V_{cell}}{d} = (P + \varepsilon_0 E) \frac{V_{cell}}{d} \tag{4.4}$$

where: d - the thickness of the Fe-Rh film, V_{cell} - the volume of the primitive cell and V_{cell} = $a^3/2 = 0.013\,\text{nm}^3$ with a = 2.978 Å .

A change of 1.1×10^{-4} electrons per unit cell is estimated for P = 29 μC/cm^2 at E = 18.3 kV/cm and d = 220 nm. Assuming all these electrons contribute a spin magnetic moment (1 Bohr magneton / electron), this leads to a maximum induced magnetic moment of 1.1×10^{-4} μ_B which is a very small value. The Fe-Rh films have a simple cubic structure with a = 2.978 Å, hence a change of $\sim 1.47\times10^{-5}$ % is estimated on the 220 nm thick film assuming 2 μ_B per $Fe_{51}Rh_{49}$ alloy atom [94].

Furthermore, the strain mechanism depends on the polarization P differently from the charge mechanism. +P and -P give opposite induced charges but +P and -P create the same strain. Hence, T_t would depend on P in an even way for the strain mechanism and a odd way for the charge mechanism. The measured T_t(E) curves have mainly an even character so strain does appear to be the mechanism responsible for the Tt changes.

4.4.3.2 The strain-mediated coupling effect

The E-field-induced strain of the PMN-PT substrate is assumed to be perfectly transferred to the Fe-Rh films. As a result, Fe-Rh films undergo an in-plane compressive or expansive

strain depending on the magnitude and direction of E-field with respect to E_C and the polaratization $\overrightarrow{P}$. In this section, we discuss the influence of strain on resistance and the transition temperature.

The strain-mediated coupling effect on the change in resistance. An increase of the resistance in Fe-Rh films is due to combined changes in length l, width w, thickness t and resistivity ρ as follows:

$$\begin{aligned}\frac{\partial R}{R} &= \frac{\partial l}{l} - \frac{\partial t}{t} - \frac{\partial w}{w} + \frac{\partial \rho}{\rho} \\ &= d_{31}^p E_3 - d_{33}^p E_3 - d_{31}^p E_3 + \frac{\partial \rho}{\rho} \\ &= \frac{\partial \rho}{\rho} - d_{33}^p E_3 \end{aligned} \tag{4.5}$$

where: d_{31}^p and d_{33}^p - the piezoelectric coefficients, E_3 - the external electric field, $\vec{E_3} \| [001]$.

According to equation 4.5, the increase of resistance in the Fe-Rh film is caused by the change in the geometry and the resistivity. First, we discuss the influence of the change in the geometry. In particular, for $d_{33}^p = 2000\,\mathrm{pC/N}$ at room temperature, $E_3 = 18.3\,\mathrm{kV/cm}$ and $E_3 = 3\,\mathrm{kV/cm}$, we have the change in resistance of -0.37 % and -0.06 % for 18.3 and 3 kV/cm, respectively due to the change in geometry. This value is much smaller than the change in resistance around the transition temperature (21.5 % and 14 % as shown on Fig. 4.9d).

Furthermore, one can see that the change in resistance is opposite in sign to the change due to the geometry. The resistance of Fe-Rh films increases with the external electric field in our experiments. It should be mentioned that the E-field-induced strain is decreased when the temperature is close to T_C, resulting in a reduction of the influence of geometry on the change in resistance. Thereby, we can conclude that the strain-induced resistivity change is the main contribution to the change in resistance of the Fe-Rh films. It was reported that the resistivity increases with hydrostatic pressure around T_t [25]. However, the E-field-induced strain is anisotropic, which is different from the isotropic pressure considered in literature.

As mentioned above, the change in resistance around the transition temperature due to strain is large while this change is quite small for other temperatures, e.g. at low temperatures. One can see that the contribution of strain not only increases the resistance around the transition temperature, but also shifts the onset of transition to the FM phase to higher temperatures. This implies that the contribution of strain here is to tune the transition between FM and AFM phases. In the following part, we discuss the strain effect on the phase change of Fe-Rh films.

The strain-mediated coupling effect on the phase change. The total piezoelectric strain due to the PMN-PT substrate can be decomposed into anisotropic strain, in which volume of sample is changed, and the anisotropic strain, in which the volume is constant. It can be expressed as follows:

Total strain from substrate = Isotropic strain (volume changes) + Anisotropic strain

(constant volume)

Before discussing the strain coupling on the phase change, we would like to make a short summary of elasticity including: the general relations between strain and stress, definations of Poisson's ratio and Young's modulus, and a special case of the isotropic pressure.

Definations: the Young's modulus E_Y connects the stress to strain: $E_Y = \sigma_z/\varepsilon_z$ (with $\sigma_x = \sigma_y = 0$) and Poisson's ratio ν: ν = -$\varepsilon_x/\varepsilon_z$ assuming that $\varepsilon_x = \varepsilon_y$, where: ε_x, ε_y and ε_z - the strain along the x, y and z-axis, respectively; σ_x, σ_y and σ_z - the stress along the x, y and z-axis, respectively.

Strain to stress relations: $\varepsilon_z = \sigma_z/E_Y$, $\varepsilon_x = \varepsilon_y$ = -$\nu\sigma_z/E_Y$ assuming $\sigma_x = \sigma_y$.

In general case, the cube material is subjected to combined normal stresses, the combined strains are given as follows:

$$\varepsilon_z = \frac{\sigma_z}{E_Y} - \frac{\nu\sigma_x}{E_Y} - \frac{\nu\sigma_y}{E_Y},\ \varepsilon_y = \frac{\sigma_y}{E_Y} - \frac{\nu\sigma_x}{E_Y} - \frac{\nu\sigma_z}{E_Y},\ \varepsilon_x = \frac{\sigma_x}{E_Y} - \frac{\nu\sigma_y}{E_Y} - \frac{\nu\sigma_z}{E_Y} \tag{4.6}$$

The hydrostatic pressure: P = -σ_x = -σ_y = -σ_z, and ε_x = -(1-2ν)P/E_Y. Then, we have an important relation between the hydrostatic pressure and the volume change dV:

$$\frac{dV}{V} = \varepsilon_x + \varepsilon_y + \varepsilon_z = -3\frac{1-2\nu}{E_Y}P \tag{4.7}$$

where: V - the volume of the material.

Now, we discuss the phase change of FeRh due to the strain coupling between PMN-PT and FeRh. First, we evaluate the change in the transition temperature of the heterostructure caused by an isotropic strain. When an electric field is applied along the out-of-plane direction of the PMN-PT substrate, a strain is created by this field. We can estimate the change in transition temperature due to the strain of the PMN-PT substrate using the result of the hydrostatic pressure as follows.

The film volume change dV when piezoelectric strain is applied as:

$$\frac{dV}{V} = \varepsilon_x + \varepsilon_y + \varepsilon_z \tag{4.8}$$

Since the piezoelectric strain is uniform in plane we have: $\varepsilon_x = \varepsilon_y$. Using elasticity relations in the linear regime for a plate, stressed in plane and without stress out-of-plane ($\sigma_z = 0$), we have :

$$\varepsilon_z = \frac{-2\nu}{1-\nu}\varepsilon_x \tag{4.9}$$

Since $\varepsilon_x = d_{31}^p E_3$, the volume change becomes:

$$\frac{dV}{V} = 2\varepsilon_x + \varepsilon_z = \left(2 - \frac{2\nu}{1-\nu}\right)\varepsilon_x = \left(2 - \frac{2\nu}{1-\nu}\right) d_{31}^p E_3 \tag{4.10}$$

where: d_{31}^p - the piezoelectric coefficient.

For a numerical estimation, we use d_{31}^p = -1000 pC/N and $\nu = 0.31$. The value of d_{31}^p is taken from the supplier's datasheet, and the value of Poisson's ratio is usual for metals,

from 0.25 to 0.35. We obtain that a E_3 = 3 kV/cm electric field produces a -0.03 % in-plane strain and a dV/V = -0.03 % change of volume, while with E_3 = 18.3 kV/cm, we have: ε_x = -0.18 % and dV/V = -0.2 %.

Isotropic compressive pressure causes a shift in the transition temperature of the Fe-Rh material to higher temperature by dT_t/dp = 4.33 - 6.3 K/kbar [23, 25]. This ratio depends on the temperature and $dT_t/dp \sim$ 4.33 K/kbar and 3.9 K/kbar at 350 K and 383 K, respectively. Here, we can take an average value $dT_t/dp \sim$ 4 K/kbar. An estimation for FeRh compressibility is that a 1% volume decrease corresponds to $\sim$ 18 kbar pressure [101]. So, a 1% volume isotropic decrease is associated to a $\sim$ 72 K increase of the transition temperature.

A volume change dV = -0.03 % corresponding to E_3 = 3 kV/cm leads to a shift in the transition temperature of $\sim$ 2.4 K. While a volume change of dV = -0.2 % corresponding to E_3 = 18.3 kV/cm shifts T_t up to 14.5 K (sample #1).

One can see that comparing to the experiment data ($\triangle$T = 20 K), the piezoelectric strain effect on the FeRh transition can partially be explained using a volume effect when the order goes from FM to AFM (cooling) with E-field of 18.3 kV/cm. However, the calculated value of the shift in T_t at the E-field of 3 kV/cm is significantly smaller than that in experiment. In the calculation above, we assumed that the strain of the PMN-PT substrate is linear with E-field. In reality, the strain behavior S(E) can be non-linear as discussed in chapter 1 and it also depends on the temperature, i.e. it is reduced when the temperature is close to the T_C of the PMN-PT substrate.

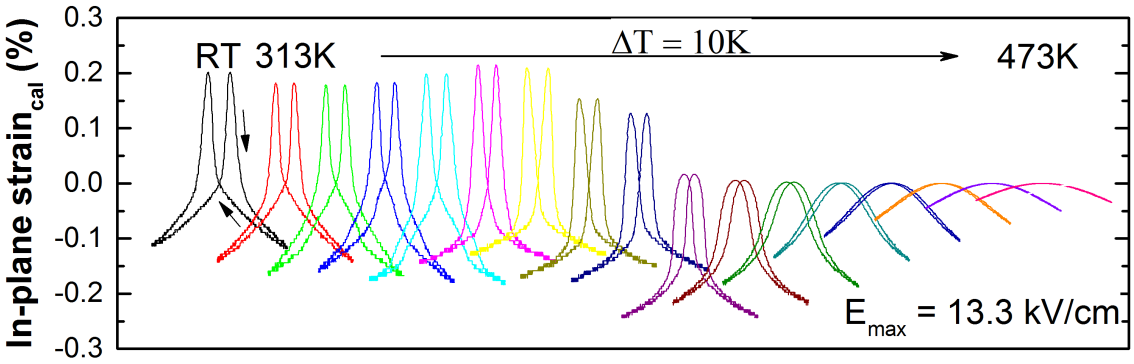

Figure 4.13. *The in-plane strain, calculated from P(E) loops with a maximum E-field of 13.3 kV/cm, is as a function of electric field at various temperatures.*

To discuss this non-linear strain, we calculated the strain of the substrate at various temperatures, which can be expressed as a function of the polarization [124, 128]:

$$\varepsilon_x = Q_{12} \cdot P_3^2 \tag{4.11}$$

where: Q_{12} - the transverse electrostriction coefficient along the x-axis (the in-plane direction) (m^4/C^2), P_3 - the polarization of the substrate. ε_x - the in-plane strain.

The electrostriction coefficient Q_{12} is determined from the P(E) and S(E) curves at room temperature (see Figs. 4.1b and 4.2a). Because the P(E) and S(E) curves of our

PMN-PT substrate are consistent with values in litherature and the supplier's datasheet, the calculated value Q_{12} can be used. It was reported that this coefficient is insensitive to temperature in PMN-PT [129], so we used Q_{12} calculated at room temperature for calculations at high temperature.

The calculated strain curve of S(E) at various temperatures is shown in figure 4.13 with the maximum E-field of 13.3 kV/cm. It was reported that the calculation matches the experiment for the region from the maximum field to zero field and deviates for the region around E_C [124]. Hence, this calculation is only used for the region from a maximum strain at the maximum E-field to zero.

The maximum E-field used in measurements of P(E) curves at high temperatures is 13.3 kV/cm ($\sim$ 400 V), while the maximum E-field used to investigate the strain control of phase change in Fe-Rh films is 18.3 kV/cm. Figure 4.1b shows that polarization is linear with E-field in the range from 13.3 to 18.3 kV/cm, and the P(E) curve at 13.3 kV/cm is a minor loop of the P(E) curve at 18.3 kV/cm. Hence, strain at 18.3 kV/cm can be achieved by an extrapolation.

Strains of $\sim$ -0.13 and $\sim$ -0.19 % at the E-fields of $\pm$3 and $\pm$18.3 kV/cm at 350 K are obtained, respectively, using the calculated in-plane strain curve at 350 K. As a result, the volume change is -0.14 % and -0.21 % at E-fields of 3 and 18.3 kV/cm when the order changes from a FM state to an AFM state. The calculated transition temperatures are shifted by up to 10 and 15 K under these strains. These calculated results are still 1.5 - 2 times smaller than the experimental data.

We can see that the change in transition temperature $\triangle$T does not change with strain in sample #2 and only slightly change in the sample #1 during heating. This can be explained as follows. The transition temperature during heating $T_{\text{t-heating}}$ is quite high (i.e. $\sim$ 390 K in sample #2), while figure 4.2b shows that the polarization of PMN-PT at 390 K is on the inflection of the curve, which is close to T_C. Because strain depends on the square of polarization, it implies that strain at $T_{\text{t-heating}}$ can be quite small. Applying a high electric field stablizes the ferroelectric phase, resulting in a shift of the E_C (E), P_r(E) in the high temperature direction, which can be the reason for a small change in $\triangle$T at 18.3 kV/cm compared to no detected change at smaller field in the AFM to FM transition.

However, a similar calculation gives opposite results to experiments in the case of a tensile strain applied to sample #2. A calculation of the change in the density of states of the FM and AFM phases in the Fe-Rh material showed no significant difference between 0.1 % tensile and compressive strains in literature (see the supplementary in [10]). Moreover, the transition temperature $T_{\text{t-cooling}}$ was shifted by up to 22 K when $E_{\text{applied}} < E_C$, as shown in figure 4.12a, which implies a non-linear dependence of $\triangle$T on strain. The behavior of $\triangle$T as a function of in-plane strain ε_x is different in sign and magnitude than predictions using an isotropic model, evidencing a non-linear behaviour of the effect with volume. Hence, modifications in the phase change of Fe-Rh films deposited on piezoelectric substrates, as a function of substrate mediated strain, are attributed to the anisotropic strain rather than the isotropic one.

Discussion of our results with respect to papers published during the thesis. In this final part, we would like to discuss some publications which appeared during the thesis, related to studies by Cherifi et al. "Electric-field control of magnetic order above room temperature" published in Nature materials in 2014 [9], and Lee et al. "Large resistivity modulation in mixed-phase metallic systems" published in Nature communications in 2015 [10]. These papers reported the change of magnetic order in FeRh films on a $BaTiO_3$ substrate (Cherifi et al.) and resistance in FeRh films on a PMN-PT substrate (Lee et al). We compare: (1) samples, (2) measurement methods, (3) results.

The idea in the first paper was to change the magnetic order of the heterostructure $BaTiO_3$ 500 μm/FeRh 22 nm using E-fields. An increase in T_t by about 25 K with 0.4 kV/cm is found through M(T) under a DC voltage. In $BaTiO_3$, the E-field-induced strain is composed of strain due to the piezoelectric effect and strain due to domain reorientation. In the case of the piezoelectric effect, the crystal is distorted and the lattice parameters are changed. On the other hand, a strain induced by domain reorientation between in-plane domains and out-of-plane domains does not lead to a change in the lattice constants. The strain created by the piezoelectric effect can be estimated as mention above: $\varepsilon_x = d_{31} \cdot E_3 = -1.4 \times 10^{-6} = -1.4 \times 10^{-4}$ % with d_{31} = -33.4 pC/N for a (001) single domain crystal $BaTiO_3$ [130, 131], E_3 = 21 V/0.5 mm. Meanwhile, the strain induced by domain rotation is -0.47 % in the paper mentioned above [9]. Therefore, the strain induced by the piezoelectric effect can be neglected.

In our research, the idea was also to tune the phase of the magnetocaloric material and Fe-Rh was chosen as a model system to explore. The transport measurement R(T) was used to monitor the effect. The transition temperature in our structure is shifted up to 22 K with 0.32 kV/cm, which is the same order of magnitude as their study. Although both $BaTiO_3$ and PMN-PT are piezoelectric substrates, the origin of the substrate strain can be different. The E-field-induced strain in the PMN-PT substrate is due to the piezoelectric effect. This means that the magnetic order in the heterostructure is controlled by domain reorientation in the case of $BaTiO_3$ but by the piezoelectric effect in the case of PMN-PT. However, the influence of strain in both cases on Fe-Rh films may be the same.

The thickness of the film also affects the result because the strain is transfered from the substrate to the film. Hence, a thinner film can achieve a bigger strain. However, the interfacial charge effect may alter the magnetic properties in this case. As a result, the mechanism of the phase change in the heterostructure of $BaTiO_3$/FeRh composes of the domain reorientation and the interfacial charge effect. On the other hand, the mechanism of tuning the phase change in our PMN-PT/Ta/FeRh/Ta samples is only due to the piezoelectric effect.

Finally, the change in transition temperature in the hybrid $BaTiO_3$/FeRh structure is calculated by DFT assuming an isotropic strain. Meanwhile, the anisotropic strain is attributed to the phase change in the hybrid structure in this thesis experimentally.

In the second paper, the heterostructure is of 0.72PMN-0.28PT (001)/FeRh 50 nm which is similar to the 0.7PMN-0.3PT (001)/FeRh 220 nm samples studied in this thesis. Lee et

al. used transport measurements to study the magnetoelectric effect. Their idea was to study the change in resistivity of the FeRh film in the heterostructure under the E-field-induced strain. A 8 % change in the electrical resistivity of FeRh films was reported for ±6.7 kV/cm at 368 K, which is near the transition temperature. Although they did not report on the change in transition temperature due to the applied voltage, this change can be estimated from their data, and it is of the same order as the value in [9] and this thesis.

The 8 % change in the resistivity is calculated from a formula: $\triangle\rho/\rho_{\min} = [\rho(\mathrm{E}) - \rho_{\min}]/\rho_{\min}$, where $\rho_{\min}$ is the minimum resistivity taken at each isothermal resistivity curves ρ(E) for various temperatures. Using the first sweep R(E) at 380 K, a change of about 8 % can be estimated for our sample (see Fig. 4.10d). The relative change in resistance $\triangle$R/R(E=0) reaches 26.8 % close to the transition temperature with a small field (see Eqn. 4.1 and Fig. 4.10b).

4.5 Chapter summary

Heterostructures of PMN-PT (001)/Ta/FeRh/Ta were prepared and the E-field-induced phase change as well as the resistance change through the strain effect are explored above room temperature. The FeRh films directly deposited on PMN-PT have the same high quality as the films deposited on Si. A complete AFM-FM transition is obtained. A change in the transition temperature up to 22 K at a low E-field of 0.32 kV/cm is achieved. In addition, the large change in resistance under the induced strain is also observed around the transition temperature. The volume change alone does not explain the transition temperature shift and the anisotropy seems necessary to enhance the shift. This work demonstrates the ability to tune the phase in the magnetocaloric material as well as the resistivity/resistance using a relatively low voltage.

CHAPTER 5

Preparation and characterization of $La(Fe,Si)_{13}$ thin films

5.1 Introduction

$La(Fe,Si)_{13}$ is one of the most efficient magnetocaloric materials as mentioned in Chapter (see Fig. 1.1). Studies to date have focused on $La(Fe,Si)_{13}$-based bulk alloys, with no reports on $La(Fe,Si)_{13}$ in film form. One aim of this thesis was to produce films to serve as model systems to study the influence of composition and strain. Within the group we worked on the preparation of LaFeSi films on large substrates with the aim to produce compositionally graded samples. A first study, carried out by a post-doc working on the DRREAM project (N.H. Dung), concerned magnetron sputtering of relatively thin films (t $\leq$ 350 nm) using a composite target consisting of a base of pure Fe and superposed pieces of La and Si. This target geometry was chosen to maximise the composition spread, which was dependent on both the size and position of the superposed elements. Despite producing films with compositions spanning either side of the 1:13 stoichiometry, the desired phase was not attained in these films. In a second part of the study, in which I worked directly with N.H. Dung, triode sputtering of a homogeneous alloy target was used to produce films of thickness in the range 30 nm to 5.3 μm. In this case a spread in film composition across the substrate is achieved thanks to the difference in the solid cone of sputtering of the constituent elements. In this chapter, I will only describe the study on triode sputtered films in which I was directly involved.

5.2 Sample preparation

A La-Fe-Si alloy target was prepared by induction melting from pieces of La, Fe and Si (atomic ratio La:Fe:Si = 1.2:11.5:1.5). La-Fe-Si films, with Ta buffer and capping layers, were deposited by triode sputtering onto thermally oxidized Si(001) wafers at a rate of 3.8 μmh^{-1}. The films were deposited at $T_{dep} \sim 530$ K (no power to the heater of the substrate holder, but substrate heated by the plasma) and then annealed at high temperature for 5 min under secondary vacuum in a Rapid Thermal Processing (RTP) furnace. Annealing leads to the formation of cracks in the films. Hydrogen absorption by annealed films was conducted at 2 bar and 623 K for 2h. Note that no obvious additional cracking, nor film peel-off, was observed following hydrogenation.

5.3 Sample characterisation

Upon post-deposition annealing in the range 750 - 900°C, the formation of the desired La(Fe,Si)$_{13}$ phase was achieved in the central region of films of thickness 2 μm and above (e.g. Figure 5.1). This position dependent behaviour is attributed to the spread in film composition and possibly thickness / stress (the thickness drops off towards the edge of the wafer, reaching a value of 50 % in 100 mm wafers). The relative amount of the La(Fe,Si)$_{13}$ phase, as estimated from M(H) curves, dropped with distance from the centre of the substrate. Increasing the film thickness led to a reduction in the amount of α-Fe at a given position on the substrate. Structural and magnetic properties of optimised films are detailed below.

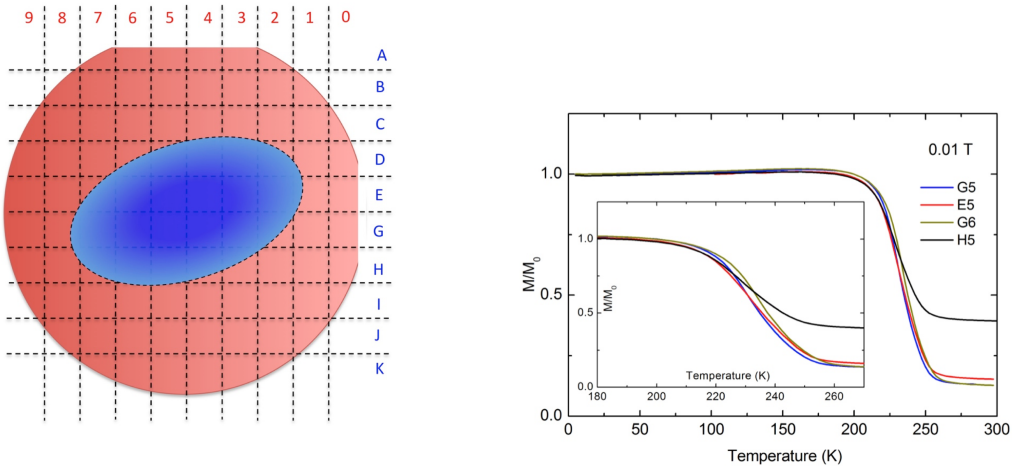

Figure 5.1. *(a) Schematic showing the region, in blue, on a La-Fe-Si film deposited on a 4-inch Si wafer where the La(Fe,Si)$_{13}$ phase formed after annealing (t_{LaFeSi} = 2.2 μm, T_{anneal} = 800°C). (b) Representative M(T) curves measured upon cooling, under 0.01 T.*

The as-deposited 5.3 μm films exhibit very broad XRD peaks corresponding to α-Fe (not shown). Figure 5.2 shows room-temperature XRD patterns for La-Fe-Si films after post-deposition heat treatment at 1073 and 1173 K. It can be seen that the La-Fe-Si films crystalize in the NaZn$_{13}$-type cubic structure. Additional diffraction peaks are attributed to α-Fe, a La-rich phase, Fe_7Ta_3 and Fe-containing β-Ta. The formation of the latter two phases due to diffusion between the main layer and the buffer and capping layers during the annealing process is supported by a literature report on the binary Ta-Fe systems [132]. No NaZn$_{13}$-type phase was detected after annealing below 973 K (data not shown).

Cross-sectional backscattered electron SEM images of La-Fe-Si films before and after heat treatment are shown in the inset of Fig. 5.2. The very small bright areas in the images of the post-deposition annealed samples are attributed to the La-rich phase identified by XRD. Moreover, the increase in the thickness of the buffer and capping layers, and the apparent formation of two distinct sub-layers in the annealed samples, support our conclusion concerning diffusion from the main layer into the buffer and capping layers to

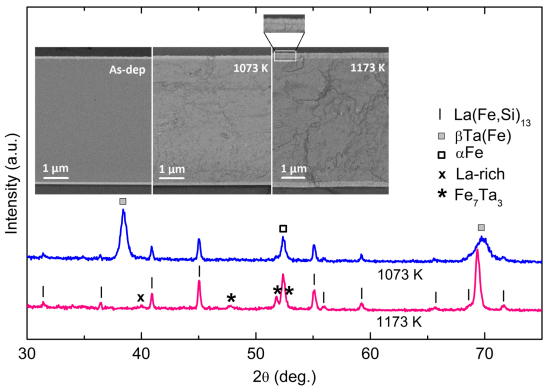

Figure 5.2. *Room temperature XRD pattern for the La-Fe-Si films after annealing at 1073 and 1173 K. The inset shows cross-sectional backscattered electron SEM images for the La-Fe-Si films before (left) and after annealing at 1073 K (middle) and 1173 K (right).*

form two distinct Fe-Ta phases.

Considering the La-Fe-Si films before and after annealing at 1173 K, EDX analysis conducted on the as-deposited and annealed films indicate compositions of $LaFe_{11.2}Si_{1.9}$ and $LaFe_{10.9}Si_{2.1}$, respectively. This change in composition may be attributed to the diffusion of Fe into the Ta layers. The lattice constant at room temperature (a = 11.456 Å) of the annealed $LaFe_{10.9}Si_{2.1}$ films derived from XRD analysis is very close to that reported for bulk alloy of the same composition [34, 36].

Figure 5.3a shows magnetization as a function of temperature in a field of 0.01 and 0.1 T measured in the in-plane direction for the La-Fe-Si film after annealing at 1173 K. A broad transition from the paramagnetic to the ferromagnetic state suggests a second-order magnetic phase transition with T_C = 245 K. While no information could be found concerning the magnetic properties of Fe_7Ta_3 or Fe-containing β-Ta, Fe_2Ta is reported to be a Pauli paramagnet [133]. The remanent magnetisation above the transition is thus attributed to the α-Fe phase identifed in XRD patterns. In-plane and out-of-plane M(H) curves measured at 5 K and 300 K are compared in Fig. 5.3b. The difference between these curves at 5 K is attributed to shape anisotropy in the La-Fe-Si layer (demag factor 1) while the small difference at 300 K suggests that the α-Fe inclusions are almost spherical (demag factor 1/3). From the value of the saturation magnetization at 5 K and 300 K, the amount of the α-Fe impurity and the spontaneous magnetization of the $LaFe_{10.9}Si_{2.1}$ phase at 5 K are roughly estimated to be of the order of 5 vol.%. and 9.3×10^5 Am^{-1}, respectively. Using the Maxwell relations [30] for the magnetization isotherms near T_C (see Fig. 5.3b), the isothermal entropy change is estimated to be about 60 $kJm^{-3}K^{-1}$ for a 7 T field change (see Fig. 5.3c). These values are comparable to that of bulk alloy with the same composition [29, 34, 36].

While thermal hysteresis is a signature of a first-order transition, it is not expected to occur in materials showing a second-order magnetic phase transition [134]. Despite the fact

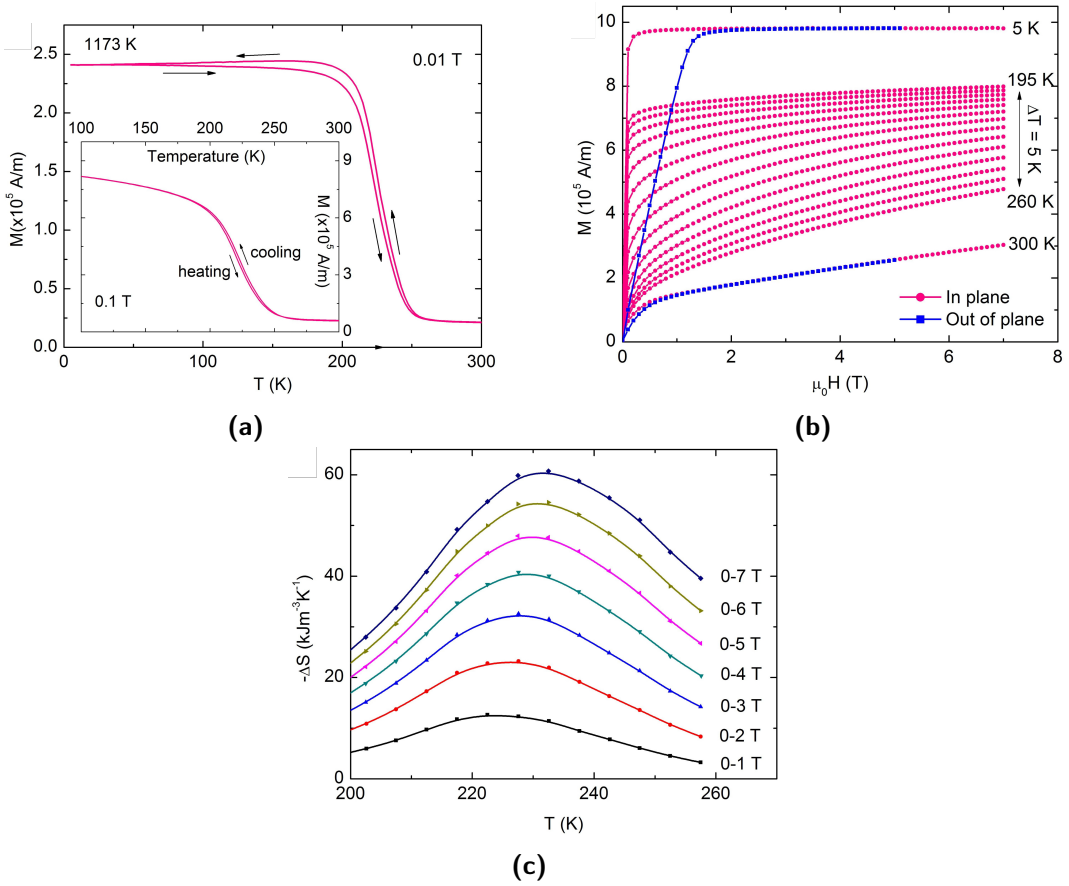

Figure 5.3. *Temperature-dependent magnetization on cooling and heating measured in the in-plane direction in magnetic fields of 0.01 T and 0.1 T (inset) (a), the magnetization as a function of magnetic field in the in-plane and out-of-plane directions (b), and the isothermal entropy change under field changes in the vicinity of T_C (c) for the La-Fe-Si films after annealing at 1173 K.*

that our films appear to show a second-order transition, we observe clearly the separation of the magnetization curves on cooling and heating in the vicinity of T_C (see Fig. 5.3a). What is more, T_C measured on heating is smaller than that measured on cooling. This is contrary to the usually observed thermal hysteresis in materials with a ferro – paramagnetic phase transition of first order nature which exhibit a larger T_C on heating than that on cooling [37, 135]. It should be noted that the M(T) data were recorded in sweep mode at various rates of temperature change from 1 to 5 K/min. No considerable change of the M(T) curves was observed due to different heating or cooling rates, indicating that the observed negative thermal hysteresis is not an instrumental artifact caused by thermal lag.

From Fig. 5.3a, we can also see the thermal irreversibility of the magnetization far below T_C in a low field of 0.01 T. Note that such a phenomenon was not observed in a higher field of 0.1 T (see inset of Fig. 5.3a). This thermal irreversibility may originate from the thermal evolution of strain in the La-Fe-Si layer caused by the neighboring layers since the La(Fe,Si)$_{13}$ materials display a negative thermal expansion in the vicinity of T_C [33, 38]. Thermal irreversibility of the strain may happen, weakly affecting the magnetic anisotropy and leading to such an unusual magnetic phenomenon. This thermally irreversible behavior

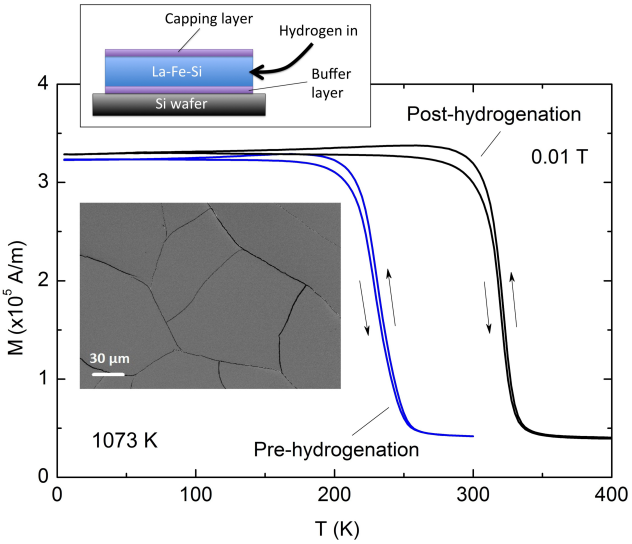

Figure 5.4. *Temperature-dependent magnetization on cooling and heating in an in-plane magnetic field of 0.01 T for a 1073 K annealed La-Fe-Si film before and after hydrogenation. Insets show a top-view image of the sample that is acquired with an in-lens detector and schematic demonstration of the hydrogenation process.*

of the strain may also give rise to different values of T_C upon cooling and heating, resulting in the observed inverse thermal hysteresis.

Comparing the M(T) curves measured in the in-plane configuration for the 1073 K annealed sample before and after hydrogention (see Fig. 5.4), it can be seen that T_C is increased by approximately 100 K upon hydrogenation. Hydrogen absorption may occur through the capping layer, as Ta is highly permeable to hydrogen [136], through cracks formed during the post-deposition annealing step, that can be clearly observed in plan-view SEM imaging (see insets of Fig. 5.4), are expected to serve as fast routes for hydrogen entry to the La-Fe-Si layer. The magnetic transition is found to be sharper in hydrogenated films. Finally, the unusual phenomena described above persist after hydrogentation.

In summary, the preparation of $La(Fe,Si)_{13}$ in thin-film form has been reported for the first time. While films show values of Curie temperature, lattice constant, field-induced isothermal entropy change and spontaneous magnetization comparable with values reported for bulk material of similar composition, they also display unusual features, i.e. irreversible M(T) curves and an inverse thermal hysteresis. Elucidation of the origin of these effects requires further investigation. Films can be hydrogenated so as to increase the transition temperature to above room temperature. The successful fabrication of $La(Fe,Si)_{13}$ thin films opens prospects for the study of material properties and for the exploitation of the phase change use in micro-systems applications.

CHAPTER 6

Conclusions and Prospects

6.1 Conclusions

This thesis deals with the study and control of phase transition characteristics in magnetic phase change materials produced in film form. While the main emphasis is on the Fe-Rh system, La-Fe-Si was also studied. In the case of FeRh-based films, the influence of both composition and strain were studied. The former was achieved using a combinatorial approach in which compositionally graded films were deposited on large wafers and magnetic and structural characterization made as a function of position. The influence of strain was studied with the use of piezo-electric substrates. La-Fe-Si films were successfully prepared and the transition temperature was modified by the introduction of interstitial hydrogen. The main results on each material system can be summarized as follows.

Compositionally graded Fe-Rh films were prepared by magnetron sputtering of a composite target comprised of an Fe base and superposed pieces of Rh placed on one side of the Fe base. The Rh content varied linearly across the substrate. The amount of Rh was modified by changing the surface area of Rh on the target, so as to achieve close to equi-atomic composition near the centre of the substrate. The ferromagnetic to antiferromagnetic (FM-AFM) transition was achieved in a certain composition range, as revealed by magnetization and resistivity measurements, both made as a function of temperature and/or magnetic field. The effects of post-deposition annealing conditions on the M(T) behavior was studied for various compositions. Addition of a third element (Pt or Ni) to the FeRh layer was achieved by deposition of a thin layer of the material as buffer and capping layer followed by post-deposition annealing leading to diffusion of the Pt or Ni into the FeRh layer. As expected from previous studies, addition of Pt (Ni) led an increase (decrease) of the transition temperature. This shift in transition temperature is exploited to facilitate characterization of the magneto-structural change in a given experimental set-up.

We established that a change in optical properties occurs on passing from material in the FM state to material in the AFM state, as the Rh content is increased across the substrate. This optical transition can be seen by the naked eye as an abrupt change in optical contrast at the FM-AFM interface. It occurs in Fe-Rh, Fe-Rh-Pt and Fe-Rh-Ni films and can be moved in a reversible manner by heating or cooling the sample. Ellipsometry measurements were used to quantify the change in optical properties at the FM-AFM

interface and provide evidence for an electronic contribution to the first order transition in Fe-Rh based films.

By studying the temperature dependent position of the optical transition, we were able to construct a phase diagram of the Fe-Rh-Pt system. The thus established phase diagram was coherent with results from XRD and VSM-SQUID measurements. Such a detailed phase diagram based on a continuous variation of composition, evidences an enhanced stability (higher transition temperature) of the antiferromagnetic phase for a specific composition, which is close to the equiatomic one.

Having succeeded in producing high quality Fe-Rh films displaying the desired AFM-FM transition, we then studied the influence of strain on the transition characteristics. This was achieved by depositing films of the optimum composition on a (001) PMN-PT piezoelectric substrate, positioned in the appropriate region of the substrate holder. Strain control of the phase change in these PMN-PT/FeRh heterostructures was investigated through transport measurements using set-ups developed in this thesis. It was found that the transition temperature could be shifted by up to 22 K upon application of a low electric field ($10\,\mathrm{V} \sim 0.32\,\mathrm{kV/cm}$). The strain-induced resistance change is large, which is attractive for applications. The AFM state is stabilized in strained films, the in-plane strain being compressive or tensile. Such experiments suggest that the anisotropic character of the piezo-electric strain plays a dominant role compared to the isotropic volume change.

In the case of the La-Fe-Si system, we succeeded in preparing films of $La(Fe,Si)_{13}$ for the first time. Compositionally graded films were produced by triode sputtering of a homogeneous alloy target, thanks to the difference in solid angle of sputtering of the constituent elements. While the optimal films show values of Curie temperature, lattice constant, field-induced isothermal entropy change and spontaneous magnetization comparable with values reported for bulk material of similar composition, they also display unusual features, i.e. irreversible M(T) curves and an inverse thermal hysteresis. Elucidation of the origin of these effects requires further investigation. The transition temperature was increased by 100 K, from below room temperature to above room temperature, upon hydrogenation.

6.2 Prospects

The Fe-Rh system has proved to be a very good model system for studying magnetic phase transitions and holds much potential for future studies. In the short term, we could extend the strain study by using (011) PMN-PT as the piezoelectric substrate. The in-plane strain anisotropy of a (011) PMN-PT substrate is compressive along the [100] direction, tensile along the [01-1] direction, and a stronger effect is expected than for the (001) PMN-PT used in the present study. Extending the study to anisotropic in-plane strains using (011) PMN-PT cuts would allow to understand more deeply the strain control of the transition. The strain study could be extended to Fe-Rh-Ni alloys, which have a stronger response to pressure than the Fe-Rh-Pt films studied so far. Besides, simulation of strain control of the phase change could be performed to predict and understand in more depth the physics

involved. Reducing the transition temperature of FeRh (using Ni substitution for example) would allow to keep the study temperature range away from PMN-PT Curie temperature.

In the mid-term, we could extend the use of the optical transition in compositionally graded Fe-Rh-based films to establish the phase diagram of samples doped with various elements. This could help to extend the temperature range of application of Fe-Rh samples. Studying these graded films opens new routes, for example it becomes possible to decorrelate the effect of composition from the effects of disorder by using as parameters position along the graded films and annealing conditions.

On the long term, we could explore the potential for exploiting 1) the optical transition in Fe-Rh-based films and 2) strain control of the FM-AFM transition in FeRh-based films.

In the case of the $La(Fe,Si)_{13}$ system, though we succeeded in producing films for the first time ever, we had problems with reproducing the results. We tentatively attribute this to Cu contamination following a modification in the sputtering system. In the short term we need to reproduce the results and then in the mid-term we could study the influence of strain on the transition characteristics, by depositing optimized films on piezo-electric substrates. This study would benefit from the experience gained with the Fe-Rh system. In the long term, we could explore the potential for exploiting the magnetostructural phase change in $La(Fe,Si)_{13}$ films in micro-systems, be it for cooling or actuation.

Beyond the interest in studying phase change characteristics, hybrid phase change - piezo systems are of interest for studying magneto-elastic mediated electric field control of magnetisation. This aspect will be studied in collaboration with two other members of MNM, L. Ranno and A. Bernand-Mantel and will complement their work on direct electric field effects on magnetism. Such hybrid systems may also be used for energy harvesting in which the temperature or magnetic field induced modification of the magnetic state of the phase change material may induce strain in the piezoelectric layer.

APPENDIX A

Strain-induced magnetic anisotropy control in a hybrid structure PZT/Glass/Ni

A.1 Introduction

The electrical control of magnetic properties using composite materials is of interest. A series of experimental studies reported the ability to control the Curie temperature, magnetization, magnetization reversal spin polarization or even the phase change [73, 137, 138, 139, 69, 140, 9]. On the theoretical side, the total free energy (see Eqn. 1.10 in chapter 1) is used to predict the effect [62, 67, 66, 73, 68, 63, 64, 70, 65, 141, 142, 71].

One of the most used piezoelectric materials is perovskite PZT, while Nickel is one of the most well-known magneto-elastic materials. Nickel is chosen as a model system to study the ME effect due to its advantages such as a well-known material, a prototype of 3d ferromagnetism, the Curie temperature above room temperature $T_C \sim 631\,K$, the high magnetization at RT and the high magnetostriction $\lambda \sim -32.9 \times 10^{-6}$. Although many publications reported the strain control of magnetic properties in the hybrid structure using Nickel, the strain control of the out-of-plane (OOP) magnetic anisotropy has not been reported yet.

In this work, we demonstrate anisotropy field control in the hybrid structure of PZT/Glass/Ni via a strain-mediated coupling. This effect was monitored using transport measurements. Nickel-based hybrid structures were also used as test structures to validate our developed set-ups.

A.2 Strain-induced magnetic anisotropy control

A.2.1 Preparation of the hybrid structure

The hybrid structure of piezoelectricity/ferromagnetism is PZT 180 μm/Glass 100 μm/Ni 30 nm. Nickel film was deposited on a glass, and then they were glued onto a commerical PZT disc using glue. Thicknesses of PZT and Nickel film were measured using a FESEM machine (not shown here). The top and bottom of PZT were covered by silver paste layers which play the role of electrodes for applying electric fields (E-fields). By using this structure, we rule out the charging effect and the interfacial effect between the PZT

substrate and Ni film. As a trade-off, the strain transfered from substrate to the Nickel film can be weakened due to the glass layer. However, a test of the strain transfer on a structure of PZT/glass allowed to break the slide of glass, which infers a good transfer of strain from substrate to glass (and film).

Magnetic measurements (M(T) and M(H)) were characterized using a VSM-SQUID machine (not shown here). These measurements were done on the sample glass/Ni (without the PZT substrate). The results showed that the Curie temperature is 631 K and the magnetization value is $M_S \sim 465\times10^3$ A/m which are consistent with values in literature. Moreover, the anisotropic magnetoresistance effect (AMR) is around 0.55 % at RT (not shown here).

A.2.2 Dependence of anisotropy field H_a on temperature

Dependence of anisotropy field H_a of the Nickel film on temperature was shown in figure A.1b. Each data point in the figure A.1b is a complete measurement of the AMR effect R(H) as shown in figure A.1a. The figure A.1a also showed the method to extract H_a from R(H) loops.

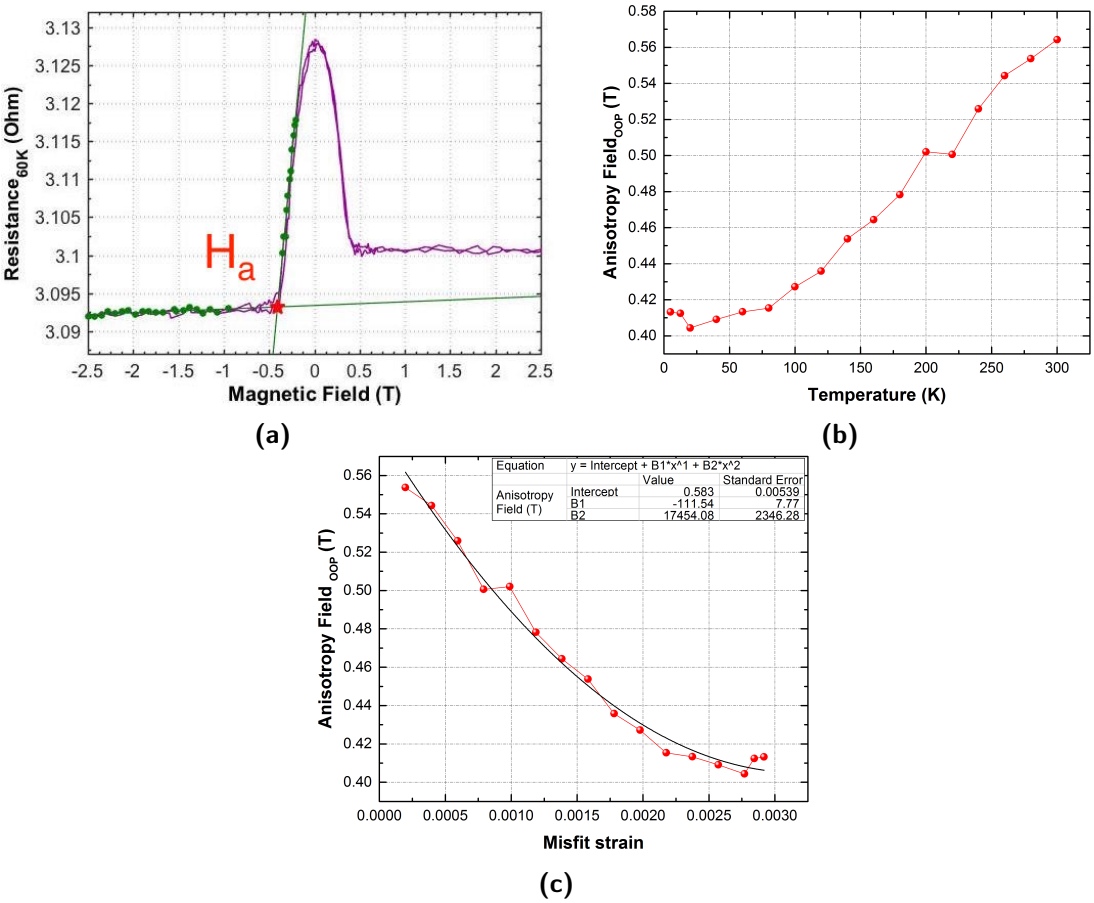

Figure A.1. *(a) A magnetoresistance measurement of the heterostructure at 60 K and the method to extract H_a. (b) Dependence of OOP anisotropy field on temperature. (c) Dependence of OOP anisotropy field on the calculated misfit strain.*

The figure A.1b shows that H_a decreases upon cooling, though the demagnetizing field increases. The dependence of H_a on temperature is quite linear in the temperature range between 100 K and 300 K, while this dependence is non-linear below 50 K. In the linear range, the change of OOP anisotropy field H_a against temperature is:

$$\mu_0 \frac{\triangle H_a}{\triangle T} \simeq 0.5\, mT.K^{-1} \tag{A.1}$$

The change of H_a accounted for by differential thermal expansion between substrate and film, which can be calculated as follows. Thermal expansions of Si and Ni at room temperature are 3 and 12.89 μm/(m.K), respectively. We used thermal expansion data of Si for glass. The misfit strain u between the substrate and the free standing film is expressed as: u = (3 - 12.89)(T-300). Using this relationship, the dependence of anisotropy field on this misfit strain $H_a(u)$ is calculated as shown in figure A.1c (the red curve). A polynominal function with the order of 2 was used to fit the $H_a(u)$ curve (the black one), resulting in an intercept of 0.583 T. It means that when no strain between substrate and film, the anisotropy field is 0.583 T.

For a quantitative comparison, we calculate $B = \mu_0 M$ using magnetic experimental data from measurements using VSM SQUID. With $M_S = 4.65 \cdot 10^5$ A/m, $\mu_0 = 4\pi \cdot 10^{-7}$ N/A^2 (or T·m/A), we have B $\simeq$ 0.584 T which is good agreement with the result above.

The large difference in thermal expansions infers that Ni film are in-plane tensile when cooled down. Having a negative magnetostriction, the easy-axis reorientation in Ni film will occur from the in-plane direction to the OOP direction during cooling. Due to the complicated behaviour of the thermal expansion of substrate at low temperature, the dependence of H_a on temperature is non-linear at low temperature as shown in figure A.1b.

Although an use of temperature-induced-strain can change the anisotropy field, this process is complex because of involvement of temperature and non-linear thermal expansions. Hence, an active strain using a piezoelectric substrate is of interest. In the following parts, we present the control of resistance and anisotropy field using the E-field-induced-strain.

A.2.3 Dependence of resistance on the electric field

We measured resistance of the Ni film versus E-field R(E) at room temperature without external magnetic field. Figure A.2a shows the relative change in resistance as a function of E-field, defined as $\triangle R/R_{min} = \left[R(E) - R_{min}\right]/R_{min}$, where R_{min} is the minimum resistance of the R(E) curve. This relative change reaches maximum value at E = $\pm$17.8 kV/cm and becomes zero around $\pm$8 kV/cm, which are electric coercive fields of PZT. This value implies that the PZT substrate used at here is a soft piezoceramics [47].

We also obtain the in-plane strain of the PZT substrate S(E) using the Ni film as a strain gauge with a gauge factor of -12.1 [143], as shown in figure A.2b. The piezoelectric constant d_{31} of PZT can be estimated using the linear part from 0 to $\pm E_C$: $d_{31} \simeq$ -414 pm/V, which is a little larger than typical value of soft piezoceramic materials ($\sim$ 300 pm/V). The

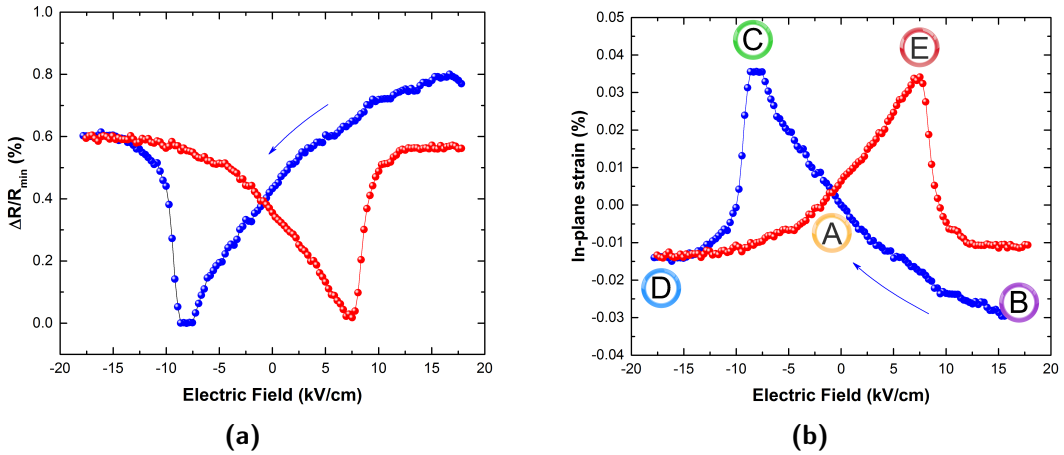

Figure A.2. *(a) The relative change in resistance as a function of E-field in the heterostructure. (b) In-plane strain of the PZT substrate using the Ni film as a strain gauge.*

contribution of domain reorientation in PZT under E-field can be a reason for obtaining this higher value. In addition, the change of resistance can be influenced by the AMR effect. A measurement of the strain using a real strain gauge is needed to compare and asset this result.

In brief, the typical butterfly curve is proof of a good transfer from the elastic strain of PZT to the Ni film. In the following section, strain control of OOP anisotropy field is described.

A.2.4 E-field-induced-strain control of anisotropy field H_a

Showing a good strain transfer from substrate to film, the OOP anisotropy field now can be controlled using E-field through strain from the PZT substrate. Anisotropy fields H_a were measured using transport measurements R(H) on a full loop S(E) of the PZT substrate. Each data point of H_a was was extracted from a complete measurement of R(H) curves as same as above (A.2.2). Figure A.3a shows a control of OOP anisotropy field using E-field.

A butterfly shaped curve H_a(E) is clearly shown in figure A.3a, implying the strain coupling between the PZT substrate and Ni film. Because of the glass layer between PZT and Ni, the interfacial and charge mediated couplings are rule out. The change in H_a is clearly caused by the strain controlled by an external E-field. We also see that the change in H_a is quite linear when the applied electric field is smaller than the coercive field ($E_3 < |E_C|$). Applying an electric field of 17.8 kV/cm, changes H_a by 54 mT. The relative change in OOP anisotropy field can be estimated (see Fig. A.3b):

$$\frac{\triangle H}{H_a(E=0)} = \frac{H_a(E_{max}) - H_a(E=0)}{H_a(E=0)} \simeq 10\,\% \tag{A.2}$$

corresponding to $\sim 0.56\,\%/(\mathrm{kV/cm})$.

Besides that, we also have the change of H_a on the electric field which is calculated as follows:

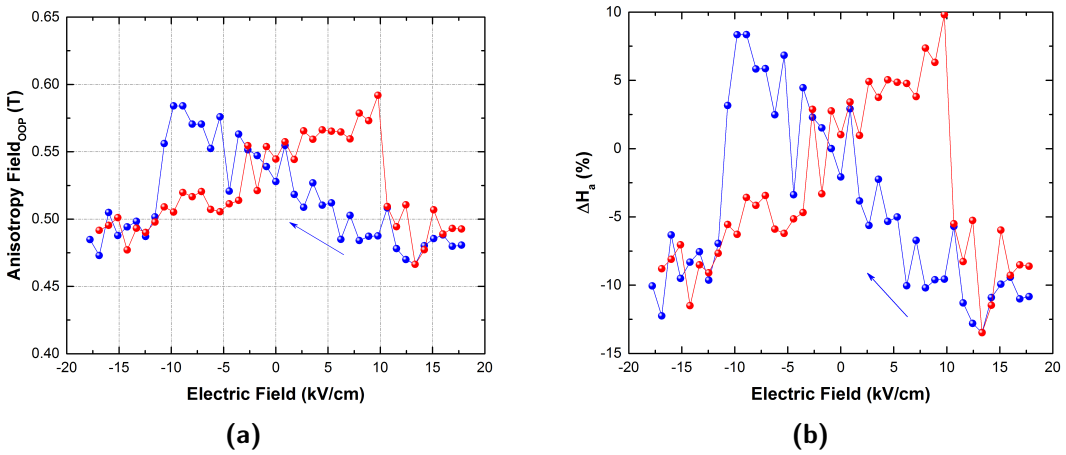

Figure A.3. *(a) Control of OOP anisotropy field in the heterostructure PZT/Glass/Ni through E-field-induced-strain by experiment. (b) The change in H_a is as a function of E-field.*

$$\mu_0 \frac{\triangle H}{\triangle E} = \frac{H_a(E_{max}) - H_a(E=0)}{\triangle E} \simeq 3\, mT/(kV/cm) \tag{A.3}$$

One can see that $H_a(E)$ tracks a same change trend as the stimulus in-plane strain of PZT. From A to B in the figure A.2b, the in-plane strain is compressive, which leads to a promotion of the easy-axis in the in-plane direction. As a result, the OOP anisotropy field decreases exhibiting a similar variation trend with the magnetic coercive field H_C against strain [137]. While the in-plane strain is expansive from A to C, resulting in an increase of H_a. In this case, a rotation of magnetization from in-plane to OOP occurs, impling an increase of H_C. Because of the symmetry, the behaviour of H_a against E-fields could be understood in the mechanism.

A.3 Conclusions

In summary, we have reported the ability to control the OOP anisotropy field using the heterostructure PZT/Glass/Ni, through the E-field-induced-strain. This study demonstrates strain control of the OOP anisotropy field of Ni in the heterostructure. Applying E-field of 17.8 kV/cm, the anisotropy field is changed by 54 mT (10 % of the demagnetizing field).

APPENDIX B

Strain control of the magnetic coercive field in the ultra thin film Co

B.1 Introduction

Electric field control of ferromagnetism can be interesting for storage applications. Mechanisms for this E-field control of magnetic properties are (i) the interfacial coupling, (ii) the charging coupling, (iii) the strain coupling, mentioned in the chapter 1. The ultra thin film Co here has a perpendicular magnetic anisotropy. The E-field control of domain wall nucleation in the ultra thin film Co through the charging effect was reported by A. Bernand-Mantel et al. in 2013 [144]. In this study, we report the E-field control of the magnetic coercive field H_C in the ultra thin film Co through the strain coupling.

B.2 Strain control of the magnetic coercive field in the ultra thin film Co

The ultra thin film Co was deposited on a glass in order to avoid the interfacial coupling, the charging coupling and the roughness of the PZT substrate. The Co film in this study was deposited in a same way as A. Bernand-Mantel did [144]. A Glass 100 μm/Ta 5 nm / Pt 2 nm / Co 0.8 nm /AlO_x multilayer stack was stuck to the PZT substrate using glue. The ultrathin magnetic film is characterized by out of plane anisotropy as shown in figure B.1a, which is measured using polar Kerr microscopy (MOKE). Here, the magnetic field is applied in the oup of plane direction. The external electric field is also applied to the PZT substrate in the out of plane direction as well. All the measuremts were performed at room temperature. We note that the raw image intensity data was processed to remove a linear background signal.

The dependence of the measured coercivity value on the electric field applied to the PZT substrate $H_C(E)$ is shown in figure B.1b. Each data point corresponds to a complete hysteresis loop in the Kerr microscope. A first remark is that the signal is very stable considering that the measurements are made over a time span of roughly 4 hours. The $H_C(E)$ has a typical butterfly shape, which is a feature of the E-field-induced-strain behaviour of PZT. A 1 % change in coercivity is measured, but equipment limits such as mechanical stability, drift need to be checked for a confirmation of this change.

The Kerr signal of the heterostructure as a function of the applied E-field $I_{Kerr}(E)$ is

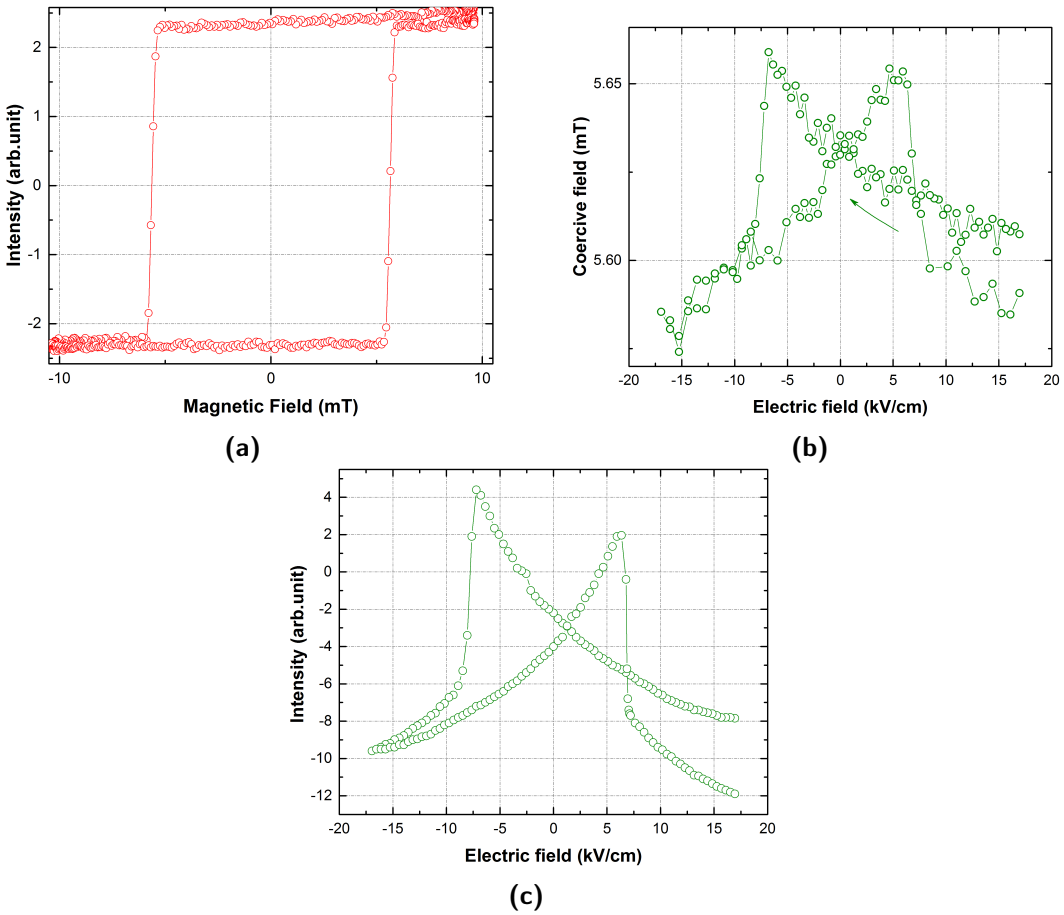

Figure B.1. *(a) M(H) loop of a Glass/Ta 5 nm/Pt 2 nm/Co 0.8 nm/AlO_x multilayer stack glued to the PZT substrate. (b) The dependence of the coercivity in the Co layer on the applied electric field to PZT. (c) The Kerr signal of the heterostructure is as a function of the applied voltage.*

measured and shown in figure B.1c. The Kerr signal reflects the spontaneous magnetization of the ultra film Co. Hence, the $I_{Kerr}(E)$ describes the electrical control of the magnetism through the strain coupling. We can see that this curve exhibits a butterfly shape which is consistent with the strain against E-field loop of the PZT substrate and the $H_C(E)$ above. Two peaks corresponding to the electric coercive field of PZT are obtained with the similar values as well.

B.3 Conclusion

In this study, we reported the strain control of the magnetic coercive field in the ultra thin film Co. The observed signal is stable although it took 4 hours to measure. Besides that, the Kerr signal as a function of the applied electric field is also characterized. However, the change in H_C is small. A choice of more suitable Co samples having a smaller magnetic anisotropy can increase this change.

References

[1] O. Gutfleisch, M. A. Willard, E. Brück, C. H. Chen, S. G. Sankar, and J. P. Liu, "Magnetic Materials and Devices for the 21st Century: Stronger, Lighter, and More Energy Efficient," *Advanced Materials*, vol. 23, no. 7, pp. 821–842, 2011. [Online]. Available: http://dx.doi.org/10.1002/adma.201002180

[2] K. G. Sandeman, "Magnetocaloric materials: The search for new systems," *Scripta Materialia*, vol. 67, no. 6, pp. 566 – 571, 2012, viewpoint Set No. 51: Magnetic Materials for Energy. [Online]. Available: http://www.sciencedirect.com/science/article/pii/S1359646212001595

[3] J. Liu, T. Gottschall, K. P. Skokov, J. D. Moore, and O. Gutfleisch, "Giant magnetocaloric effect driven by structural transitions," *Nature Materials*, vol. 11, no. 7, pp. 620–626, July 2012.

[4] D. A. Porter, K. E. Easterling, and M. Y. Sherif, *Phase transformations in metals and alloys*, 3rd ed. CRC Press, Taylor & Francis Group, 2009.

[5] J. A. Ricodeau and D. Melville, "Model of the antiferromagnetic-ferromagnetic transition in FeRh alloys," *Journal of Physics F: Metal Physics*, vol. 2, no. 2, p. 337, 1972. [Online]. Available: http://stacks.iop.org/0305-4608/2/i=2/a=024

[6] D. Bourgault, J. Tillier, P. Courtois, D. Maillard, and X. Chaud, "Large inverse magnetocaloric effect in Ni45Co5Mn37.5In12.5 single crystal above 300 K," *Applied Physics Letters*, vol. 96, no. 13, 2010. [Online]. Available: http://scitation.aip.org/content/aip/journal/apl/96/13/10.1063/1.3372633

[7] M. Fallot, *Ann. Phys.*, vol. 10, pp. 291–332, 1938.

[8] X. Marti, I. Fina, C. Frontera, J. Liu, P. Wadley, Q. He, R. J. Paull, J. D. Clarkson, J. Kudrnovský, I. Turek, J. Kuneš, D. Yi, J.-H. Chu, C. T. Nelson, L. You, E. Arenholz, S. Salahuddin, J. Fontcuberta, T. Jungwirth, and R. Ramesh, "Room-temperature antiferromagnetic memory resistor," *Nature Materials*, vol. 13, no. 4, pp. 367–374, April 2014.

[9] R. O. Cherifi, V. Ivanovskaya, L. C. Phillips, A. Zobelli, I. C. Infante, E. Jacquet, V. Garcia, S. Fusil, N. Briddon, P. R. abd Guiblin, A. Mougin, A. A. Ünal, F. Kronast, S. Valencia, B. Dkhil, A. Barthélémy, and M. Bibes, "Electric-field control of magnetic order above room temperature," *Nature Materials*, vol. 13, no. 4, pp. 345–351, April 2014.

[10] Y. Lee, Z. Q. Liu, J. T. Heron, J. D. Clarkson, J. Hong, C. Ko, M. D. Biegalski, , U. Aschauer, S. L. Hsu, M. E. Nowakowski, J. Wu, H. M. Christen, S. Salahuddin, J. B. Bokor, N. A. Spaldin, D. G. Schlom, and R. Ramesh, "Large resistivity

modulation in mixed-phase metallic systems," *Nature Communications*, vol. 6, July 1st 2015.

[11] P. A. Algarabel, M. R. Ibarra, C. Marquina, A. del Moral, J. Galibert, M. Iqbal, and S. Askenazy, "Giant room-temperature magnetoresistance in the FeRh alloy," *Applied Physics Letters*, vol. 66, no. 22, pp. 3061–3063, 1995. [Online]. Available: http://scitation.aip.org/content/aip/journal/apl/66/22/10.1063/1.114278

[12] J. van Driel, R. Coehoorn, G. J. Strijkers, E. Brück, and F. R. de Boer, "Compositional dependence of the giant magnetoresistance in Fe_xRh_{1-x} thin films," *Journal of Applied Physics*, vol. 85, no. 2, pp. 1026–1036, 1999. [Online]. Available: http://scitation.aip.org/content/aip/journal/jap/85/2/10.1063/1.369224

[13] L. J. Swartzendruber, "The Fe-Rh (Iron-Rhodium) System," *Bulletin of Alloy Phase Diagrams*, vol. 5, no. 5, pp. 456–462, 1984.

[14] M. Takahashi and R. Oshima, "Annealing Effect on Phase Transition of Equiatomic FeRh Alloy," *Materials Transactions, JIM*, vol. 36, no. 6, pp. 735–742, 1995.

[15] S. Inoue, H. Y. Y. Ko, and T. Suzuki, "Magnetic Properties of Single-Crystalline FeRh Alloy Thin Films," *Magnetics, IEEE Transactions on*, vol. 44, no. 11, pp. 2875–2878, Nov 2008.

[16] E. Bertaut, F. d. Bergevin, and G. Roult, "Neutron Diffraction Study of $Fe_{0.4}Rh_{0.53}$," *Comptes Rendus de l'Académie des Sciences*, vol. 256, pp. 1688–1691, 1963.

[17] G. Shirane, R. Nathans, and C. W. Chen, "Magnetic Moments and Unpaired Spin Densities in the Fe-Rh Alloys," *Phys. Rev.*, vol. 134, pp. A1547–A1553, Jun 1964. [Online]. Available: http://link.aps.org/doi/10.1103/PhysRev.134.A1547

[18] V. Moruzzi and P. Marcus, "Magnetic structure in FeRh from constrained total-energy calculations," *Solid State Communications*, vol. 83, no. 9, pp. 735 – 738, 1992. [Online]. Available: http://www.sciencedirect.com/science/article/pii/0038109892901542

[19] J. S. Kouvel, "Unusual Nature of the Abrupt Magnetic Transition in FeRh and Its Pseudobinary Variants," *Journal of Applied Physics*, vol. 37, no. 3, pp. 1257–1258, 1966. [Online]. Available: http://scitation.aip.org/content/aip/journal/jap/37/3/10.1063/1.1708424

[20] S. Maat, J.-U. Thiele, and E. E. Fullerton, "Temperature and field hysteresis of the antiferromagnetic-to-ferromagnetic phase transition in epitaxial FeRh films," *Phys. Rev. B*, vol. 72, p. 214432, Dec 2005. [Online]. Available: http://link.aps.org/doi/10.1103/PhysRevB.72.214432

[21] J. B. McKinnon, D. Melville, and E. W. Lee, "The antiferromagnetic-ferromagnetic transition in iron-rhodium alloys," *Journal of Physics C: Solid State Physics*, vol. 3, no. 1S, p. S46, 1970. [Online]. Available: http://stacks.iop.org/0022-3719/3/i=1S/a=306

[22] R. Barua, F. Jiménez-Villacorta, and L. H. Lewis, "Predicting magnetostructural trends in FeRh-based ternary systems," *Applied Physics Letters*, vol. 103, no. 10, 2013. [Online]. Available: http://scitation.aip.org/content/aip/journal/apl/103/10/10.1063/1.4820583

[23] R. C. Wayne, "Pressure Dependence of the Magnetic Transitions in Fe-Rh Alloys," *Phys. Rev.*, vol. 170, pp. 523–527, Jun 1968. [Online]. Available: http://link.aps.org/doi/10.1103/PhysRev.170.523

[24] A. I. Zakharov, A. M. Kadomtseva, R. Z. Levitin, and E. G. Ponyatovkii, "Magnetic and magnetoelastic properties of a metamagnetic iron-rhodium alloy," *Soviet Physics JETP*, 1964.

[25] L. I. Vinokurova, A. V. Vlasov, and M. Pardavi-Horváth, "Pressure effects on magnetic phase transitions in FeRh and FeRhIr alloys," *Phys. Status Solidi B*, vol. 78, pp. 353–357, 1976.

[26] M. P. Annaorazov, S. A. Nikitin, A. L. Tyurin, K. A. Asatryan, and A. K. Dovletov, "Anomalously high entropy change in FeRh alloy," *Journal of Applied Physics*, vol. 79, no. 3, pp. 1689–1695, 1996. [Online]. Available: http://scitation.aip.org/content/aip/journal/jap/79/3/10.1063/1.360955

[27] Y. Ohtani and I. Hatakeyama, "Features of broad magnetic transition in FeRh thin film," *Journal of Magnetism and Magnetic Materials*, vol. 131, no. 3, pp. 339 – 344, 1994. [Online]. Available: http://www.sciencedirect.com/science/article/pii/030488539490278X

[28] M. A. de Vries, M. Loving, A. P. Mihai, L. H. Lewis, D. Heiman, and C. H. Marrows, "Hall-effect characterization of the metamagnetic transition in FeRh," *New Journal of Physics*, vol. 15, no. 1, p. 013008, 2013. [Online]. Available: http://stacks.iop.org/1367-2630/15/i=1/a=013008

[29] K. A. Gschneidner Jr., V. K. Pecharsky, and A. O. Tsokol, "Recent developments in magnetocaloric materials," *Reports on Progress in Physics*, vol. 68, no. 6, p. 1479, 2005. [Online]. Available: http://stacks.iop.org/0034-4885/68/i=6/a=R04

[30] E. Brück, "Developments in magnetocaloric refrigeration," *Journal of Physics D: Applied Physics*, vol. 38, no. 23, p. R381, 2005. [Online]. Available: http://stacks.iop.org/0022-3727/38/i=23/a=R01

[31] V. Franco, J. Blázquez, B. Ingale, and A. Conde, "The Magnetocaloric Effect and Magnetic Refrigeration Near Room Temperature: Materials and Models," *Annual Review of Materials Research*, vol. 42, no. 1, pp. 305–342, 2012. [Online]. Available: http://dx.doi.org/10.1146/annurev-matsci-062910-100356

[32] A. Smith, C. R. Bahl, R. Bjørk, K. Engelbrecht, K. K. Nielsen, and N. Pryds, "Materials Challenges for High Performance Magnetocaloric Refrigeration Devices," *Advanced Energy Materials*, vol. 2, no. 11, pp. 1288–1318, 2012. [Online]. Available: http://dx.doi.org/10.1002/aenm.201200167

[33] R. Huang, Y. Liu, W. Fan, J. Tan, F. Xiao, L. Qian, and L. Li, "Giant Negative Thermal Expansion in NaZn13-Type La(Fe, Si, Co)13 Compounds," *Journal of the American Chemical Society*, vol. 135, no. 31, pp. 11 469–11 472, 2013, pMID: 23885928. [Online]. Available: http://dx.doi.org/10.1021/ja405161z

[34] B. G. Shen, J. R. Sun, F. X. Hu, H. W. Zhang, and Z. H. Cheng, "Recent Progress in Exploring Magnetocaloric Materials," *Advanced Materials*, vol. 21, no. 45, pp. 4545–4564, 2009. [Online]. Available: http://dx.doi.org/10.1002/adma.200901072

[35] L. F. Bao, F. X. Hu, L. Chen, J. Wang, J. R. Sun, and B. G. Shen, "Magnetocaloric properties of $La(Fe,Si)_{13}$-based material and its hydride prepared by industrial mischmetal," *Applied Physics Letters*, vol. 101, no. 16, 2012. [Online]. Available: http://scitation.aip.org/content/aip/journal/apl/101/16/10.1063/1.4760262

[36] K. Niitsu, S. Fujieda, A. Fujita, and R. Kainuma, "Microstructure and magnetic properties of as-quenched cubic and tetragonal $La(Fe_{1-x}Si_x)_{13}$ & compounds," *Journal of Alloys and Compounds*, vol. 578, pp. 220 – 227, 2013. [Online]. Available: http://www.sciencedirect.com/science/article/pii/S092583881301219X

[37] J. Lyubina, R. Schäfer, N. Martin, L. Schultz, and O. Gutfleisch, "Novel Design of $La(Fe,Si)_{13}$ Alloys Towards High Magnetic Refrigeration Performance," *Advanced Materials*, vol. 22, no. 33, pp. 3735–3739, 2010. [Online]. Available: http://dx.doi.org/10.1002/adma.201000177

[38] F.-x. Hu, B.-g. Shen, J.-r. Sun, Z.-h. Cheng, G.-h. Rao, and X.-x. Zhang, "Influence of negative lattice expansion and metamagnetic transition on magnetic entropy change in the compound $LaFe_{11.4}Si_{1.6}$," *Applied Physics Letters*, vol. 78, no. 23, pp. 3675–3677, 2001. [Online]. Available: http://scitation.aip.org/content/aip/journal/apl/78/23/10.1063/1.1375836

[39] A. Fujita, S. Fujieda, Y. Hasegawa, and K. Fukamichi, "Itinerant-electron metamagnetic transition and large magnetocaloric effects in $La(Fe_xSi_{1-x})_{13}$ compounds and their hydrides," *Phys. Rev. B*, vol. 67, p. 104416, Mar 2003. [Online]. Available: http://link.aps.org/doi/10.1103/PhysRevB.67.104416#j#

[40] B. R. Hansen, L. T. Kuhn, C. Bahl, M. Lundberg, C. Ancona-Torres, and M. Katter, "Properties of magnetocaloric $La(Fe,Co,Si)_{13}$ produced by powder metallurgy," *Journal of Magnetism and Magnetic Materials*, vol. 322, no. 21, pp. 3447 – 3454, 2010. [Online]. Available: http://www.sciencedirect.com/science/article/pii/S0304885310004385

[41] M. Getzlaff, *Fundamentals of Magnetism*. Springer, 2008.

[42] W. Eerenstein, N. D. Mathur, and J. F. Scott, "Multiferroic and magnetoelectric materials," *Nature Reviews*, vol. 442, pp. 759–765, 17 August 2006.

[43] D. Damjanovic, "Ferroelectric, dielectric and piezoelectric properties of ferroelectric thin films and ceramics," *Reports on Progress in Physics*, vol. 61, no. 9, pp. 1267–1324, Sep 1998.

[44] C. R. Bowen, H. A. Kim, P. M. Weaver, and S. Dunn, "Piezoelectric and ferroelectric materials and structures for energy harvesting applications," *Energy Environ. Sci.*, vol. 7, pp. 25–44, 2014. [Online]. Available: http://dx.doi.org/10.1039/C3EE42454E

[45] T. Tsurumi, Y. Kumano, N. Ohashi, T. Takenaka, and O. Fukunaga, "90^o Domain Reorientation and Electric-Field-Induced Strain of Tetragonal Lead Zirconate Titanate Ceramics," *Jpn. J. Appl. Phys.*, vol. 36, pp. 5970–5975, 1997.

[46] S.-E. Park and T. R. Shrout, "Ultrahigh strain and piezoelectric behavior in relaxor based ferroelectric single crystals," *Journal of Applied Physics*, vol. 82, no. 4, pp. 1804–1811, 1997. [Online]. Available: http://scitation.aip.org/content/aip/journal/jap/82/4/10.1063/1.365983

[47] V. Giurgiutiu and S. E. Lyshevski, *Micromechatronics: Modeling, Analysis, and Design with MATLAB*, 2nd ed., S. E. Lyshevski, Ed. CRC Press, May 2009.

[48] J. J. Liu, Y. C. Zhou, A. K. Soh, and J. Y. Li, "Engineering domain configurations for enhanced piezoelectricity in barium titanate single crystals," *Applied Physics Letters*, vol. 88, no. 3, 2006. [Online]. Available: http://scitation.aip.org/content/aip/journal/apl/88/3/10.1063/1.2166480

[49] B. Noheda, D. E. Cox, G. Shirane, J. Gao, and Z.-G. Ye, "Phase diagram of the ferroelectric relaxor (1-x)$PbMg_{1/3}Nb_{2/3}O_3$-x$PbTiO_3$," *Phys. Rev. B*, vol. 66, p. 054104, Aug 2002. [Online]. Available: http://link.aps.org/doi/10.1103/PhysRevB.66.054104

[50] G. A. Smolenskiy and I. E. Chupis, "Ferroelectromagnets," *Soviet Physics Uspekhi*, vol. 25, no. 7, p. 475, 1982. [Online]. Available: http://stacks.iop.org/0038-5670/25/i=7/a=R02

[51] C. W. Nan, M. I. Bichurin, S. Dong, D. Viehland, and G. Srinivasan, "Multiferroic magnetoelectric composites: Historical perspective, status, and future directions," *Journal of Applied Physics*, vol. 103, 2008.

[52] C. A. F. Vaz, J. Hoffman, C. H. Ahn, and R. Ramesh, "Magnetoelectric coupling effects in multiferroic complex oxide composite structures," *Advanced materials*, vol. 22, pp. 2900–2918, 2010.

[53] ——, "Magnetoelectric Coupling Effects in Multiferroic Complex Oxide Composite Structures," *Advanced Materials*, vol. 22, no. 26-27, pp. 2900–2918, 2010. [Online]. Available: http://dx.doi.org/10.1002/adma.200904326

[54] M. Weisheit, S. Fähler, A. Marty, Y. Souche, C. Poinsignon, and D. Givord, "Electric Field-Induced Modification of Magnetism in Thin-Film Ferromagnets," *Science*, vol. 315, no. 5810, pp. 349–351, 2007. [Online]. Available: http://science.sciencemag.org/content/315/5810/349

[55] W. Eerenstein, M. Wiora, J. L. Prieto, J. F. Scott, and N. D. Mathur, "Giant sharp and persistent converse magnetoelectric effects in multiferroic epitaxial heterostructures," *Nature Materials*, vol. 6, pp. 348 – 351, April 8^{th} 2007.

[56] C. Thiele, K. Dörr, S. Fähler, L. Schultz, D. C. Meyer, A. A. Levin, and P. Paufler, "Voltage-controlled epitaxial strain in $La_{0.7}Sr_{0.3}MnO_3/Pb(Mg_{1/3}Nb_{2/3})O_3 - PbTiO_3$(001) films," *Applied Physics Letters*, vol. 87, p. 262502, December 20^{th} 2005.

[57] L. W. Martin, Y. H. Chu, and Ram, "Advances in the growth and characterization of magnetic, ferroelectric, and multiferroic oxide thin films," *Materials Science and Engineering R*, vol. 68, pp. 89–133, 2010.

[58] F. Tsui, M. C. Smoak, T. K. Nath, and C. B. Eom, "Strain-dependent magnetic phase diagram of epitaxial La0.67Sr0.33MnO3 thin films," *Applied Physics Letters*, vol. 76, no. 17, pp. 2421–2423, 2000. [Online]. Available: http://scitation.aip.org/content/aip/journal/apl/76/17/10.1063/1.126363

[59] M. Angeloni, G. Balestrino, N. G. Boggio, P. G. Medaglia, P. Orgiani, and A. Tebano, "Suppression of the metal-insulator transition temperature in thin $La_{0.7}Sr_{0.3}MnO_3$ films," *Journal of Applied Physics*, vol. 96, no. 11, pp. 6387–6392, 2004.

[60] C. Thiele, K. Dörr, O. Bilani, J. Rödel, and L. Schultz, "Influence of strain on the magnetization and magnetoelectric effect in $La_{0.7}A_{0.3}MnO_3/PMN-PT(001)(A = Sr, Ca)$," *Physical Review B*, vol. 75, p. 054408, February 12^{th} 2007.

[61] N. D'Souza, M. S. Fashami, S. Bandyopadhyay, and J. Atulasimha, "Experimental Clocking of Nanomagnets with Strain for Ultralow Power Boolean Logic," *Nano Letters*, vol. 16, no. 2, pp. 1069–1075, 2016, pMID: 26744913.

[62] N. A. Pertsev, "Giant magnetoelectric effect via strain-induced spin reorientation transitions in ferromagnetic films," *Phys. Rev. B*, vol. 78, p. 212102, Dec 2008. [Online]. Available: http://link.aps.org/doi/10.1103/PhysRevB.78.212102

[63] N. A. Pertsev and H. Kohlstedt, "Resistive switching via the converse magnetoelectric effect in ferromagnetic multilayers on ferroelectric substrates," *Nanotechnology*, vol. 21, no. 47, p. 475202, 2010. [Online]. Available: http://stacks.iop.org/0957-4484/21/i=47/a=475202

[64] N. A. Pertsev, H. Kohlstedt, and R. Knöchel, "Ferromagnetic resonance in epitaxial films: Effects of lattice strains and voltage control via ferroelectric substrate," *Phys. Rev. B*, vol. 84, p. 014423, Jul 2011. [Online]. Available: http://link.aps.org/doi/10.1103/PhysRevB.84.014423

[65] N. A. Pertsev, "Strain-mediated electric-field control of multiferroic domain structures in ferromagnetic films," *Applied Physics Letters*, vol. 102, no. 11, pp. –, 2013. [Online]. Available: http://scitation.aip.org/content/aip/journal/apl/102/11/10.1063/1.4795938

[66] J.-M. Hu, C.-W. Nan, and L.-Q. Chen, "Size-dependent electric voltage controlled magnetic anisotropy in multiferroic heterostructures: Interface-charge and strain comediated magnetoelectric coupling," *Phys. Rev. B*, vol. 83, p. 134408, Apr 2011. [Online]. Available: http://link.aps.org/doi/10.1103/PhysRevB.83.134408

[67] J.-M. Hu and C. W. Nan, "Electric-field-induced magnetic easy-axis reorientation in ferromagnetic/ferroelectric layered heterostructures," *Phys. Rev. B*, vol. 80, p. 224416, Dec 2009. [Online]. Available: http://link.aps.org/doi/10.1103/PhysRevB.80.224416

[68] J.-M. Hu, Z. Li, J. Wang, and C. W. Nan, "Electric-field control of strain-mediated magnetoelectric random access memory," *Journal of Applied Physics*, vol. 107, no. 9, pp. –, 2010. [Online]. Available: http://scitation.aip.org/content/aip/journal/jap/107/9/10.1063/1.3373593

[69] J.-M. Hu, Z. Li, L.-Q. Chen, and C. W. Nan, "Design of a Voltage-Controlled Magnetic Random Access Memory Based on Anisotropic Magnetoresistance in a Single Magnetic Layer," *Advanced Materials*, vol. 24, pp. 2869–2873, 2012.

[70] J. M. Hu, T. N. Yang, L. Q. Chen, and C. W. Nan, "Voltage-driven perpendicular magnetic domain switching in multiferroic nanoislands," *Journal of Applied Physics*, vol. 113, no. 19, pp. –, 2013. [Online]. Available: http://scitation.aip.org/content/aip/journal/jap/113/19/10.1063/1.4804157

[71] J. M. Hu, T. Yang, J. Wang, H. Huang, J. Zhang, and C.-W. Chen, Long-Qingand Nan, "Purely Electric-Field-Driven Perpendicular Magnetization Reversal," *Nano Letters*, vol. 15, no. 1, pp. 616–622, 2015, pMID: 25549019. [Online]. Available: http://dx.doi.org/10.1021/nl504108m

[72] R.-C. Peng, J. J. Wang, J.-M. Hu, L.-Q. Chen, and C.-W. Nan, "Electric-field-driven magnetization reversal in square-shaped nanomagnet-based multiferroic heterostructure," *Applied Physics Letters*, vol. 106, no. 14, 2015.

[73] M. Weiler, A. Brandlmaier, S. Geprägs, M. Althammer, M. Opel, C. Bihler, H. Huebl, M. S. Brandt, R. Gross, and S. T. B. Goennenwein, "Voltage controlled inversion of magnetic anisotropy in a ferromagnetic thin film at room temperature," *New Journal of Physics*, vol. 11, no. 1, p. 013021, 2009.

[74] G. Yu, Z. Wang, M. Abolfath-Beygi, C. He, X. Li, K. L. Wong, P. Nordeen, H. Wu, G. P. Carman, X. Han, I. A. Alhomoudi, P. K. Amiri, and K. L. Wang, "Strain-induced modulation of perpendicular magnetic anisotropy in Ta/CoFeB/MgO structures investigated by ferromagnetic resonance," *Applied Physics Letters*, vol. 106, no. 7, pp. –, 2015. [Online]. Available: http://scitation.aip.org/content/aip/journal/apl/106/7/10.1063/1.4907677

[75] K. Wasa, I. Kanno, and H. Kotera, Eds., *Handbook of Sputtering Technology*, second edition ed. Oxford: William Andrew Publishing, 2012.

[76] D. K. Maurya, A. Sardarinejad, and K. Alameh, "Recent Developments in R.F. Magnetron Sputtered Thin Films for pH Sensing Applications-An Overview," *Coatings*, vol. 4, no. 4, p. 756, 2014.

[77] G. Ciuta, "Une tude exprimentale de la coercivit des aimants NdFeB," Ph.D. dissertation, University of Grenoble, 2013.

[78] [Online]. Available: http://hyperphysics.phy-astr.gsu.edu/hbase/quantum/bragg.html

[79] V. K. Pecharsky and P. Y. Zavalij, Eds., *Fundamentals of powder diffraction and structural characterization of materials*. Springer, 2009.

[80] G. Williamson and W. Hall, "X-ray line broadening from filed aluminium and wolfram," *Acta Metallurgica*, vol. 1, no. 1, pp. 22 – 31, 1953. [Online]. Available: http://www.sciencedirect.com/science/article/pii/0001616053900066

[81] R. W. Simmonds, "Thermal physics: Quantum interference heats up," *Nature*, vol. 492, no. 7429, pp. 358 – 359, December 2012.

[82] S. Tumanski, *Handbook of magnetic measurements*. CRC Press, Taylor & Francis Group, 2011.

[83] M. Losurdo and K. Hingerl, Eds., *Ellipsometry at the Nanoscale*. Springer, 2013.

[84] [Online]. Available: http://www.jawoollam.com/tutorial_4.html

[85] H. G. Tompkins and E. A. Irene, Eds., *Handbook of ellipsometry*. Springer, 2005.

[86] C. B. Sawyer and C. H. Tower, "Rochelle salt as a dielectric," *Physical Review*, vol. 35, 1930.

[87] R. Waser, U. Bottger, and S. Tiedke, *Polar Oxides: Properties, Characterization, and Imaging*. Wiley-VCH, 2005.

[88] M. Annaorazov, K. Asatryan, G. Myalikgulyev, S. Nikitin, A. Tishin, and A. Tyurin, "Alloys of the FeRh system as a new class of working material for magnetic refrigerators," *Cryogenics*, vol. 32, no. 10, pp. 867 – 872, 1992. [Online]. Available: http://www.sciencedirect.com/science/article/pii/001122759290352B

[89] M. R. Ibarra and P. A. Algarabel, "Giant volume magnetostriction in the FeRh alloy," *Phys. Rev. B*, vol. 50, no. 6, pp. 4196–4199, Aug 1994. [Online]. Available: http://link.aps.org/doi/10.1103/PhysRevB.50.4196

[90] Y. Ohtani and I. Hatakeyama, "Antiferro-ferromagnetic transition and microstructural properties in a sputter deposited FeRh thin film system," *Journal of Applied Physics*, vol. 74, no. 5, pp. 3328–3332, 1993. [Online]. Available: http://scitation.aip.org/content/aip/journal/jap/74/5/10.1063/1.354557

[91] J. Cao, N. T. Nam, S. Inoue, H. Y. Y. Ko, N. N. Phuoc, and T. Suzuki, "Magnetization behaviors for FeRh single crystal thin films," *Journal of Applied Physics*, vol. 103, no. 7, 2008. [Online]. Available: http://scitation.aip.org/content/aip/journal/jap/103/7/10.1063/1.2828812

[92] W. Lu, P. Huang, Z. Chen, C. He, Y. Wang, and B. Yan, "Magnetization studies of first-order magnetostructural phase transition in polycrystalline FeRh thin films," *Journal of Physics D: Applied Physics*, vol. 45, no. 43, p. 435001, 2012. [Online]. Available: http://stacks.iop.org/0022-3727/45/i=43/a=435001

[93] J. M. Lommel and J. S. Kouvel, "Effects of Mechanical and Thermal Treatment on the Structure and Magnetic Transitions in FeRh," *Journal of Applied Physics*, vol. 38, no. 3, pp. 1263–1264, 1967. [Online]. Available: http://scitation.aip.org/content/aip/journal/jap/38/3/10.1063/1.1709570

[94] E. M. Hofer and P. Cucka, "Magnetic properties of Rh-rich FeRh alloy," *J. Phys. Chem. Solids.*, vol. 27, pp. 1552–1555, April 1966.

[95] M. K. Chattopadhyay, S. B. Roy, A. K. Nigam, K. J. S. Sokhey, and P. Chaddah, "Metastability and giant relaxation across the ferromagnetic to antiferromagnetic transition in $Ce(Fe_{0.96}Ru_{0.04})_2$," *Phys. Rev. B*, vol. 68, p. 174404, Nov 2003. [Online]. Available: http://link.aps.org/doi/10.1103/PhysRevB.68.174404

[96] J. Zhong, Z. H. Jin, and K. Lu, "Melting, superheating and freezing behaviour of indium interpreted using a nucleation-and-growth model," *Journal of Physics: Condensed Matter*, vol. 13, no. 50, p. 11443, 2001. [Online]. Available: http://stacks.iop.org/0953-8984/13/i=50/a=304

[97] S. O. Mariager, L. Le Guyader, M. Buzzi, G. Ingold, and C. Quitmann, "Imaging the antiferromagnetic to ferromagnetic first order phase transition of FeRh," *ArXiv e-prints*, Jan. 2013.

[98] C. Baldasseroni, C. Bordel, A. X. Gray, A. M. Kaiser, F. Kronast, J. Herrero-Albillos, C. M. Schneider, C. S. Fadley, and F. Hellman, "Temperature-driven nucleation of ferromagnetic domains in FeRh thin films," *Applied Physics Letters*, vol. 100, no. 26, 2012. [Online]. Available: http://scitation.aip.org/content/aip/journal/apl/100/26/10.1063/1.4730957

[99] L. Zsoldos, "Lattice parameter change of FeRh alloys due to antiferromagnetic-ferromagnetic transformation," *Phys. Stat. Sol.*, vol. 20, pp. K25–K28, 1967.

[100] J. S. Kouvel, "Magnetic properties at high pressures," in *The proceedings of the AIME Symposium, "Metallurgy of High Pressures and High Temperatures"*, 1963.

[101] K. Kamenev, Z. Arnold, J. Kamard, and N. V. Baranov, "Pressure induced giant volume magnetostriction in the $(Fe_{1-x}Ni_x)_{49}Rh_{51}$ alloys," *Journal of Applied Physics*, vol. 81, no. 8, pp. 5680–5682, 1997. [Online]. Available: http://scitation.aip.org/content/aip/journal/jap/81/8/10.1063/1.364634

[102] Y. Waseda, E. Matsubara, and K. Shinoda, *X-Ray Diffraction Crystallography.* Springer, 2011.

[103] H. Miyajima, S. Yuasa, and Y. Otani, "First-Order Magnetic Phase Transitions Observed in bct FeRh–Pt, Pd Systems," *Japanese Journal of Applied Physics*, vol. 32, no. S3, p. 232, 1993. [Online]. Available: http://stacks.iop.org/1347-4065/32/i=S3/a=232

[104] H. E. Kissinger, "Variation of peak temperature with heat rate in differential thermal analysis," *Journal of Research of the National Bureau of Standards*, vol. 57, no. 4, pp. 217–221, October 1956.

[105] C. B. Ndao, "Matériaux magnétiques en couches. Etudes des systèmes FePt et FeRh," Ph.D. dissertation, Université de Grenoble, April 2011.

[106] L.-Y. Chen and D. W. Lynch, "Ellipsometric studies of magnetic phase transitions of Fe-Rh alloys," *Phys. Rev. B*, vol. 37, pp. 10 503–10 509, Jun 1988. [Online]. Available: http://link.aps.org/doi/10.1103/PhysRevB.37.10503

[107] M. A. Khan, C. Koenig, and R. Riedinger, "Interband dielectric constants in antiferromagnetic, ferromagnetic and paramagnetic phases of FeRh," *Journal of Physics F: Metal Physics*, vol. 13, no. 8, p. L159, 1983. [Online]. Available: http://stacks.iop.org/0305-4608/13/i=8/a=004

[108] R. Engel-Herbert and T. Hesjedal, "Calculation of the magnetic stray field of a uniaxial magnetic domain," *Journal of Applied Physics*, vol. 97, no. 7, 2005. [Online]. Available: http://scitation.aip.org/content/aip/journal/jap/97/7/10.1063/1.1883308

[109] C. Kittel, "Model of Exchange-Inversion Magnetization," *Phys. Rev.*, vol. 120, pp. 335–342, Oct 1960. [Online]. Available: http://link.aps.org/doi/10.1103/PhysRev.120.335

[110] J. M. Lommel, "Thermodynamics of the First-Order Transition in FeRh," *Journal of Applied Physics*, vol. 40, no. 9, pp. 3880–3881, 1969. [Online]. Available: http://scitation.aip.org/content/aip/journal/jap/40/9/10.1063/1.1658300

[111] P. Tu, A. J. Heeger, J. S. Kouvel, and J. B. Comly, "Mechanism for the First-Order Magnetic Transition in the FeRh System," *Journal of Applied Physics*, vol. 40, no. 3, pp. 1368–1369, 1969. [Online]. Available: http://scitation.aip.org/content/aip/journal/jap/40/3/10.1063/1.1657670

[112] C. Koenig, "Self-consistent band structure of paramagnetic, ferromagnetic and antiferromagnetic ordered FeRh," *Journal of Physics F: Metal Physics*, vol. 12, no. 6, p. 1123, 1982. [Online]. Available: http://stacks.iop.org/0305-4608/12/i=6/a=013

[113] J. Ivarsson, G. Pickett, and J. Tóth, "The electronic heat capacity of nearly stoichiometric ordered FeRh alloys," *Physics Letters A*, vol. 35, no. 3, pp. 167 – 168, 1971. [Online]. Available: http://www.sciencedirect.com/science/article/pii/0375960171901289

[114] B. Fogarassy, T. Kemény, L. Pál, and J. Tóth, "Electronic Specific Heat of Iron-Rhodium and Iron-Rhodium-Iridium Alloys," *Phys. Rev. Lett.*, vol. 29, pp. 288–291, Jul 1972. [Online]. Available: http://link.aps.org/doi/10.1103/PhysRevLett.29.288

[115] J. Y. Rhee and D. W. Lynch, "Optical properties of Fe-Rh alloys," *Phys. Rev. B*, vol. 51, pp. 1926–1927, Jan 1995. [Online]. Available: http://link.aps.org/doi/10.1103/PhysRevB.51.1926

[116] V. L. Moruzzi and P. M. Marcus, "Antiferromagnetic-ferromagnetic transition in FeRh," *Phys. Rev. B*, vol. 46, pp. 2864–2873, Aug 1992. [Online]. Available: http://link.aps.org/doi/10.1103/PhysRevB.46.2864

[117] D. W. Cooke, F. Hellman, C. Baldasseroni, C. Bordel, S. Moyerman, and E. E. Fullerton, "Thermodynamic Measurements of Fe-Rh Alloys," *Phys. Rev. Lett.*, vol. 109, p. 255901, Dec 2012. [Online]. Available: http://link.aps.org/doi/10.1103/PhysRevLett.109.255901

[118] M. E. Gruner, E. Hoffmann, and P. Entel, "Instability of the rhodium magnetic moment as the origin of the metamagnetic phase transition in $\alpha -$ FeRh," *Phys. Rev. B*, vol. 67, p. 064415, Feb 2003. [Online]. Available: http://link.aps.org/doi/10.1103/PhysRevB.67.064415

[119] R. Y. Gu and V. P. Antropov, "Dominance of the spin-wave contribution to the magnetic phase transition in FeRh," *Phys. Rev. B*, vol. 72, p. 012403, Jul 2005. [Online]. Available: http://link.aps.org/doi/10.1103/PhysRevB.72.012403

[120] T. H. E. Lahtinen, K. J. A. Franke, and S. van Dijken, "Electric-field control of magnetic domain wall motion and local magnetization reversal," *Scientific Reports*, vol. 2, no. 258, 2012. [Online]. Available: http://dx.doi.org/10.1038/srep00258

[121] M. Ghidini, R. Pellicelli, J. Prieto, X. Moya, J. Soussi, J. Briscoe, S. Dunn, and N. Mathur, "Non-volatile electrically-driven repeatable magnetization reversal with no applied magnetic field," *Nat Commun*, vol. 4, no. 1453, 02 2013. [Online]. Available: http://dx.doi.org/10.1038/ncomms2398

[122] D. Pantel, S. Goetze, D. Hesse, and M. Alexe, "Reversible electrical switching of spin polarization in multiferroic tunnel junctions," *Nature Materials*, vol. 11, no. 4, pp. 289–293, 04 2012. [Online]. Available: http://dx.doi.org/10.1038/nmat3254

[123] Z.-G. Ye, Ed., *Handbook of advanced dielectric, piezoelectric and ferroelectric materials: Synthesis, properties and applications*. Woodhead Publishing, 2008.

[124] M. G. Cain, Ed., *Characterisation of Ferroelectric Bulk Materials and Thin Films*, ser. Springer Series in Measurement Science and Technology. Springer, 2014, vol. 2.

[125] I. Suzuki, M. Itoh, and T. Taniyama, "Elastically controlled magnetic phase transition in Ga-FeRh/BaTiO3(001) heterostructure," *Applied Physics Letters*, vol. 104, no. 2, 2014. [Online]. Available: http://scitation.aip.org/content/aip/journal/apl/104/2/10.1063/1.4861455

[126] A. Sehirlioglu, D. A. Payne, and P. Han, "Thermal expansion of phase transformations in $(1-x)Pb(Mg_{1/3}, Nb_{2/3}O_3 - xPbTiO_3$: evidence for preferred domain alignment in one of the <001> directions for melt-grown crystals," *Phys. Rev. B*, vol. 72, p. 214110, Dec 2005. [Online]. Available: http://link.aps.org/doi/10.1103/PhysRevB.72.214110

[127] H. Ibach and H. Lüth, *Solid-State Physics An introduction to principles of materials science*, 4th ed. Springer, 2009.

[128] K. Uchino, S. Nomura, L. E. Cross, S. J. Jang, and R. E. Newnham, "Electrostrictive effect in lead magnesium niobate single crystals," *Journal of Applied Physics*, vol. 51, no. 2, pp. 1142–1145, 1980. [Online]. Available: http://scitation.aip.org/content/aip/journal/jap/51/2/10.1063/1.327724

[129] F. Li, L. Jin, Z. Xu, D. Wang, and S. Zhang, "Electrostrictive effect in Pb(Mg1/3Nb2/3)O3-xPbTiO3 crystals," *Applied Physics Letters*, vol. 102, no. 15, 2013. [Online]. Available: http://scitation.aip.org/content/aip/journal/apl/102/15/10.1063/1.4802792

[130] Z.-G. Ye, Ed., *Handbook of Advanced Dielectric, Piezoelectric and Ferroelectric Materials*, ser. Woodhead Publishing Series in Electronic and Optical Materials. Woodhead Publishing, 2008.

[131] S. Wada, H. Kakemoto, and T. Tsurumi, "Enhanced Piezoelectric Properties of Piezoelectric Single Crystals by Domain Engineering," *MATERIALS TRANSACTIONS*, vol. 45, no. 2, pp. 178–187, 2004.

[132] V. Witusiewicz, A. Bondar, U. Hecht, V. Voblikov, O. Fomichov, V. Petyukh, and S. Rex, "Experimental study and thermodynamic re-assessment of the binary Fe–Ta system," *Intermetallics*, vol. 19, no. 7, pp. 1059 – 1075, 2011. [Online]. Available: http://www.sciencedirect.com/science/article/pii/S096697951100080X

[133] H. Wijn, Ed., *Magnetic Properties of Metals d-Elements, Alloys and Compounds*. Springer, 1991.

[134] A. M. Tishin and Y. I. Spichkin, *The magnetocaloric effect and its applications*. Institute of Physics Publishing, Bristol, Philadelphia, 2003.

[135] J. Lyubina, K. Nenkov, L. Schultz, and O. Gutfleisch, "Multiple Metamagnetic Transitions in the Magnetic Refrigerant $La(Fe,Si)_{13}H_x$," *Phys. Rev. Lett.*, vol. 101, p. 177203, Oct 2008. [Online]. Available: http://link.aps.org/doi/10.1103/PhysRevLett.101.177203

[136] K. S. Rothenberger, B. H. Howard, R. P. Killmeyer, A. V. Cugini, R. M. Enick, F. Bustamante, M. V. Ciocco, B. D. Morreale, and R. E. Buxbaum, "Evaluation of tantalum-based materials for hydrogen separation at elevated temperatures and pressures," *Journal of Membrane Science*, vol. 218, no. 1–2, pp. 19 – 37, 2003. [Online]. Available: http://www.sciencedirect.com/science/article/pii/S0376738803001340

[137] J. Wang, J. Ma, Z. Li, Y. Shen, Y. Lin, and C. W. Nan, "Switchable voltage control of the magnetic coercive field via magnetoelectric effect," *Journal of Applied Physics*, vol. 110, no. 4, pp. –, 2011. [Online]. Available: http://scitation.aip.org/content/aip/journal/jap/110/4/10.1063/1.3626748

[138] T. Wu, B. Alexandre, P. Zhao, K. P. Mohanchandra, K. Wong, K. L. Wang, C. S. Lynch, and G. P. Carman, "Giant electric-field-induced reversible and permanent magnetization reorientation on magnetoelectric $Ni/(011)[Pb(Mg_{1/3}Nb_{2/3})O_3]_{(1-x)}-[PbTiO_3]_x$ heterostructure," *Applied Physics Letters*, vol. 98, no. 1, pp. –, 2011. [Online]. Available: http://scitation.aip.org/content/aip/journal/apl/98/1/10.1063/1.3534788

[139] H. C. Xuan, L. Y. Wang, Y. X. Zheng, Y. L. Li, Q. Q. Cao, S. Y. Chen, D. H. Wang, Z. G. Huang, and Y. W. Du, "Electric field control of

magnetism without magnetic bias field in the $Ni/Pb(Mg_{1/3}Nb_{2/3})O_3 - PbTiO_3/Ni$ composite," *Applied Physics Letters*, vol. 99, no. 3, pp. –, 2011. [Online]. Available: http://scitation.aip.org/content/aip/journal/apl/99/3/10.1063/1.3616137

[140] M. Feng, J.-j. Wang, J.-M. Hu, J. Wang, J. Ma, H.-B. Li, Y. Shen, Y.-H. Lin, L.-Q. Chen, and C.-W. Nan, "Optimizing direct magnetoelectric coupling in $Pb(Zr,Ti)O_3/Ni$ multiferroic film heterostructures," *Applied Physics Letters*, vol. 106, no. 7, 2015.

[141] J. J. Wang, J.-M. Hu, L.-Q. Chen, and C.-W. Nan, "Strain-domain structure and stability diagrams for single-domain magnetic thin films," *Applied Physics Letters*, vol. 103, no. 14, pp. –, 2013. [Online]. Available: http://scitation.aip.org/content/aip/journal/apl/103/14/10.1063/1.4824165

[142] J. J. Wang, J. M. Hu, J. Ma, J. X. Zhang, L. Q. Chen, and C. W. Nan, "Full 180^o Magnetization Reversal with Electric Fields," *Scientific Reports*, vol. 4, no. 7507, 2014.

[143] S. P. Venkateshan, *Mechanical measurements*, 2nd ed. Wiley, 2015.

[144] A. Bernand-Mantel, L. Herrera-Diez, L. Ranno, S. Pizzini, J. Vogel, D. Givord, S. Auffret, O. Boulle, I. M. Miron, and G. Gaudin, "Electric-field control of domain wall nucleation and pinning in a metallic ferromagnet," *Applied Physics Letters*, vol. 102, no. 12, 2013. [Online]. Available: http://scitation.aip.org/content/aip/journal/apl/102/12/10.1063/1.4798506

Résumé

Le sujet de cette thèse est l'étude et le contrôle de la transition de phase dans des films magnétiques de la famille des magnétocaloriques. Dans le cas de films de FeRh déposés par pulvérisation cathodique, l'influence de la composition et de la contrainte sur la transition antiferromagnétique-ferromagnétique a été étudié. Les caractérisations structurales, magnétiques et électriques ont été faites, en fonction de la position, sur des films à gradient de composition latéral. La substitution partielle par un troisième élément (Ni ou Pt) a été utilisée pour augmenter ou baisser la température de la transition de phase. Nous avons mis en évidence une transition optique lors de la transition de phase. L'utilisation de ce contraste optique nous a permis de construire le diagramme de phase de FeRhPt. Les détails obtenus par cette approche qui permet de faire varier la composition de façon continue nous ont permis de mettre en évidence un optimum de stabilité pour la phase antiferromagnétique (un maximum de la transition de température) proche de la composition équiatomique. Le développement d'une structure intégrée, substrat piézoélectrique (PMN-PT) / film magnétique (FeRh), a permis d'étudier l'effet d'une contrainte piézoélectrique sur la transition à l'aide de montages de transport (sous champ magnétique, sous contrainte, à température variable) développés pendant la thèse. La température de transition peut être décalée de 22 K à l'aide d'une tension de 10 V (soit un champ électrique de 320 V/cm). La variation de résistance induite par la contrainte est grande, ce qui est attractif pour les applications. L'état antiferromagnétique est stabilisé par la contrainte piézoélectrique qui est anisotrope. L'anisotropie de la contrainte joue un rôle important pour modéliser ce résultat. Pour la première fois, nous avons réussi à préparer des films du matériau magnéto-calorique $La(Fe,Si)_{13}$. Les films optimisés présentent des propriétés similaires à celles du massif (température de Curie, paramètre de maille, variation d'entropie isotherme sous champ et aimantation spontanée). Cependant ils montrent aussi des propriétés nouvelles comme des cycles M(T) irréversibles et un hystérésis thermique inversé.